Spring 2016

The mantle transition zone beneath South America from stacking of P-to-S receiver functions

B. A. Goetze

Recommended Citation

Goetze, B. A., "The mantle transition zone beneath South America from stacking of P-to-S receiver functions" (2016). *Masters Theses*. 7500.
https://scholarsmine.mst.edu/masters_theses/7500

THE MANTLE TRANSITION ZONE BENEATH SOUTH AMERICA FROM STACKING OF P-TO-S RECEIVER FUNCTIONS

by

BRUNO DE ALMEIDA GOETZE

A THESIS

Presented to the Graduate Faculty of the

MISSOURI UNIVERSITY OF SCIENCE AND TECHNOLOGY

In Partial Fulfillment of the Requirements for the Degree

MASTER OF SCIENCE IN GEOLOGY AND GEOPHYSICS

2016

Approved by

Stephen Gao, Advisor
Kelly Liu, Co-Advisor
Neil Anderson

ABSTRACT

The Mantle Transition Zone (MTZ) beneath South America is investigated with stacking of Receiver Functions (RFs) of converted P-to-S phases from the velocity discontinuities at 410 km (d410) and 660 km (d660). A total of 785 seismic stations provided 22,235 high quality RFs, allowing 1,717 MTZ thickness measurements in circular bins of 2° radius. An apparent MTZ structure is derived using the IASP91 reference model, where the d410 mean depth is 409.1 km and the d660 is 661.5 km, and the mean MTZ thickness is 251.8 km. This model presents coherent depressions and uplifts of the discontinuities matching well known velocity anomalies. After experimenting with eleven tomography models, a velocity correction adopting the SAW642ANb model with a 50 km top layer of the JOINT model was found to be the best approach towards a true depth model. This model wields a mean d410 at 413.2 km and the d660 at 662.8 km, whereas the MTZ thickness is 249.6 km. The correlation of depths and MTZ thickness variations supports previously determined Clapeyron Slopes (γ) of 2 MPa/K for the d410 and -3 MPa/K for the d660, reconciling γ with seismic observations. The results are fateful to the tectonic structure of South America, where colder-than-normal MTZ anomalies are found along the Andes, while hotter-than-normal anomalies are found along the Atlantic coast. The latter observed MTZ characteristics spatially correspond well with rift related structures and the former to locations where subducted slab has been inferred. The main inference from these observations is that tectonic processes play a major role in the control of thermal and chemical proprieties of the MTZ.

ACKNOWLEDGMENTS

I thank Dr. Gao and Dr. Liu for providing me with a renewed passion towards Earth sciences. Their very present and bold guidance will leave me with lessons for life and I am deeply thankful for having the opportunity to be a student under their tutoring. In my journey in geosciences, I can never forget the support and friendship that my advisors have always offered me, they have a great deal of responsibility on where I am and where I can be. Therefore, I also thank Dr. Karen Adami-Rodrigues, Dr. Leonardo Renner, and M.S. Camile Urban, my advisors during my undergraduate career.

Gratitude is expressed towards everyone involved in the acquisition and storage of data employed in this study. I thank Dr. Marcelo Assumpção and M.S. Bruno Collaço from the Universidade de Sao Paulo, for their support in the acquisition of data. I also thank Drs. George Araujo de França and Marcelo Peres Rocha from the Universidade de Brasilia, and Dr. John Booker from the University of Washington, for their insightful discussions during the AGU Fall Meeting 2015, but specially for presenting a sincere and unpretentious stance, qualities that sometimes are rare. Dr. Mei Feng was very solicitous in providing the data for this study. I acknowledge the CAPES and the Missouri S&T faculty as exceptional factors in my academic development. I am grateful for the friendship of my colleagues in B40, in which Dr. Youqiang Yu played a decisive role.

Lastly, I thank my family for their support and encouragement. My wife, Emanuele Ambrosi, is paramount in all my achievements, it is impossible to imagine my trajectory without her love.

TABLE OF CONTENTS

Page

SECTION

APPENDICES

LIST OF ILLUSTRATIONS

LIST OF TABLES

NOMENCLATURE

Symbol/Term	Description
γ	Clapeyron Slope
RF	Receiver Function
MTZ	Mantle Transition Zone
d410	Seismic velocity discontinuity at 410 km depth
d660	Seismic velocity discontinuity at 660 km depth
Δ	Earthquake epicentral distance (°)
Mc	Magnitude cut-off
STD	Standard Deviation
SNR	Signal-to-noise ratio
Vp	Velocity of the primary wave
Vs	Velocity of the secondary wave
R	Correlation Coefficient
PGA	Ponta Grossa Arch
SMA	Serra do Mar Arch
APIP	Alto Parnaiba Igneous Province
SFH	Sao Francisco High
EARS	East African Rift System
Teleseismic	Earthquakes that occur at $\Delta \geq 30°$ from the station
Stagnant	Horizontal deflection of the slab in the MTZ

1 INTRODUCTION

The Mantle Transition Zone (MTZ) is a layer of the mantle bounded by two major velocity discontinuities. The upper discontinuity is referred to as d410, as it happens at a depth of ~410 km, and the lower discontinuity as d660, since it occurs at a depth of ~660 km. These discontinuities represent a seismic velocity “jump” of ~4% and ~6%, respectively, in the reference Earth model IASP91 (Kennett and Engdahl, 1991).

Under the assumption that the Mantle has a Pyrolitic composition, the simplest interpretation is that the discontinuities are mineral phase transitions; from olivine to wadsleyite at the d410, and from ringwoodite to perovskite at the d660 (Ringwood, 1975). Direct evidence for mineral phase transition comes from mineral inclusions in diamonds (Pearson *et al*., 2014, Zedgenizov *et al*., 2015). This interpretation is considered rather simple for the d410, but can be more complex for the d660 (Deuss, 2009, Dorogokupets *et al*., 2015). Olivine is less than 70% of the mantle’s composition, a phase change from majorite garnet to postspinel occurs at the d660, and since it has an opposite Clapeyron slope (γ) to the ringwoodite to perovskite phase transition, it counterbalances the effects of temperature variations, making a change of the MTZ thickness harder to correlate to the layer physical state (Tauzin *et al*., 2008).

Even if just the olivine to wadsleyite and ringwoodite to perovskite phase transitions are considered, it is a challenging task to correlate the MTZ structure to its physical state, because estimates of the magnitude of these γ are varied. There is an agreement that the olivine to wadsleyite phase transition is an exothermic reaction and has a positive γ, while the ringwoodite to perovskite phase transition is an endothermic reaction and has a negative γ, but several magnitude values for these Clapeyron slopes have been proposed. Therefore, the MTZ will present thinning or thickening, if abnormally hot or cold, respectively, indicating temperatures departing from average values of ~1700° K (d410) and ~1800° K (d660) (Fukao *et al*., 2009). Even with some difficulties in observing opposite depth changes of the discontinuities (Flanagan and Shearer, 1998); usually a broadening of the MTZ where it interacts with a colder subducted slab has been reported (Helffrich, 2000).

The estimates of the d410 γ vary between 1.5 to 3.0 MPa/K, and the d660 γ between -0.4 to -4.0 MPa/K (Gao and Liu, 2014a). Estimates from studies of the d410 γ and d660 γ have reported greater magnitudes for the d410 (Bina and Helffrich, 1994, Dorogokupets *et al*., 2015), and this presents a contradiction with seismic observations, since the observed topography variations of the d660 are larger than that of the d410 (Flanagan and Shearer, 1998, Helffrich, 2000).

Recent experimental measurements have reported small γ values for anhydrous mineral phase changes, based on this results they proposed that the only manner to reconcile mineral physics with the seismological observations is through the incorporation of significant volumes of water (~2 wt%) into the system (Litasov *et al*., 2005, Ghosh *et al*., 2013), which is supported by water bearing ringwoodite mineral inclusions in diamonds (Pearson *et al*., 2014).

The mineral phase transitions can be even more complex if the effects of different ratios of Mg and Fe in the olivine composition are considered (Bina and Helffrich, 2014). Additionally, the perceived topography observed by seismology may vary due to effects of temperature over the discontinuities sharpness, and perceived depths can be affected by seismic wave’s frequency (Helffrich and Bina, 1994) and inelastic attenuation (Liu, 2003).

South America has had little seismological research performed on the upper mantle structure relative to its dimensions and importance for the understanding of its role in the global geodynamic model. Although the tectonic processes and seismic structure near surface are relatively well known, the same cannot be said about its deeper structure i.e., upper mantle and MTZ. The majority of the geophysical information available for the mantle structure in South America comes from studies at global or regional scales. Its past connection to the African continent and subsequent development of the Atlantic Ocean, accompanied by extensive magmatic activity (Almeida and Carneiro, 1989), and the onset of the world’s largest orogenic system developed by continent-ocean subduction zone (Ramos, 2009), are some of the most recent and significant tectonic process on the earth’s surface.

The subduction of oceanic slab beneath the continent and the Mesozoic-Cenozoic volcanic activity related to the opening of the South Atlantic, if better understood can tell a great deal about the mantle chemical evolution, physical proprieties and geodynamic processes. This is the first attempt to establish a continental knowledge framework for the MTZ beneath South America observing P-to-S conversions from the discontinuities in Receiver Functions (RFs).

1.1 MAJOR TECTONIC AND MAGMATIC PROVINCES OF SOUTH AMERICA

The Meso-Neoarchean history of the South American continent (Figure 1.1) is well represented in the Amazon and Sao Francisco, where the oldest rock samples have

3.4 Ga (Cordani *et al*, 2000). The Transamazonian Cycle took place on the Meso-Paleoproterozoic and was responsible for the majority of the continental crust formation, this was when the São Francisco and Amazon cratons formed a stable proto-continent (Schobbenhaus and Brito Neves, 2003). In the Neoproterozoic several mobile belts were developed, such as the Borborema and Tocatins Province, among others. During the Neoproterozoic to the Cambrian, the Brasiliano Orogenic Cycle was responsible for extensive granite emplacement in the Mantiqueira and Borborema Provinces, and along the Transbrasiliano lineament (Schobbenhaus and Brito Neves, 2003, Brito Neves and Fuck, 2014). At this time the South American and African proto-continents were linked into a great landmass called Gondwana.

In the Cretaceous, the opening of the Atlantic Ocean was accompanied by tholeiitic lava flows (Parana-Etendeka flood basalts), sills and basic intrusions concentrated within Paleozoic synclines, while coeval Alkaline, peralkaline, basaltic magmatism and kimberlitic intrusions along Brasiliano mobile belts are part of the Late Mesozoic magmatism in South America (Schobbenhaus and Brito Neves, 2003).

A generalized uplift of the South America Platform occurred between the end of the Late Jurassic and the Early Cretaceous (Milani *et al*., 2007b). According to Milani *et al*., (2007a) following the end of Permian, all Brazilian sedimentary basins experienced progressive aridity conditions, evolving to desert environments during the Triassic, until the deposition/intrusion of widespread Eojurassic (concentrated in the north) and Eocretaceous magmatism. The sedimentation was restricted in these times and interrupted during the Triassic everywhere, with the exception of basins developed to the south (Brito Neves, 2002) of the latitude 28°S. All Brazilian basins underwent diachronous restructuring during the Late Jurassic to the Early Cretaceous, while in the north it began in Permian times (Brito Neves, 2002). The restructuration involved the development of linear uplifted arches and extensive intrusive and extrusive magmatic activity (Brito Neves, 2002).

In the period between 225 Ma to 100 Ma the continental evolution is related to the rifting of the Pangea supercontinent (Brito Neves, 2002). Two major phases of magmatic activity in the Brazilian platform, at 180-210 Ma (restricted to the north) and 130 Ma (widespread), these ages are associated with major rifting phases (Mizusaki *et al*., 2002). The former age is linked to the opening of the North Atlantic Ocean, while the latter is relative to the South Atlantic Ocean (Mizusaki *et al*., 2002). Mizusaki *et al* (2002) shows that significant peaks of magmatic activity can also be seen at 90 Ma, 50 Ma and 10 Ma in the Brazilian platform. Geraldes *et al*., (2013) highlights four magmatic phases for the South Atlantic, from 80 to 60 Ma and 20 Ma to recent times with intense magmatic activity, while the periods from 105 to 90 Ma and 50 to 20 Ma the magmatic activity was infrequent. According to Geraldes *et al.,* (2013), magmatic occurrences from the Late Cretaceous to Cenozoic in the southeast coast of Brazil are not clear and still open for debate.

Proposed models for the magmatism goes from shallow sources releasing magmas trough adiabatic processes (Almeida and Carneiro, 1989, Guarino *et al*., 2013, Felgate, 2014), delamination (Bizzi *et al*., 1995, Read *et al*., 2004), to plumes rooted in the deep mantle (Gibson *et al*., 1995, Gibson *et al*., 1997, Thompson *et al*., 1998, Sgarbi *et al*., 2004). Similarly, mantle plume activity (Fodor *et al*., 1998, Mizusaki *et al*., 2002), adiabatic melts (Almeida, 2006), and Edge-Driven Convection (King and Ritsema, 2000, King, 2007, Knesel *et al.*, 2011, Perlingeiro *et al.*, 2013), are the competing models proposed for the Cenozoic magmatism in the northeast of Brazil.

The Andean Belt displays basement inliers with Neoproterozoic ages, and rare Paleo-Mesoproterozoic rocks. The region has experienced orogenic activity for the last 500 Ma, through the Famatinian, Gondwanic (Hercynian – this cycle is responsible for the accretion of the Patagonia Massif to the South America continent), and the Meso-Cenozoic Andean Cycles (Cordani *et al*, 2000), where a significant amount of terranes were accreted to the Andean Belt.

The subduction zone structure has a relatively high complexity. The Nazca slab changes its dip along the strike of the subduction zone, from sub-horizontal (flat-slab) to steep plunges, where the seismic energy released by the flat-slab zones is 3 to 5 times greater than in the steep regions (Ramos and Aleman, 2000). The stagnant slab in the Central Andes generates earthquakes in the depth range of 520-620 km, but no earthquake occurs from 325 to 520 km, while rare earthquakes occur in the deflected portion (Liu *et al.*, 2003). This deflected portion of the slab reaches areas beneath Paraguay and west of Brazil (Liu *et al.*, 2003, Rocha *et al.*, 2011).

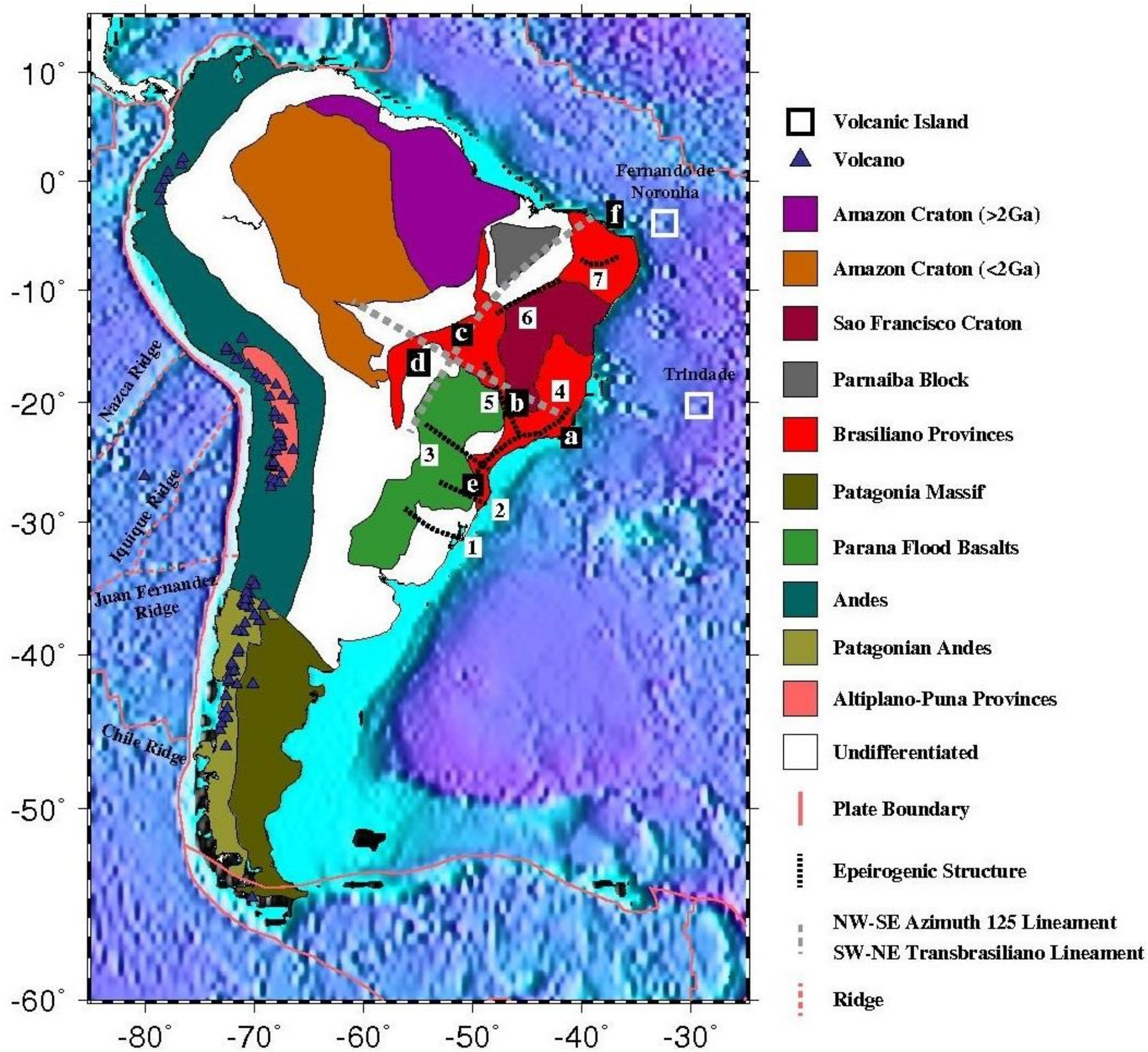

Figure 1.1. Simplified map of the geological provinces of South America. Focus is given to provinces that are pertinent to the observations of this work. The numbers indicate the epeirogenic structures: Rio Grande High (1), Torres Syncline (2), Ponta Grossa Arch (3), Serra do Mar Arch (4), Alto Parnaiba Arch (5), Sao Francisco High (6), and Borborema Plateau (7). Letters indicate approximated location of the alkaline provinces with Late Cretaceous and Cenozoic ages: Serra do Mar Igneous Province (a), Alto Parnaiba Igneous Province (b), Ipora Igneous Province (c), Porexeu Ignous Province (d), Lages Complex (e), and Messejana and Ceara-Mirim Volcanisms (f). The geological elements are modified from Alkmim (2015), Santos *et al*., (2008), Castro *et al*., (2014), Bird (2003), Scire (2015), Barbosa and Sabate (2002), Thiede and Vasconcelos (2010). Holocene volcanoes are from the Global Volcanism Program (2013).

2 DATA AND METHODS

Teleseismic data at epicentral distances between 30° to 100° used in this study were requested from the data centers IRIS DMC (Incorporated Research Institutions for Seismology Data Management Center), IAG-USP (Centro de Sismologia da Universidade de Sao Paulo), RSBR (Rede Sismografica Brasileira), and GFZ (GEOFON German Research Center for Geosciences). The dataset for this study consisted of all temporary and permanent stations deployed in South America (Figure 2.1) that had its data stored in one of the above datacenters until the end of the month of May of 2015 (for stations and networks information see the Appendix A).

Events were chosen with the NEIC (National Earthquake Information Center) catalog (USGS, 2015). The cut-off magnitude (Mc) was defined as $Mc = 4.2 - 0.5 * \left(\frac{Z}{700}\right) + 1.5 * (\Delta - \frac{30}{150})$, where Z is the depth measured in kilometers and Δ is the epicentral distance in degrees. Although the equation allows Mc values smaller than 4, since the earthquake catalog only has events with magnitude equal or greater than 4; this is the minimum magnitude value of the selected events. In practice, shallow teleseismic events (Z = 0 km) were selected with a Mc of 4.2 when near the stations (Δ = 30°), whereas events deeper than 280 km from the same Δ had a Mc equal to 4. At greater Δ values, such as 90°, shallow events had a Mc of 4.8, and if deep (Z =700 km), Mc will be 4.3. The reason for lower Mc values than the commonly adopted in other studies, such as Mc equal to 5.5 (e.g. Pinheiro and Julia, 2014), is that the majority of the dataset comes from temporary stations with operation periods usually ranging from one to six months, and also to benefit from the events coming from the nearby Andes subduction zone. One of the advantages of the adopted Mc values, other than the obvious densification of the dataset, was that the azimuthal distribution of the events became more balanced.

The seismograms were bandpass filtered between 0.02 and 0.2 Hz, after it the signal-to-noise (SNR) ratio related to first arrival on the vertical component was checked following Gao and Liu (2014a), if the SNR was below 4.0 the seismogram was rejected. A weighted filter was applied to reduce the influence of the PP arrival (Gao and Liu, 2014b). A total of 785 broadband seismic stations (Figure 2.1) provided 29,464 seismograms which were converted to receiver functions (RFs). Additional verification of the SNR was performed over the RFs first arrival, rejecting SNR smaller than 1.5, and if the SNR of the P wave coda was less than 1.2, following Gao and Liu (2014a).

The product of the last step was verified visually, rejecting inadequate RFs according to the criteria defined by Ammon (1997). Afterwards, an auto-correlation procedure was adopted to remove RFs in order to reduce the SNR even further. It consisted in stacking the RFs from one station and rejecting each RF of the same station that the first 40s of the trace had a correlation of less than 0.6 with the stacked trace. At total of 4,113 RFs were rejected visually and another 3,116 RFs by the auto-correlation procedure. Therefore, the major downside of the low Mc adopted, low SNR, was compensated.

The South America MTZ model employs 22,235 RFs. Noteworthy, the data lacks coverage of continental portions beneath the Amazon rainforest in Brazil and Colombia, north of Peru, Argentine Patagonia, the country border between Argentina and Uruguay, the country border between Suriname and French Guiana, and in areas adjacent to the subduction zone in Paraguay, Argentine, and Bolivia.

The radial RFs employed in this study were calculated using the method described in Ammon (1991). The travel time required for the P-to-S converted phase from the discontinuities to reach the surface, relative to the P phase arrival, was inverted with the velocities provided by the 1D reference Earth model IASP91 (Kennett and Engdahl, 1991), providing the apparent depths of the d410 and d660.

The inversion approach considers the non-plane wavefront (Gao and Liu, 2014b) in the estimation of the travel time of converted phases from the MTZ discontinuities. This reduces the bias associated with the assumption of the same ray parameter for the first arrival and the converted phase, which for events closer to the stations (Δ~30°), the estimated travel time for the d660 converted phase, can be incorrect by as much as 0.4 seconds (Gao and Liu, 2014b).

Stacked traces were produced with the RF’s piercing point projected at the depth of 535 km (Dueker and Sheehan, 1997) that falls within a 2° radius from the bins center defined at each latitude/longitude coordinate pair spaced by 1° from each other (Figure 2.1). The trace is accepted only if the bin contains four or more RFs. These traces were inspected visually and rejected if they were too noisy, or did not showed a distinctive peak from the candidate discontinuities, or if the peaks were inconsistent with the peaks of the surrounding traces.

The peaks accepted by the visual inspection are assigned a vertical search range of 40 km centered at it; this range is employed to perform a bootstrap analysis. The bootstrap involves the random selection of 2/3 of the RFs and re-sampling of 1/2 of this population to measure the standard deviation (STD) of peaks from the average obtained when this processes is repeated 10 times, providing the uncertainty associated with each peak (Liu *et al.*, 2003).

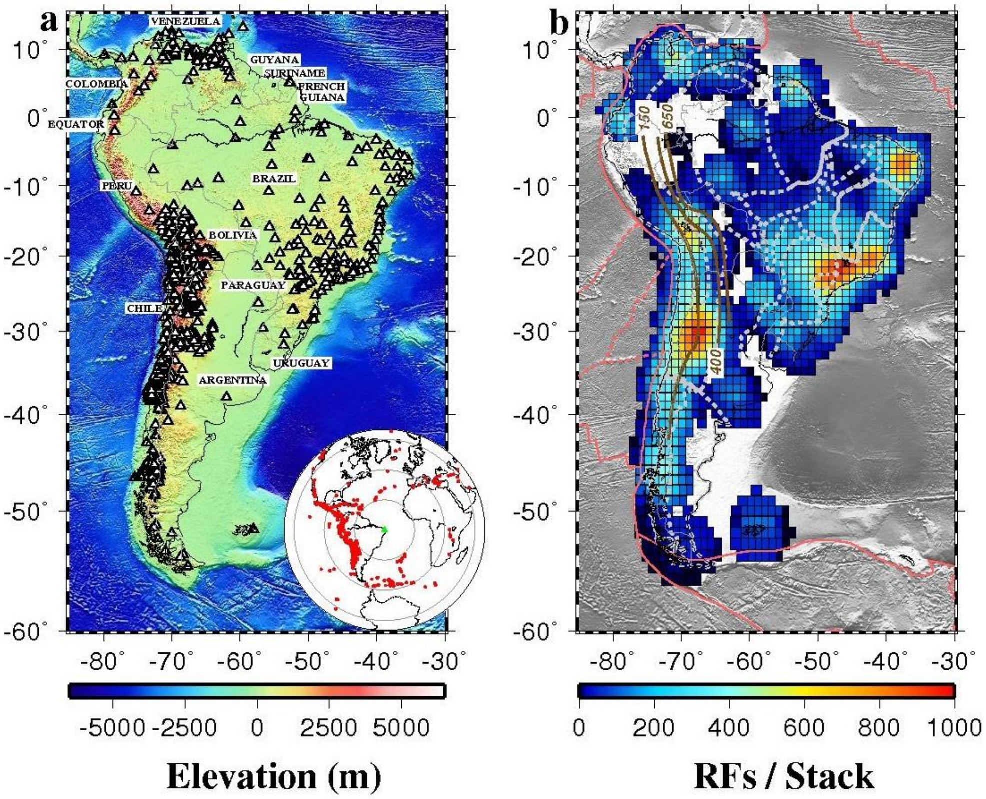

Figure 2.1. Data coverage maps. (Left) Stations used in this study, indicated by a white triangle, country names are informed in capital letters and states have only the first letter capitalized. Inset map shows the location of earthquake (red dots) used in the station RCBR (green dot). (Right) Maps of amount of RFs for each stacked trace, white dotted lines indicate geological provinces (see Figure 1.1) and brown lines are the Nazca slab contours at 150, 400 and 650 kms.

After establishing an apparent depth model, the most likely “true depth” model was sought. To achieve this task, a correction using the most recent 3D tomography models was pursued, ten global whole earth or mantle models and one regional upper mantle model were tested, encompassing a wide variety of seismic phases and tomography techniques. The tested global models were the LHEB08 (Li *et al*., 2008), GyPSuM (Simmons *et al*., 2010), LLNL-G3Dv3 (Simmons *et al*., 2012), HMSL (Houser *et al*., 2008), S362ANI+M (Moulik and Ekstrom 2014), SAW642ANb (Panning *et al*., 2010), TX2011 (Grand 2002, and IRIS DMC 2011a), SEMUCB-WM1 (French and Romanowicz 2014), S40RTS (Ritsema *et al*., 2011), and SPani (Tesoniero *et al*., 2015); the regional model was the JOINT (Feng *et al*., 2007).

The transformation of the apparent depths to true depths is made using the equation 8 of Gao and Liu (2014b). To adopt this procedure the velocities from each model were formatted into grids spaced in 1° by 1° and at 10 km depth intervals; because this is how the apparent depth model was constructed. For each model that provided data in grids or blocks bigger than 1° by 1°, the data was interpolated using the spline interpolator. When interpolation in the vertical axis was required, a linear interpolator was used. If the model data was provided in blocks or layers the values were simply replicated within the layer or block at the required intervals. If the model provided only Vp or Vs velocities, the absent phase was calculated using the Vp/Vs ratios of the IASP91. Models provided only with velocity perturbations (%), were converted to velocity values taking into account the model own 1D reference model. Models providing anisotropic velocities (Vsh and Vsv), were converted to isotropic S-velocities (Vs), using the equation $Vs = \sqrt{(2Vsv^2 + Vsh^2)/3}$ (Panning and Romanowicz, 2006). The majority of the velocity models data was obtained at the IRIS DMC (2011b). All images, but one (Figure 4.3), were generated using the Generic Mapping Tools software (Wessel and Smith, 1998).

3 RESULTS

3.1 APPARENT DEPTH MTZ MODEL

A total of 1,717 stacked traces provided a reliable d410 or d660 peak, where 1,370 of these allowed the identification of both peaks. Maps with the apparent depths of the d410 and d660, and resulting MTZ thickness are presented in the Figure 3.1. This model average depth of the d410 found beneath South America is 409.1±9.7 km and that of the d660 is 661.5±11.5 km, while the mean MTZ thickness is 251.8±10.8 km. These values are in agreement with the depths provided by the reference models AK135 (Kennett *et al*., 1995) and IASP91 (Kennett and Engdahl, 1991), with the thickness estimated in the global study of Chevrot *et al*., (1999), and the Gao and Liu (2014a) measurements in the central and eastern USA. The Appendix B and C presents E-W and N-S cross-sections, respectively, across the entire study area.

The correlation coefficient (R) between the discontinuities is 0.48. Considering the anti-correlation of the γ, this result indicates that the topography variations are significantly affected by velocity anomalies. Coherent depressions or uplifts of the discontinuities are most likely artifacts created by velocity perturbations in the crust and/or upper mantle. The maps clearly display several features that can be accounted for by well-known velocity anomalies in the crust and/or upper mantle.

Depression of the d410 and d660, without an associated thickness anomaly, is seen beneath the Altiplano and Puna provinces, this is related to well-known low velocities bodies in the lithosphere (Chmielowski *et al*., 1999, Zandt *et al*., 2003, Scire 2015 and references therein). A very intense low velocity anomaly (depression of the d410 by more than 30 km) in the upper mantle is observed beneath Patagonia (anomaly

'F'), described by Russo *et al*., (2010), while the d660 is even lower (>50 km depression) than the d410. Another anomaly due to low velocity is observed in the Brazilian side of the country border with Bolivia, this anomaly in the upper mantle has been discussed by Feng *et al*., (2007) and van der Lee *et al*., (2001). Additionally, a low velocity feature observed in the coastal area of Colombia and Equator, is also present in the tomography model of Feng *et al*., (2007). Similarly, but with uplifted discontinuities, anomalies are caused by higher velocities in the Archean portion of the Amazon craton, the Sao Francisco craton and the Parnaiba Block, this patterns are similar to high velocity anomalies observed by the S-wave tomography of Feng *et al*., (2007).

A thickening of the MTZ by 30 km is observed along the Central Andes (anomaly 'D') associated with the entrainment of the Nazca slab in the MTZ, where significant depression of the d660 is observed centered beneath Paraguay. This feature extends laterally (~800 km) to the east after the slab reaches the discontinuity, and is considered evidence that the slab is stagnant in this location. An uplift of the d410 in the Southern Andes (anomaly 'E') is likely to represent the entrainment of a slab segment in the MTZ, a lesser intensity feature parallel to it is observed in the east. Two areas of significant thickening are observed at the north of the subduction zone, between Venezuela and Colombia (anomaly 'H'), and beneath the north of Bolivia and the north-east of Brazil (anomaly 'I'). Smaller anomalies related to thickening of the MTZ are observed beneath Uruguay (anomaly 'K') and in the south of Brazil (anomaly 'J').

Two large anomalies related to thinning of the MTZ are perceived beneath the central region of Brazil (anomalies 'B' and 'C'), and smaller anomalies can be seen to the south and east of these positions. The most intense thinning of the MTZ occurs in the north-east of Brazil (anomaly ‘A’). Remarkably these features are coincident with areas where intraplate volcanism took place in the Late Cretaceous and Cenozoic. The first two anomalies located closer to the central portion of Brazil are mostly an expression of uplift (by 10 km) of the d660, while the north-east anomaly is caused by displacement (by 20 km) of the d410. Two narrower MTZ anomalies occur around the South America/Caribbean (anomaly ‘L’) and the South America/Scotia plate (anomaly ‘G’) boundaries.

Other features of smaller expression than the ones addressed up to this point can be noticed in the MTZ maps, but these will not be dealt in this report. Interpretation of anomalies at the borders of the study area is avoided due to its partial coverage. This work deals with the larger scale and most prominent continental features, in an attempt to establish a continental knowledge framework for the MTZ in South America.

In a broader view, anomalies in the west (H, I, D, K and E), along the Andes, show thickening of the MTZ, while anomalies in the east (A, B, C), along the Atlantic coast, show reduced MTZ thickness. This pattern reflects the latest tectonic events that took place at the South America continent. Slab subduction in its western margin, and rifting related to the opening of the Atlantic Ocean in the eastern coast. These anomalies are highlighted in the Figures 3.1, 3.2, and 3.3.

3.2 TRUE DEPTH MTZ MODEL

The MTZ parameters after each velocity correction are summarized in the table 3.1 and maps of these corrections are presented in the Appendix D. The velocity correction using the models SPani and SAW642ANb are the ones that reduce the R (0.31

and 0.35, respectively) between the discontinuities the most. Reduction of the R can also be obtained if the velocity model provides an incoherent correction, therefore increasing the standard deviation (STD) of discontinuities, which is not the case for the tested models, except for the JOINT model. This correction slightly increases the d410 STD, but reduces the d660 STD significantly, therefore it is still considered a valid correction.

Visually, the models HMSL, JOINT, and SAW642ANb are the three models that remove more effectively the influence of the high velocity anomalies associated with the Archean cratons and the low velocities anomalies in the east of the subduction zone. Considering these factors, the SAW642ANb model is taken as the best model for the estimation of the true depths. The assessment made in this work cannot be accounted as an evaluation of tomography models accuracy. The fact is that, SAW642ANb is one of the models where the data is provided with Vs and Vp velocities in the format required for the correction, not requiring any transformation (interpolation, conversion, etc). This is likely to be one of the reasons why the model provides superior results for correction purposes.

SAW642ANb does not possess velocity perturbations in the top 20 km, and after this depth the velocities are too high for crustal velocity structure. Due to the large similarities between the velocity anomalies observed in the apparent depth model and the JOINT model, that has the highest resolution among the tested velocity models. It seems appropriate that the velocity correction using the SAW642ANb model be completed by the crustal velocity structure of the JOINT model, suppressing the velocities provided in the former. Therefore, the velocity correction with a combination of the SAW642ANb model with a layer of 50, 100 and 150 km of the velocity structure of the JOINT model was tested, but not restricted only to SAW642ANb. Combination of models that provide only P-wave velocity with models that provide only S-wave velocity were also attempted.

The tests confirmed that the use of the SAW642ANb model with a 50 km layer of the JOINT model in the top (Figure 3.4) wielded even lower R (0.31) between the discontinuities than any other model or model combination and this is considered the closest approach to the true depth model. The average depth of the d410 is 418.5 km on the original SAW642ANb correction, dropping to 414.7 km with the replacement of the top layer by the JOINT model, while the d660 goes from 668.0 km to 664.3 km, and, logically, the MTZ thickness of 249.6 km is unchanged by this combination.

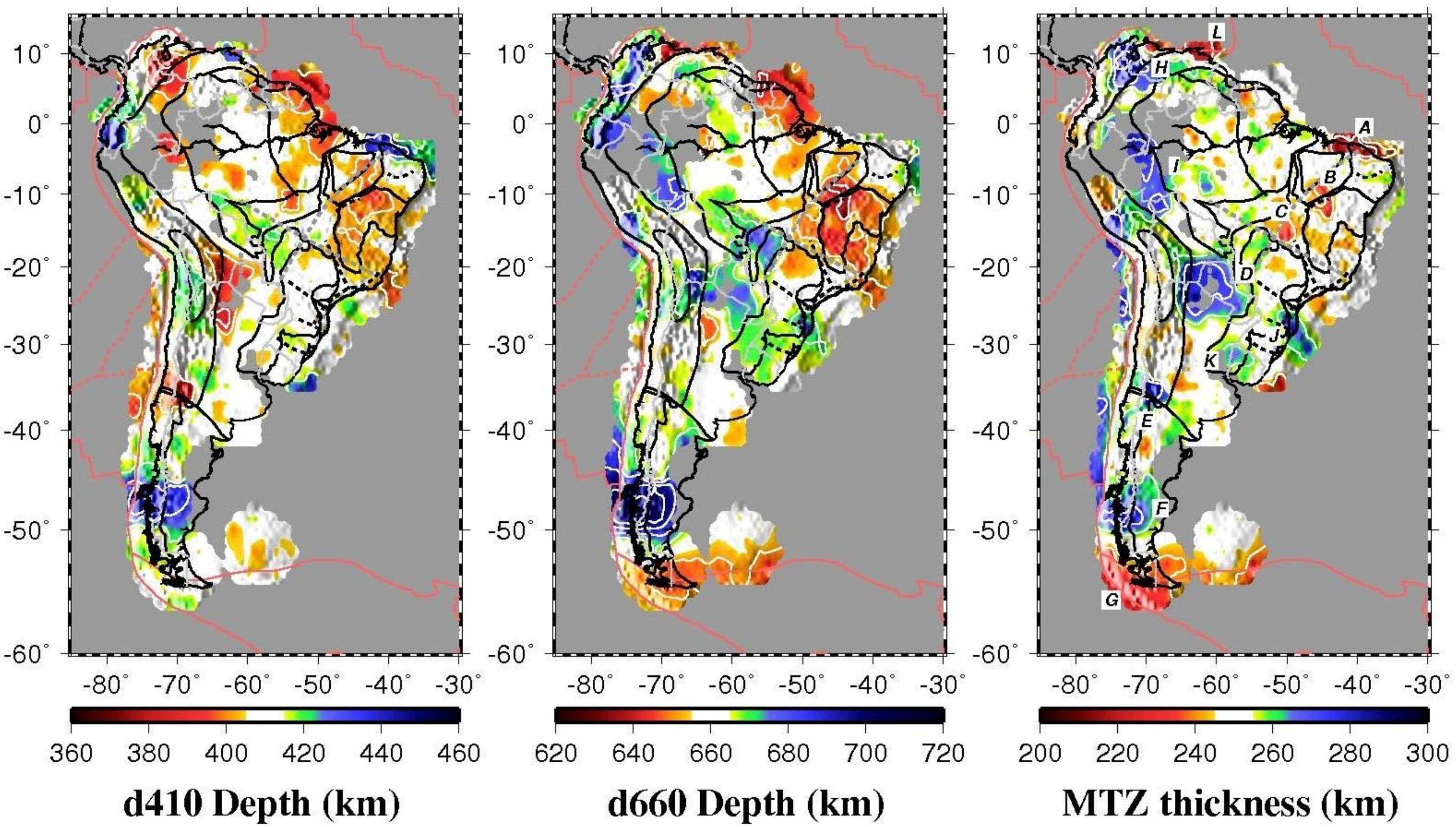

Figure 3.1. Apparent depth of the d410 (left) and d660 (center), and MTZ thickness (right) maps. Black lines are geological provinces showed in the Figure 1.1, red lines are plate boundaries, dotted red lines are ridges, dotted black lines are epeirogenic structures, dotted grey lines are lineaments, and grey lines are country boundaries. Letters indicate anomalies discussed in the text and white lines inside anomalies are 10 km contours.

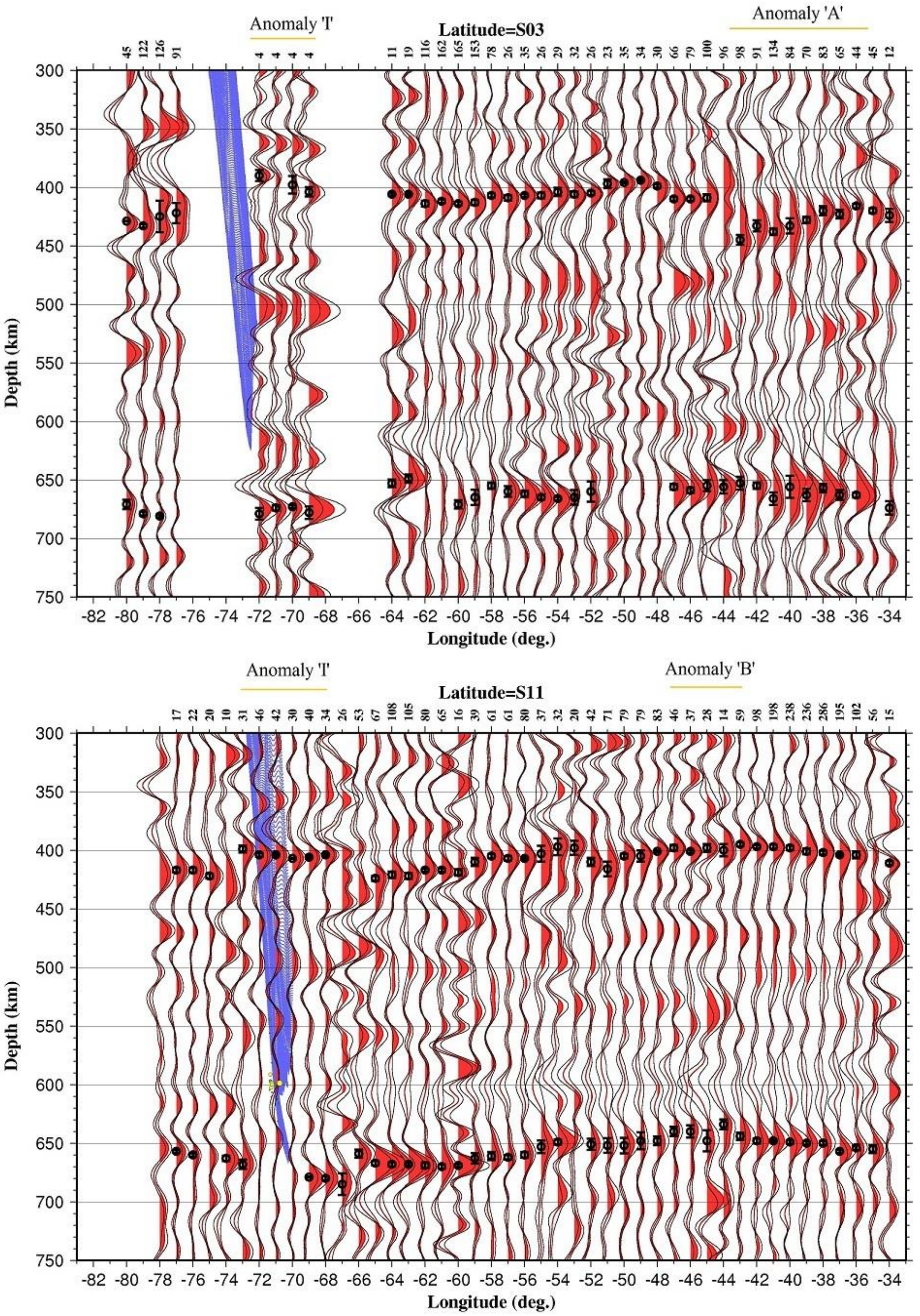

Figure 3.2. E-W cross sections along selected latitudes. Blue lines are slab contours. Green (Magnitude<6) and yellow (Magnitude≥6) circles are earthquakes. Number of RFs in each stacked trace are indicated on the top of it. Anomalies are indicated by yellow bars. Black circles are the interpreted depths of the discontinuities and associated bars are its STD.

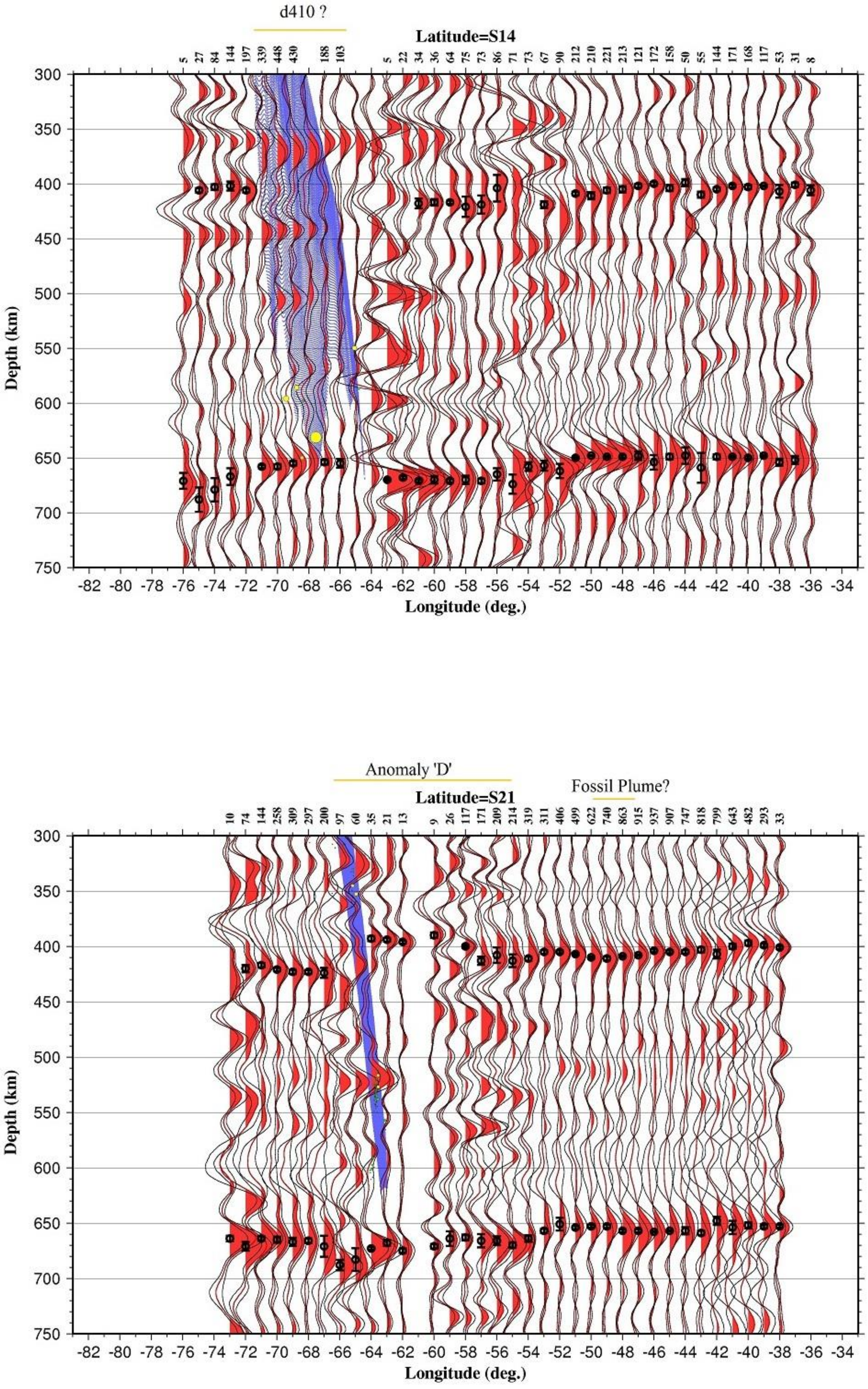

Figure 3.2. E-W cross sections along selected latitudes. Cont.

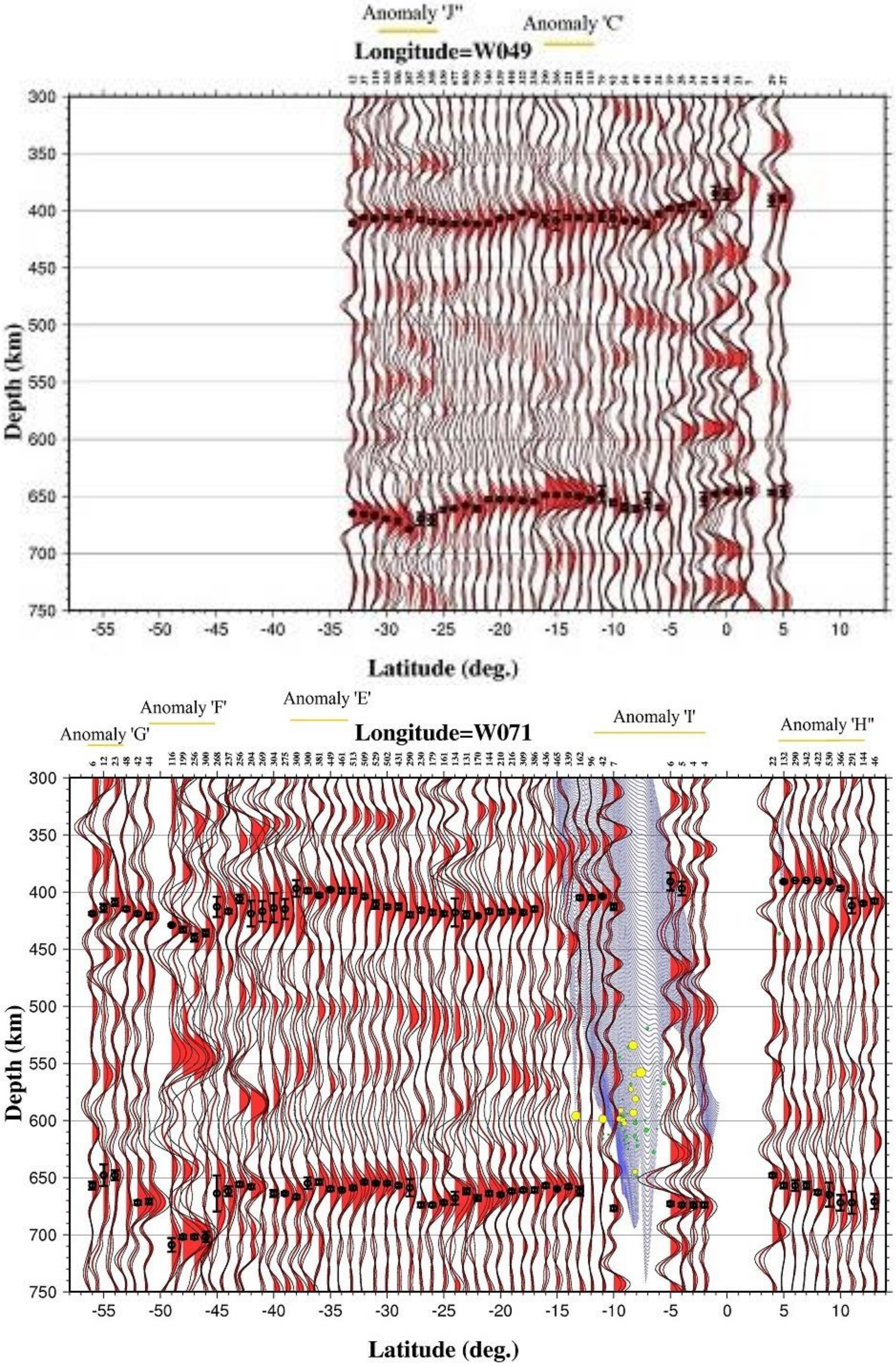

Figure 3.3. N-S cross sections along selected longitudes. Elements and symbols have the same meaning as in the Figure 3.2.

Table 3.1. Apparent depth model and true depth models statistical parameters. Average (A), standard deviation (S), Range of measurements (D), and correlation coefficient between d410 and d660 depths (R).

	d410			d660			MTZ		d410-d660
	A	S	D	A	S	D	A	S	R
IASP91	409.2	9.7	75.0	661.5	11.5	103.0	251.8	10.8	0.48
GYPSUM	405.9	9.0	66.9	648.8	10.8	82.2	242.9	10.9	0.41
HMSL	417.3	9.7	77.8	670.4	10.3	91.6	253.0	11.1	0.38
JOINT	408.2	10.1	79.9	660.4	10.9	101.8	252.3	10.8	0.47
S362ANI+M	421.6	9.4	71.4	676.8	12.2	95.3	255.2	11.7	0.43
SAW642ANb	418.5	9.3	67.5	668.1	11.1	81.1	249.6	11.7	0.35
TX2011	414.1	8.9	67.4	663.3	10.7	85.0	249.2	11.1	0.37
SEMUCB-WM1	411.2	9.1	67.5	663.5	10.8	85.0	252.3	11.3	0.36
S40RTS	412.1	8.9	68.1	664.1	10.0	89.7	252.0	10.5	0.39
LHEB08	409.0	9.7	75.1	661.0	11.0	102.5	252.1	10.8	0.46
SPani	405.3	8.8	69.8	648.3	10.0	77.1	243.0	11.0	0.33
LLNL-G3Dv	413.1	9.3	73.0	665.2	10.6	98.8	252.0	10.8	0.42
JOINT + SAW642ANb*	413.2	9.3	72.4	662.8	10.5	84.5	249.6	11.7	0.31

* Velocity model where the top 50 km velocities comes from the JOINT model, and the deeper velocity structure is from the SAW642ANb model.

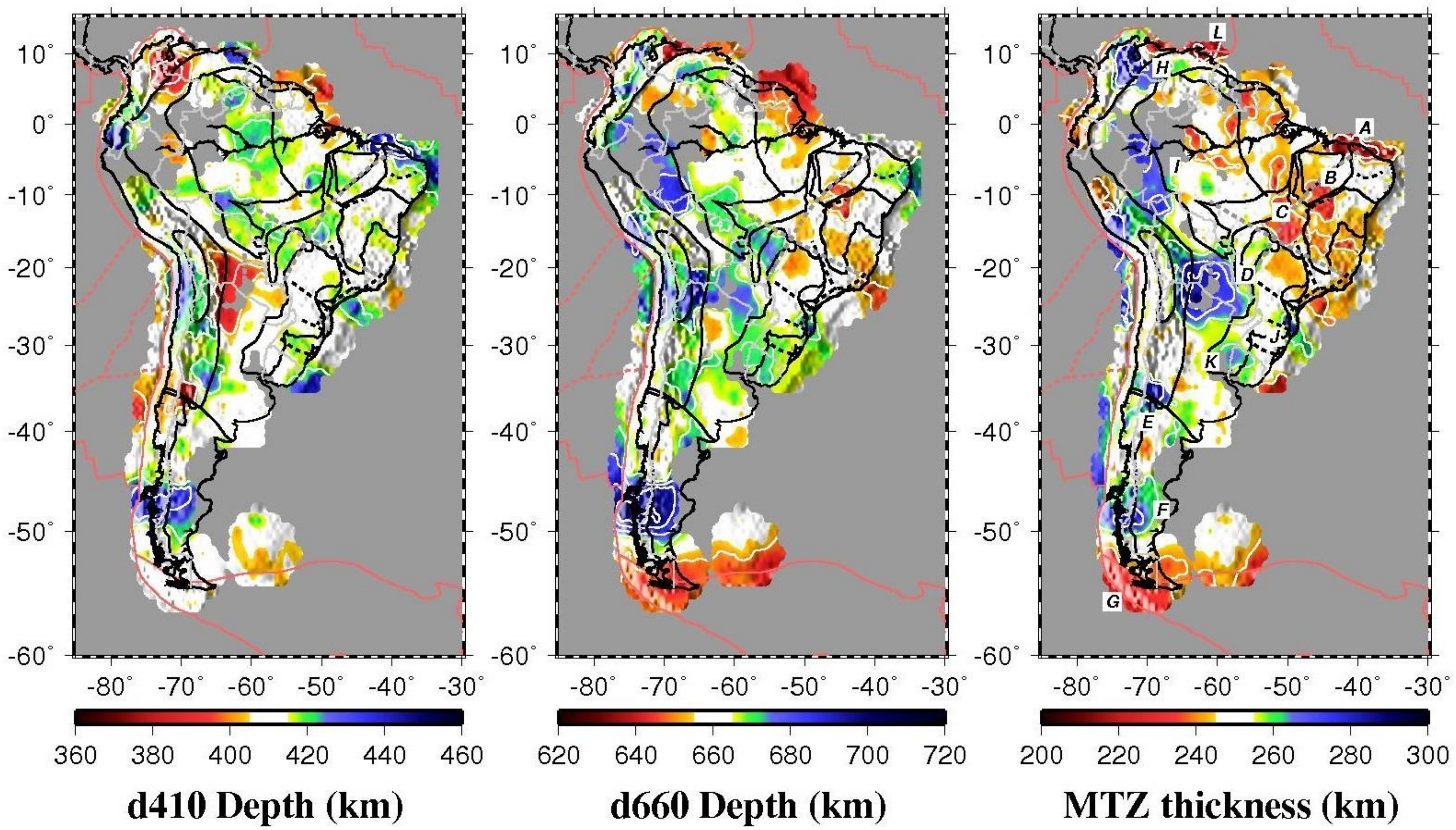

Figure 3.4. True depth of the d410 (left) and d660 (center), and MTZ thickness (right) maps. Symbols are the same as in Figure 3.1.

4 DISCUSSIONS

4.1 MTZ MODEL ASSESMENT

The uncertainties related to the definition of the d410 and d660 depths, and MTZ thickness are displayed in the Figure 4.1. It can be observed that no anomaly presents a systematic relationship with an increased uncertainty; the larger uncertainty values are usually isolated and dispersed. To confirm this assertion the correlation between the absolute distance of each measure from the average depth of the discontinuities and MTZ thickness against its STD was verified and no significant correlation exists. These test related to the d410 and d660 depths and MTZ thickness variations wielded an R of 0.04, 0.12 and 0.1, respectively. Similarly, the correlation between the number of RFs in each stacked trace and the deviation from the average values was tested. The variations in depth of the d410, d660 and thickness of the MTZ show no correlation with the quantity of RFs in each stacked trace. This analysis wielded R values of -0.02, -0.1 and -0.12, respectively.

In describing and interpreting the results, anomalous areas were defined as those with ±10 km deviance from reference values of 410 km for the d410, 660 km for the d660 and 250 km for the MTZ thickness. This threshold represents values close to the STD of the average discontinuities depths and MTZ thickness, and is two times larger than the average uncertainty (STD) associated with each measurement. This value also is below the 15 percentile and above the 85 percentile of the depths and thickness observations; therefore less than 30% of the investigated area is consider anomalous. The model is able to resolve virtually all expressive velocity anomalies in the lithosphere and upper mantle previously identified within its scale. These observations allow the inference that the MTZ model is robust.

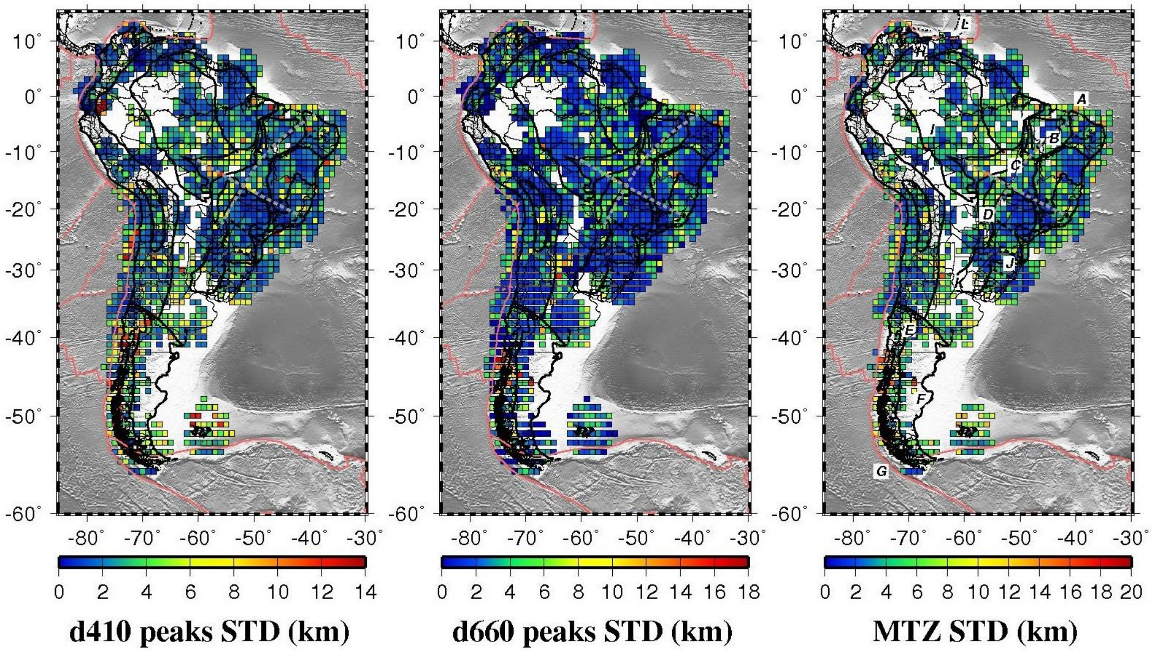

Figure 4.1. STD associated with the peaks for each stack of the d410 (left), d660 (center), and MTZ thickness (right). Symbols are the as in figure 3.1.

The resolution of the MTZ model is consider to be ~400 km, which is related to the stacking of RFs within 2° of the central point in each stacked trace. This is the worse resolution possible, since the resolution is dependent in the density and location of piercing points around one stack. Earthquakes have well defined source location and each station may present a preferred path for incoming waves (poor azimuthal coverage), this focusing implies in higher resolution, but the measurement would not be representative of the entire region covered by the stacked trace, and it would be displaced from its central point. However, this effect is expected to be reduced, since the use of low Mc allowed better azimuthal coverage. Another factor that may change resolution is the fact that 1° of longitude represents greater lengths in the equator than towards the pole, therefore the resolution will be slightly increased towards the southernmost areas of the model.

In the true depth maps, with the best correction described above, it can be observed that the larger velocity anomaly features related to the cratons and the Parnaiba Block are no longer observed. Instead, this feature was replaced by depressions of the d410 surrounding the previously uplifted areas, while the regional uplift of the d660 in this area was removed, the MTZ anomalies became much thinner and more spread, especially along the north of Brazil. However, the velocity anomalies with smaller area in the Patagonia and in the country border between Brazil and Bolivia persisted. In general, this model enlarged the MTZ anomalies. These are the counterpoints of the attempted velocity correction, and for all corrections using global models, due to large contrast in resolution with the MTZ model. The fact is that the correct removal of the high velocity features (uplift) of the d410 is accompanied by the introduction of depressed d410 between the previously existent high velocity anomalies, in a pattern similar to matching puzzle pieces, introducing artifacts in the discontinuities topography caused by the low resolution of the velocity model.

It is likely that a thinner MTZ anomaly, indicating hotter temperatures, is related to low velocity anomaly in the MTZ. This explains the observed enlargement of the Central Brazil related anomalies (‘B’ and ‘C’). Similarly, for thicker-than-normal anomalies, higher velocities should be observed and there is also enlargement (‘D’ and ‘K’). However, in some areas where no MTZ anomaly existed before the correction, new anomalies can observed (e.g northwest of Brazil). This indicates that artifacts in the MTZ thickness observations may have been created by the much smaller resolution of the global velocity model. It is noteworthy that the true depth model anomalies in Brazil were enlarged in areas coincident with areas were rift related magmatism was more intense, as well as the subduction related anomalies. However, anomalies that are not seen in the both models (apparent depth and true depth) will not be discussed, because they are most likely artifacts. At least until a higher resolution velocity model comprising the crust and upper mantle of South America is available; this is likely to be the closest approximation to the MTZ true structure.

One of the most important observations of the true depth model is that, previously to the velocity correction, the anomalies ‘B’ and ‘C’ were characterized by uplifted d410 and even more uplifted d660, this would lead to an interpretation that the d660 was associated with extremely hot thermal anomaly, while the d410 was cold, therefore the thermal anomaly was restricted to the MTZ and Lower Mantle, hence it could not be associated to events observed towards the surface. However, this is caused by the fast velocity anomalies associated with the cratons, and after the velocity correction, the anomaly ‘C’ presents a coincident depression of the d410 by 10 km, while the anomaly ‘B’ can be associated to a depression of the d410 in its western flank, and therefore they can be used to infer thermal anomalies extending into the upper mantle.

Maps showing the amplitude of the d410 and d660 peaks, normalized by the P wave arrival amplitude, are presented in the Figure 4.2. These maps show systematic patterns associated with the d410, and d660 depths and the MTZ thickness anomalies. However, it also reveals a more complex interplay between amplitude patterns related to anomalies and broader regional signatures. For instance, the anomaly ‘C’ in Central Brazil appears as a circular pattern of higher amplitude in the d660 amplitude maps, which matches the d660 uplift, and is the expected response for a hotter temperature anomaly, since this should amplify the velocity contrast in the d660 increasing the peak amplitude. However there is a very distinct low amplitude signature all around this region, occupying most of the Brazilian country area between 13°S and 30°S, in the d410 and d660 amplitude maps. Similarly, the anomaly ‘D’ show higher amplitudes on the d410 amplitude map, compatible with higher velocities in the MTZ, while along the Andes a low amplitude pattern is observed. The areas below the cratons also presents a regional high amplitude pattern. These broader amplitudes patterns do not allow any significant correlation of the (R=0) d410 and d660 amplitudes with the d410 and d660 depth variations or the MTZ thickness variations.

The predominance of different ray parameters can explain the regional patterns, since RFs from greater epicentral distances have a lower amplitude ratio between the P wave and the converted P-to-S phase (Ammon, 1991). As earthquakes occur along well defined zones and the stations are spread over the continent, this could cause systematic amplitude variations. However, due to the resemblance of this greater scale patterns with the tectonic provinces, it is likely that they reflect mantle proprieties. Therefore, attenuation and velocity are the most likely candidates to explain the observed amplitude variations, attenuation and velocity variations are related to the chemical and thermal proprieties of the mantle. Since the thermal response (MTZ anomalies) are discernible from the regional patterns, then it must be interpreted as related to large scale chemical variations.

According to Cammarano and Romanowicz (2008) the presence of significant volumes of water (>0.5 wt%) will increase the attenuation, the observation of low amplitudes in the Andes is a fact in agreement with the recent inferences regarding the presence of significant volumes of water in the MTZ transported by subducted slabs. The Brazilian regional low amplitudes are most likely related to chemical alterations caused by the Brasiliano orogeny and rift magmatism related to the Atlantic Ocean opening (enriched mantle), which is more attenuating, while the cratons are unaffected by these processes and have regionally higher amplitudes (depleted mantle) (Artemieva *et al.*, 2004).

The highest amplitudes of the d660 observed associated with anomaly ‘I’ are related to stacked traces with low quantities of RFs and are likely to be artifacts generated by noisier traces, areas in the edges of the resolved MTZ structure frequently show high amplitudes that may relate to noise.

The most significant drawback in the observation of MTZ anomalies using the P-to-S conversion is the fact that thickness variations are measured only vertically. In this method, if the d410 presents a 6 km depression and normal d660, while an adjacent area presents a normal d410, but the d660 is uplifted by 6 km, both areas will not be consider anomalous. However, if the measure was made off the normal orientation, this would wield a thinning greater than 10 km and thus anomalous MTZ. From the observations of the results, it is possible to assert that the d410 and d660 anomalies are hardly vertically coherent, especially in the areas affected by subduction, but also hardly untrue for other areas. This may lead to some displacement of the observed MTZ anomalies from the locations where the related structures are located, and also might lead to underestimations of anomalous observations.

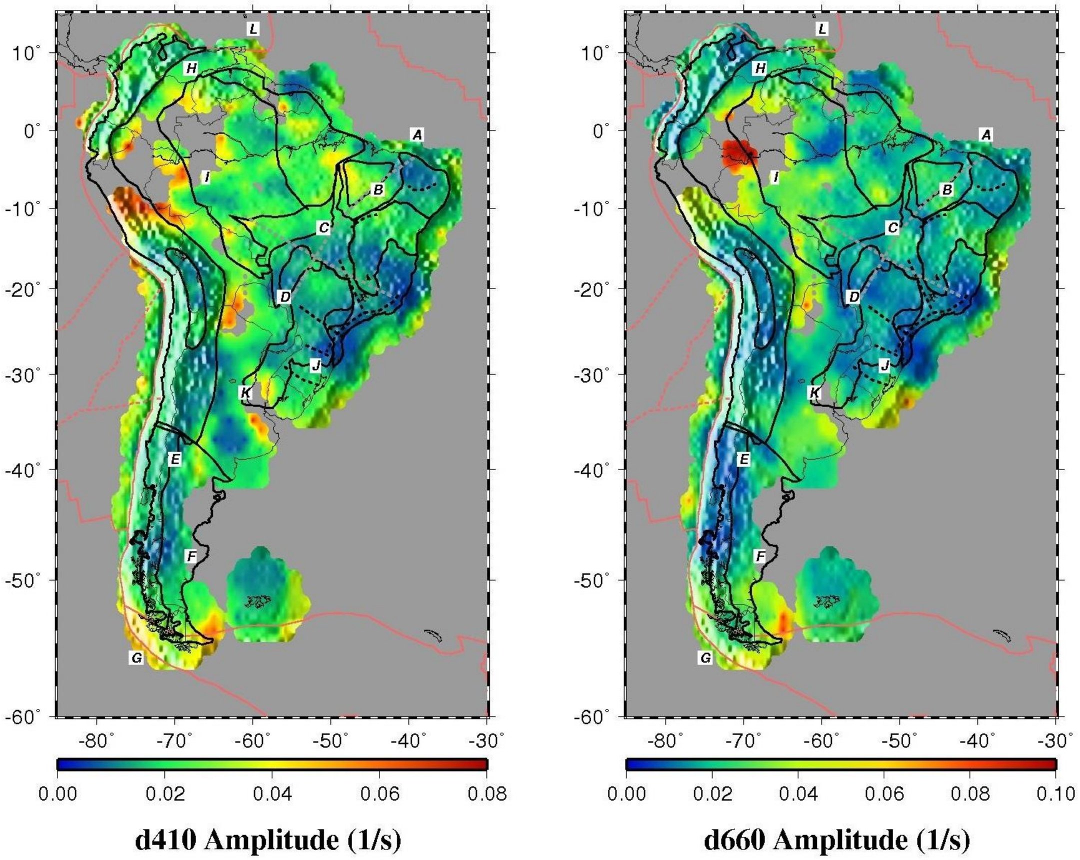

Figure 4.2. Amplitude of the d410 (left) and d660 (right) peaks, normalized by the P-wave. Symbols are the same as in Figure 3.1.

4.2 CLAPEYRON SLOPES

The relationship between the variations in the depth of the d410 (Δd410) and d660 (Δd660) in respect to the MTZ thickness variations (ΔMTZ) were tested, revealing pertinent results (Figure 4.3). The apparent model show a high correlation (R=0.65) between the d660 and MTZ variations, but the d410 and MTZ correlation is weak

(R=0.33). The same test using the true depth model provided more satisfactory results. The R between the d410 and MTZ thickness is -0.5 and the linear model adjusted to this data has a slope of -0.4, the same analysis considering the d660 has a correlation of 0.66 and a slope of 0.6. There is no significant change in the slope of the d660 from the apparent to the true depth model, but the d410 changes more significantly as the R is improved by the velocity correction.

According to Bina and Helffrich, (1994) and Helffrich (2000) the d410 γ has a magnitude higher than the d660 γ, while seismic observations have found greater amplitude in the topographic variations of the d660. This observation is supported by the present results, where the d410 has showed a topography variation range of 75 km and the d660 of 103 km, and sustained even after the velocity correction, where the range is 72.4 km for the d410 and 84.5 km for the d660. Lebedev *et al*., (2002) determined γ values based on seismological data, the estimated d410 γ was found to be 2 MPa/K and for the d660 γ was -3.3 MPa/K. These values are supported by the relationship ($0.604*\Delta d660 – 0.395*\Delta d410 = \Delta MTZ$) obtained by the linear regression adjusted to the MTZ thickness variations and the discontinuities depths variations observed in this study.

The difference between the theoretical and experimental γ values, and the seismic observation of the discontinuities behavior could be related to a possible role of the d660 as a thermal boundary, broadening of the d410 under anomalous cold environment (Bina and Helffrich, 1994), or due to more complex chemical variations than generally assumed (Helffrich, 2000). Clear broadening of the d410 peaks when the discontinuity is shallower was not perceived in the cross sections, or lower amplitudes related to broader MTZ, hence the role of the d660 as a thermal boundary or chemical variations are considered more likely. Regardless of the reasons for the contradiction, it seems more appropriated to follow Lebedev *et al*., (2002). Therefore, the MTZ temperature anomalies inferred from here on are calculated adopting these γ values, assuming that an equal variation in the discontinuities produced thermal anomalies, and a range was estimated by the difference between the thermal anomalies created if only one of the discontinuities caused the thickness variation.

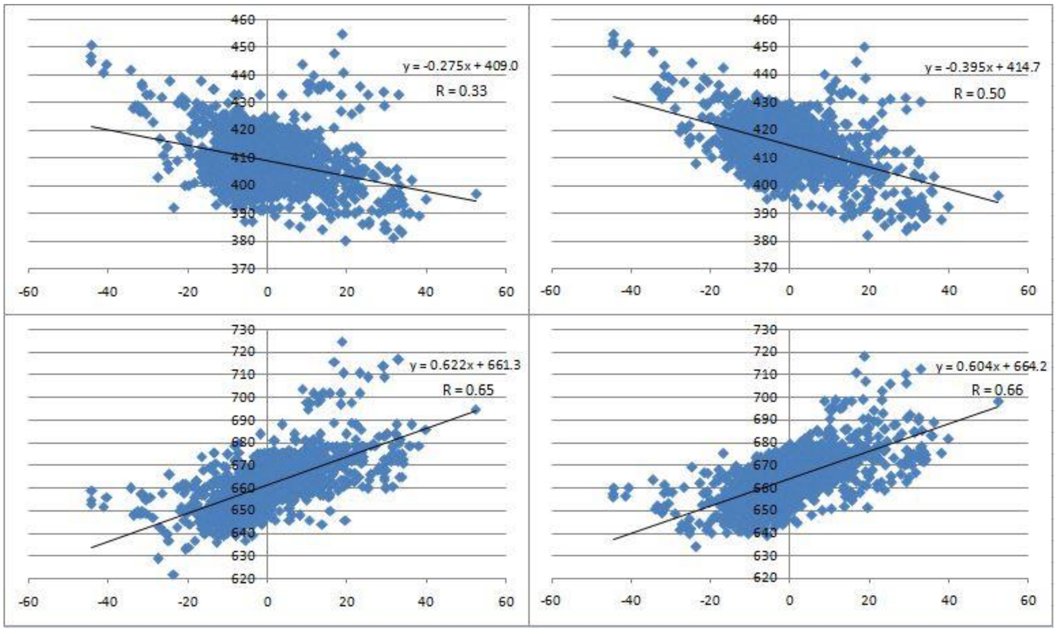

Figure 4.3. Correlation between the variation in the d410 (top) and d660 (bottom) depth (vertical axis), and the MTZ thickness (minus 250 km) (horizontal axis). Apparent depth model (left) and the true depth model (right).

4.3 NORTHEAST BRAZIL ANOMALY (A)

In the northeast edge of Brazil, thinning of the MTZ along the equatorial margin is related to a depressed d410, and higher-than-normal temperatures are most likely restricted to the MTZ and upper mantle. This anomaly is oriented E-W and it is position is coincident with intraplate alkaline volcanic activity during the Cenozoic regionally distributed along the same orientation, the Messejana volcanism – including the Mundau Volcanism (Almeida, 2006) – and the Fernando de Noronha volcanic island chain. This orientation is also close to the orientation of the uplift axis of the Borborema Plateau indicated by Alkmim, (2015) (see Figure 1.1), that recognizes the Borborema Plateau as one of the three most prominent basement highs of Brazil. To support the following discussions, pertinent geological elements were plotted over the MTZ thickness map in the Figure 4.4.

Fodor *et al.*, (1998) observed that the track of the Fernando de Noronha volcanic chain could explain the alkaline rocks in northeast Brazil, these authors found geochemical affinities between basaltic rocks from the northeast Brazil and the Fernando de Noronha Island, and inferred plume activity and crustal delamination processes. Mizusaki *et al.*, (2002) performed a geochronology study of the Brazilian coastal areas, from the data for the northeast portion of Brazil these authors identified that there is a westerly age progression for the E-W Fernando de Noronha chain and intrusions along the coast, considering it as evidence of buoyant melts from a hotspot that emplaced Cenozoic alkaline rocks in the Equatorial margin of Brazil.

King and Ritsema (2000) and King (2007) pointed out that the volcanic activity in the Fernando de Noronha Island fitted the required geometry for the development of a convective cell by the edge-driven convection mechanism. Knesel *et al.*, (2011) and Perlingeiro *et al.*, (2013) performed additional geochronology study and verified overlapping ages between the onshore volcanism and the volcanic activity in the Fernando de Noronha Island, concluding that no clear age progression exists and that the volcanic activity is more likely the product of edge-driven convection. Almeida *et al.*, (1988), Almeida *et al.*, (1996) and Almeida (2006) related these volcanic occurrences to hotspot related adiabatic melts triggered by stress relieve along the extension of the Romanche and Fernando de Noronha ocean fracture zones.

Oliveira and Medeiros (2012) studied the isostatic state of the Borborema Plateau (see Figure 1.1), inferring buried loads possibly related to mafic underplating in the area, but due to the absence of typical features for this phenomenon, stress due to warped structures between the crust and/or mantle layers could not be ruled out. The MTZ beneath the Borborema Province (Brasiliano Province in the northeast corner of Brazil, see Figure 1.1) was studied by Pinheiro and Julia (2014) and no thermal anomaly was found, although this study overlaps less than ¼ of the anomaly ‘A’, on its southeast corner. There is a significant difference in resolution between the latter study and the present study, Pinheiro and Julia (2014) study stacked RFs admitting a maximum radius of 1°, while the present study uses 2°, there is a chance that the present model broadens the anomaly, therefore no overlap may exist. Alternatively, the reason for divergences may reside in the fact that the methodological approaches are distinct. Schmerr and Garnero (2007) using SS precursors imaged similar MTZ structure to what is observed here.

The observed hotter-than-normal mantle for the northeast of Brazil excludes the hypothesis of a mantle plume originated in the lower mantle as the cause for the magmatic activity, because no abnormal temperatures associated with the d660 was perceived, but cannot judge between upper mantle buoyant hotspot melts, hotspot related adiabatic melts, or edge driven convection melts. Although, it must be made clear that for edge-driven convection to be possible a specific geometry of the lithosphere is required.

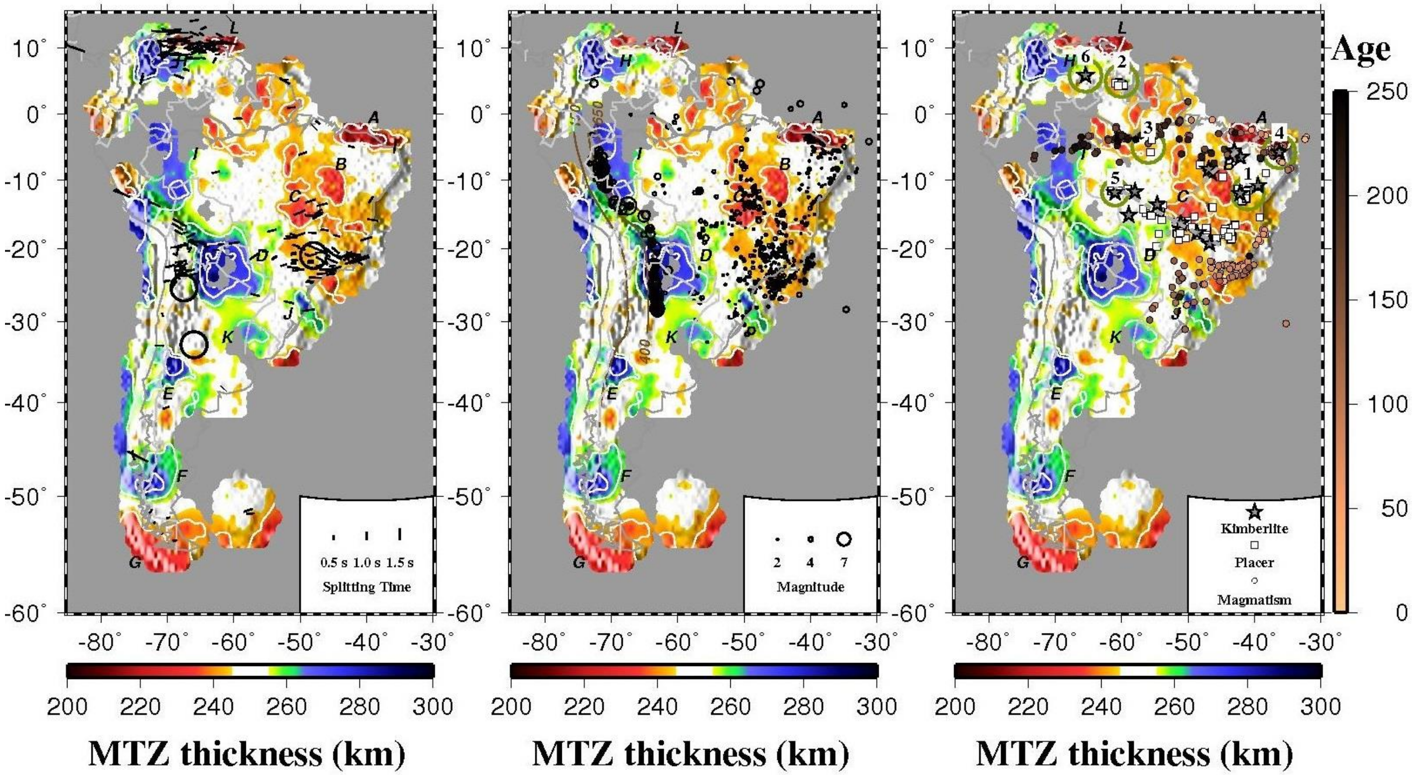

Figure 4.4. True depth MTZ thickness and geological elements. Seismic anisotropy (Left), bars are fast orientation (Russo and Silver, 1994, Growdon *et al.*, 2009, Masy *et al.*, 2011, Assumpcão *et al.*, 2006, Assumpcão *et al*., 2011, James and Assumpcão, 1996 and Heintz *et al.*, 2003) and circles are proposed plumes (Wolbern *et al.*, 2009, Burd et al., 2013, VanDecar et al., 1995). Seismicity (center), along the Andes only earthquakes below 400 km were plotted (USGS, 2105) and all the Brazilian earthquakes were plotted (RSBR, 2014). (Right) Magmatism (Mizusaki *et al*., 2002 and Geraldes *et al*., 2013), vertical scale represents magmatic age. Kimberlites (Kaminsky *et al*., 2009b, Kamisky *et al*., 2006, Neto *et al*., 2015) are stars and diamond placers (CPRM, 2015) are squares. Numbers 1 and 6 are kimberlites older than 600 Ma (Kaminsky *et al*., 2006, Pereira and Fuck 2007), 5 are kimberlites older than 220 Ma (Hunt *et al*., 2009), 4 is a newly discovered kimberlite without age (Neto *et al*., 2015), and 2 and 3 are diamonds placers, without discovery of kimberlites. Cretaceous kimberlites occur along the Azimuth 125 Lineament and Jurassic-Cretaceous kimberlites occur along the Transbrasiliano Lineament.

As emphasized by King and Ritsema (2000) and King (2007), this geometry is achieved as the volcanic island of Fernando de Noronha is distant between 600 to 1000 km from a high velocity anomaly indicating a thicker lithosphere, and at this distance the thermal instability is large and convection occurs. This model has been generalized to rocks in the coastal areas, however, as the convective flow approaches the lithosphere, the tendency is downwelling, upwelling occurs in the opposite end of the convective cell, and since coastal areas are less than 600 km distant from the high velocity anomaly, these facts inhibits such generalization of this magmatic model. Additionally, the thermal anomaly identified is oriented E-W along the equatorial continental margin, coincidently the same direction of the Fernando de Noronha chain and prominent ocean fracture zones, although not conclusive, the expected orientation of the thermal anomaly should lie oriented between the island and the thicker lithosphere (NE-SW) in order for it to be considered as evidence of an edge-driven convection cell. Furthermore, Assumpcao *et al.*, (2011) measures seismic anisotropy oriented N-S at the northeast edge of the Borborema Province (Figure 4.4), and in order for edge-driven convection to explain the volcanic activity, the expected seismic anisotropy should be oriented between NE-SW and E-W to support this mantle flow mechanism.

Given the matching orientation of the MTZ anomaly orientation, oceanic fracture zones, regional volcanic trend, and the trend of the uplift of the Borborema Plateau, it is consider very likely that the intraplate volcanism is caused by adiabatic melts associated with stress accommodation along the projection of the ocean fracture zones; as the ocean expands, there is stress at the mid-ocean ridge. This stress could be transferred to northeast portion of Brazil, since it is closer to the mid-ocean ridge than any other area of the continent. Supporting evidence is the fact that the mid ocean ridge suffers one of the most significant displacement by a transform fault than other areas of the Atlantic Ocean (~900 km), which has accentuated topography, one of the largest associated to the effect of a transform fault in this ocean. This topographic effects can also be observed in the opposite side of the ocean, along the Ghana coast. Therefore, supporting what is proposed by Almeida *et al*., (1988), Almeida *et al*., (1996) and Almeida (2006), the thermal anomaly in the MTZ is likely to be the result of the interplay between stress, adiabatic melts and passive upwelling of mantle material.

Compelling arguments favoring these inferences are the facts that in this area high heat flow (200 mW/m^2) and geothermal gradients (60-80°K/km) (Almeida, 2006) are observed, as well as one of the highest intraplate seismicity rates of South America (Bezerra *et al*., 2007) (Figure 4.4). Although this anomaly has been correlated to the Cenozoic magmatism, it is possible that this anomaly could have been in place since the Cretaceous or even longer period.

The Apatite fission-track study of Morais Neto *et al*., (2009) identifies a regional cooling event in the Borborema Province at 100-90 Ma related to topographic uplift and rift related magmatism. The Ceara-Mirim magmatism (143-113 Ma) occurs as dikes swarms (where individual dikes can be a few kilometers long and up to 400 meters thick) oriented E-W (Angelim *et al*., 2006) along a ±350 km long zone (Archanjo *et al*., 2002), which is the same orientation of the MTZ thermal anomaly. This anomaly implies a current increment of 285±55°K in temperatures.

4.4 CENTRAL AND SOUTHEAST BRAZIL ANOMALIES (B, C, AND J)

Anomalous thin MTZ, matching the position of the anomalies ‘B’ and ‘C’, can be seen in the global MTZ models of Deuss (2009), Lawrence and Shearer (2008), and Houser *et al*., (2008). The anomalies (B, C and J) have a general NW-SE orientation, which is the same trend of Cretaceous kimberlite emplacement along the ‘Azimuth 125° Lineament’ and alkaline magmatism along the oriental coast of Brazil.

The anomalies orientation is also compatible with prominent epeirogenic structures found along the oriental coast of the Brazilian platform (Figure 1.1), where magmatic conduits interpreted as feeders for the Parana Flood Basalts and volcanism in the Alto Parnaiba Igneous Province (APIP) are found (Almeida and Carneiro, 1989, Lima *et al*., 2014, Brod *et al*., 2000, Karfunkel *et al*., 2014). In the Ponta Grossa Arch (PGA), swarms with hundreds of dikes occur, where dikes can reach 1 km in thickness (Almeida and Carneiro, 1989). According with Almeida and Carneiro (1989), the Cretaceous magmatism is controlled by arches and faulted flexures. Therefore, an association between MTZ thinning, large scale crustal uplift and volcanism is envisioned (Figure 4.4). Additionally, these thermal anomalies in the MTZ are also coincident with high seismicity (Figure 4.4).

The Alto Parnaiba Arch (APA) and the Serra do Mar Arch (SMA) are two of the three most prominent uplifted structures in Brazil, the third is the Borborema Plateau (Alkmim, 2015) discussed in section 4.3. Coincidently, the APA and the SMA form a triaxial junction in the vicinity of the anomaly ‘C’. The SMA has alkaline magmatic activity from the Late Cretaceous to the Eocene (Thompson *et al*., 1998), while in the APA uplift during the Early Cretaceous was associated with mantle upwelling by Gibson *et al*., (1995), Campos and Dardenne, (1997a), and its associated magmatism (APIP) is considered one of the most volumetric mafic-alkaline provinces in the world (Bologna *et al*., 2006). Gibson *et al*., (1997) and Kaminsky *et al*., (2009b) highlight that the magmatism occurs along Brasiliano Provinces.

Another feature that can be related to the thermal events is the Sao Francisco High (SFH), but no specific information related to its evolution was found. Uplift of this structure between the end of Permian and the Early Cretaceous is inferred, the main uplift phase in the Early Cretaceous, because in this period there is no sedimentation in the adjacent Sanfransciscana Basin, but during the Aptian thicker conglomerates accumulates in its northern edge (Campos and Dardenne, 1997b), matching the expected sedimentation pattern of a basin base level change (depression) relative to its northern border, the SFH. Therefore, in all structural highs surrounding these anomalies, uplift during the Cretaceous is inferred. Additionally, these anomalies are very close to locations where Cretaceous basaltic sills or sequences are more voluminous, such as the Parnaiba Basin, the Parana Basin northern depocenter and in the Rio Grande Syncline (Almeida and Carneiro, 1989).

Between the anomaly ‘J’ and ‘C’, hotter-than-normal thermal disturbances with similar trend are observed surrounding the VanDecar *et al*., (1995) fossil plume conduit. This velocity anomaly is confined to the upper mantle and as it reaches the depth of 500-600 km, it changes in to a larger N-S oriented feature (Schimmel *et al*., 2003). Liu *et al*., (2003) investigated the MTZ in this area, and a hotter-than-normal thermal disturbance was not found, but this study had a resolution which is approximately two times lower than that of the present study. Schimmel *et al*., (2003) and Rocha *et al*., (2011) also found low velocities related to the Late Cretaceous magmatic provinces, which these authors interpreted as being confined to the upper mantle (<250 km). Observing their results the low velocity patterns associated with the magmatic provinces is less clear in the 300-350 km depth slices, especially in the Schimmel *et al*., (2003) results, but they match the locations of the igneous provinces in the depth slices of 500 and 700 km. The low velocities in the tomography images at 500 and 700 km are in agreement with the MTZ structure found in the present study.

In several Cretaceous alkaline provinces, manifestation of a mantle plume has been suggested (Bizzi *et al*., 1995, Gibson *et al*., 1995, Gibson *et al*., 1997, Thompson *et al*., 1998, Sgarbi *et al*., 2004, Hunt *et al*., 2009, Hayman *et al*., 2005, and Bulanova *et al*., 2010), and delamination has also been invoked as a component of the APIP magmatism (Bizzi *et al*., 1995, Read *et al*., 2004). There is no age progression for the Alkaline magmatism (Almeida and Carneiro, 1989, Gibson *et al*., 1997), or at least for kimberlitic magmatism occurring along the Azimuth 125° Lineament, comparable ages are found for kimberlites from its western (Kaminsky *et al*., 2010) and eastern (Felgate, 2014, Guarino *et al*., 2013) extremes.

Contemporaneous magmatic activity occurred in several areas, separated by 400-500 km, inhibiting a plume origin in the view of Guarino *et al*., (2013) and Felgate, (2014), since conceiving magmatic activity of a plume head greater than 1200 km focused along an alignment is a complex task (Felgate, 2014), nonetheless Gibson *et al*., (1995), Gibson *et al*., (1997), and Thompson *et al*., (1998) elaborated a model to reconcile these structures with the impact of a plume head, while Almeida and Carneiro (1989), Guarino *et al*., (2013) and Felgate (2014) consider that melts from a source located in the asthenosphere is more likely. Almeida and Carneiro (1989) stated that the period corresponded to a time of high spread rates and large rotations; therefore generalized heating of the mantle and changes in intraplate stress triggered the magmatic activity.

In favor of a plume model, it is found that these anomalies (‘B’ and ‘C’) have an expressive uplift of the d660, a strong argument favoring upwelling material from the lower mantle, additionally the Trindade plume head proposed by Thompson *et al*., (1998) fit the anomalies ‘B’ and ‘C’. The larger and more intense places of these anomalies are contained inside the 600 km radius of the proposed plume head, while the ESE tail of the anomaly ‘C’, which is the most intense, is positioned along the inferred plume path. However, the current dimensions of the MTZ anomalies, if it were generated at more than 130-90 Ma, are a fraction of its original size and anomalous temperature values.

The Juina Kimberlites in the western extreme of the Azimuth 125° Lineament have by far the better constrained source for its magmas, their relation to melts from a subducted slab has been well established by a thorough assessment of mineral inclusions in diamonds and carbon isotope signatures (Hayman *et al*., 2005, Brenker *et al*., 2007, Wirth *et al*., 2007, Wirth *et al*., 2009, Kaminsky and Belousova, 2009, Kaminsky *et al*., 2009a, Kamisnky *et al*., 2010, Bulanova *et al*., 2010, Walter *et al*., 2011, Pearson *et al*., 2014, Thomson *et al*., 2014, Zedgenizov *et al*., 2014a, Zedgenizov *et al*., 2014b, Zedgenizov *et al*., 2015, Kaminsky *et al*., 2015). The aforementioned authors were able to find the expected paragenesis generated by the presence of a slab in the MTZ or greater depths, and the coexistence of organic and deep mantle carbon isotope signatures associated with the same intrusions, and its association to a lower mantle plume uprising was proposed in Hayman *et al*., (2005) and Bulanova *et al*., (2010).

To reconcile the plume model with the magmatic activity along the Azimuth 125° Lineament would require evoking a superplume, with a plume head at least twice the size of the one proposed by Gibson *et al.*, (1997) and Thompson *et al*., (1998) or in Segev (2002). This superplume would have more than half the size of the superplume proposed by Larsson (1991) to have been emplaced in the middle of the Pacific Ocean. However, no matter how a plume model is conceived, the questioning of Felgate (2014) is still hard to be answered by these models, why a plume with a 1000 or 3000 km diameter head provokes intrusion and extrusion in narrow zones as the Azimuth 125° Linement, or the Transbrasiliano lineament which so far we have not addressed, but bringing this kimberlite occurrences of Jurassic-Cretaceous ages (Kaminsky *et al*., 2009b) into the discussion creates an even more complex problem to explain by plume models.

Attempts to relate kimberlite emplacement and lower mantle melts are fairly common. An example can be cited as the study of Torsvik *et al*., (2010), according to this study kimberlite intrusions occurred when the continental shelf was underlain by a Large Low Velocity Zone (LLVZ) located above the core-mantle boundary. Hunt *et al*., (2009) informs ages between 360 and 300 Ma, from an internal exploration report, since the study is not available, it is questionable, but if kimberlites with these ages are compared with the 355 Ma reconstruction show by Torsvik *et al*., (2010), these kimberlites would have been emplaced very far from LLVZs. The main ages for kimberlite emplacement in Brazil (630 Ma, 230 Ma, and 120-90 Ma) were not investigated in the Torsvik *et al.*,

(2010) work, but if they were, it is likely that almost none of them would fall above a LLVZ.

Magnetotelluric studies by Bologna *et al*., (2006), and Padilha *et al*., (2006) also revealed an anisotropic electric structure, where the higher conductive structure has a NW-SE trend to a depth of 410 km along the APA. These authors concluded that the Cretaceous magmatism is the likely cause for it. A distinct pattern, matching the MTZ anomalies trend, is observed on the seismic anisotropy study of Assumpção *et al*., (2011), were the predominant faster seismic velocities are oriented between WSW-ENE, consistent with the Absolute plate motion direction, but around the MTZ anomalies they are often oriented NW-SE (see compilation of shear wave splitting measurements in Figure 4.4). This pattern is inconsistent with the anisotropy pattern expected to be developed by a mantle plume, as predicted in Karato *et al*., (2008). These features suggests tectonically controlled magmatism.

Except for the Baikal rift, observed seismic anisotropy along rifts is oriented along the rift axis or slightly oblique to it (Gao *et al*., 1997 and Vauchez *et al*., 2000). Another diagnostic feature of the geodynamic mechanisms related to the magmatism is the slender NW-SE regional magnetic lineaments associated with intrusions along the APA and PGA (Geraldes *et al*., 2013). Magnetic lineaments parallel to the axis of a continental rift were observed by Bridges *et al*., 2012.

Padilha *et al*., (2006), Bologna *et al*., (2006) and Bologna *et al*., (2011) noticing high conductivity anomalies in the same area of the MTZ anomaly ‘B’, discussed that altered mantle composition due to the magmatic activity was the cause for the anomaly. Although, the mentioned authors presented a reasonable discussion for chemical alteration in detriment of a thermal origin; thermal anomalies found in the MTZ on the present study may contribute to higher-than-normal upper mantle temperatures, and, therefore, to the higher conductivities. The evaluation of seismic heterogeneity by Rocha *et al*., (2011) supports the role of chemical and thermal variations in the generation of these anomalies.

These MTZ anomalies coincide with the lowest Bouguer gravity anomalies observed in the Brazilian country by Sá *et al*., (1993), which is the expected Bouguer gravity anomaly pattern for a significantly hotter mantle. The study of Molina and Ussami (1999) shows geoid anomalies matching the positions of anomalies seen in the MTZ and highlighted the correlation with Cretaceous rifting and uplift, and Cretaceous to Cenozoic magmatism.

The anomalies 'B' and 'C' represent a 10 km thinner-than-normal MTZ, they are related to an anomalous temperature increase of 145±30°K. The anomaly 'J' is a 10 km thicker-than-normal MTZ, however due to its association with Cretaceous magmatism (Lages complex and nearby dike swarms), positive geoid anomalies, and uplift (Florianopolis High) with the same trend (Molina and Ussami, 1999), and the fact that there is a matching low velocity anomaly at the 500 and 700 km depth slices of the tomography model of Rocha *et al*., (2011), allows the suggestion of hotter-than-normal temperatures, instead of colder-than-normal. This could be a garnet enriched MTZ, as suggested in Deuss *et al*., (2006), leading to depression of the d410 and even greater depression of the d660, causing thickening of the MTZ under higher-than-normal temperatures, of similar intensity to the anomalies 'B' and 'C'. If the Garnet enrichment is a true feature, one could argue that this is evidence that crustal delamination may have taken place and that the material has foundered into the MTZ (e.g. Anderson, 2007).

To relate the observed MTZ anomalies with the Cretaceous uplift and magmatism would require a high level of coupling between the crust and upper mantle layers for the past 130-80 Ma, which is what has been suggested by VanDecar *et al*., (1995), Schimmel *et al*., (2003), Padilha *et al*., (2006), and Bizzi *et al*., (1995). Alternatively, this could be an apparent coupling, since the paleomagnetic study of Besse and Courtillot (2002) finds that South America's apparent polar wander shows small motion for the last 200 Ma and is considered to be fixed for the last 50 Ma. However, in the Absolute Plate Motion model of Gripp and Gordon (2002), the South America Plate moved over 260 km relative to the deep mantle in the last 5.8 Ma. Therefore, there is enough evidence to assume that this anomaly is indicating coupling between lithosphere, upper mantle and MTZ. The implication of this inference is that that the volcanic islands chains in the west side of the South Atlantic Ocean are fed by lower mantle plumes or they are the product of adiabatic melts. As discussed for the anomaly 'A', a lower mantle source is not a suitable source for the magmatism in the Fernando de Noronha volcanic island chain.

It is expressed here that the interpretation of these MTZ anomalies is simpler if adiabatic melts related to the Cretaceous rifting process are assumed. Their large dimensions, and related widespread magmatism and uplift, are incompatible with plume conduits, and passive upwelling and adiabatic melts are more suited.

Rifting of the South Atlantic started at ±130Ma and the effective separation took place at ±90 Ma (Mizusaki *et al*., 2002). Rifting stretched the lithosphere favoring upwelling of the lithosphere and mantle. This process is supported by the sedimentary record, or lack of it, and the uplift of several arches prior to the magmatic activity.

Uplift and volcanism in regions that extends hundreds of kms from the rift axis is observed in East African Rift System (EARS) and in the Rio Grande Rift (Gao *et al*., 1999). According to the model of Gao *et al*., (1999) upwelling generates partial melts modifying and eroding the lithosphere in a region far greater than the region of rifting onset. In the present model, the kimberlitic intrusions are related to the rift attempt to develop triple junctions (Azimuth 125° Lineament and Transbasiliano Lineament). Besides the kimberlite magmatism, significant tholeiitic dikes and sills were intruded along the Transbrasiliano lineament in the Late Cretaceous (Brito Neves and Fuck 2014) and alkaline and carbonatite intrusions occurred along the Azimuth 125° Lineament at similar ages.

The main phase of the rifting processes between South America and Africa is attributed to the onset of volcanism of the Parana-Etedenka flood basalts; this volcanism started at 134.7 Ma, and over a period of ±3 My (Renne *et al*., 1996, Thiede and Vasconcelos, 2010) more than 1,700,000 km^3 (Frank *et al*., 2009) of volcanic rocks was deposited at the surface. This rock volume will represent a larger volume of magma, if the loss of volatile content is considerate. Its relatively short span seems inconsistent with long lived lower mantle plume models, additionally age progression trends such as the Hawaii-Emperor volcanic island chain, usually suspected to be the product of a mantle plume, are absent.

This volume of magmatic extrusion, if generated by adiabatic melt (rifting), seems to be more than sufficient to promote an upwelling of mantle material and even of some Lower Mantle material into the MTZ, or closer depths to the surface, this is similar to the understanding expressed by Molina and Ussami (1999) observing thermal anomalies in the mantle. This level of extrusion and upwelling would raise the geothermal gradients, promoting partial melting in different levels of the upper mantle, as suggested by Guarino *et al.*, (2013).

Volcanism along the Azimuth 125° Lineament and Transbrasiliano Lineament can be seen as extrusion related to the attempt of the rift to propagate along this lineaments, a process similar, but in a much less evolved stage than an aulacogen, since the process was interrupted before the rift valley was formed along these lineaments. A Cretaceous aulacogen does exists along the coast near the MTZ anomalies 'B' and 'C' (Reconcavo/Tucano/Jatoba Basin). This aulacogen is divided in three basins by a NW-SE and a NE-SW epeirogenic structure. The kimberlite intrusions along the Azimuth 125° Lineament are interrupted at the border of the Amazon Craton, this is a typical feature of rifting, where rift propagation only takes place along weaker/altered lithosphere affected by Proterozoic to recent tectonic processes. As denoted for the EARS, the rift usually propagates along Proterozoic mobile belts avoiding cratons, such as the Tanzanian Craton, and the Baikal rift system bordering the Siberian Craton. In Brazil, the rift followed structures of similar age, the Brasiliano Provinces. The magmas from a mantle with a raised geothermal reflect the variability of the mantle and the buoyancy associated with its heterogeneity, similar to what is proposed in Anderson (2007). The interpretations expressed here do not differ significantly from what has been expressed by Almeida and Carneiro (1989).

4.5 CENTRAL ANDES ANOMALIES (D, E, I, AND K)

This area is noteworthy, since even with hundreds of RFs in each stacked trace, frequently the definition of peaks from the discontinuities was considered questionable, especially for the d410. Because of this, the Andes area between 12°S and 18°S is perceived as results with lower confidence relative to the rest of its areas. The d410 peaks, where the slab enters the MTZ, often vanish or bifurcate (Figure 3.2). According to Deuss (2007), double or broad peaks could be due to the effect of multiple phase transitions, focusing and defocusing by short wavelength topography or influence of a mantle plume. It is interpreted that in this areas a more complex velocity structure takes place. This phenomenon could be related to the presence of a water saturated layer locally, in a similar manner to what is suggested by Bercovici and Karato (2003), or to more complex mineral phase transitions, related to chemical or temperature variations effects (Bina and Helffrich, 2014).

Braunmiller *et al*., (2006) reported a d410 at 370 km depths and MTZ thickened by 45 km in this area. Prominent peaks around these depths were observed in the present study, always surrounding areas that are entrained by the slab, but never as a continuous uplift from 410 km to 370 km depths. These peaks from a depth of 370 km interface are independent from the observation of the d410 peaks, which means that peaks at 370 km will appear occasionally with a clear d410 peak or without it, and often deeper peaks, around 450 km, also appear.

This study cannot confirm or exclude the d410 mineral phase change occurring at 370 km depths, but from this work’s perception, the frequent disappearance of the d410 depth is an independent process from the processes related to the occurrence of other interfaces, except for the fact that these are variations triggered by the interaction with the slab. The occasionally combined or isolated effects of water and/or chemical variations and/or multi-step mineral phase transitions can account for these results.

These observations are in agreement with the results of Contenti *et al*., (2012) that reported absence of the d410 in the northern portion of the mentioned area, relating it to slab induced compositional anomalies. Difficulties in resolving the d410 in the southern portion of this area were also reported by Collier and Helffrich (2001). Similar observations were also made by Schmerr and Garnero (2007).

According to Fukao and Obayashi (2013) tomography images, in the Central Andes the slab is stagnant in the MTZ, approximately between 17°S and 27°S, while between 27°S and 33°S the slab is still stagnant, but it has detached from its upper portion above the d410. This interpretation is in accordance with the anomalous MTZ structures, 'D' between 17-27°S and 'K' between 27-33°S, there is a striking resemblance between the intensity and position of the velocity anomalies and the MTZ anomalies, where the velocity anomaly is stronger and closer to the subduction zone between 17°S-27°S, while the correspondent MTZ anomaly is thicker (30 km), and between 27°S-33°S, the slab is further away from the subduction zone and the velocity anomaly is less intense, in agreement with the position of the less thick MTZ anomaly (10 km).

The deflection of the Nazca slab, above the d660, in the Central Andes (anomaly 'D'), is inferred by the occurrence of deep isolated earthquakes inside the MTZ, the P-to-S conversion study of the MTZ by Liu *et al*., (2003), and was observed by diverse tomography studies (Engdahl *et al.*, 1995, Widiyantoro, 1997, Rocha *et al.*, 2011, Simmons *et al.*, 2012, Fukao and Obayashi, 2013).

In the area corresponding to the anomaly ‘I’ Fukao and Obayashi (2013) imaged the slab descending directly through the MTZ, becoming trapped in the uppermost portion of the lower mantle, while Contenti *et al*., (2012) and Scire (2015) inferred a stagnant slab thickened by buckling or folding in the MTZ. The southern portion of this anomaly is a well resolved feature and the 20 km thickening of the MTZ associated with depression of the d660 is in agreement with structure proposed by the latter authors. If the Fukao and Obayashi (2013) results are brought to the discussion, although these authors see the slab in the lower mantle, it is also possible to observe in their tomography images, a smaller velocity anomaly in the MTZ, disconnected from the slab, but in a similar position to the MTZ thickness anomaly, this could mean that a stagnant slab fragment was left behind. The northern portion of this MTZ thickness anomaly can be considered questionable, since a considerable portion of this area is defined with the minimum amount of RFs and the d660 amplitudes are at odds (Figure 4.2). Indication that the anomalies ‘I’ and ‘D’, are robust features can be considered by the fact that earthquakes beyond 400 km depths cluster into two locations coincident with the location of these anomalies (Figure 4.4).

In the southern Central Andes, the anomaly ‘E’ occurs as a very significant and distinctive uplift of the d410. Pesicek *et al*., (2012) tomography demonstrated two parallel high velocity structures with the same strike of the subduction zone, and interpreted that the slab suffered a vertical tear, leaving a displaced slab fragment inside the MTZ. The anomaly ‘E’ has a very similar pattern, and a parallel thicker anomaly structure is observed to its east. Therefore, it is believed that the anomaly ‘E’ confirms the Pesicek *et al*., (2012) results and interpretation. The anomaly ‘E’ is likely to be a slab fragment, while the eastern parallel feature is the subducting slab. The colder expression of the anomaly ‘E’ than the continuous slab is coherent with the hypothesis of an older slab fragment, therefore originally colder and interacting with the surrounding mantle for a longer period.

Small mantle plumes conduit (radius <100 km) have been inferred by Wolbern *et al*., (2009) based on P-to-S conversions from the MTZ (centered approximately at 25.5°S and 67.5°W), and another plume (centered at 33°S and 66°W) has been suggested by Burd *et al*., (2013), based on magnetotelluric observations (Figure 4.4), associated with a slab window inferred by Anderson *et al*,. (2007), and Pesicek *et al*., (2012). Surrounding the first area small magnitude MTZ thinning is observed, but much more intense thinning is observed near the Burd *et al*., (2013) plume, favoring this latter result. The temperature increase associated with this feature can be as high as 285±55 °K. Due to the lack of resolution to image this features, this study cannot discard the existence of such plumes.

Liu *et al.*, (2003) study observed a thickening of 30 km, and inferred a 300°C decrease in local temperatures in the Central Andes related to the stagnant slab. The present study also finds as much as 30 km thickening for the anomaly ‘D’, which overlaps the Liu *et al*., (2003) study area, reassuring the present results. However, due to consideration of different γ, here the decrease of temperatures is inferred to be 430±80°K for the anomaly ‘D’, the anomalies ‘I’ and ‘E” are associated with an anomalous temperature reduction of 285±55°K, and the anomaly ‘K’ is an expression of 145±30°K colder-than-normal MTZ.

4.6 NORTHERN ANDES ANOMALIES (H AND L)

In the Northern Andes, Huang *et al*. (2010) observed two anomalous thickening of the MTZ and related it to the Atlantic (eastern anomaly) and Nazca (western anomaly) slabs entrainment into the MTZ beneath Venezuela. Bezada *et al*., (2010) performed a tomography study and combined its observation with the results of Huang *et al*., (2010), interpreting that the western anomalous MTZ area was associated with the subducted Caribbean slab.

The anomaly ‘H’ is an expressive thickening of the MTZ beneath Venezuela and Colombia, where larger values (>30 km) are found towards the countries border (western portion). The western anomaly of Huang *et al*., (2010) is coincident with the anomaly ‘H’, Bezada *et al*., (2010) informs more than 60 km thickening of the MTZ for this anomaly. There is a large discrepancy of resolution between the present study and the study of Huang *et al*., (2010), the latter having a two times larger resolution; hence a direct relation between the anomalies is not simple, but the results are alike for their western anomaly, except for the fact that the perceived thickening is less intense in the present model, it is possible that the anomaly is smeared/smoothed due to lower resolution. A slab in the MTZ in the western portion of the anomaly ‘H’ can be consider a very well resolved feature, however defining if it is caused by the Caribbean or the Nazca slab seems to require further studies.

The eastern anomaly in Huang *et al*., (2010) is a 30 km thickening of the MTZ, however the present study finds a 20 km thinning of the MTZ (anomaly ‘L’) in this area. The non-detection of thickening may be due to differences in resolution; however the Huang *et al*., (2010) study do not have coverage of areas surrounding the anomaly to north, east and west directions, so it is incapable to demonstrate thinning surrounding the thicker anomaly. The same pattern observed for the anomaly ‘L’ can be observed in Schmerr and Garnero (2007). These observations reveal the need for further studies in this area in order to gain better understanding of these thicker and thinner MTZ structures. Entrainment of the Atlantic slab in the MTZ beneath South America has been inferred by tomography, as in Bezada *et al*., (2010) and VanDecar *et al*., (2003).

The anomaly ‘H’ has 430±80°K colder-than-normal temperatures, whereas the anomaly ‘L’ represents a 285±55°K increase in temperatures. However, Bezada *et al.*, (2010) and Huang *et al.*, (2010) inferred 170°K to 333°K colder-than-normal temperatures in an area overlapping part of the anomaly ‘L’. For the observation of hotter-than-normal MTZ it is speculated if perhaps shear stress could generate heat at depths greater than the lithosphere and account for the observed hotter-than-normal MTZ, since it occurs associated with a transform fault at the boundary between the South American and Caribbean plates. Hotter-than-normal upper mantle (Kearey *et al.*, 2009, p.226) and MTZ (Gao and Liu, 2014a) is also observed associated with the San Andreas Fault.

4.7 PATAGONIA ANOMALIES (F AND G)

Matching the anomaly ‘F’ feature, a low P-wave velocity anomaly and highly anisotropic (splitting time >3s) upper mantle structure was observed by Russo *et al.*, (2010) to depths of 200 km, and was interpreted as the combined effect of a slab window and associated subduction of the Chile ridge. The d410 is lowered by as much as 40 km and an even lower d660 (±60 km) is observed in the same area, the d410 depression is likely caused by the velocity anomaly reported by Russo *et al.,* (2010), but since the d660 is deeper than the d410, either a velocity anomaly of ~1.1% occurs inside the MTZ, or in contrast the MTZ is colder than normal, but this would imply in higher velocities instead making it hard to explain the 40 km depression of the d410.

The observation of hotter-than-normal upper mantle (Russo *et al.*, 2010) and the MTZ structure can be reconciled if associated to a Garnet enrichment. This kind of mineral phase transition takes place at much hotter temperatures than usual, deepening the d410 and the d660 even more, leading to a thickened MTZ (Deuss *et al.*, 2006). The existence of this zone can account for a positive thermal anomaly of 200°K to 400°K, depending on how much of the depth observations are being affected by velocity anomalies. Alternatively, if only the γ of olivine phase transitions is taken into consideration, this region could have 150° to 250° colder-than-normal temperatures; however this degree of thermal incoherence on the mantle column (MTZ and upper mantle) seems unlikely. The identification of Garnet enrichment may indicate crustal delamination, as discussed for the anomaly ‘J’.

Anomaly ‘G’ occurs associated with the triple junction between the South America, Antarctic and Scotia Plates, and a transform fault between South American and Scotia plates. This is a very similar context to what was discussed for the anomaly ‘L’. The ocean floor along this anomaly has a curious topography, and geoid anomalies have been inferred by Ernesto *et al.*, (2002). A thermal anomaly in the MTZ of 145±30°K hotter-than-normal temperatures is inferred, and upper mantle heat by shear stress is suggested.

5 CONCLUSIONS

This is the first continent-scale P-to-S RFs study of the MTZ beneath South America, and the highest resolution study to cover the continent. High seismic velocities in the upper mantle are associated with Archean cratons and the Parnaiba Block, while low velocities are seen in Patagonia, the Altiplano-Puna provinces, and in the Brazilian side of the country border shared with Bolivia. The majority of the previous observations from tomography, magnetotellurics, gravity, geoid and MTZ anomalies are in accordance with the present results, assuring its robustness.

The closest approximation to the true MTZ structure indicates an average d410 depth of 413.2 km, the d660 is 662.8 km, and the MTZ thickness is 249.6 km. Previously determined Claperyon slopes of 2 MPa/K and -3.3 MPa/K, for the d410 and the d660, respectively, are supported by this results.

Anomalies ‘A’, ‘B’ and ‘C’ are interpreted as passive upwelling mantle due to adiabatic magmatic activity. Two anomalies are interpreted as the Nazca plate’s stagnant slabs (‘D’ and ‘K’), while other anomalies can be slab fragments trapped in the MTZ (‘I’ and ‘E’). The anomaly ‘H’ is related to a stagnant slab, but further studies are required to distinguish between the Nazca or Caribbean slab. Anomalies ‘L’ and ‘G’ are tentatively related to heat generated by stress along transform plate boundaries. Evidence of garnet enriched MTZ is observed at two locations (anomalies ‘F’ and ‘J’).

The model reveals complex velocity structures around the Nazca slab, most likely related to chemical variations, but this variations are not restricted to this area based on the amplitude observations and MTZ anomalies related to garnet enrichment.

The hypothesis of a great degree of coupling between crust and upper mantle layers in the Brazilian platform becomes stronger with the observation that the MTZ is also reflecting this intriguing situation.

Hotter-than-normal anomalies (‘A’, ‘B’, ‘C’ and ‘J’) in the MTZ have a remarkable correlation with rift related processes and structures, while colder-than-normal anomalies (‘D’, ‘K’, ‘E’, ‘I’, and ‘H’) are found concentrated around subduction zone. This results indicates that the MTZ is significantly affected by tectonic processes.

APPENDIX A

STATIONS AND NETWORK INFORMATION

Table 1. Data information. Networks (NET) and stations (ST) names, stations latitude (LAT) and longitude (LON), and link to more information about the data sources.

NET	ST	LAT	LON	DATA INFORMATION
2B	BB06	-25.546	-68.372	http://doi.org/10.14470/7O092361
2B	BB16	-26.630	-65.866	http://doi.org/10.14470/7O092361
2B	BB18	-26.543	-66.363	http://doi.org/10.14470/7O092361
2B	EW01	-26.741	-67.011	http://doi.org/10.14470/7O092361
2B	EW05	-26.786	-66.295	http://doi.org/10.14470/7O092361
2B	EW06	-26.849	-66.128	http://doi.org/10.14470/7O092361
2B	EW07	-26.895	-66.044	http://doi.org/10.14470/7O092361
2B	EW08	-26.936	-65.789	http://doi.org/10.14470/7O092361
2B	EW22	-26.952	-65.693	http://doi.org/10.14470/7O092361
2B	GALAN	-25.845	-66.948	http://doi.org/10.14470/7O092361
2B	NS01	-26.098	-67.426	http://doi.org/10.14470/7O092361
2B	NS03	-26.315	-67.387	http://doi.org/10.14470/7O092361
2B	NS04	-26.420	-67.337	http://doi.org/10.14470/7O092361
2B	NS19	-26.039	-67.407	http://doi.org/10.14470/7O092361
2B	NS20	-25.932	-67.371	http://doi.org/10.14470/7O092361
2B	NS22	-25.757	-67.266	http://doi.org/10.14470/7O092361
2B	NS23	-25.663	-67.226	http://doi.org/10.14470/7O092361
2B	NS26	-25.415	-67.207	http://doi.org/10.14470/7O092361
3A	L002	-38.255	-72.257	http://www.fdsn.org/networks/detail/3A_2010
3A	L003	-38.295	-72.416	http://www.fdsn.org/networks/detail/3A_2010
3A	L005	-38.263	-72.794	http://www.fdsn.org/networks/detail/3A_2010
3A	L006	-38.289	-72.897	http://www.fdsn.org/networks/detail/3A_2010
3A	L007	-38.169	-73.367	http://www.fdsn.org/networks/detail/3A_2010
3A	L009	-37.030	-73.521	http://www.fdsn.org/networks/detail/3A_2010
3A	L101	-37.364	-73.658	http://www.fdsn.org/networks/detail/3A_2010
3A	L103	-37.339	-71.532	http://www.fdsn.org/networks/detail/3A_2010
3A	L104	-37.860	-72.089	http://www.fdsn.org/networks/detail/3A_2010
3A	L105	-38.455	-71.362	http://www.fdsn.org/networks/detail/3A_2010
3A	L106	-38.337	-71.810	http://www.fdsn.org/networks/detail/3A_2010
3A	L201	-38.508	-73.145	http://www.fdsn.org/networks/detail/3A_2010
3A	QC08	-38.272	-73.201	http://www.fdsn.org/networks/detail/3A_2010
3A	U16B	-36.858	-73.080	http://www.fdsn.org/networks/detail/3A_2010
3A	U40B	-36.633	-72.859	http://www.fdsn.org/networks/detail/3A_2010
3A	U69B	-34.371	-71.176	http://www.fdsn.org/networks/detail/3A_2010
3A	UO2B	-37.206	-72.981	http://www.fdsn.org/networks/detail/3A_2010
AI	DSPA	-53.954	-68.267	http://dx.doi.org/doi:10.7914/SN/AI

Table 1. Data information. Cont.

BL	AGVB	-19.739	-50.233	http://www.fdsn.org/networks/detail/BL
BL	APOB2	-18.508	-52.074	http://www.fdsn.org/networks/detail/BL
BL	APOB	-18.547	-52.025	http://www.fdsn.org/networks/detail/BL
BL	AQDA	-20.480	-55.700	http://www.fdsn.org/networks/detail/BL
BL	AQDB	-20.476	-55.700	http://www.fdsn.org/networks/detail/BL
BL	AREB	-21.363	-46.123	http://www.fdsn.org/networks/detail/BL
BL	ATDB	-21.290	-42.861	http://www.fdsn.org/networks/detail/BL
BL	BAMB	-20.040	-46.031	http://www.fdsn.org/networks/detail/BL
BL	BARB	-21.222	-43.801	http://www.fdsn.org/networks/detail/BL
BL	BB15B	-21.041	-48.531	http://www.fdsn.org/networks/detail/BL
BL	BB16B	-21.034	-48.586	http://www.fdsn.org/networks/detail/BL
BL	BB19B	-21.066	-48.528	http://www.fdsn.org/networks/detail/BL
BL	BB22B	-21.054	-48.505	http://www.fdsn.org/networks/detail/BL
BL	BEB11	-21.069	-48.502	http://www.fdsn.org/networks/detail/BL
BL	BEB4B	-21.082	-48.507	http://www.fdsn.org/networks/detail/BL
BL	BEB	-1.450	-48.444	http://www.fdsn.org/networks/detail/BL
BL	BESB	-6.657	-43.558	http://www.fdsn.org/networks/detail/BL
BL	BRSB	-22.535	-45.585	http://www.fdsn.org/networks/detail/BL
BL	BSCB	-20.998	-44.764	http://www.fdsn.org/networks/detail/BL
BL	BSFB	-18.831	-40.847	http://www.fdsn.org/networks/detail/BL
BL	C2SB	-18.769	-52.838	http://www.fdsn.org/networks/detail/BL
BL	CACB	-21.680	-46.733	http://www.fdsn.org/networks/detail/BL
BL	CAMB	-21.784	-41.429	http://www.fdsn.org/networks/detail/BL
BL	CANB	-22.968	-50.378	http://www.fdsn.org/networks/detail/BL
BL	CAPB	-22.813	-51.016	http://www.fdsn.org/networks/detail/BL
BL	CAUB	-8.177	-36.010	http://www.fdsn.org/networks/detail/BL
BL	CCUB	-18.425	-51.212	http://www.fdsn.org/networks/detail/BL
BL	CDCB	-20.237	-44.718	http://www.fdsn.org/networks/detail/BL
BL	CDSB	-18.766	-52.839	http://www.fdsn.org/networks/detail/BL
BL	CLDB	-10.873	-55.797	http://www.fdsn.org/networks/detail/BL
BL	CMPA	-19.579	-54.169	http://www.fdsn.org/networks/detail/BL
BL	CNLB	-29.315	-50.853	http://www.fdsn.org/networks/detail/BL
BL	CORB	-17.743	-48.689	http://www.fdsn.org/networks/detail/BL
BL	CPSB	-30.412	-53.443	http://www.fdsn.org/networks/detail/BL
BL	CRJB	-6.170	-50.155	http://www.fdsn.org/networks/detail/BL
BL	CRTB	-13.432	-44.582	http://www.fdsn.org/networks/detail/BL
BL	CS6B	-5.495	-36.671	http://www.fdsn.org/networks/detail/BL
BL	DIAM	-18.295	-43.665	http://www.fdsn.org/networks/detail/BL
BL	ESAR	-23.021	-44.440	http://www.fdsn.org/networks/detail/BL

Table 1. Data information. Cont.

BL	FRMB	-20.488	-45.639	http://www.fdsn.org/networks/detail/BL
BL	FRTB	-23.344	-49.564	http://www.fdsn.org/networks/detail/BL
BL	FURB	-20.678	-46.278	http://www.fdsn.org/networks/detail/BL
BL	GNSB	-15.264	-49.086	http://www.fdsn.org/networks/detail/BL
BL	IBIB	-21.777	-48.814	http://www.fdsn.org/networks/detail/BL
BL	IBTB	-23.853	-50.270	http://www.fdsn.org/networks/detail/BL
BL	IGAB	-23.252	-46.116	http://www.fdsn.org/networks/detail/BL
BL	IGCB	-1.127	-47.609	http://www.fdsn.org/networks/detail/BL
BL	ITAB	-27.235	-52.131	http://www.fdsn.org/networks/detail/BL
BL	ITPB	-15.989	-39.628	http://www.fdsn.org/networks/detail/BL
BL	ITQB	-29.664	-56.628	http://www.fdsn.org/networks/detail/BL
BL	ITRB	-19.704	-50.359	http://www.fdsn.org/networks/detail/BL
BL	JATB	-17.893	-51.493	http://www.fdsn.org/networks/detail/BL
BL	JFOB	-21.728	-43.326	http://www.fdsn.org/networks/detail/BL
BL	JNRB	-15.468	-44.505	http://www.fdsn.org/networks/detail/BL
BL	JUQB	-24.093	-47.716	http://www.fdsn.org/networks/detail/BL
BL	MARB	-24.452	-51.504	http://www.fdsn.org/networks/detail/BL
BL	MCI6	-16.807	-43.893	http://www.fdsn.org/networks/detail/BL
BL	MCI7	-16.779	-43.821	http://www.fdsn.org/networks/detail/BL
BL	MCI8	-16.660	-43.920	http://www.fdsn.org/networks/detail/BL
BL	MCI9	-16.698	-43.893	http://www.fdsn.org/networks/detail/BL
BL	NATB	-21.055	-42.004	http://www.fdsn.org/networks/detail/BL
BL	NAVB	-21.434	-54.184	http://www.fdsn.org/networks/detail/BL
BL	NOVB	-28.611	-49.558	http://www.fdsn.org/networks/detail/BL
BL	NUPB	-20.663	-47.686	http://www.fdsn.org/networks/detail/BL
BL	OLIB	-20.879	-48.931	http://www.fdsn.org/networks/detail/BL
BL	PACB	-21.607	-51.262	http://www.fdsn.org/networks/detail/BL
BL	PARB	-23.338	-45.622	http://www.fdsn.org/networks/detail/BL
BL	PAZB	-15.137	-50.863	http://www.fdsn.org/networks/detail/BL
BL	PCMB	-21.607	-51.262	http://www.fdsn.org/networks/detail/BL
BL	PDCB	-12.531	-39.124	http://www.fdsn.org/networks/detail/BL
BL	PEXB	-12.106	-48.301	http://www.fdsn.org/networks/detail/BL
BL	PLTB	-31.764	-53.605	http://www.fdsn.org/networks/detail/BL
BL	PMNB	-18.540	-46.440	http://www.fdsn.org/networks/detail/BL
BL	POPB	-22.457	-52.837	http://www.fdsn.org/networks/detail/BL
BL	PORB	-13.330	-49.079	http://www.fdsn.org/networks/detail/BL
BL	PP1A	-17.600	-54.880	http://www.fdsn.org/networks/detail/BL
BL	PP1B	-17.600	-54.880	http://www.fdsn.org/networks/detail/BL
BL	PPDB	-22.033	-51.314	http://www.fdsn.org/networks/detail/BL

Table 1. Data information. Cont.

BL	PRCB	-17.270	-46.819	http://www.fdsn.org/networks/detail/BL
BL	PTGB	-24.721	-52.012	http://www.fdsn.org/networks/detail/BL
BL	PTMB	-21.463	-57.476	http://www.fdsn.org/networks/detail/BL
BL	RCLB	-22.419	-47.531	http://www.fdsn.org/networks/detail/BL
BL	RIFB	-20.074	-47.502	http://www.fdsn.org/networks/detail/BL
BL	ROIB	-24.296	-51.135	http://www.fdsn.org/networks/detail/BL
BL	SICB	-23.625	-49.877	http://www.fdsn.org/networks/detail/BL
BL	SJI1	-21.182	-49.199	http://www.fdsn.org/networks/detail/BL
BL	SJMB	-18.703	-41.185	http://www.fdsn.org/networks/detail/BL
BL	SLMB	-16.571	-50.346	http://www.fdsn.org/networks/detail/BL
BL	SNVB	0.905	-51.877	http://www.fdsn.org/networks/detail/BL
BL	STMB	-2.752	-54.957	http://www.fdsn.org/networks/detail/BL
BL	TLMB	-24.073	-50.700	http://www.fdsn.org/networks/detail/BL
BL	TRCB	-22.795	-52.636	http://www.fdsn.org/networks/detail/BL
BL	TRIB	-20.672	-51.326	http://www.fdsn.org/networks/detail/BL
BL	TRMB	-18.092	-44.929	http://www.fdsn.org/networks/detail/BL
BL	TRRB	-22.154	-43.196	http://www.fdsn.org/networks/detail/BL
BL	TRSB	-4.873	-42.706	http://www.fdsn.org/networks/detail/BL
BL	VABB	-23.002	-46.966	http://www.fdsn.org/networks/detail/BL
BR	AGBLB	-9.039	-37.045	http://www.fdsn.org/networks/detail/BR
BR	ARAG	-15.706	-51.812	http://www.fdsn.org/networks/detail/BR
BR	BOAV	2.395	-60.523	http://www.fdsn.org/networks/detail/BR
BR	CZSB	-7.730	-72.705	http://www.fdsn.org/networks/detail/BR
BR	ETMB	-9.817	-66.214	http://www.fdsn.org/networks/detail/BR
BR	IPMB	-17.983	-48.212	http://www.fdsn.org/networks/detail/BR
BR	ITTB	-4.367	-55.734	http://www.fdsn.org/networks/detail/BR
BR	JAN7	-15.058	-44.311	http://www.fdsn.org/networks/detail/BR
BR	JANB	-15.058	-44.311	http://www.fdsn.org/networks/detail/BR
BR	MACA	-3.162	-60.684	http://www.fdsn.org/networks/detail/BR
BR	MALB	-1.853	-54.265	http://www.fdsn.org/networks/detail/BR
BR	MC01	-16.707	-43.942	http://www.fdsn.org/networks/detail/BR
BR	MCPB	-0.360	-52.057	http://www.fdsn.org/networks/detail/BR
BR	NPGB	-7.045	-55.358	http://www.fdsn.org/networks/detail/BR
BR	PRPB	-6.172	-49.815	http://www.fdsn.org/networks/detail/BR
BR	PTLB	-15.449	-59.137	http://www.fdsn.org/networks/detail/BR
BR	ROSB	-2.897	-44.125	http://www.fdsn.org/networks/detail/BR
BR	SALB	-15.901	-55.694	http://www.fdsn.org/networks/detail/BR
BR	SALV	-15.901	-55.694	http://www.fdsn.org/networks/detail/BR
BR	SDBA	-12.409	-44.903	http://www.fdsn.org/networks/detail/BR

Table 1. Data information. Cont.

BR	SMTB	-8.862	-47.589	http://www.fdsn.org/networks/detail/BR
BR	SNDB	-11.974	-51.294	http://www.fdsn.org/networks/detail/BR
BR	TBTG	-4.187	-69.909	http://www.fdsn.org/networks/detail/BR
BR	TMAB	-2.370	-48.096	http://www.fdsn.org/networks/detail/BR
BR	VILB	-12.953	-60.200	http://www.fdsn.org/networks/detail/BR
C1	AC01	-26.148	-70.599	http://www.fdsn.org/networks/detail/C1
C1	AC02	-26.836	-69.129	http://www.fdsn.org/networks/detail/C1
C1	AC04	-28.205	-71.074	http://www.fdsn.org/networks/detail/C1
C1	AC05	-28.836	-70.274	http://www.fdsn.org/networks/detail/C1
C1	AP01	-18.371	-70.342	http://www.fdsn.org/networks/detail/C1
C1	BI02	-36.663	-71.273	http://www.fdsn.org/networks/detail/C1
C1	BI03	-36.844	-73.026	http://www.fdsn.org/networks/detail/C1
C1	BO01	-34.392	-71.085	http://www.fdsn.org/networks/detail/C1
C1	BO02	-34.792	-70.781	http://www.fdsn.org/networks/detail/C1
C1	BO03	-34.496	-71.961	http://www.fdsn.org/networks/detail/C1
C1	CO01	-29.977	-70.094	http://www.fdsn.org/networks/detail/C1
C1	CO02	-31.204	-71.000	http://www.fdsn.org/networks/detail/C1
C1	CO03	-30.839	-70.689	http://www.fdsn.org/networks/detail/C1
C1	CO04	-32.043	-70.975	http://www.fdsn.org/networks/detail/C1
C1	DG06	-33.479	-70.527	http://www.fdsn.org/networks/detail/C1
C1	LC01	-38.898	-71.876	http://www.fdsn.org/networks/detail/C1
C1	LL01	-42.379	-72.413	http://www.fdsn.org/networks/detail/C1
C1	LL03	-41.138	-72.403	http://www.fdsn.org/networks/detail/C1
C1	MG01	-54.932	-67.630	http://www.fdsn.org/networks/detail/C1
C1	MT01	-33.864	-71.251	http://www.fdsn.org/networks/detail/C1
C1	MT02	-33.259	-71.138	http://www.fdsn.org/networks/detail/C1
C1	MT03	-33.494	-70.510	http://www.fdsn.org/networks/detail/C1
C1	MT05	-33.392	-70.738	http://www.fdsn.org/networks/detail/C1
C1	MT09	-33.776	-70.989	http://www.fdsn.org/networks/detail/C1
C1	TA01	-20.566	-70.181	http://www.fdsn.org/networks/detail/C1
C1	TA02	-20.271	-70.131	http://www.fdsn.org/networks/detail/C1
C1	VA01	-33.023	-71.637	http://www.fdsn.org/networks/detail/C1
C1	VA03	-32.764	-70.551	http://www.fdsn.org/networks/detail/C1
C1	VA05	-33.657	-71.614	http://www.fdsn.org/networks/detail/C1
CM	CAP2	8.650	-77.360	http://www.fdsn.org/networks/detail/CM
CM	HEL	6.234	-75.548	http://www.fdsn.org/networks/detail/CM
CM	MON	8.778	-75.665	http://www.fdsn.org/networks/detail/CM
CM	OCA	8.240	-73.320	http://www.fdsn.org/networks/detail/CM
CM	PRA	3.695	-74.901	http://www.fdsn.org/networks/detail/CM

Table 1. Data information. Cont.

CM	RUS	5.893	-73.083	http://www.fdsn.org/networks/detail/CM
CM	TUM	1.836	-78.726	http://www.fdsn.org/networks/detail/CM
CM	URI	11.700	-71.990	http://www.fdsn.org/networks/detail/CM
CU	BBGH	13.143	-59.559	http://www.fdsn.org/networks/detail/CU/
CU	BCIP	9.167	-79.837	http://www.fdsn.org/networks/detail/CU/
CU	GRGR	12.132	-61.654	http://www.fdsn.org/networks/detail/CU/
CX	HMBCX	-20.278	-69.888	http://doi.org/10.14470/PK615318
CX	MNMCX	-19.131	-69.596	http://doi.org/10.14470/PK615318
CX	PATCX	-20.821	-70.153	http://doi.org/10.14470/PK615318
CX	PB01	-21.043	-69.487	http://doi.org/10.14470/PK615318
CX	PB02	-21.320	-69.896	http://doi.org/10.14470/PK615318
CX	PB03	-22.049	-69.753	http://doi.org/10.14470/PK615318
CX	PB04	-22.334	-70.149	http://doi.org/10.14470/PK615318
CX	PB05	-22.853	-70.202	http://doi.org/10.14470/PK615318
CX	PB06	-22.706	-69.572	http://doi.org/10.14470/PK615318
CX	PB07	-21.727	-69.886	http://doi.org/10.14470/PK615318
CX	PB08	-20.141	-69.153	http://doi.org/10.14470/PK615318
CX	PB09	-21.796	-69.242	http://doi.org/10.14470/PK615318
CX	PB10	-23.513	-70.554	http://doi.org/10.14470/PK615318
CX	PB11	-19.761	-69.656	http://doi.org/10.14470/PK615318
CX	PB12	-18.614	-70.328	http://doi.org/10.14470/PK615318
CX	PB13	-18.336	-69.502	http://doi.org/10.14470/PK615318
CX	PB14	-24.626	-70.404	http://doi.org/10.14470/PK615318
CX	PB16	-18.335	-69.508	http://doi.org/10.14470/PK615318
CX	PSGCX	-19.597	-70.123	http://doi.org/10.14470/PK615318
C	CCH2	-36.603	-72.077	http://www.fdsn.org/networks/detail/C/
C	GO01	-19.669	-69.194	http://www.fdsn.org/networks/detail/C/
C	GO02	-25.163	-69.590	http://www.fdsn.org/networks/detail/C/
C	GO03	-27.594	-70.235	http://www.fdsn.org/networks/detail/C/
C	GO04	-30.173	-70.799	http://www.fdsn.org/networks/detail/C/
C	GO05	-35.010	-71.930	http://www.fdsn.org/networks/detail/C/
C	GO06	-39.584	-71.472	http://www.fdsn.org/networks/detail/C/
C	GO07	-43.114	-73.664	http://www.fdsn.org/networks/detail/C/
C	GO08	-48.465	-72.557	http://www.fdsn.org/networks/detail/C/
C	GO09	-51.271	-72.338	http://www.fdsn.org/networks/detail/C/
GE	LVC	-22.618	-68.911	http://doi.org/10.14470/TR560404
GE	RIOB	-10.150	-67.747	http://doi.org/10.14470/TR560404
GT	BDFB	-15.642	-48.015	http://dx.doi.org/doi:10.7914/SN/GT
GT	CPUP	-26.331	-57.331	http://dx.doi.org/doi:10.7914/SN/GT

Table 1. Data information. Cont.

GT	LPAZ	-16.288	-68.131	http://dx.doi.org/doi:10.7914/SN/GT
GT	PLCA	-40.733	-70.551	http://dx.doi.org/doi:10.7914/SN/GT
G	COYC	-45.573	-72.081	http://www.fdsn.org/networks/detail/G/
G	KOG	5.207	-52.732	http://www.fdsn.org/networks/detail/G/
G	MPG	5.110	-52.645	http://www.fdsn.org/networks/detail/G/
G	PEL	-33.144	-70.675	http://www.fdsn.org/networks/detail/G/
G	SPB	-23.593	-47.427	http://www.fdsn.org/networks/detail/G/
II	EFI	-51.675	-58.064	http://dx.doi.org/doi:10.7914/SN/II
II	HOPE	-54.284	-36.488	http://dx.doi.org/doi:10.7914/SN/II
IU	BOCO	4.587	-74.043	http://dx.doi.org/doi:10.7914/SN/IU
IU	LCO	-29.011	-70.700	http://dx.doi.org/doi:10.7914/SN/IU
IU	LVC	-22.613	-68.911	http://dx.doi.org/doi:10.7914/SN/IU
IU	OTAV	0.238	-78.451	http://dx.doi.org/doi:10.7914/SN/IU
IU	PTGA	-0.731	-59.967	http://dx.doi.org/doi:10.7914/SN/IU
IU	RCBR	-5.827	-35.901	http://dx.doi.org/doi:10.7914/SN/IU
IU	SAML	-8.949	-63.183	http://dx.doi.org/doi:10.7914/SN/IU
IU	SDV	8.884	-70.634	http://dx.doi.org/doi:10.7914/SN/IU
IU	TRQA	-38.057	-61.979	http://dx.doi.org/doi:10.7914/SN/IU
NB	NBAN	-9.669	-36.275	http://www.fdsn.org/networks/detail/NB/
NB	NBCA	-8.226	-36.013	http://www.fdsn.org/networks/detail/NB/
NB	NBCL	-4.224	-38.291	http://www.fdsn.org/networks/detail/NB/
NB	NBCP	-12.594	-39.182	http://www.fdsn.org/networks/detail/NB/
NB	NBIT	-14.977	-39.533	http://www.fdsn.org/networks/detail/NB/
NB	NBLA	-10.993	-37.789	http://www.fdsn.org/networks/detail/NB/
NB	NBLI	-7.365	-36.950	http://www.fdsn.org/networks/detail/NB/
NB	NBMA	-7.365	-38.764	http://www.fdsn.org/networks/detail/NB/
NB	NBMO	-3.311	-40.041	http://www.fdsn.org/networks/detail/NB/
NB	NBPA	-5.750	-37.112	http://www.fdsn.org/networks/detail/NB/
NB	NBPB	-5.546	-39.584	http://www.fdsn.org/networks/detail/NB/
NB	NBPN	-10.847	-40.199	http://www.fdsn.org/networks/detail/NB/
NB	NBPS	-4.394	-41.446	http://www.fdsn.org/networks/detail/NB/
NB	NBPV	-6.418	-35.291	http://www.fdsn.org/networks/detail/NB/
NB	NBRF	-8.680	-35.127	http://www.fdsn.org/networks/detail/NB/
NB	NBTA	-9.122	-38.063	http://www.fdsn.org/networks/detail/NB/
ON	ALF01	-20.617	-40.725	http://dx.doi.org/doi:10.7914/SN/ON
ON	CAM01	-21.826	-41.657	http://dx.doi.org/doi:10.7914/SN/ON
ON	CMC01	-15.360	-39.519	http://dx.doi.org/doi:10.7914/SN/ON
ON	DUB01	-22.081	-42.374	http://dx.doi.org/doi:10.7914/SN/ON
ON	GDU01	-13.720	-39.575	http://dx.doi.org/doi:10.7914/SN/ON

Table 1. Data information. Cont.

ON	GUA01	-16.584	-39.805	http://dx.doi.org/doi:10.7914/SN/ON
ON	JAC01	-24.811	-48.102	http://dx.doi.org/doi:10.7914/SN/ON
ON	MAJ01	-27.397	-49.012	http://dx.doi.org/doi:10.7914/SN/ON
ON	MAN01	-22.865	-43.964	http://dx.doi.org/doi:10.7914/SN/ON
ON	NAN01	-17.844	-40.126	http://dx.doi.org/doi:10.7914/SN/ON
ON	PET01	-24.290	-47.275	http://dx.doi.org/doi:10.7914/SN/ON
ON	RIB01	-19.314	-40.394	http://dx.doi.org/doi:10.7914/SN/ON
ON	SLP01	-23.324	-45.156	http://dx.doi.org/doi:10.7914/SN/ON
ON	TER01	-28.532	-49.129	http://dx.doi.org/doi:10.7914/SN/ON
ON	TIJ01	-25.324	-49.005	http://dx.doi.org/doi:10.7914/SN/ON
ON	VAS01	-22.280	-43.443	http://dx.doi.org/doi:10.7914/SN/ON
PR	AUA1	12.506	-70.011	http://www.fdsn.org/networks/detail/PR/
VE	GUNV	10.145	-62.943	http://www.fdsn.org/networks/detail/VE
VE	GURV	7.760	-63.085	http://www.fdsn.org/networks/detail/VE
VE	IMOV	12.359	-70.902	http://www.fdsn.org/networks/detail/VE
VE	ITEV	11.355	-63.132	http://www.fdsn.org/networks/detail/VE
VE	LUEV	5.843	-61.461	http://www.fdsn.org/networks/detail/VE
VE	MERV	9.262	-66.297	http://www.fdsn.org/networks/detail/VE
VE	MONV	11.955	-69.971	http://www.fdsn.org/networks/detail/VE
VE	ORIV	9.070	-63.418	http://www.fdsn.org/networks/detail/VE
VE	PAYV	5.421	-67.656	http://www.fdsn.org/networks/detail/VE
VE	QARV	10.206	-70.523	http://www.fdsn.org/networks/detail/VE
VE	SANV	9.501	-69.537	http://www.fdsn.org/networks/detail/VE
VE	SOCV	8.284	-70.857	http://www.fdsn.org/networks/detail/VE
VE	TERV	9.959	-69.287	http://www.fdsn.org/networks/detail/VE
VE	TURV	10.447	-67.838	http://www.fdsn.org/networks/detail/VE
VE	VIGV	8.840	-71.364	http://www.fdsn.org/networks/detail/VE
VE	VIRV	10.503	-72.406	http://www.fdsn.org/networks/detail/VE
WC	HATO	12.180	-68.958	http://www.fdsn.org/networks/detail/WC
X1	ANT	-45.393	-72.786	http://ds.iris.edu/mda/X1?timewindow=2007-2008
X1	CHA	-45.451	-72.789	http://ds.iris.edu/mda/X1?timewindow=2007-2008
X1	ELI	-45.889	-72.297	http://ds.iris.edu/mda/X1?timewindow=2007-2008
X1	LAP	-45.500	-72.632	http://ds.iris.edu/mda/X1?timewindow=2007-2008
X1	LLP	-45.341	-72.699	http://ds.iris.edu/mda/X1?timewindow=2007-2008
X1	MEL	-43.901	-72.858	http://ds.iris.edu/mda/X1?timewindow=2007-2008
X1	PCI	-44.758	-72.702	http://ds.iris.edu/mda/X1?timewindow=2007-2008
X1	PUY	-44.746	-72.995	http://ds.iris.edu/mda/X1?timewindow=2007-2008
X1	RCL	-45.586	-72.184	http://ds.iris.edu/mda/X1?timewindow=2007-2008
X1	RIE	-45.537	-72.723	http://ds.iris.edu/mda/X1?timewindow=2007-2008

Table 1. Data information. Cont.

X1	RMA	-45.262	-72.265	http://ds.iris.edu/mda/X1?timewindow=2007-2008
X1	RPS	-45.398	-73.102	http://ds.iris.edu/mda/X1?timewindow=2007-2008
X1	TOR	-45.321	-73.088	http://ds.iris.edu/mda/X1?timewindow=2007-2008
X1	VVE	-45.367	-72.573	http://ds.iris.edu/mda/X1?timewindow=2007-2008
X6	BB01	-27.424	-68.144	http://ds.iris.edu/mda/X1?timewindow=2007-2008
X6	BB02	-27.111	-68.090	http://ds.iris.edu/mda/X1?timewindow=2007-2008
X6	BB03	-27.488	-68.257	http://ds.iris.edu/mda/X1?timewindow=2007-2008
X6	BB04	-26.540	-68.021	http://ds.iris.edu/mda/X1?timewindow=2007-2008
X6	BB07	-25.516	-67.618	http://ds.iris.edu/mda/X1?timewindow=2007-2008
X6	BB08	-26.016	-67.918	http://ds.iris.edu/mda/X1?timewindow=2007-2008
X6	BB09	-26.525	-68.099	http://ds.iris.edu/mda/X1?timewindow=2007-2008
X6	BB10	-26.379	-67.691	http://ds.iris.edu/mda/X1?timewindow=2007-2008
X6	BB11	-27.113	-66.944	http://ds.iris.edu/mda/X1?timewindow=2007-2008
X6	BB12	-27.513	-67.125	http://ds.iris.edu/mda/X1?timewindow=2007-2008
X6	BB13	-27.641	-66.598	http://ds.iris.edu/mda/X1?timewindow=2007-2008
X6	BB14	-27.597	-65.979	http://ds.iris.edu/mda/X1?timewindow=2007-2008
X6	BB15	-27.341	-66.370	http://ds.iris.edu/mda/X1?timewindow=2007-2008
X6	BB19	-26.306	-67.062	http://ds.iris.edu/mda/X1?timewindow=2007-2008
X6	BB22	-26.157	-69.237	http://ds.iris.edu/mda/X1?timewindow=2007-2008
X6	BB23	-25.367	-69.426	http://ds.iris.edu/mda/X1?timewindow=2007-2008
X6	BB24	-27.833	-68.098	http://ds.iris.edu/mda/X1?timewindow=2007-2008
X6	BB25	-27.620	-68.543	http://ds.iris.edu/mda/X1?timewindow=2007-2008
X6	EW09	-26.684	-67.184	http://ds.iris.edu/mda/X1?timewindow=2007-2008
X6	EW10	-26.592	-67.262	http://ds.iris.edu/mda/X1?timewindow=2007-2008
X6	EW11	-26.666	-67.676	http://ds.iris.edu/mda/X1?timewindow=2007-2008
X6	EW12	-26.685	-67.774	http://ds.iris.edu/mda/X1?timewindow=2007-2008
X6	EW13	-26.652	-67.877	http://ds.iris.edu/mda/X1?timewindow=2007-2008
X6	EW14	-26.709	-68.003	http://ds.iris.edu/mda/X1?timewindow=2007-2008
X6	EW16	-26.851	-68.277	http://ds.iris.edu/mda/X1?timewindow=2007-2008
X6	EW17	-26.885	-68.427	http://ds.iris.edu/mda/X1?timewindow=2007-2008
X6	EW18	-26.906	-68.552	http://ds.iris.edu/mda/X1?timewindow=2007-2008
X6	EW19	-26.881	-68.666	http://ds.iris.edu/mda/X1?timewindow=2007-2008
X6	EW20	-26.910	-68.767	http://ds.iris.edu/mda/X1?timewindow=2007-2008
X6	NS05	-26.513	-67.403	http://ds.iris.edu/mda/X1?timewindow=2007-2008
X6	NS06	-26.616	-67.440	http://ds.iris.edu/mda/X1?timewindow=2007-2008
X6	NS07	-26.668	-67.551	http://ds.iris.edu/mda/X1?timewindow=2007-2008
X6	NS08	-26.784	-67.648	http://ds.iris.edu/mda/X1?timewindow=2007-2008
X6	NS09	-26.910	-67.653	http://ds.iris.edu/mda/X1?timewindow=2007-2008
X6	NS10	-27.051	-67.688	http://ds.iris.edu/mda/X1?timewindow=2007-2008

Table 1. Data information. Cont.

X6	NS11	-27.113	-67.703	http://ds.iris.edu/mda/X1?timewindow=2007-2008
X6	NS12	-27.228	-67.757	http://ds.iris.edu/mda/X1?timewindow=2007-2008
X6	NS14	-27.444	-67.694	http://ds.iris.edu/mda/X1?timewindow=2007-2008
X6	NS15	-27.480	-67.603	http://ds.iris.edu/mda/X1?timewindow=2007-2008
X6	NS16	-27.569	-67.613	http://ds.iris.edu/mda/X1?timewindow=2007-2008
X6	NS17	-27.708	-67.625	http://ds.iris.edu/mda/X1?timewindow=2007-2008
X6	NS18	-27.901	-67.629	http://ds.iris.edu/mda/X1?timewindow=2007-2008
XB	FELL	-52.057	-70.005	http://www.fdsn.org/networks/detail/XB_2005
XB	HAMB	-53.614	-70.931	http://www.fdsn.org/networks/detail/XB_2005
XB	MILO	-51.568	-72.620	http://www.fdsn.org/networks/detail/XB_2005
XB	SALM	-52.549	-72.030	http://www.fdsn.org/networks/detail/XB_2005
XB	VTDF	-54.139	-68.706	http://www.fdsn.org/networks/detail/XB_2005
XE	BATO	-19.626	-65.437	http://ds.iris.edu/mda/XE?timewindow=1994-1995
XE	CHIT	-20.077	-66.886	http://ds.iris.edu/mda/XE?timewindow=1994-1995
XE	CHUQ	-17.945	-67.818	http://ds.iris.edu/mda/XE?timewindow=1994-1995
XE	COLL	-16.922	-68.315	http://ds.iris.edu/mda/XE?timewindow=1994-1995
XE	CRIS	-19.375	-65.930	http://ds.iris.edu/mda/XE?timewindow=1994-1995
XE	CRUZ	-19.103	-66.221	http://ds.iris.edu/mda/XE?timewindow=1994-1995
XE	DOOR	-19.354	-67.223	http://ds.iris.edu/mda/XE?timewindow=1994-1995
XE	HIZO	-19.607	-68.326	http://ds.iris.edu/mda/XE?timewindow=1994-1995
XE	ITIT	-20.255	-63.158	http://ds.iris.edu/mda/XE?timewindow=1994-1995
XE	LAJO	-17.776	-67.479	http://ds.iris.edu/mda/XE?timewindow=1994-1995
XE	LIRI	-19.852	-68.849	http://ds.iris.edu/mda/XE?timewindow=1994-1995
XE	PACH	-19.869	-69.420	http://ds.iris.edu/mda/XE?timewindow=1994-1995
XE	PICH	-19.812	-63.721	http://ds.iris.edu/mda/XE?timewindow=1994-1995
XE	POOP	-18.387	-67.018	http://ds.iris.edu/mda/XE?timewindow=1994-1995
XE	ROSL	-19.486	-64.178	http://ds.iris.edu/mda/XE?timewindow=1994-1995
XE	SALI	-19.621	-67.726	http://ds.iris.edu/mda/XE?timewindow=1994-1995
XE	SCHO	-19.148	-64.643	http://ds.iris.edu/mda/XE?timewindow=1994-1995
XE	SICA	-17.292	-67.749	http://ds.iris.edu/mda/XE?timewindow=1994-1995
XE	TACA	-18.828	-66.734	http://ds.iris.edu/mda/XE?timewindow=1994-1995
XE	YUNZ	-19.158	-65.069	http://ds.iris.edu/mda/XE?timewindow=1994-1995
XH	CHAS	-21.960	-67.850	http://www.fdsn.org/networks/detail/XH_2008
XH	ESP01	-29.141	-64.064	http://www.fdsn.org/networks/detail/XH_2008
XH	ESP02	-29.456	-64.051	http://www.fdsn.org/networks/detail/XH_2008
XH	ESP03	-29.743	-64.014	http://www.fdsn.org/networks/detail/XH_2008
XH	ESP04	-30.772	-64.409	http://www.fdsn.org/networks/detail/XH_2008
XH	ESP05	-31.011	-64.648	http://www.fdsn.org/networks/detail/XH_2008
XH	ESP06	-31.138	-64.956	http://www.fdsn.org/networks/detail/XH_2008

Table 1. Data information. Cont.

XH	ESP07	-31.265	-65.224	http://www.fdsn.org/networks/detail/XH_2008
XH	ESP08	-31.597	-64.550	http://www.fdsn.org/networks/detail/XH_2008
XH	ESP09	-31.909	-64.658	http://www.fdsn.org/networks/detail/XH_2008
XH	ESP10	-32.152	-64.999	http://www.fdsn.org/networks/detail/XH_2008
XH	ESP11	-32.419	-65.717	http://www.fdsn.org/networks/detail/XH_2008
XH	ESP12	-32.832	-66.080	http://www.fdsn.org/networks/detail/XH_2008
XH	GUAC	-22.530	-67.490	http://www.fdsn.org/networks/detail/XH_2008
XH	LCOL	-22.280	-67.650	http://www.fdsn.org/networks/detail/XH_2008
XH	OLLA	-21.320	-68.040	http://www.fdsn.org/networks/detail/XH_2008
XH	PNEG	-22.390	-67.130	http://www.fdsn.org/networks/detail/XH_2008
XH	SONI	-21.950	-67.350	http://www.fdsn.org/networks/detail/XH_2008
XH	UYUN	-20.460	-66.750	http://www.fdsn.org/networks/detail/XH_2008
XJ	AISN	-45.411	-72.618	http://www.fdsn.org/networks/detail/XJ_2004
XJ	BALM	-45.891	-71.767	http://www.fdsn.org/networks/detail/XJ_2004
XJ	BARR	-45.735	-72.206	http://www.fdsn.org/networks/detail/XJ_2004
XJ	BERT	-47.020	-72.802	http://www.fdsn.org/networks/detail/XJ_2004
XJ	CHAC	-47.117	-72.486	http://www.fdsn.org/networks/detail/XJ_2004
XJ	CHCH	-46.599	-71.695	http://www.fdsn.org/networks/detail/XJ_2004
XJ	COCH	-47.317	-72.570	http://www.fdsn.org/networks/detail/XJ_2004
XJ	ELCO	-47.254	-72.531	http://www.fdsn.org/networks/detail/XJ_2004
XJ	ELSA	-46.607	-72.742	http://www.fdsn.org/networks/detail/XJ_2004
XJ	ENBA	-47.135	-72.054	http://www.fdsn.org/networks/detail/XJ_2004
XJ	FACH	-46.590	-72.170	http://www.fdsn.org/networks/detail/XJ_2004
XJ	GUAD	-46.863	-72.693	http://www.fdsn.org/networks/detail/XJ_2004
XJ	HUDS	-45.886	-73.221	http://www.fdsn.org/networks/detail/XJ_2004
XJ	IBAN	-46.247	-71.930	http://www.fdsn.org/networks/detail/XJ_2004
XJ	JARA	-46.517	-71.846	http://www.fdsn.org/networks/detail/XJ_2004
XJ	JOSE	-46.747	-72.543	http://www.fdsn.org/networks/detail/XJ_2004
XJ	JOVI	-46.501	-72.722	http://www.fdsn.org/networks/detail/XJ_2004
XJ	LACA	-45.706	-72.508	http://www.fdsn.org/networks/detail/XJ_2004
XJ	LAJE	-46.844	-71.998	http://www.fdsn.org/networks/detail/XJ_2004
XJ	LAMO	-45.860	-72.051	http://www.fdsn.org/networks/detail/XJ_2004
XJ	LAOH	-48.517	-72.597	http://www.fdsn.org/networks/detail/XJ_2004
XJ	LAPO	-45.703	-71.833	http://www.fdsn.org/networks/detail/XJ_2004
XJ	LASN	-46.242	-72.087	http://www.fdsn.org/networks/detail/XJ_2004
XJ	LATA	-44.744	-71.675	http://www.fdsn.org/networks/detail/XJ_2004
XJ	LATR	-45.668	-72.413	http://www.fdsn.org/networks/detail/XJ_2004
XJ	LAVA	-47.700	-73.144	http://www.fdsn.org/networks/detail/XJ_2004
XJ	LEON	-46.719	-72.994	http://www.fdsn.org/networks/detail/XJ_2004

Table 1. Data information. Cont.

XJ	LEVI	-46.348	-71.934	http://www.fdsn.org/networks/detail/XJ_2004
XJ	LNEG	-46.577	-72.642	http://www.fdsn.org/networks/detail/XJ_2004
XJ	LOVE	-46.192	-72.798	http://www.fdsn.org/networks/detail/XJ_2004
XJ	LUNA	-45.883	-72.330	http://www.fdsn.org/networks/detail/XJ_2004
XJ	MANE	-45.384	-71.985	http://www.fdsn.org/networks/detail/XJ_2004
XJ	MANI	-45.238	-72.234	http://www.fdsn.org/networks/detail/XJ_2004
XJ	MANS	-46.145	-72.388	http://www.fdsn.org/networks/detail/XJ_2004
XJ	MART	-46.837	-72.800	http://www.fdsn.org/networks/detail/XJ_2004
XJ	MAYE	-48.263	-72.427	http://www.fdsn.org/networks/detail/XJ_2004
XJ	MILI	-47.175	-71.888	http://www.fdsn.org/networks/detail/XJ_2004
XJ	MURT	-46.455	-72.680	http://www.fdsn.org/networks/detail/XJ_2004
XJ	ODGE	-46.147	-73.715	http://www.fdsn.org/networks/detail/XJ_2004
XJ	PALA	-46.296	-71.832	http://www.fdsn.org/networks/detail/XJ_2004
XJ	PCEA	-45.673	-72.221	http://www.fdsn.org/networks/detail/XJ_2004
XJ	PENI	-47.238	-72.330	http://www.fdsn.org/networks/detail/XJ_2004
XJ	PSAN	-46.593	-72.542	http://www.fdsn.org/networks/detail/XJ_2004
XJ	PUAG	-45.167	-73.513	http://www.fdsn.org/networks/detail/XJ_2004
XJ	RICA	-46.125	-72.556	http://www.fdsn.org/networks/detail/XJ_2004
XJ	RIMA	-45.311	-72.327	http://www.fdsn.org/networks/detail/XJ_2004
XJ	TRANA	-46.635	-72.840	http://www.fdsn.org/networks/detail/XJ_2004
XJ	TRANB	-46.635	-72.840	http://www.fdsn.org/networks/detail/XJ_2004
XJ	TRES	-47.406	-72.712	http://www.fdsn.org/networks/detail/XJ_2004
XJ	VIVI	-45.361	-72.457	http://www.fdsn.org/networks/detail/XJ_2004
XN	CCP2	10.879	-69.833	http://ds.iris.edu/mda/XN?timewindow=2008-2009
XN	CRP4	9.788	-69.583	http://ds.iris.edu/mda/XN?timewindow=2008-2009
XN	PPP6	8.941	-69.460	http://ds.iris.edu/mda/XN?timewindow=2008-2009
XN	RCP5	9.265	-69.498	http://ds.iris.edu/mda/XN?timewindow=2008-2009
XO	AMA	-23.561	-69.393	http://geofon.gfz-potsdam.de/waveform/archive/network.php?ncode=XO&year=1995
XO	COL	-23.786	-70.409	http://geofon.gfz-potsdam.de/waveform/archive/network.php?ncode=XO&year=1995
XO	GUA	-23.027	-69.627	http://geofon.gfz-potsdam.de/waveform/archive/network.php?ncode=XO&year=1995
XO	MIC	-22.701	-70.163	http://geofon.gfz-potsdam.de/waveform/archive/network.php?ncode=XO&year=1995
XO	MJP	-23.175	-70.320	http://geofon.gfz-potsdam.de/waveform/archive/network.php?ncode=XO&year=1995
XO	NAV	-23.772	-70.044	http://geofon.gfz-potsdam.de/waveform/archive/network.php?ncode=XO&year=1995
XO	PUN	-23.117	-69.420	http://geofon.gfz-potsdam.de/waveform/archive/network.php?ncode=XO&year=1995

Table 1. Data information. Cont.

XO	SUR	-24.245	-70.407	http://geofon.gfz-potsdam.de/waveform/archive/network.php?ncode=XO&year=1995
XO	VAL	-22.648	-69.716	http://geofon.gfz-potsdam.de/waveform/archive/network.php?ncode=XO&year=1995
XP	PL03	-22.016	-66.945	http://dx.doi.org/doi:10.7914/SN/XP_2010
XS	QC01	-32.259	-70.909	http://www.fdsn.org/networks/detail/XS_2010
XS	QC02	-37.038	-72.551	http://www.fdsn.org/networks/detail/XS_2010
XS	QC03	-37.607	-71.987	http://www.fdsn.org/networks/detail/XS_2010
XS	QC04	-37.553	-73.096	http://www.fdsn.org/networks/detail/XS_2010
XS	QC05	-38.290	-72.612	http://www.fdsn.org/networks/detail/XS_2010
XS	QC06	-33.993	-71.603	http://www.fdsn.org/networks/detail/XS_2010
XS	QC07	-37.809	-72.697	http://www.fdsn.org/networks/detail/XS_2010
XS	QC08	-38.272	-73.201	http://www.fdsn.org/networks/detail/XS_2010
XS	QC09	-33.998	-71.604	http://www.fdsn.org/networks/detail/XS_2010
XS	QC10	-37.541	-72.815	http://www.fdsn.org/networks/detail/XS_2010
XS	QC11	-37.767	-73.489	http://www.fdsn.org/networks/detail/XS_2010
XS	QC12	-34.189	-71.199	http://www.fdsn.org/networks/detail/XS_2010
XS	QC13	-33.998	-71.609	http://www.fdsn.org/networks/detail/XS_2010
XS	QC14	-37.326	-72.934	http://www.fdsn.org/networks/detail/XS_2010
XS	QF05	-34.001	-71.605	http://www.fdsn.org/networks/detail/XS_2010
XS	QF08	-35.427	-71.648	http://www.fdsn.org/networks/detail/XS_2010
XS	QF11	-36.406	-72.401	http://www.fdsn.org/networks/detail/XS_2010
XS	QF12	-34.354	-71.712	http://www.fdsn.org/networks/detail/XS_2010
XS	QF14	-35.205	-71.967	http://www.fdsn.org/networks/detail/XS_2010
XS	QF15	-35.425	-71.602	http://www.fdsn.org/networks/detail/XS_2010
XS	QF17	-34.643	-71.895	http://www.fdsn.org/networks/detail/XS_2010
XS	QF18	-35.421	-71.667	http://www.fdsn.org/networks/detail/XS_2010
XS	SAN1	-2.016	-78.349	http://www.fdsn.org/networks/detail/XS_2010
XT	ABPC	9.461	-64.821	http://www.fdsn.org/networks/detail/XT_2003
XT	ARPC	9.744	-63.797	http://www.fdsn.org/networks/detail/XT_2003
XT	BTBT	11.499	-62.501	http://www.fdsn.org/networks/detail/XT_2003
XT	CAPC	7.343	-61.826	http://www.fdsn.org/networks/detail/XT_2003
XT	CMPC	7.651	-64.073	http://www.fdsn.org/networks/detail/XT_2003
XT	CUPC	10.158	-63.826	http://www.fdsn.org/networks/detail/XT_2003
XT	EDPC	6.713	-61.639	http://www.fdsn.org/networks/detail/XT_2003
XT	FCPC	9.650	-66.834	http://www.fdsn.org/networks/detail/XT_2003
XT	JMPC	9.887	-67.397	http://www.fdsn.org/networks/detail/XT_2003
XT	LAPC	8.985	-65.772	http://www.fdsn.org/networks/detail/XT_2003
XT	LMPC2	9.356	-67.383	http://www.fdsn.org/networks/detail/XT_2003
XT	MAPC	7.417	-65.188	http://www.fdsn.org/networks/detail/XT_2003

Table 1. Data information. Cont.

XT	MNPC	8.988	-62.744	http://www.fdsn.org/networks/detail/XT_2003
XT	MOPC	6.586	-66.843	http://www.fdsn.org/networks/detail/XT_2003
XT	MUPC	8.327	-64.295	http://www.fdsn.org/networks/detail/XT_2003
XT	PAPC	8.034	-62.655	http://www.fdsn.org/networks/detail/XT_2003
XT	PFPC	8.328	-65.944	http://www.fdsn.org/networks/detail/XT_2003
XT	PRPC	8.502	-63.625	http://www.fdsn.org/networks/detail/XT_2003
XT	ROPC	9.909	-66.385	http://www.fdsn.org/networks/detail/XT_2003
XT	RPPC	8.949	-66.436	http://www.fdsn.org/networks/detail/XT_2003
XT	SMPC	8.513	-66.322	http://www.fdsn.org/networks/detail/XT_2003
XT	SRPC	9.583	-64.294	http://www.fdsn.org/networks/detail/XT_2003
XT	STPC	8.137	-66.254	http://www.fdsn.org/networks/detail/XT_2003
XT	ULPC	8.857	-67.387	http://www.fdsn.org/networks/detail/XT_2003
XT	VIPC	7.861	-62.066	http://www.fdsn.org/networks/detail/XT_2003
XT	ZUPC	8.360	-65.195	http://www.fdsn.org/networks/detail/XT_2003
XY	U01B	-37.288	-72.490	http://www.fdsn.org/networks/detail/XY_2010
XY	U03B	-37.701	-72.330	http://www.fdsn.org/networks/detail/XY_2010
XY	U04B	-37.987	-72.570	http://www.fdsn.org/networks/detail/XY_2010
XY	U05B	-37.950	-72.810	http://www.fdsn.org/networks/detail/XY_2010
XY	U06B	-37.224	-73.550	http://www.fdsn.org/networks/detail/XY_2010
XY	U07B	-38.255	-73.473	http://www.fdsn.org/networks/detail/XY_2010
XY	U08B	-36.628	-72.592	http://www.fdsn.org/networks/detail/XY_2010
XY	U09B	-38.488	-73.183	http://www.fdsn.org/networks/detail/XY_2010
XY	U10B	-38.204	-72.848	http://www.fdsn.org/networks/detail/XY_2010
XY	U11B	-37.213	-71.833	http://www.fdsn.org/networks/detail/XY_2010
XY	U12B	-37.951	-73.406	http://www.fdsn.org/networks/detail/XY_2010
XY	U14B	-36.858	-73.080	http://www.fdsn.org/networks/detail/XY_2010
XY	U15B	-38.068	-73.000	http://www.fdsn.org/networks/detail/XY_2010
XY	U16B	-37.824	-72.962	http://www.fdsn.org/networks/detail/XY_2010
XY	U26B	-36.518	-72.218	http://www.fdsn.org/networks/detail/XY_2010
XY	U27B	-36.284	-72.527	http://www.fdsn.org/networks/detail/XY_2010
XY	U28B	-36.326	-72.328	http://www.fdsn.org/networks/detail/XY_2010
XY	U29B	-36.909	-71.495	http://www.fdsn.org/networks/detail/XY_2010
XY	U32B	-36.328	-71.741	http://www.fdsn.org/networks/detail/XY_2010
XY	U33B	-36.561	-71.539	http://www.fdsn.org/networks/detail/XY_2010
XY	U34B	-36.449	-71.707	http://www.fdsn.org/networks/detail/XY_2010
XY	U36B	-36.763	-72.369	http://www.fdsn.org/networks/detail/XY_2010
XY	U37B	-36.798	-72.622	http://www.fdsn.org/networks/detail/XY_2010
XY	U40B	-36.633	-72.859	http://www.fdsn.org/networks/detail/XY_2010
XY	U41B	-36.396	-72.836	http://www.fdsn.org/networks/detail/XY_2010

Table 1. Data information. Cont.

XY	U42B	-36.915	-72.835	http://www.fdsn.org/networks/detail/XY_2010
XY	U43B	-36.222	-71.480	http://www.fdsn.org/networks/detail/XY_2010
XY	U44B	-36.093	-72.108	http://www.fdsn.org/networks/detail/XY_2010
XY	U45B	-34.741	-71.644	http://www.fdsn.org/networks/detail/XY_2010
XY	U46B	-35.063	-71.147	http://www.fdsn.org/networks/detail/XY_2010
XY	U51B	-34.649	-71.206	http://www.fdsn.org/networks/detail/XY_2010
XY	U52B	-35.797	-71.437	http://www.fdsn.org/networks/detail/XY_2010
XY	U53B	-35.871	-71.760	http://www.fdsn.org/networks/detail/XY_2010
XY	U54B	-35.546	-71.360	http://www.fdsn.org/networks/detail/XY_2010
XY	U55B	-35.701	-71.100	http://www.fdsn.org/networks/detail/XY_2010
XY	U56B	-35.291	-71.246	http://www.fdsn.org/networks/detail/XY_2010
XY	U57B	-35.494	-72.097	http://www.fdsn.org/networks/detail/XY_2010
XY	U58B	-35.375	-72.449	http://www.fdsn.org/networks/detail/XY_2010
XY	U59B	-35.913	-72.400	http://www.fdsn.org/networks/detail/XY_2010
XY	U60B	-35.878	-72.617	http://www.fdsn.org/networks/detail/XY_2010
XY	U61B	-35.567	-72.600	http://www.fdsn.org/networks/detail/XY_2010
XY	U62B	-35.659	-71.771	http://www.fdsn.org/networks/detail/XY_2010
XY	U63B	-35.725	-72.130	http://www.fdsn.org/networks/detail/XY_2010
XY	U64B	-35.398	-71.680	http://www.fdsn.org/networks/detail/XY_2010
XY	U65B	-34.964	-71.789	http://www.fdsn.org/networks/detail/XY_2010
XY	U66B	-34.906	-72.166	http://www.fdsn.org/networks/detail/XY_2010
XY	U67B	-34.487	-71.554	http://www.fdsn.org/networks/detail/XY_2010
XY	U68B	-34.408	-71.971	http://www.fdsn.org/networks/detail/XY_2010
XY	U69B	-34.371	-71.176	http://www.fdsn.org/networks/detail/XY_2010
XY	U71B	-34.090	-70.830	http://www.fdsn.org/networks/detail/XY_2010
XY	U72B	-33.979	-71.812	http://www.fdsn.org/networks/detail/XY_2010
XY	U73B	-33.916	-71.420	http://www.fdsn.org/networks/detail/XY_2010
XY	U74B	-33.600	-71.544	http://www.fdsn.org/networks/detail/XY_2010
XY	U75B	-33.381	-71.181	http://www.fdsn.org/networks/detail/XY_2010
Y4	CAPB	-22.710	-51.111	http://moho.iag.usp.br/mda/Y4/
Y4	FORT	-21.447	-46.828	http://moho.iag.usp.br/mda/Y4/
Y4	JUQB	-24.093	-47.716	http://moho.iag.usp.br/mda/Y4/
Y9	ALG	-22.859	-69.807	http://geofon.gfz-potsdam.de/waveform/archive/network.php?ncode=Y9&year=2007
Y9	ERC	-23.140	-69.875	http://geofon.gfz-potsdam.de/waveform/archive/network.php?ncode=Y9&year=2007
Y9	MEX	-23.285	-70.063	http://geofon.gfz-potsdam.de/waveform/archive/network.php?ncode=Y9&year=2007
Y9	MJC	-23.286	-70.532	http://geofon.gfz-potsdam.de/waveform/archive/network.php?ncode=Y9&year=2007

Table 1. Data information. Cont.

Y9	PUN	-23.115	-69.422	http://geofon.gfz-potsdam.de/waveform/archive/network.php?ncode=Y9&year=2007
YC	AREN	-33.616	-69.511	http://www.fdsn.org/networks/detail/YC_2000
YC	BARD	-35.764	-69.562	http://www.fdsn.org/networks/detail/YC_2000
YC	ELBO	-30.528	-70.407	http://www.fdsn.org/networks/detail/YC_2000
YC	HEDI	-30.139	-68.543	http://www.fdsn.org/networks/detail/YC_2000
YC	HUER	-32.419	-65.717	http://www.fdsn.org/networks/detail/YC_2000
YC	HURT	-30.297	-70.712	http://www.fdsn.org/networks/detail/YC_2000
YC	JUAN	-31.603	-68.233	http://www.fdsn.org/networks/detail/YC_2000
YC	LENA	-35.198	-70.040	http://www.fdsn.org/networks/detail/YC_2000
YC	LITI	-31.064	-71.245	http://www.fdsn.org/networks/detail/YC_2000
YC	LLAN	-30.395	-66.528	http://www.fdsn.org/networks/detail/YC_2000
YC	LOIC	-35.791	-70.148	http://www.fdsn.org/networks/detail/YC_2000
YC	MAUL	-36.013	-70.558	http://www.fdsn.org/networks/detail/YC_2000
YC	NEGR	-30.317	-69.756	http://www.fdsn.org/networks/detail/YC_2000
YC	NIEB	-36.033	-68.975	http://www.fdsn.org/networks/detail/YC_2000
YC	PACH	-30.193	-68.828	http://www.fdsn.org/networks/detail/YC_2000
YC	PENA	-36.203	-68.398	http://www.fdsn.org/networks/detail/YC_2000
YC	PICH	-30.908	-65.187	http://www.fdsn.org/networks/detail/YC_2000
YC	RAFA	-34.774	-68.472	http://www.fdsn.org/networks/detail/YC_2000
YC	RINC	-30.270	-67.725	http://www.fdsn.org/networks/detail/YC_2000
YC	USPA	-32.224	-69.388	http://www.fdsn.org/networks/detail/YC_2000
YJ	AGU01	-45.151	-73.509	http://ds.iris.edu/mda/YJ?timewindow=2004-2006
YJ	AMG01	-44.748	-72.214	http://ds.iris.edu/mda/YJ?timewindow=2004-2006
YJ	BAK01	-47.184	-71.974	http://ds.iris.edu/mda/YJ?timewindow=2004-2006
YJ	BMU01	-46.436	-72.672	http://ds.iris.edu/mda/YJ?timewindow=2004-2006
YJ	CAL01	-45.479	-71.604	http://ds.iris.edu/mda/YJ?timewindow=2004-2006
YJ	CHB01	-45.462	-72.817	http://ds.iris.edu/mda/YJ?timewindow=2004-2006
YJ	CHC01	-46.541	-71.735	http://ds.iris.edu/mda/YJ?timewindow=2004-2006
YJ	CHN01	-46.918	-72.735	http://ds.iris.edu/mda/YJ?timewindow=2004-2006
YJ	COC01	-47.256	-72.592	http://ds.iris.edu/mda/YJ?timewindow=2004-2006
YJ	COY01	-45.564	-72.091	http://ds.iris.edu/mda/YJ?timewindow=2004-2006
YJ	CTS01	-44.734	-72.680	http://ds.iris.edu/mda/YJ?timewindow=2004-2006
YJ	FNL01	-46.552	-72.222	http://ds.iris.edu/mda/YJ?timewindow=2004-2006
YJ	HOP01	-46.727	-75.433	http://ds.iris.edu/mda/YJ?timewindow=2004-2006
YJ	HUM01	-45.558	-73.959	http://ds.iris.edu/mda/YJ?timewindow=2004-2006
YJ	IDA01	-44.748	-72.210	http://ds.iris.edu/mda/YJ?timewindow=2004-2006
YJ	ISM01	-45.928	-73.831	http://ds.iris.edu/mda/YJ?timewindow=2004-2006
YJ	JEI02	-46.832	-71.995	http://ds.iris.edu/mda/YJ?timewindow=2004-2006

Table 1. Data information. Cont.

YJ	LPL01	-45.320	-72.708	http://ds.iris.edu/mda/YJ?timewindow=2004-2006
YJ	LSR01	-46.661	-73.859	http://ds.iris.edu/mda/YJ?timewindow=2004-2006
YJ	LTQ01	-46.642	-72.798	http://ds.iris.edu/mda/YJ?timewindow=2004-2006
YJ	MRF01	-46.726	-72.936	http://ds.iris.edu/mda/YJ?timewindow=2004-2006
YJ	PLM01	-46.177	-74.432	http://ds.iris.edu/mda/YJ?timewindow=2004-2006
YJ	RMG01	-45.907	-72.321	http://ds.iris.edu/mda/YJ?timewindow=2004-2006
YJ	RPR01	-46.222	-74.010	http://ds.iris.edu/mda/YJ?timewindow=2004-2006
YJ	SAD01	-46.753	-74.460	http://ds.iris.edu/mda/YJ?timewindow=2004-2006
YJ	VCC01	-46.121	-72.161	http://ds.iris.edu/mda/YJ?timewindow=2004-2006
YJ	VMG01	-45.176	-72.143	http://ds.iris.edu/mda/YJ?timewindow=2004-2006
YJ	VOH01	-48.468	-72.561	http://ds.iris.edu/mda/YJ?timewindow=2004-2006
YM	V03	-39.411	-71.968	http://dx.doi.org/doi:10.7914/SN/YM_2010
YM	V08	-39.449	-71.975	http://dx.doi.org/doi:10.7914/SN/YM_2010
YM	VD	-39.412	-71.941	http://dx.doi.org/doi:10.7914/SN/YM_2010
YM	VE	-39.409	-71.941	http://dx.doi.org/doi:10.7914/SN/YM_2010
YS	UTKH	-22.282	-67.013	http://ds.iris.edu/mda/YS?timewindow=2009-2013
ZA	A03	-23.335	-68.751	http://geofon.gfz-potsdam.de/waveform/archive/network.php?ncode=ZA&year=1994
ZA	A05	-22.743	-68.431	http://geofon.gfz-potsdam.de/waveform/archive/network.php?ncode=ZA&year=1994
ZA	A07	-23.654	-68.360	http://geofon.gfz-potsdam.de/waveform/archive/network.php?ncode=ZA&year=1994
ZA	A18	-21.953	-68.723	http://geofon.gfz-potsdam.de/waveform/archive/network.php?ncode=ZA&year=1994
ZA	B12	-23.324	-67.779	http://geofon.gfz-potsdam.de/waveform/archive/network.php?ncode=ZA&year=1994
ZA	B13	-23.233	-67.085	http://geofon.gfz-potsdam.de/waveform/archive/network.php?ncode=ZA&year=1994
ZA	PC05	-25.336	-67.906	http://geofon.gfz-potsdam.de/waveform/archive/network.php?ncode=ZA&year=2002
ZA	PC06	-25.305	-67.813	http://geofon.gfz-potsdam.de/waveform/archive/network.php?ncode=ZA&year=2002
ZA	PC07	-25.339	-67.731	http://geofon.gfz-potsdam.de/waveform/archive/network.php?ncode=ZA&year=2002
ZA	PC10	-25.592	-67.511	http://geofon.gfz-potsdam.de/waveform/archive/network.php?ncode=ZA&year=2002
ZA	PC13	-25.540	-67.219	http://geofon.gfz-potsdam.de/waveform/archive/network.php?ncode=ZA&year=2002
ZA	PC18	-25.746	-66.757	http://geofon.gfz-potsdam.de/waveform/archive/network.php?ncode=ZA&year=2002
ZA	RF03	-21.222	-69.901	http://geofon.gfz-potsdam.de/waveform/archive/network.php?ncode=ZA&year=2002
ZA	RF07	-21.062	-69.484	http://geofon.gfz-potsdam.de/waveform/archive/network.php?ncode=ZA&year=2002

Table 1. Data information. Cont.

ZA	RF16	-21.009	-68.352	http://geofon.gfz-potsdam.de/waveform/archive/network.php?ncode=ZA&year=2002
ZA	RF23A	-21.053	-67.765	http://geofon.gfz-potsdam.de/waveform/archive/network.php?ncode=ZA&year=2002
ZA	RF24	-20.882	-67.670	http://geofon.gfz-potsdam.de/waveform/archive/network.php?ncode=ZA&year=2002
ZA	RF36	-21.163	-66.636	http://geofon.gfz-potsdam.de/waveform/archive/network.php?ncode=ZA&year=2002
ZA	RF41	-21.439	-66.215	http://geofon.gfz-potsdam.de/waveform/archive/network.php?ncode=ZA&year=2002
ZA	RF50	-21.367	-65.532	http://geofon.gfz-potsdam.de/waveform/archive/network.php?ncode=ZA&year=2002
ZA	RF53	-21.361	-65.276	http://geofon.gfz-potsdam.de/waveform/archive/network.php?ncode=ZA&year=2002
ZA	RF55	-21.299	-65.121	http://geofon.gfz-potsdam.de/waveform/archive/network.php?ncode=ZA&year=2002
ZA	RF57	-21.428	-64.978	http://geofon.gfz-potsdam.de/waveform/archive/network.php?ncode=ZA&year=2002
ZA	RF59	-21.464	-64.757	http://geofon.gfz-potsdam.de/waveform/archive/network.php?ncode=ZA&year=2002
ZB	ARI	-24.728	-67.490	http://geofon.gfz-potsdam.de/waveform/archive/network.php?ncode=ZB&year=1997
ZB	CAM	-24.140	-66.697	http://geofon.gfz-potsdam.de/waveform/archive/network.php?ncode=ZB&year=1997
ZB	ELM	-23.972	-65.834	http://geofon.gfz-potsdam.de/waveform/archive/network.php?ncode=ZB&year=1997
ZB	FUN	-22.515	-66.178	http://geofon.gfz-potsdam.de/waveform/archive/network.php?ncode=ZB&year=1997
ZB	LAQ	-22.154	-65.729	http://geofon.gfz-potsdam.de/waveform/archive/network.php?ncode=ZB&year=1997
ZB	ORA	-22.106	-66.061	http://geofon.gfz-potsdam.de/waveform/archive/network.php?ncode=ZB&year=1997
ZB	PDM	-22.547	-65.617	http://geofon.gfz-potsdam.de/waveform/archive/network.php?ncode=ZB&year=1997
ZB	SA4	-24.267	-66.310	http://geofon.gfz-potsdam.de/waveform/archive/network.php?ncode=ZB&year=1997
ZB	SHM	-25.170	-67.069	http://geofon.gfz-potsdam.de/waveform/archive/network.php?ncode=ZB&year=1997
ZB	SOR	-23.025	-66.023	http://geofon.gfz-potsdam.de/waveform/archive/network.php?ncode=ZB&year=1997
ZB	SPQ	-24.767	-66.945	http://geofon.gfz-potsdam.de/waveform/archive/network.php?ncode=ZB&year=1997
ZB	TAC	-24.465	-67.707	http://geofon.gfz-potsdam.de/waveform/archive/network.php?ncode=ZB&year=1997
ZB	TAN	-23.127	-66.519	http://geofon.gfz-potsdam.de/waveform/archive/network.php?ncode=ZB&year=1997
ZD	FN10	-10.946	-75.228	http://ds.iris.edu/mda/ZD?timewindow=2010-2013

Table 1. Data information. Cont.

ZD	FS06	-13.667	-73.312	http://ds.iris.edu/mda/ZD?timewindow=2010-2013
ZE	CEB	-21.567	-68.364	http://geofon.gfz-potsdam.de/waveform/archive/network.php?ncode=ZE&year=1996
ZE	G07S	-34.783	-72.027	http://geofon.gfz-potsdam.de/waveform/archive/network.php?ncode=ZE&year=2010
ZE	G09S	-34.980	-71.440	http://geofon.gfz-potsdam.de/waveform/archive/network.php?ncode=ZE&year=2010
ZE	G12S	-35.236	-72.266	http://geofon.gfz-potsdam.de/waveform/archive/network.php?ncode=ZE&year=2010
ZE	G13S	-35.378	-71.961	http://geofon.gfz-potsdam.de/waveform/archive/network.php?ncode=ZE&year=2010
ZE	GA0S	-33.276	-71.277	http://geofon.gfz-potsdam.de/waveform/archive/network.php?ncode=ZE&year=2010
ZE	PIC	-20.492	-69.276	http://geofon.gfz-potsdam.de/waveform/archive/network.php?ncode=ZE&year=1996
ZE	RED	-21.295	-68.774	http://geofon.gfz-potsdam.de/waveform/archive/network.php?ncode=ZE&year=1996
ZE	SAS	-22.665	-67.952	http://geofon.gfz-potsdam.de/waveform/archive/network.php?ncode=ZE&year=1996
ZE	U57S	-35.458	-72.096	http://geofon.gfz-potsdam.de/waveform/archive/network.php?ncode=ZE&year=2010
ZE	U72S	-33.979	-71.812	http://geofon.gfz-potsdam.de/waveform/archive/network.php?ncode=ZE&year=2010
ZG	CB11	-18.224	-68.939	http://ds.iris.edu/mda/ZG?timewindow=2010-2012
ZG	CB12	-17.792	-68.287	http://ds.iris.edu/mda/ZG?timewindow=2010-2012
ZG	CB13	-17.283	-67.746	http://ds.iris.edu/mda/ZG?timewindow=2010-2012
ZG	CB14	-17.249	-65.901	http://ds.iris.edu/mda/ZG?timewindow=2010-2012
ZG	CB15	-16.906	-67.137	http://ds.iris.edu/mda/ZG?timewindow=2010-2012
ZG	CB21	-17.290	-69.214	http://ds.iris.edu/mda/ZG?timewindow=2010-2012
ZG	CB22	-17.213	-69.003	http://ds.iris.edu/mda/ZG?timewindow=2010-2012
ZG	CB23	-17.113	-68.780	http://ds.iris.edu/mda/ZG?timewindow=2010-2012
ZG	CB24	-17.024	-68.605	http://ds.iris.edu/mda/ZG?timewindow=2010-2012
ZG	CB25	-16.975	-68.420	http://ds.iris.edu/mda/ZG?timewindow=2010-2012
ZG	CB26	-16.983	-68.193	http://ds.iris.edu/mda/ZG?timewindow=2010-2012
ZG	CB27	-16.775	-68.081	http://ds.iris.edu/mda/ZG?timewindow=2010-2012
ZG	CB28	-16.548	-67.954	http://ds.iris.edu/mda/ZG?timewindow=2010-2012
ZG	CB29	-16.349	-67.817	http://ds.iris.edu/mda/ZG?timewindow=2010-2012
ZG	CB2A	-16.197	-67.699	http://ds.iris.edu/mda/ZG?timewindow=2010-2012
ZG	CB2B	-16.010	-67.613	http://ds.iris.edu/mda/ZG?timewindow=2010-2012
ZG	CB2C	-15.830	-67.565	http://ds.iris.edu/mda/ZG?timewindow=2010-2012
ZG	CB2D	-15.596	-67.391	http://ds.iris.edu/mda/ZG?timewindow=2010-2012
ZG	CB2E	-15.363	-67.103	http://ds.iris.edu/mda/ZG?timewindow=2010-2012
ZG	CB2F	-15.143	-67.036	http://ds.iris.edu/mda/ZG?timewindow=2010-2012

Table 1. Data information. Cont.

ZG	CB31	-16.438	-68.866	http://ds.iris.edu/mda/ZG?timewindow=2010-2012
ZG	CB32	-15.762	-68.651	http://ds.iris.edu/mda/ZG?timewindow=2010-2012
ZG	CB33	-15.504	-67.867	http://ds.iris.edu/mda/ZG?timewindow=2010-2012
ZG	CB34	-14.435	-67.539	http://ds.iris.edu/mda/ZG?timewindow=2010-2012
ZG	CB41	-15.656	-69.120	http://ds.iris.edu/mda/ZG?timewindow=2010-2012
ZG	CB42	-15.240	-68.747	http://ds.iris.edu/mda/ZG?timewindow=2010-2012
ZG	CB43	-14.689	-68.384	http://ds.iris.edu/mda/ZG?timewindow=2010-2012
ZG	CB44	-14.145	-67.887	http://ds.iris.edu/mda/ZG?timewindow=2010-2012
ZG	CB54	-13.768	-68.120	http://ds.iris.edu/mda/ZG?timewindow=2010-2012
ZG	CP01	-17.907	-70.157	http://ds.iris.edu/mda/ZG?timewindow=2010-2012
ZG	CP02	-17.778	-69.960	http://ds.iris.edu/mda/ZG?timewindow=2010-2012
ZG	CP03	-17.575	-69.680	http://ds.iris.edu/mda/ZG?timewindow=2010-2012
ZG	CP04	-16.558	-71.451	http://ds.iris.edu/mda/ZG?timewindow=2010-2012
ZG	CP05	-15.727	-70.900	http://ds.iris.edu/mda/ZG?timewindow=2010-2012
ZG	CP06	-17.325	-70.995	http://ds.iris.edu/mda/ZG?timewindow=2010-2012
ZG	CP07	-16.886	-70.374	http://ds.iris.edu/mda/ZG?timewindow=2010-2012
ZG	CP08	-15.923	-69.824	http://ds.iris.edu/mda/ZG?timewindow=2010-2012
ZG	CP09	-15.834	-71.471	http://ds.iris.edu/mda/ZG?timewindow=2010-2012
ZG	CP10	-15.176	-71.947	http://ds.iris.edu/mda/ZG?timewindow=2010-2012
ZG	CP11	-15.318	-70.351	http://ds.iris.edu/mda/ZG?timewindow=2010-2012
ZG	CP12	-15.237	-69.531	http://ds.iris.edu/mda/ZG?timewindow=2010-2012
ZG	CP13	-14.789	-71.445	http://ds.iris.edu/mda/ZG?timewindow=2010-2012
ZG	CP15	-14.158	-71.329	http://ds.iris.edu/mda/ZG?timewindow=2010-2012
ZG	CP16	-14.076	-70.429	http://ds.iris.edu/mda/ZG?timewindow=2010-2012
ZG	CP17	-14.190	-69.703	http://ds.iris.edu/mda/ZG?timewindow=2010-2012
ZG	CP18	-13.526	-70.896	http://ds.iris.edu/mda/ZG?timewindow=2010-2012
ZG	CP20	-12.875	-69.714	http://ds.iris.edu/mda/ZG?timewindow=2010-2012
ZL	ABRA	-31.499	-66.238	http://www.fdsn.org/networks/detail/ZL_2007
ZL	ARRO	-30.408	-69.245	http://www.fdsn.org/networks/detail/ZL_2007
ZL	BARR	-31.650	-69.416	http://www.fdsn.org/networks/detail/ZL_2007
ZL	BOZA	-31.751	-68.435	http://www.fdsn.org/networks/detail/ZL_2007
ZL	CALI	-31.283	-69.420	http://www.fdsn.org/networks/detail/ZL_2007
ZL	CASP	-31.207	-69.629	http://www.fdsn.org/networks/detail/ZL_2007
ZL	CATA	-32.274	-67.189	http://www.fdsn.org/networks/detail/ZL_2007
ZL	CHIL	-31.906	-68.775	http://www.fdsn.org/networks/detail/ZL_2007
ZL	CHUC	-31.067	-67.285	http://www.fdsn.org/networks/detail/ZL_2007
ZL	CHUM	-28.820	-66.248	http://www.fdsn.org/networks/detail/ZL_2007
ZL	CIGA	-30.144	-68.574	http://www.fdsn.org/networks/detail/ZL_2007
ZL	CLAR	-32.120	-68.985	http://www.fdsn.org/networks/detail/ZL_2007

Table 1. Data information. Cont.

ZL	COLO	-29.936	-67.110	http://www.fdsn.org/networks/detail/ZL_2007
ZL	CONE	-31.124	-68.074	http://www.fdsn.org/networks/detail/ZL_2007
ZL	CORT	-29.960	-69.640	http://www.fdsn.org/networks/detail/ZL_2007
ZL	DOCA	-30.949	-69.083	http://www.fdsn.org/networks/detail/ZL_2007
ZL	GUAL	-30.831	-68.948	http://www.fdsn.org/networks/detail/ZL_2007
ZL	GUAR	-31.894	-70.197	http://www.fdsn.org/networks/detail/ZL_2007
ZL	INPS	-31.528	-68.566	http://www.fdsn.org/networks/detail/ZL_2007
ZL	LAJA	-31.329	-68.476	http://www.fdsn.org/networks/detail/ZL_2007
ZL	LEON	-31.802	-69.324	http://www.fdsn.org/networks/detail/ZL_2007
ZL	LLAN	-30.395	-66.528	http://www.fdsn.org/networks/detail/ZL_2007
ZL	LUNA	-30.161	-67.836	http://www.fdsn.org/networks/detail/ZL_2007
ZL	MAJA	-30.687	-67.509	http://www.fdsn.org/networks/detail/ZL_2007
ZL	MALA	-30.818	-66.607	http://www.fdsn.org/networks/detail/ZL_2007
ZL	MONA	-30.939	-68.493	http://www.fdsn.org/networks/detail/ZL_2007
ZL	NIKI	-31.577	-67.870	http://www.fdsn.org/networks/detail/ZL_2007
ZL	NOQE	-31.199	-66.747	http://www.fdsn.org/networks/detail/ZL_2007
ZL	NUEV	-31.037	-69.525	http://www.fdsn.org/networks/detail/ZL_2007
ZL	PACH	-30.193	-68.828	http://www.fdsn.org/networks/detail/ZL_2007
ZL	PAGA	-30.209	-67.286	http://www.fdsn.org/networks/detail/ZL_2007
ZL	PATO	-31.897	-69.692	http://www.fdsn.org/networks/detail/ZL_2007
ZL	REGU	-31.899	-70.028	http://www.fdsn.org/networks/detail/ZL_2007
ZL	RINC	-30.270	-67.725	http://www.fdsn.org/networks/detail/ZL_2007
ZL	SASO	-31.512	-68.984	http://www.fdsn.org/networks/detail/ZL_2007
ZL	SECA	-31.271	-68.799	http://www.fdsn.org/networks/detail/ZL_2007
ZL	SOMB	-31.917	-69.022	http://www.fdsn.org/networks/detail/ZL_2007
ZL	TALA	-31.021	-68.748	http://www.fdsn.org/networks/detail/ZL_2007
ZL	TOCO	-30.659	-69.436	http://www.fdsn.org/networks/detail/ZL_2007
ZL	TUCU	-30.570	-68.626	http://www.fdsn.org/networks/detail/ZL_2007
ZL	UNSJ	-31.541	-68.576	http://www.fdsn.org/networks/detail/ZL_2007
ZL	USPA	-32.224	-69.388	http://www.fdsn.org/networks/detail/ZL_2007
ZL	VELA	-30.166	-69.475	http://www.fdsn.org/networks/detail/ZL_2007
ZL	ZOND	-31.604	-68.721	http://www.fdsn.org/networks/detail/ZL_2007
ZN	AUA	12.506	-70.011	http://ds.iris.edu/mda/ZN?timewindow=2008-2009
ZP	AS11	-38.877	-71.820	http://geofon.gfz-potsdam.de/waveform/archive/network.php?ncode=ZP&year=1999
ZP	AS15	-38.825	-71.281	http://geofon.gfz-potsdam.de/waveform/archive/network.php?ncode=ZP&year=1999
ZP	AS17	-38.896	-71.100	http://geofon.gfz-potsdam.de/waveform/archive/network.php?ncode=ZP&year=1999

Table 1. Data information. Cont.

ZP	AS22	-39.065	-68.698	http://geofon.gfz-potsdam.de/waveform/archive/network.php?ncode=ZP&year=1999
ZP	CM15	-37.712	-71.479	http://geofon.gfz-potsdam.de/waveform/archive/network.php?ncode=ZP&year=1999
ZP	CO01	-39.317	-71.582	http://geofon.gfz-potsdam.de/waveform/archive/network.php?ncode=ZP&year=1999
ZP	CP22	-38.555	-71.790	http://geofon.gfz-potsdam.de/waveform/archive/network.php?ncode=ZP&year=1999
ZP	CP29	-38.167	-71.302	http://geofon.gfz-potsdam.de/waveform/archive/network.php?ncode=ZP&year=1999
ZP	CP30	-38.147	-71.893	http://geofon.gfz-potsdam.de/waveform/archive/network.php?ncode=ZP&year=1999
ZP	CP31	-37.454	-72.143	http://geofon.gfz-potsdam.de/waveform/archive/network.php?ncode=ZP&year=1999
ZP	GP07	-37.873	-71.505	http://geofon.gfz-potsdam.de/waveform/archive/network.php?ncode=ZP&year=1999
ZP	KM01	-36.100	-72.742	http://geofon.gfz-potsdam.de/waveform/archive/network.php?ncode=ZP&year=1999
ZP	KM06	-37.218	-73.558	http://geofon.gfz-potsdam.de/waveform/archive/network.php?ncode=ZP&year=1999
ZP	KP13	-37.775	-72.952	http://geofon.gfz-potsdam.de/waveform/archive/network.php?ncode=ZP&year=1999
ZP	LP26	-38.583	-72.191	http://geofon.gfz-potsdam.de/waveform/archive/network.php?ncode=ZP&year=1999
ZQ	CB03	-26.897	-67.707	http://geofon.gfz-potsdam.de/waveform/archive/network.php?ncode=ZQ&year=2004

APPENDIX B

E-W MTZ CROSS SECTIONS

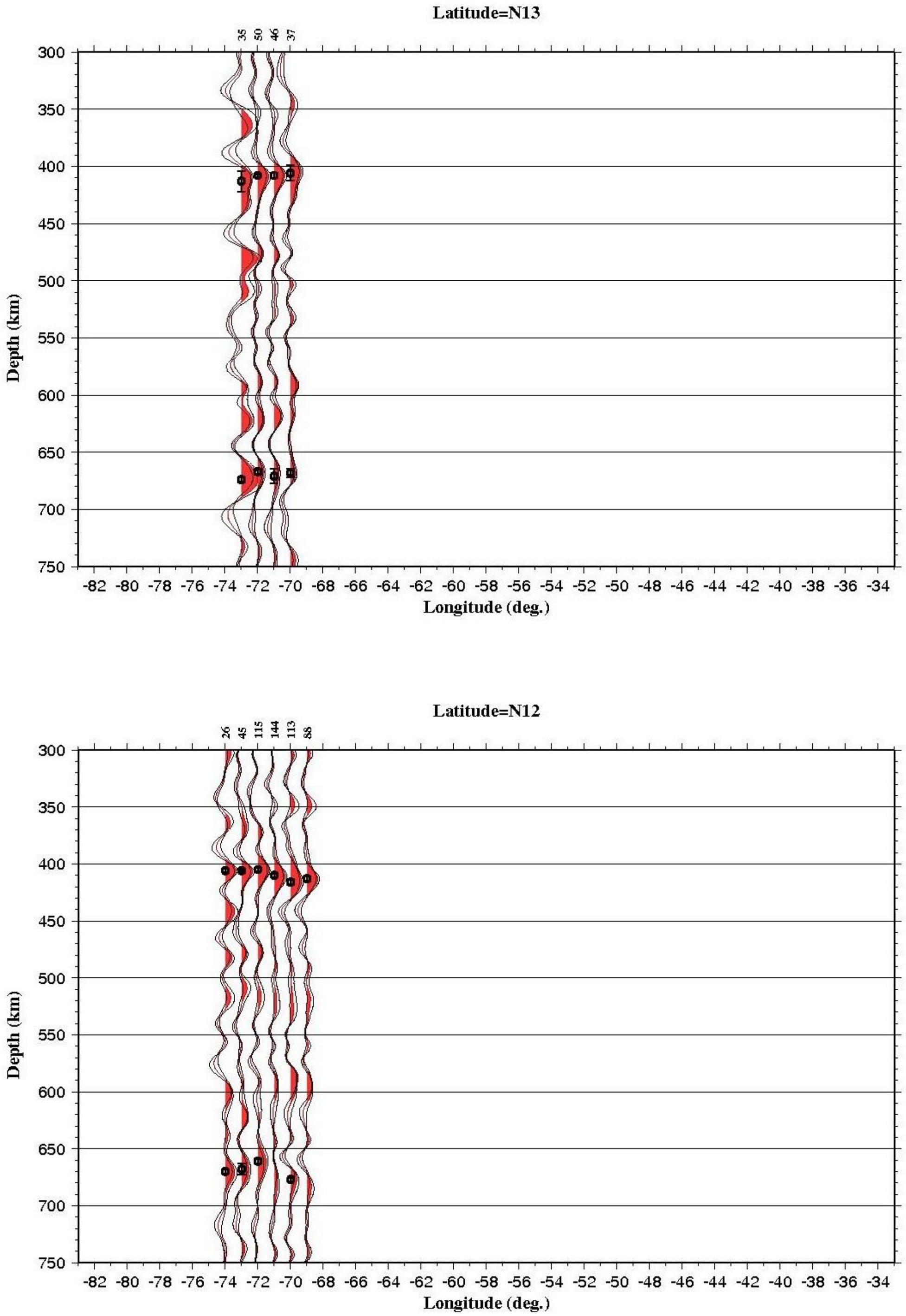

Figure 1. E-W MTZ Cross sections. Black circles are the interpreted discontinuities peaks with uncertainty bars, blue lines are slab contours and green (Magnitude<6) and yellow (Magnitude≥6) dots are earthquakes. Numbers of RFs in each stacked trace are indicated on the top of it.

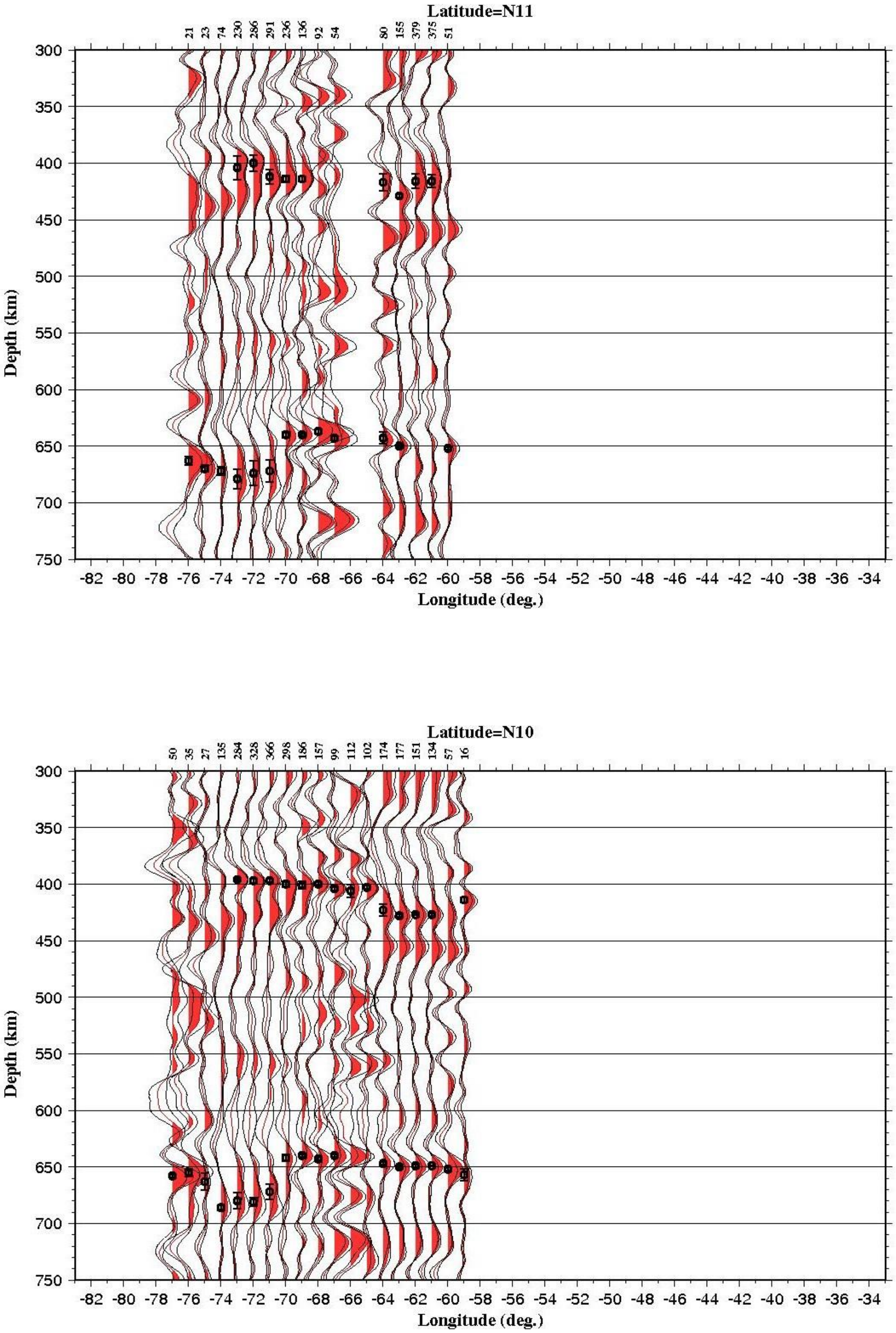

Figure 1. E-W MTZ Cross sections. Cont.

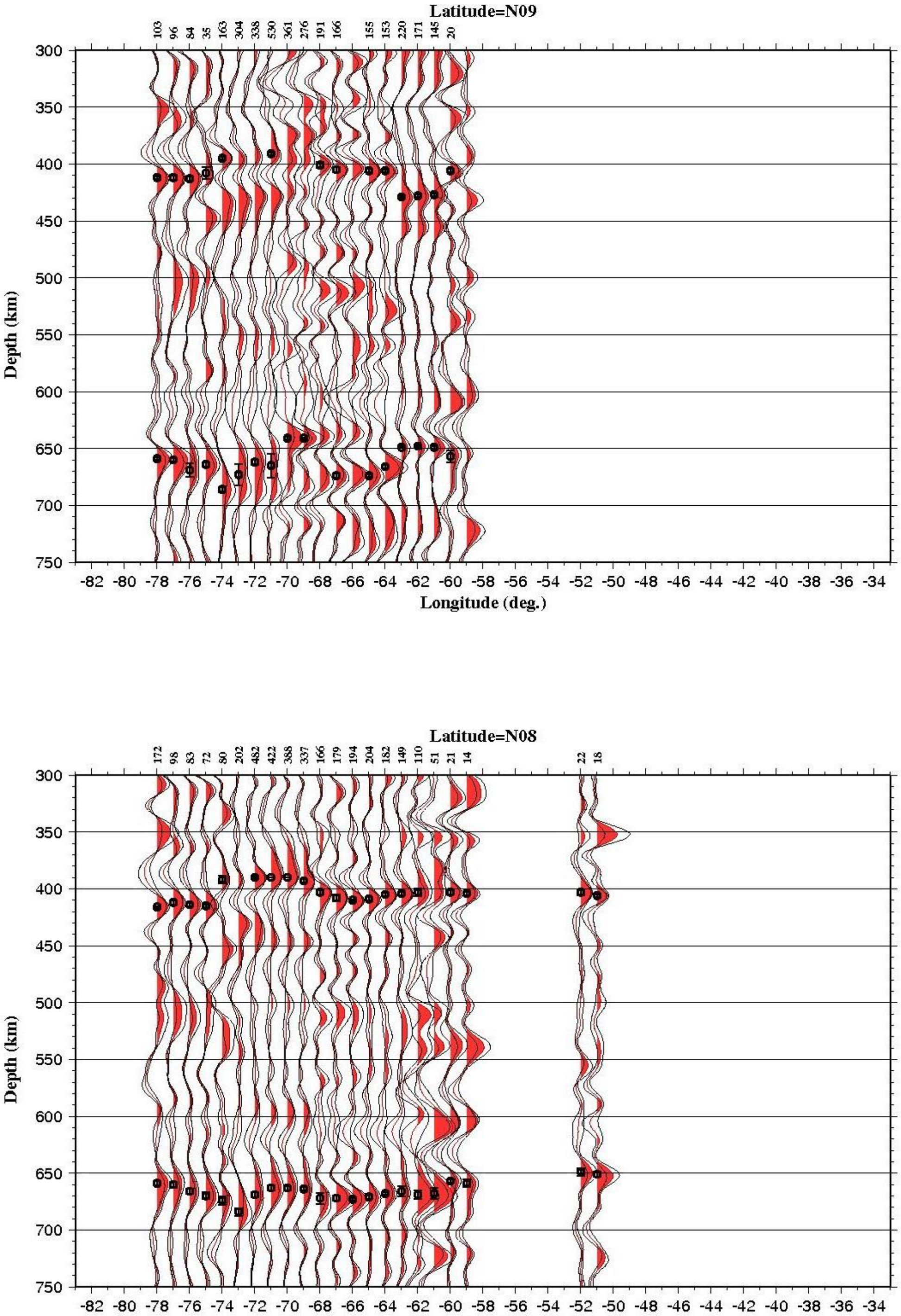

Figure 1. E-W MTZ Cross sections. Cont.

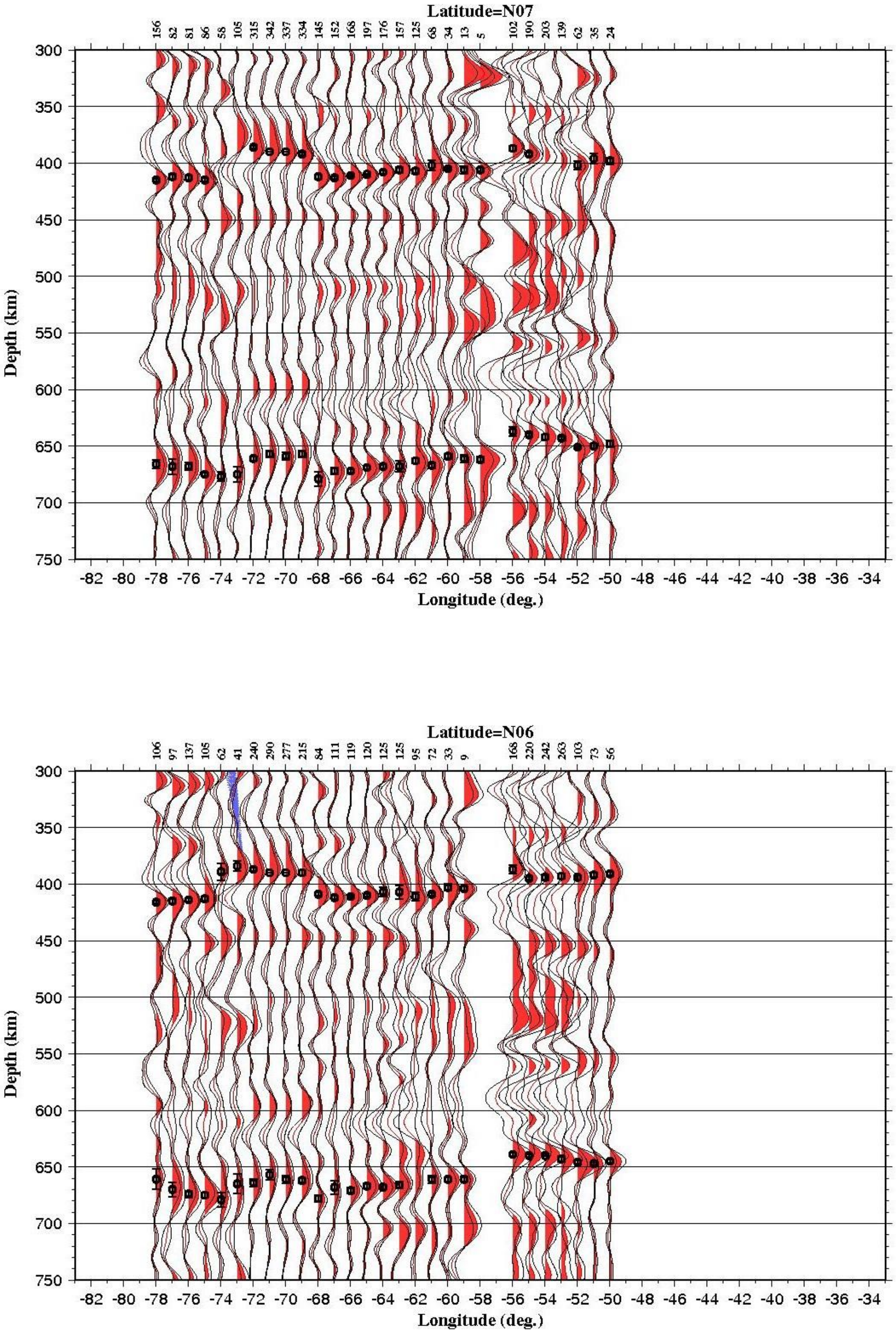

Figure 1. E-W MTZ Cross sections. Cont.

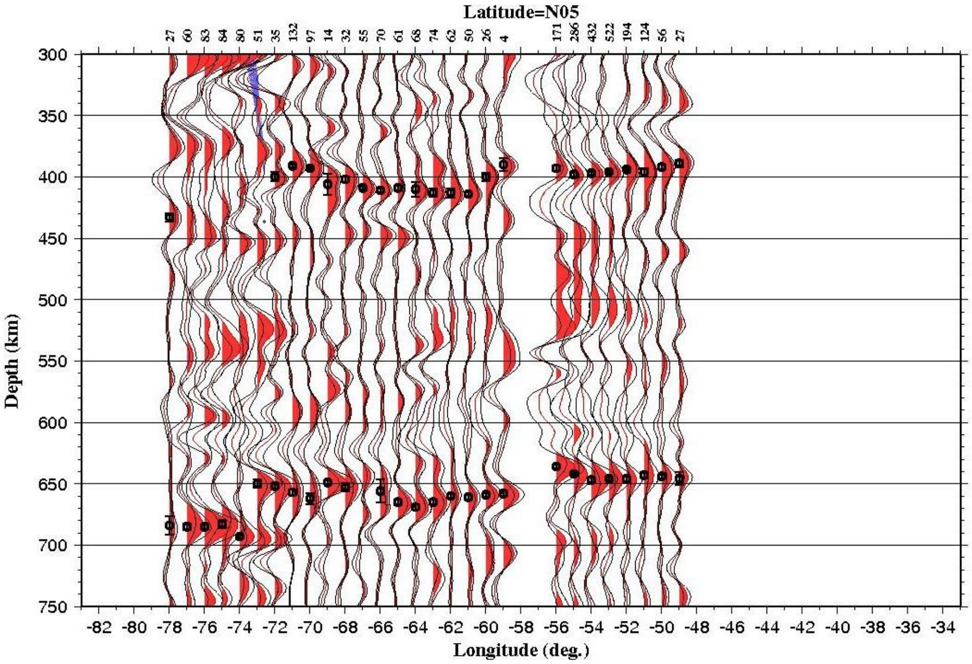

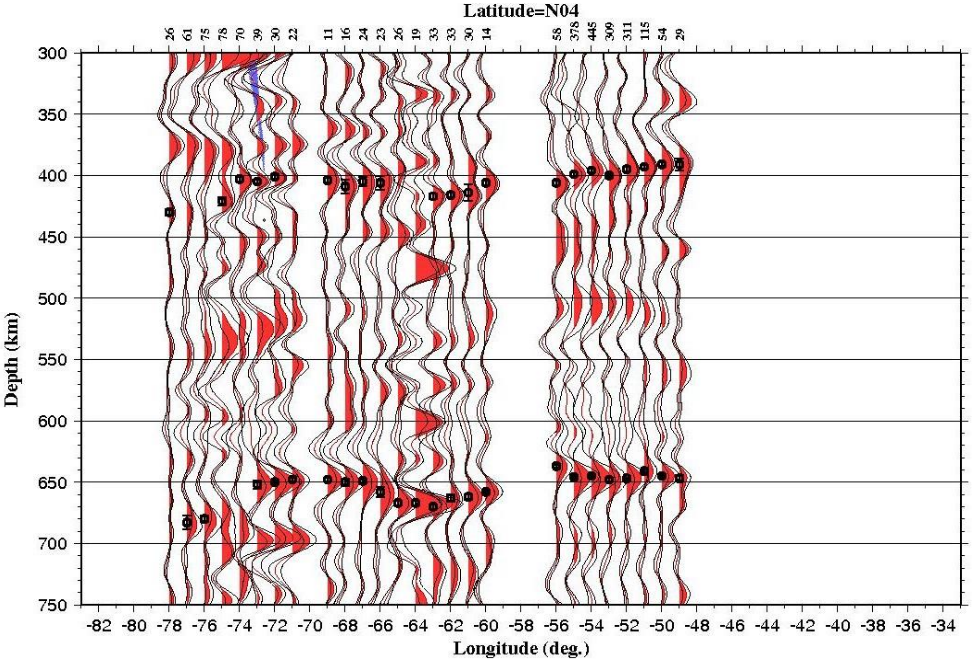

Figure 1. E-W MTZ Cross sections. Cont.

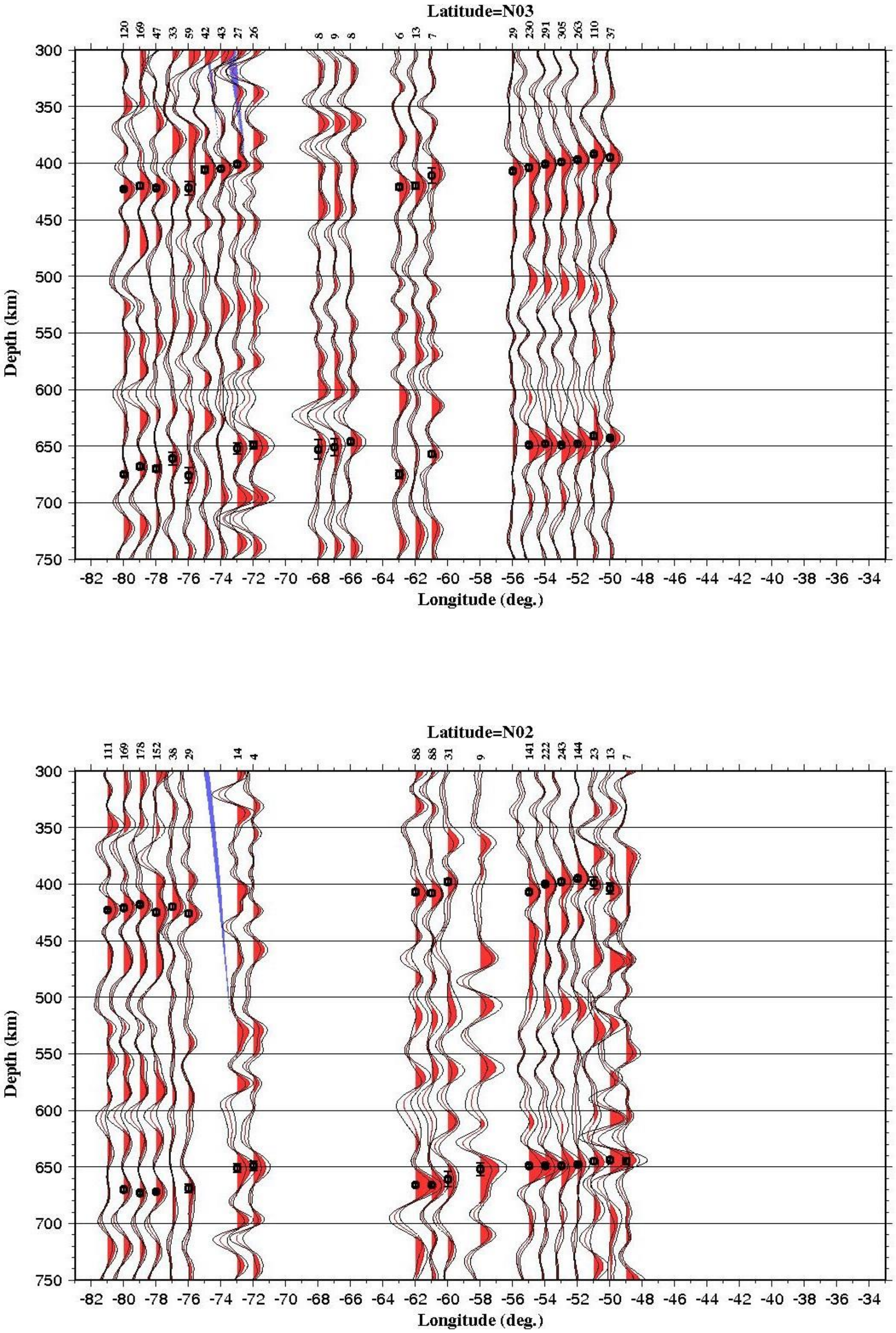

Figure 1. E-W MTZ Cross sections. Cont.

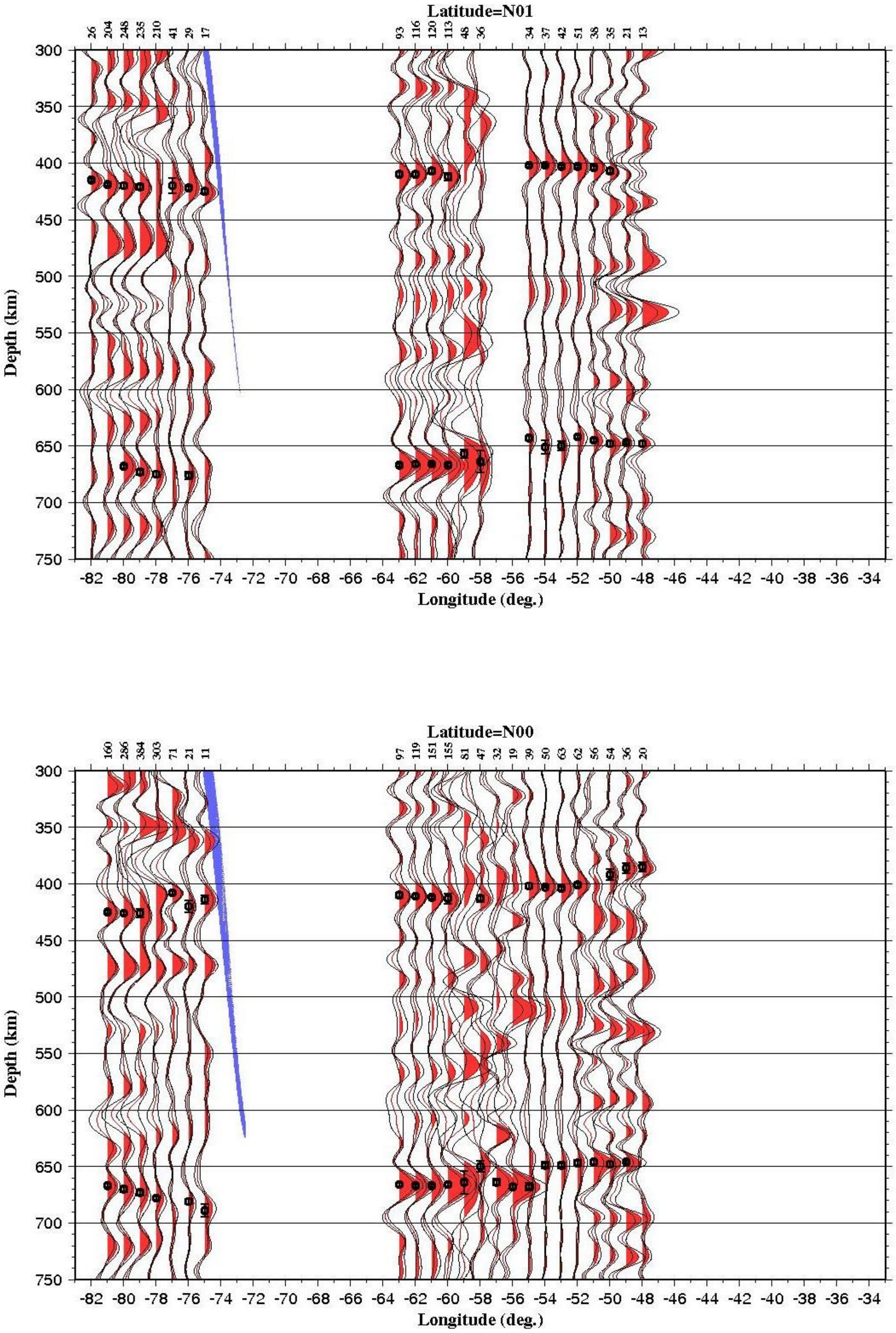

Figure 1. E-W MTZ Cross sections. Cont.

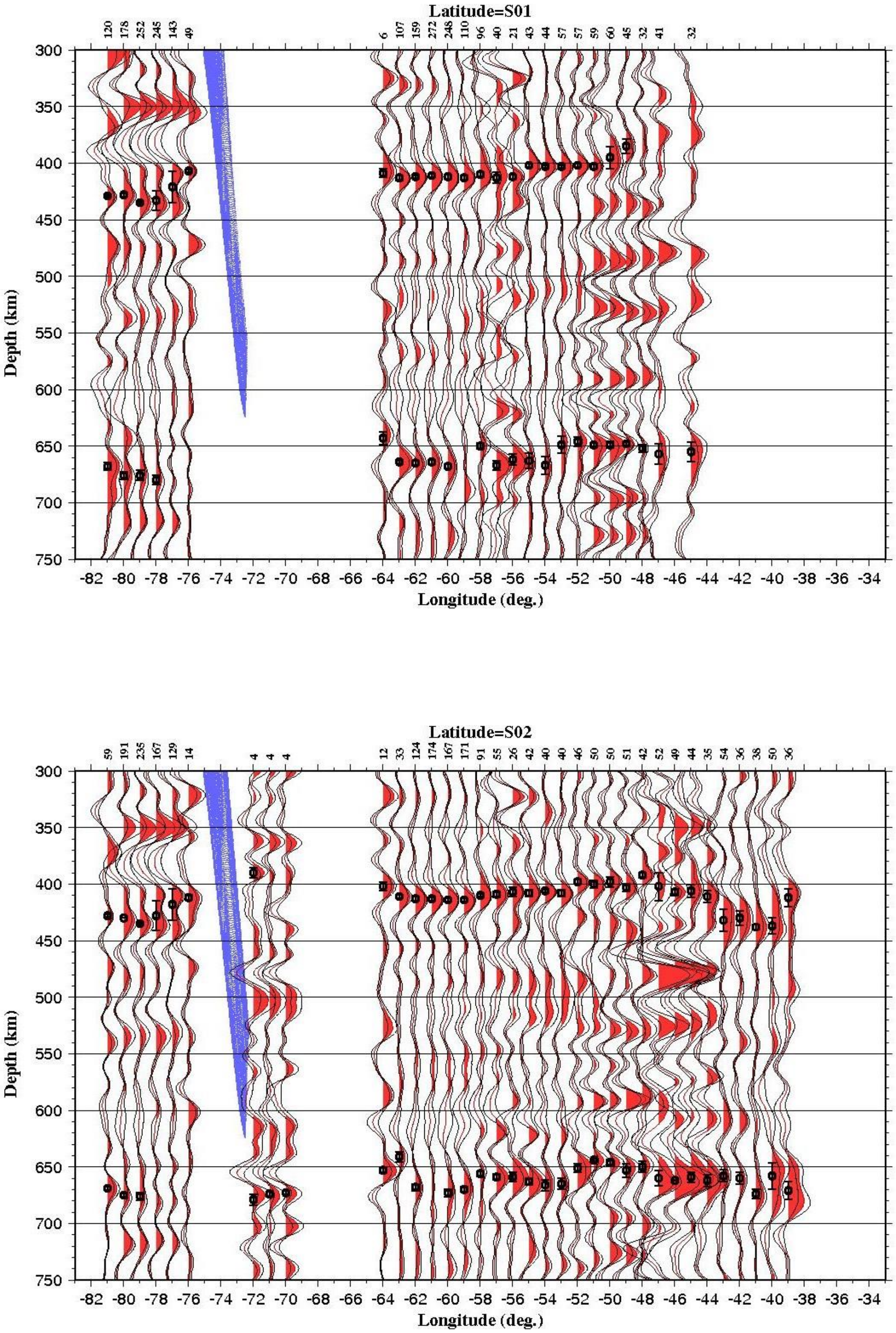

Figure 1. E-W MTZ Cross sections. Cont.

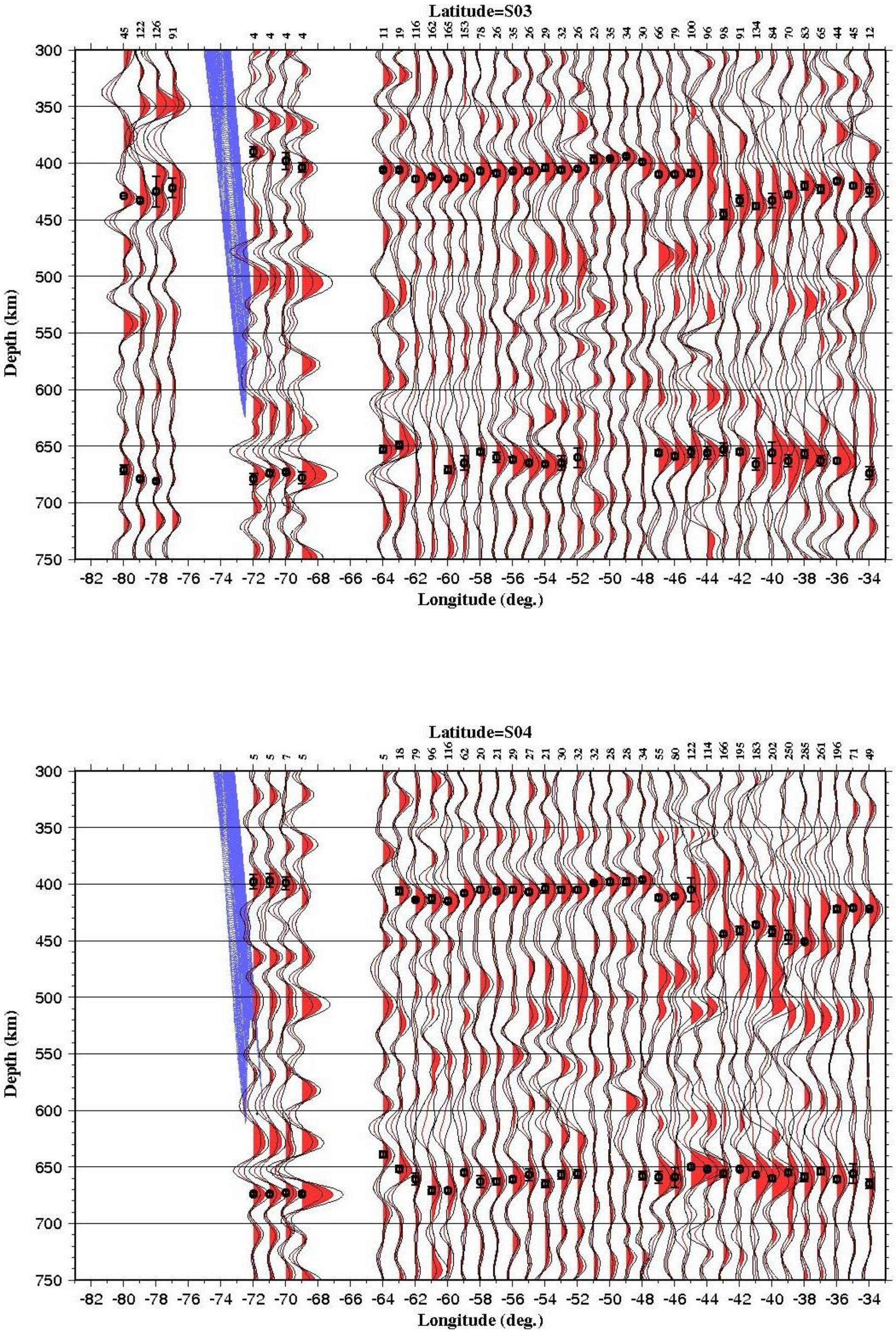

Figure 1. E-W MTZ Cross sections. Cont.

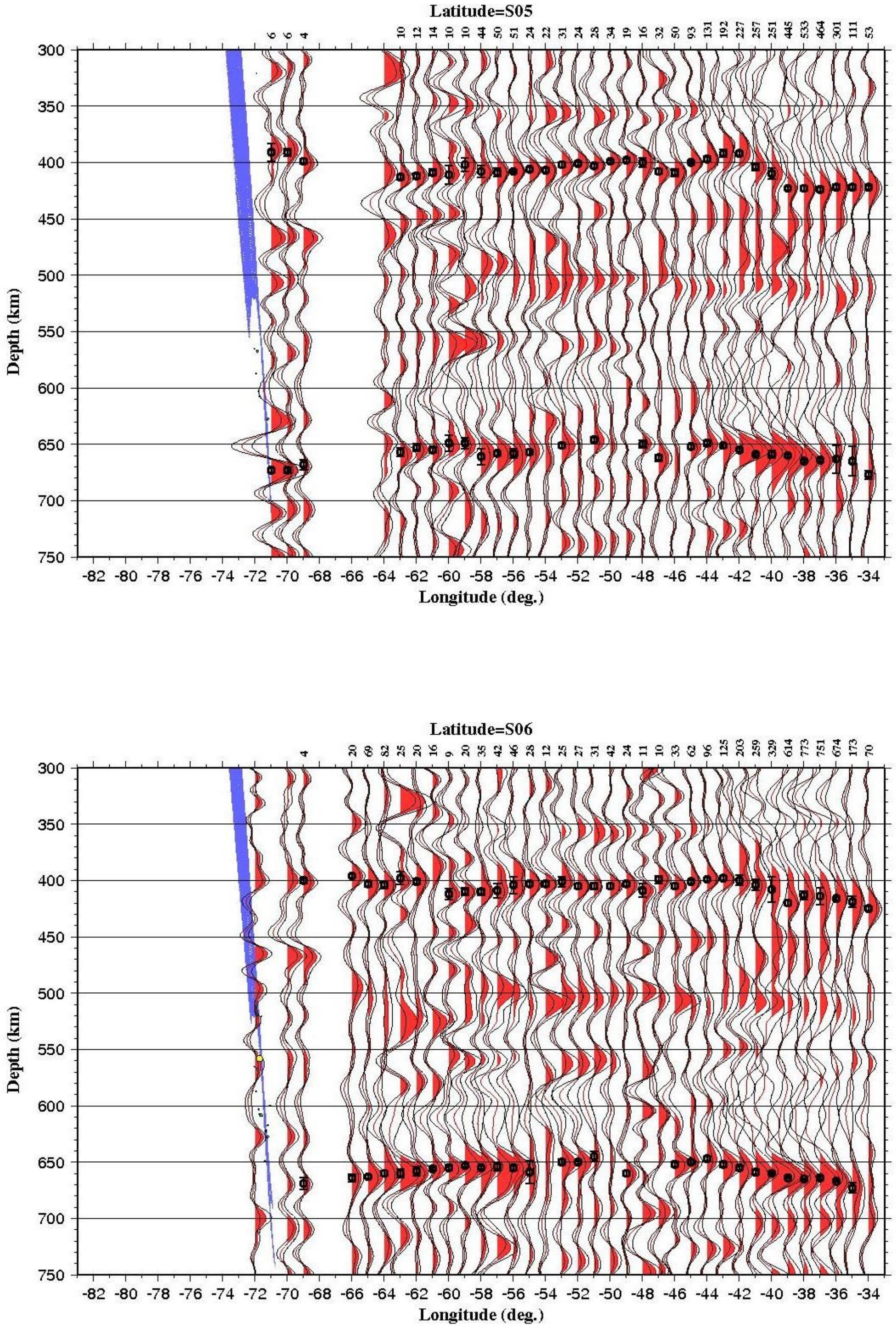

Figure 1. E-W MTZ Cross sections. Cont.

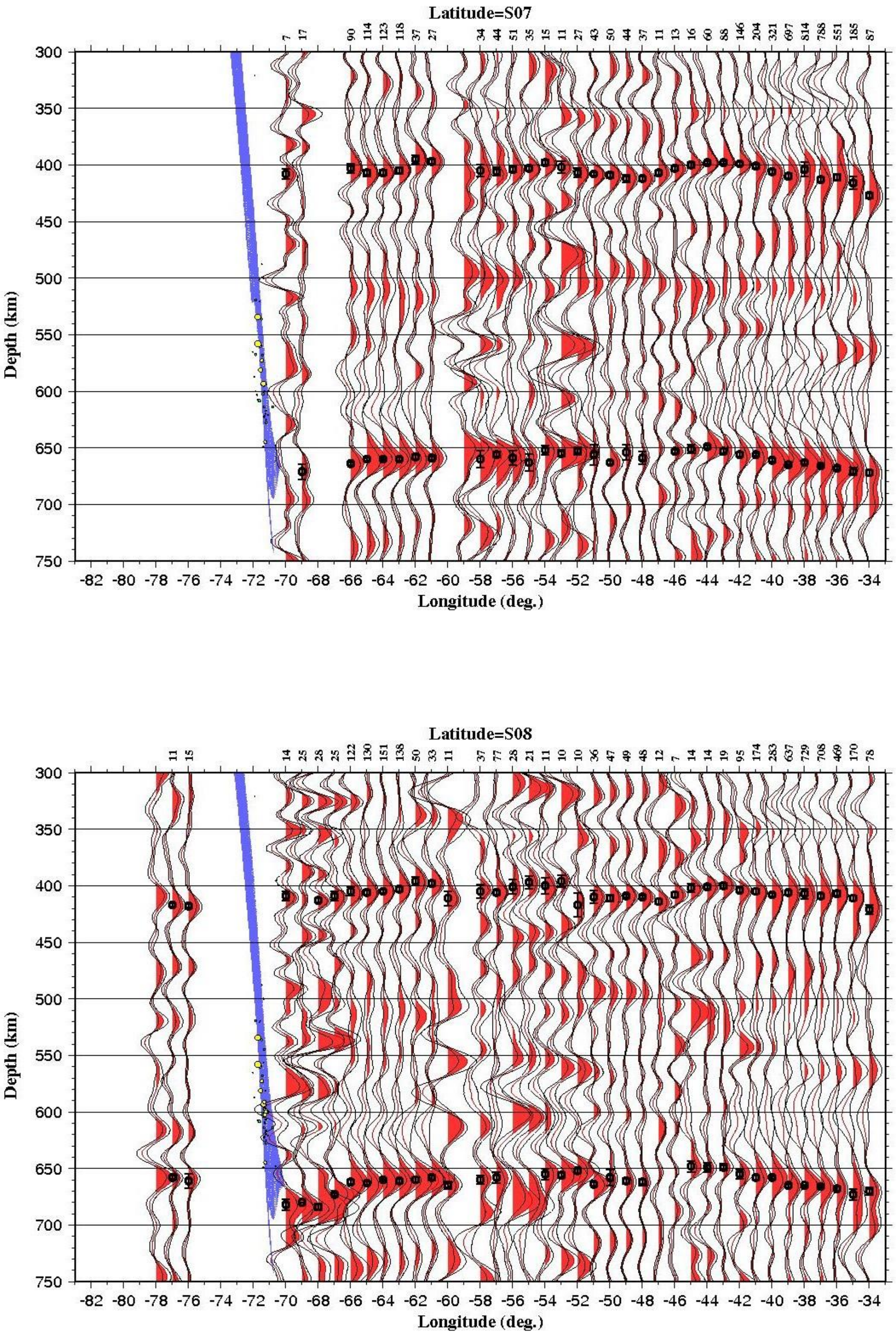

Figure 1. E-W MTZ Cross sections. Cont.

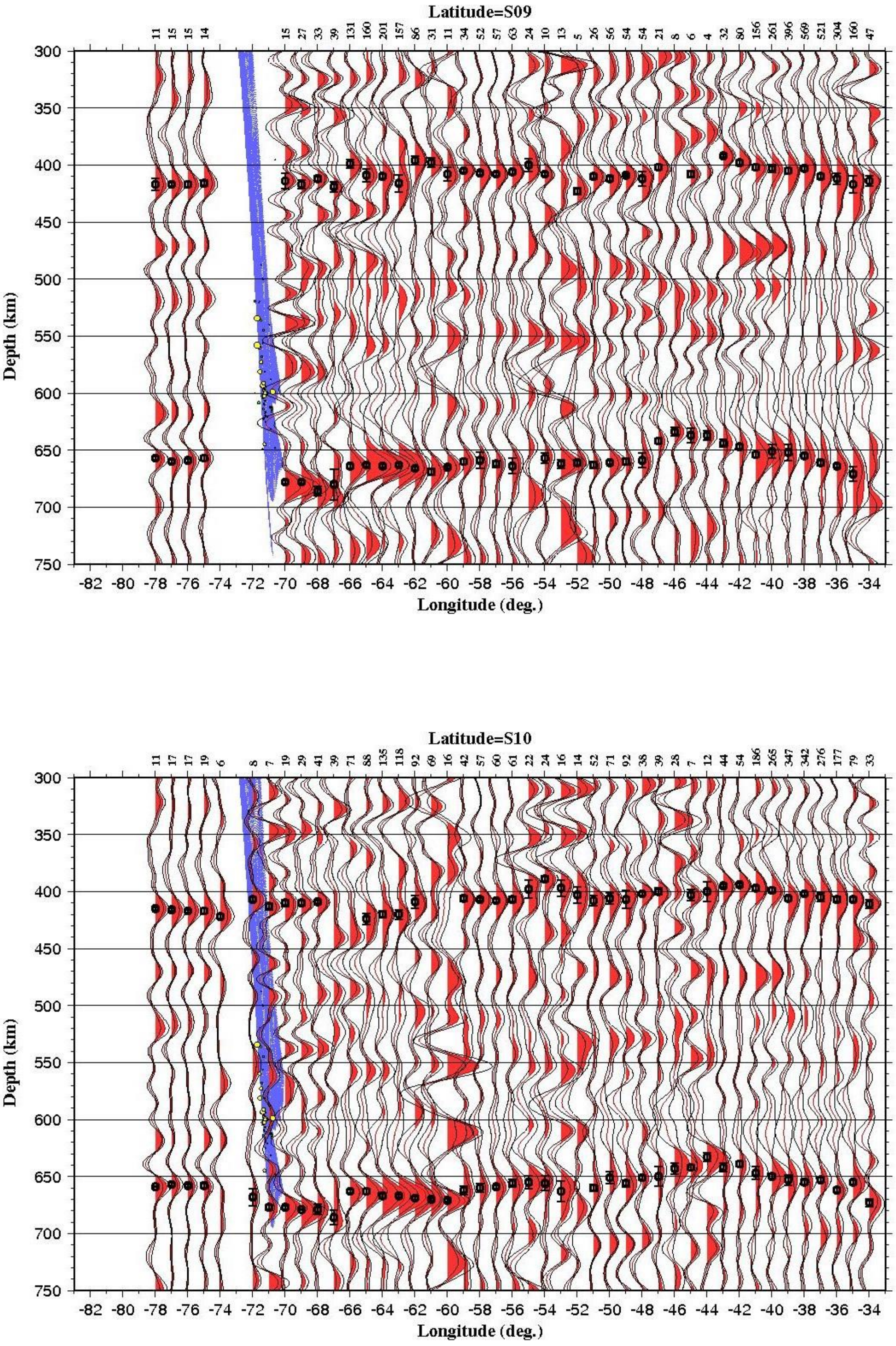

Figure 1. E-W MTZ Cross sections. Cont.

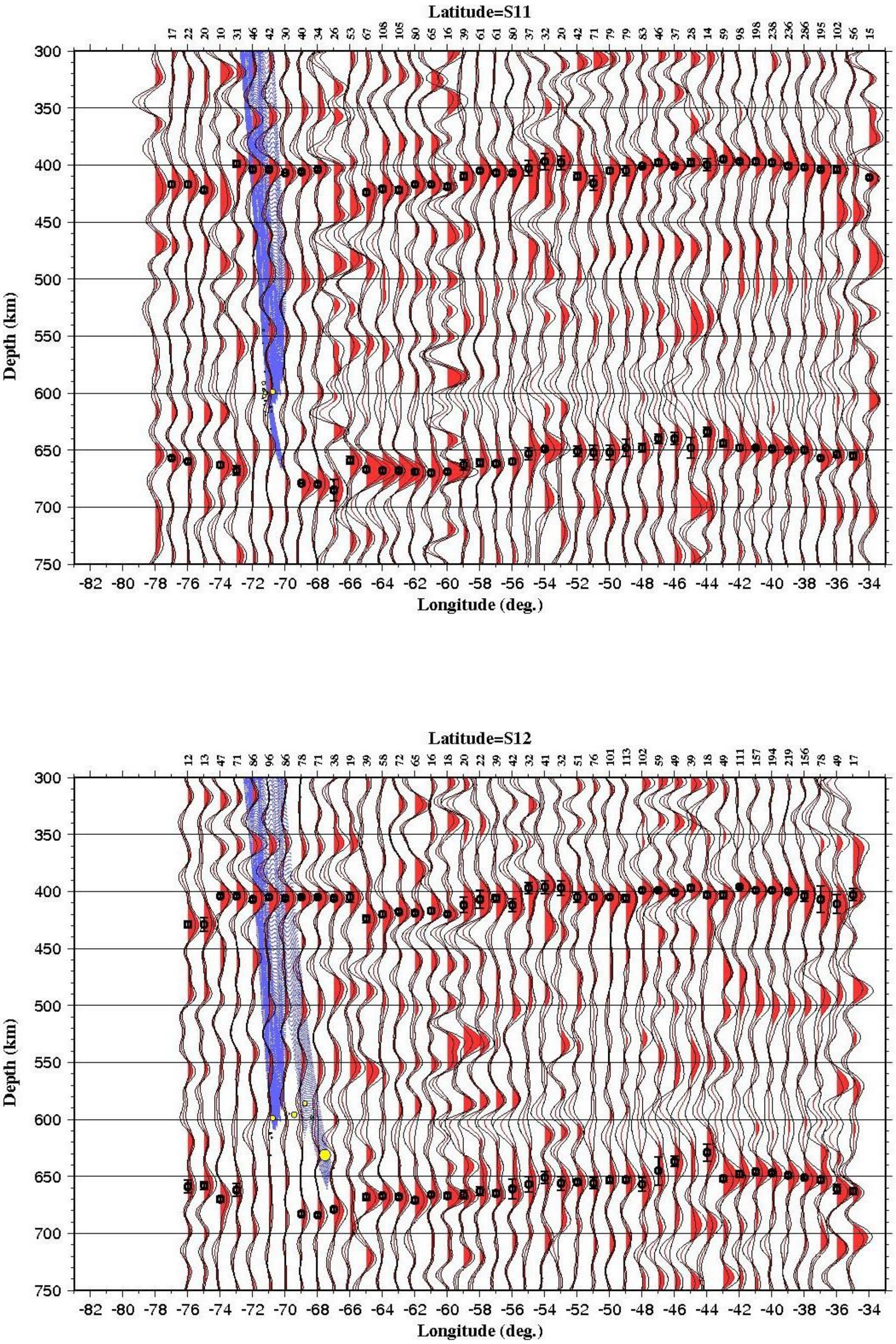

Figure 1. E-W MTZ Cross sections. Cont.

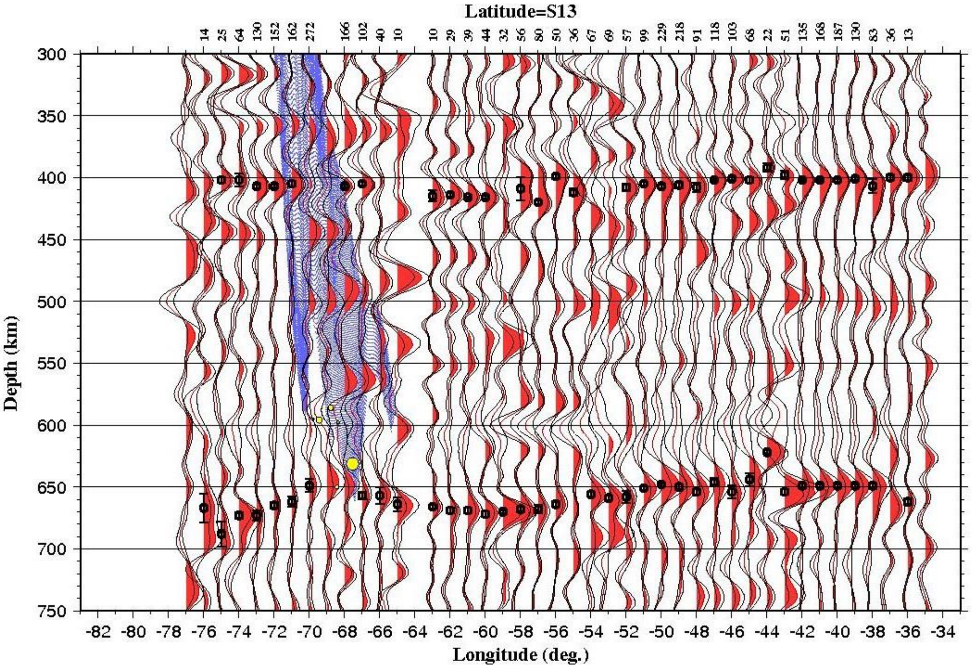

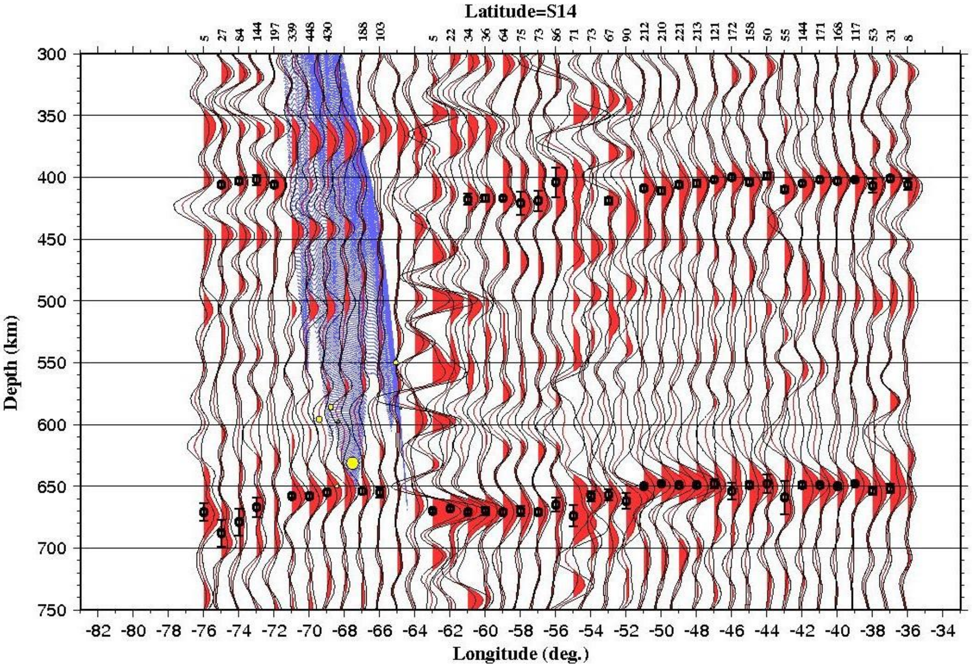

Figure 1. E-W MTZ Cross sections. Cont.

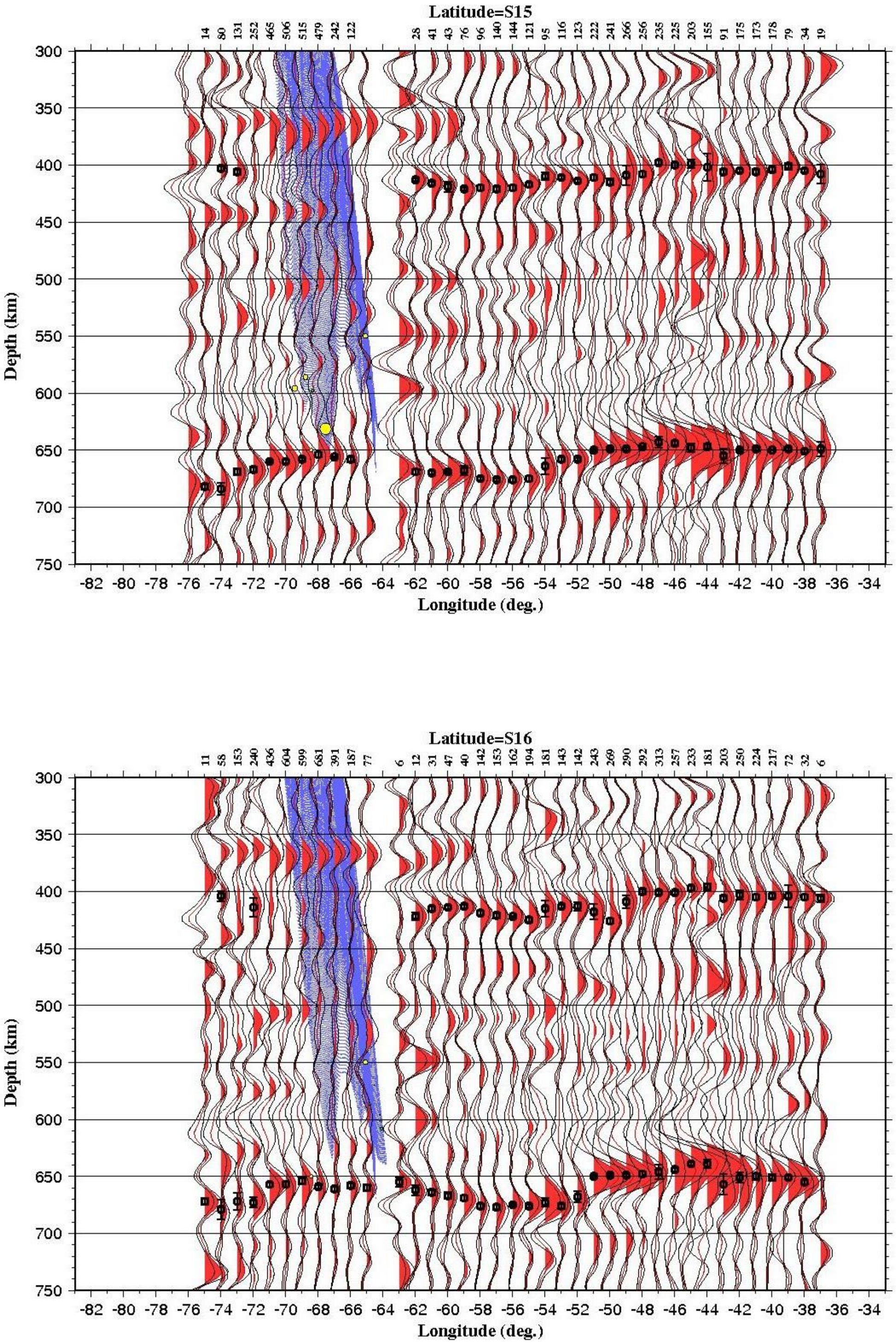

Figure 1. E-W MTZ Cross sections. Cont.

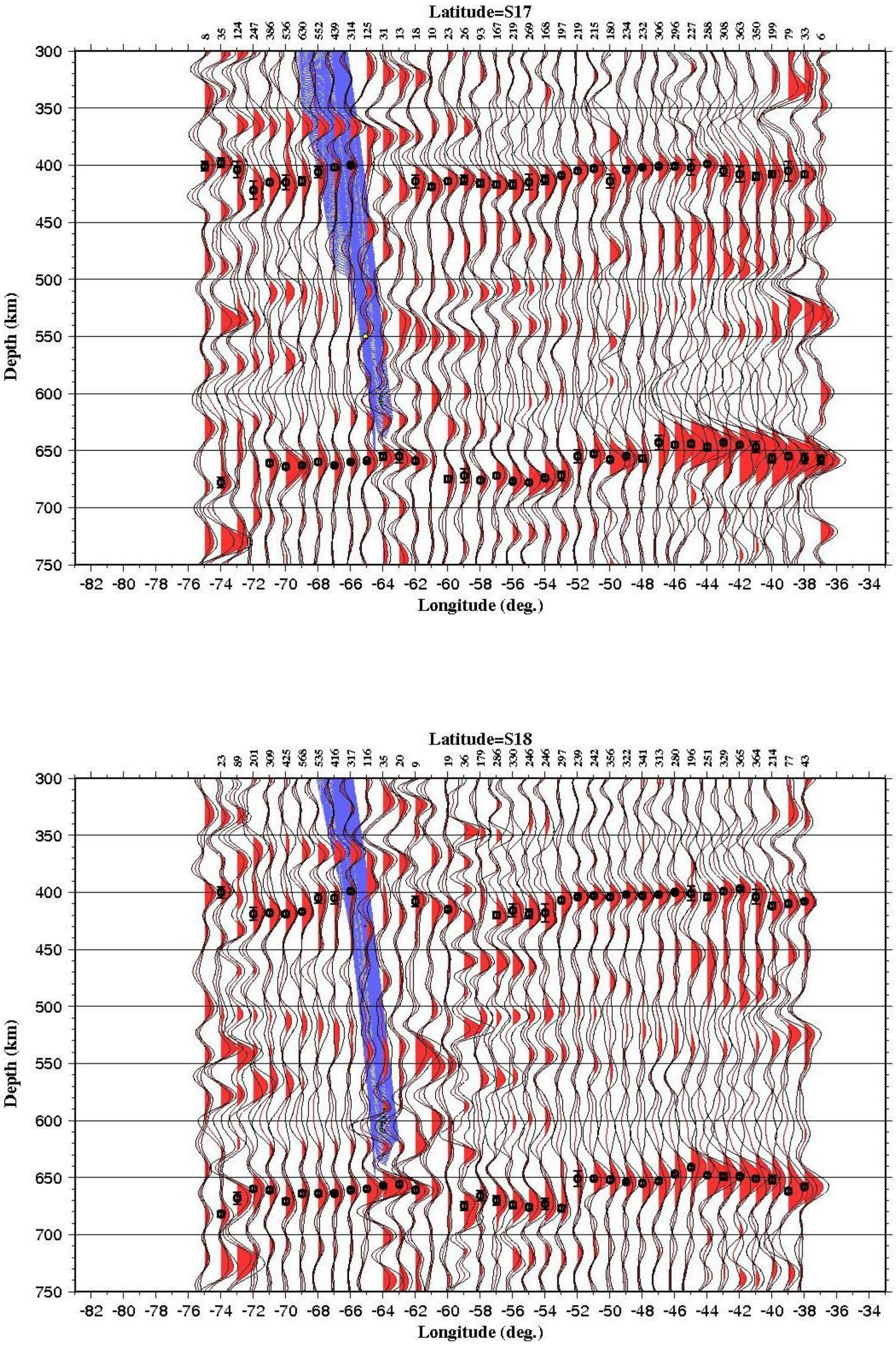

Figure 1. E-W MTZ Cross sections. Cont.

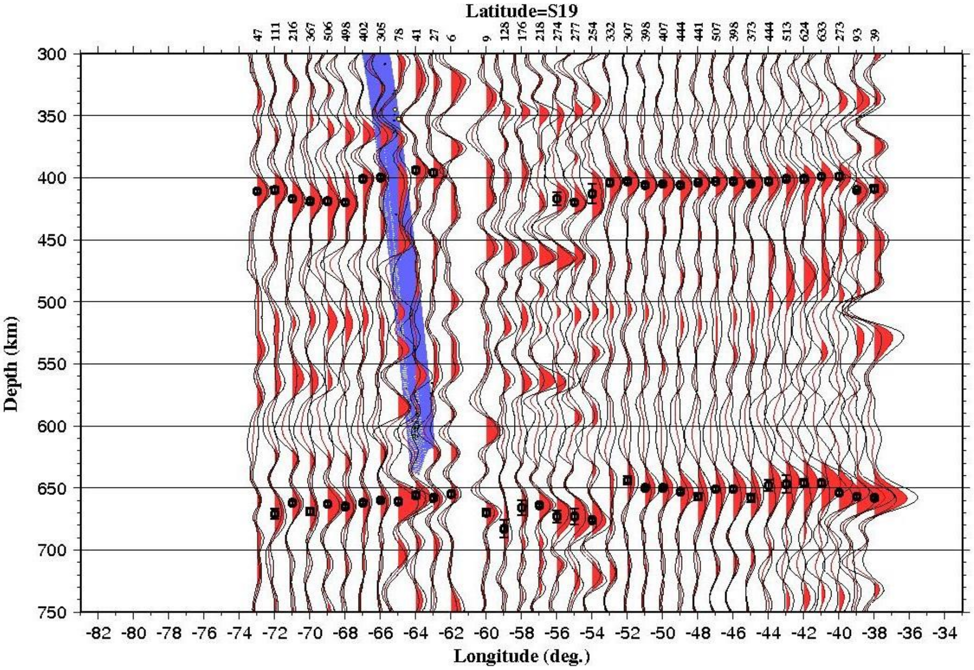

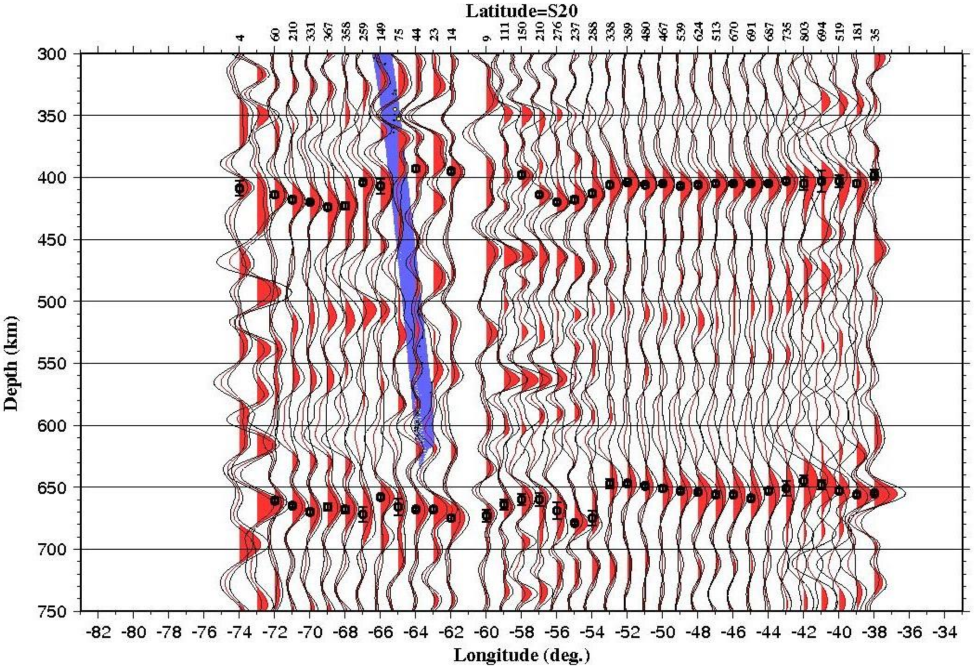

Figure 1. E-W MTZ Cross sections. Cont.

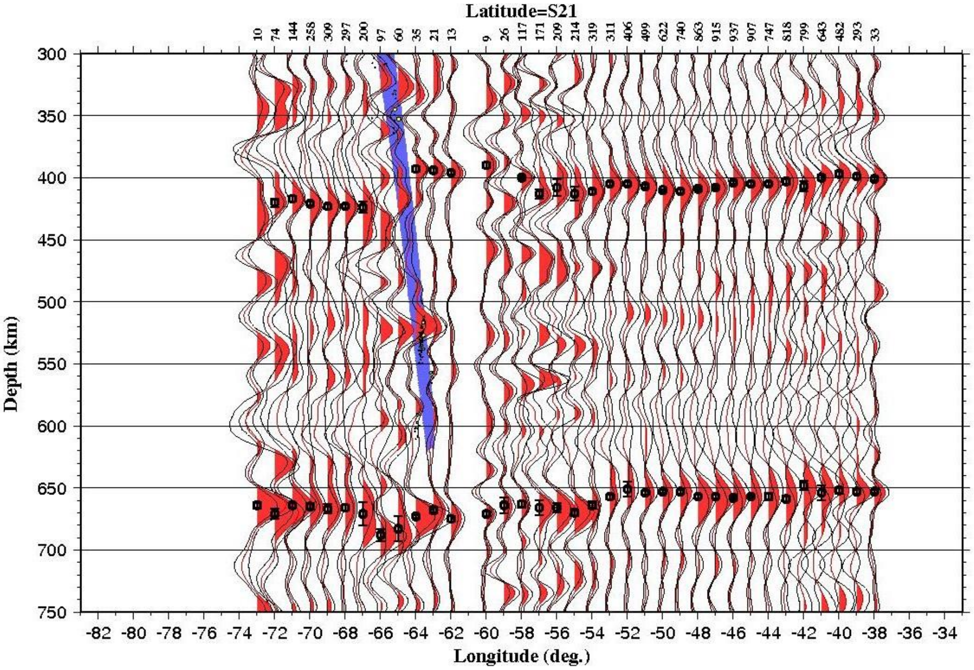

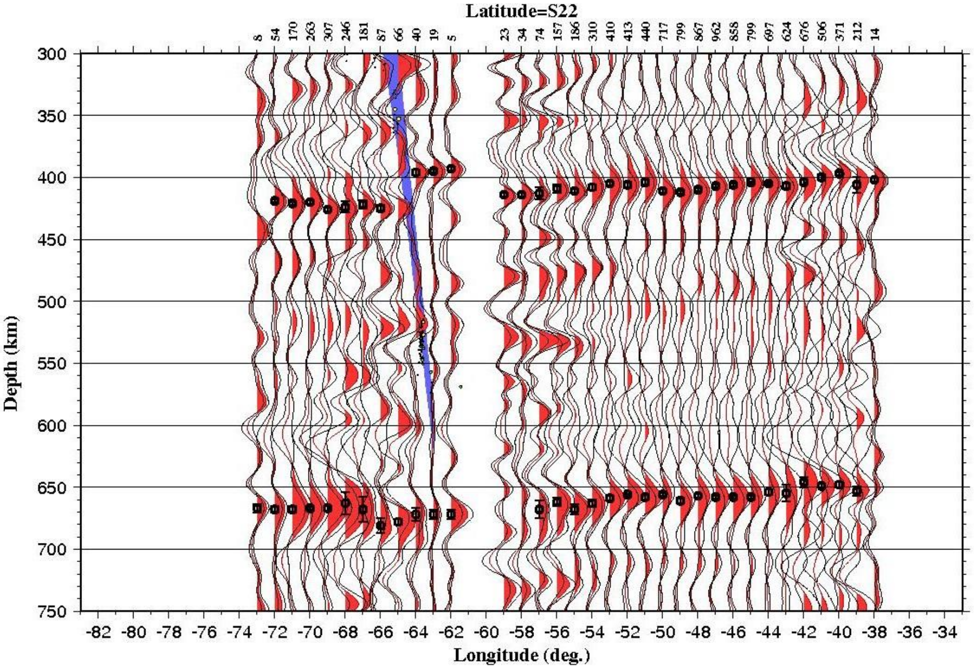

Figure 1. E-W MTZ Cross sections. Cont.

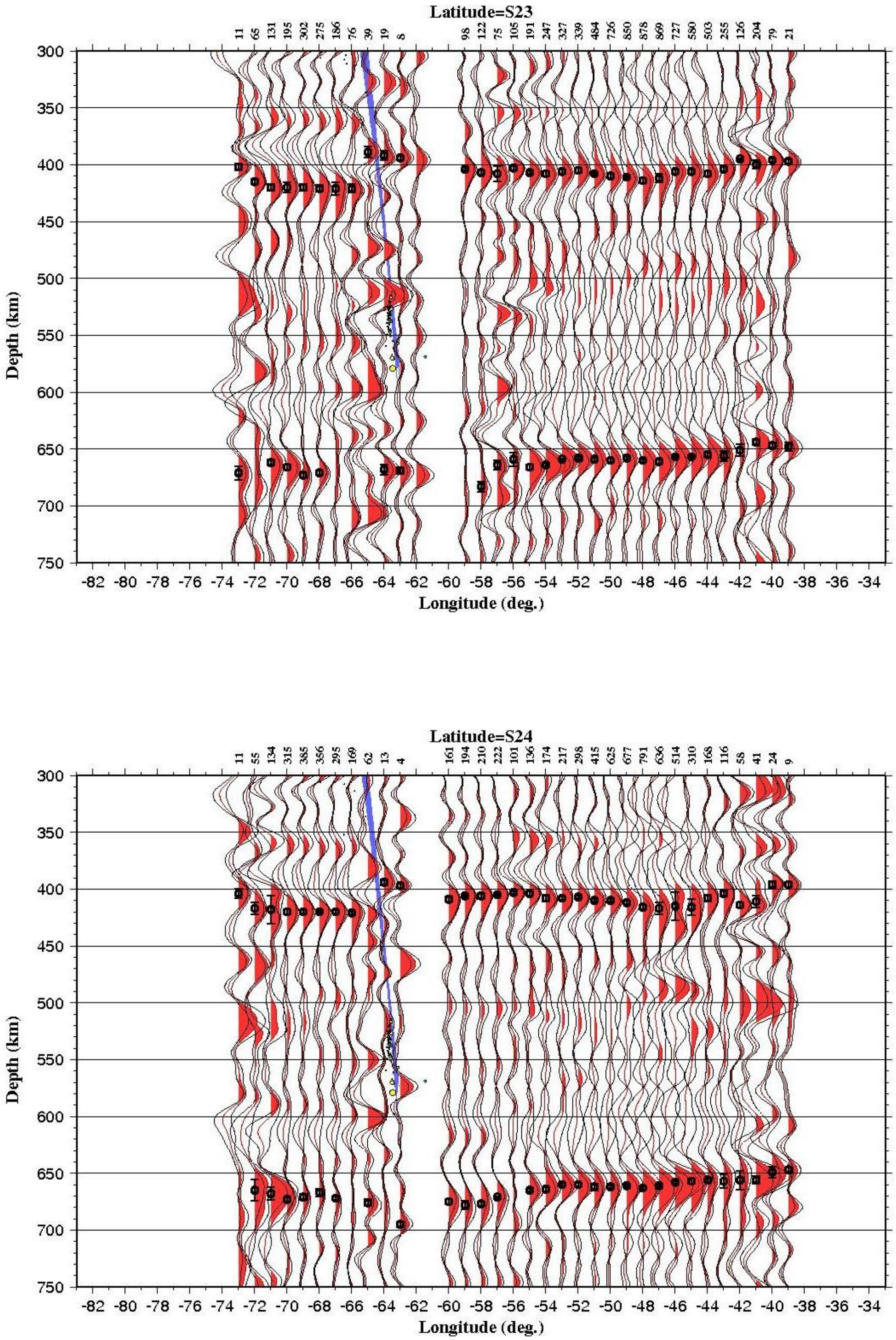

Figure 1. E-W MTZ Cross sections. Cont.

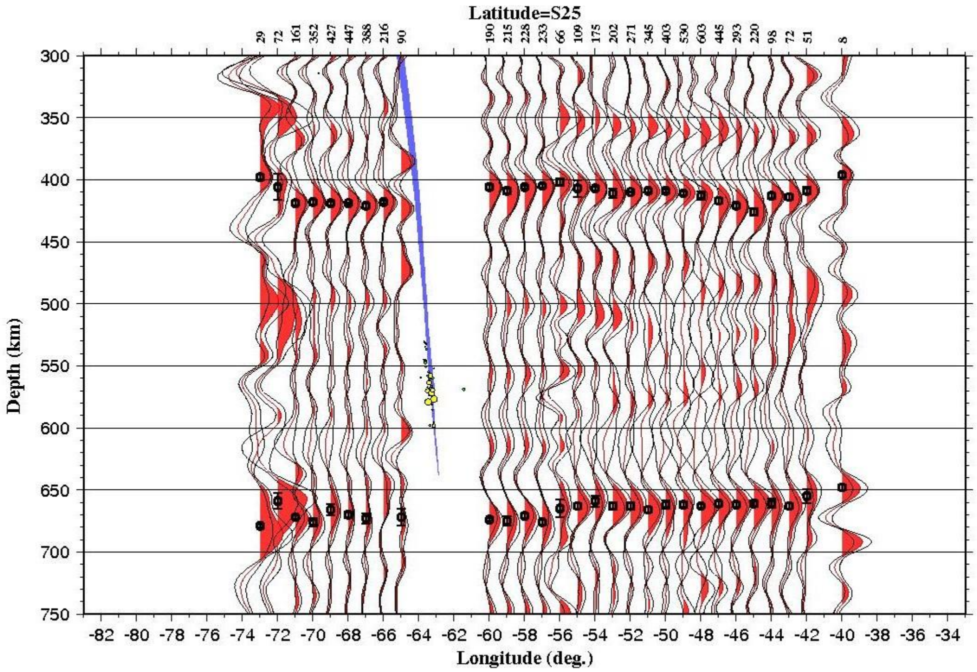

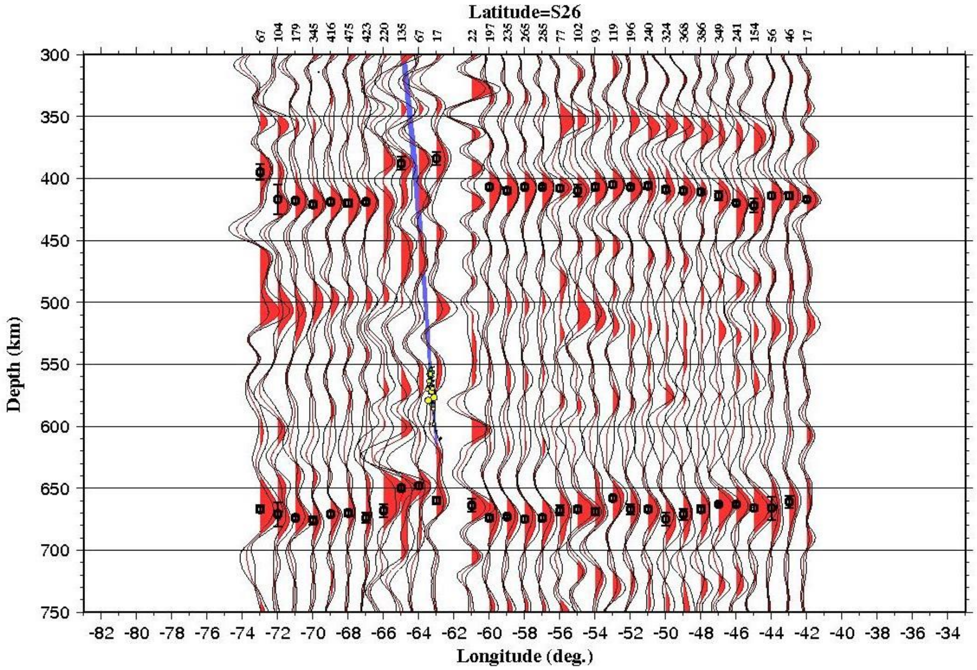

Figure 1. E-W MTZ Cross sections. Cont.

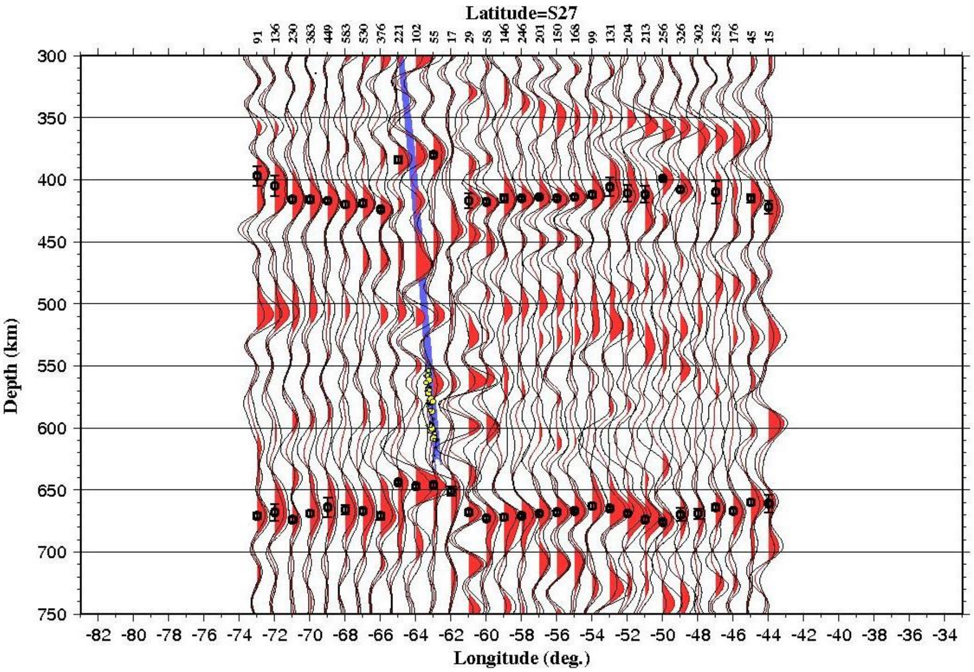

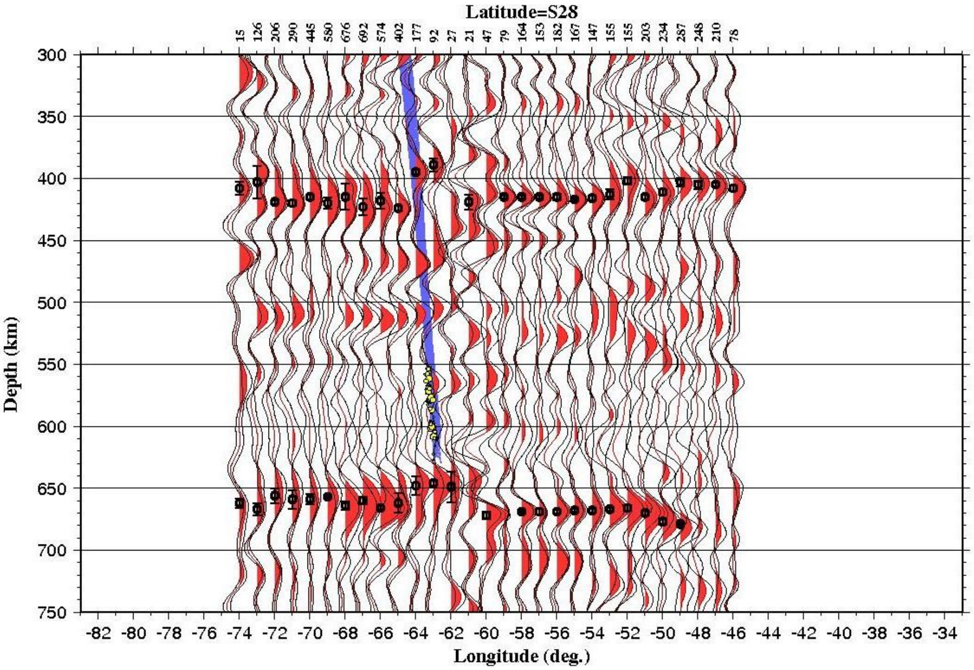

Figure 1. E-W MTZ Cross sections. Cont.

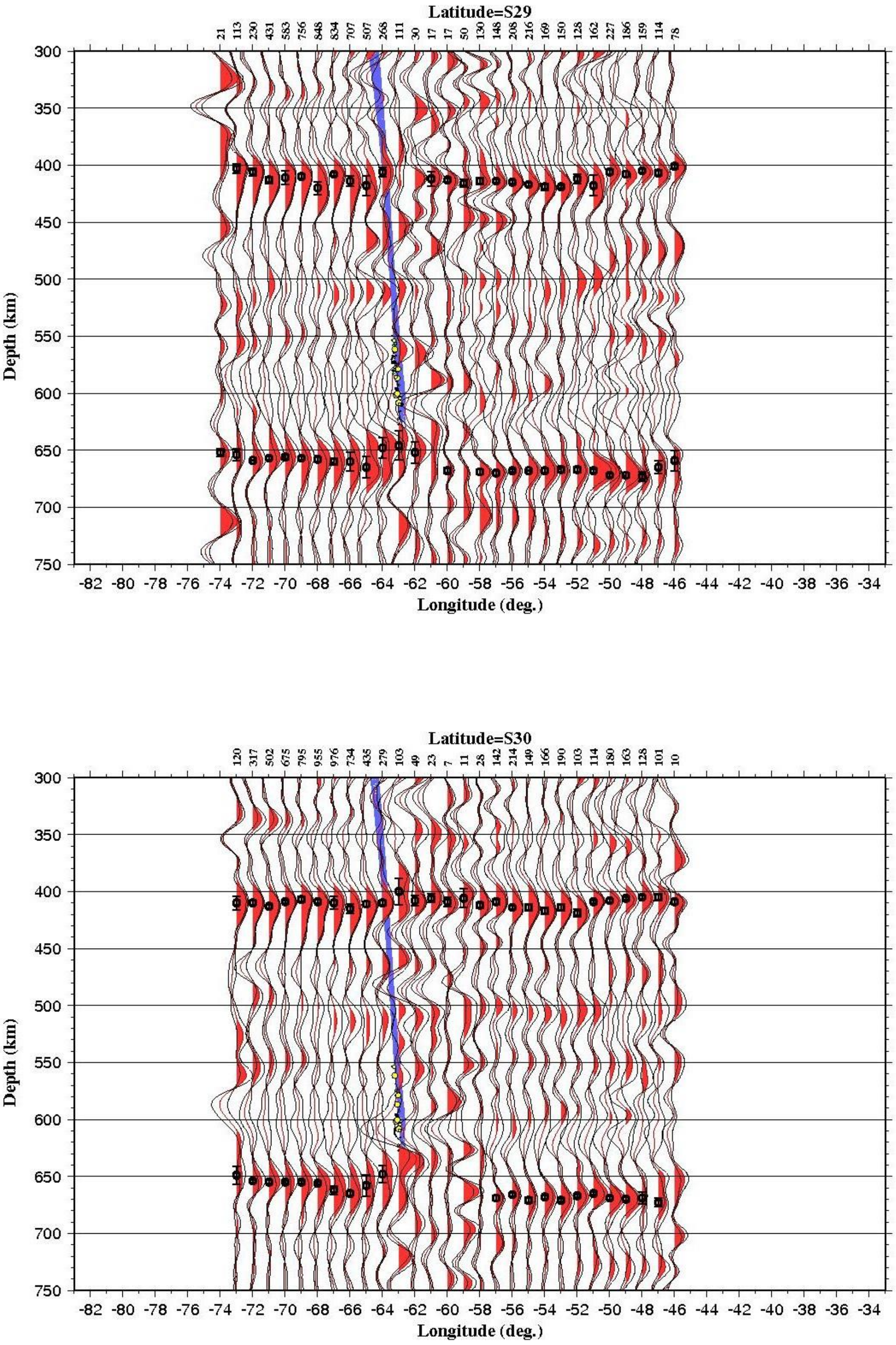

Figure 1. E-W MTZ Cross sections. Cont.

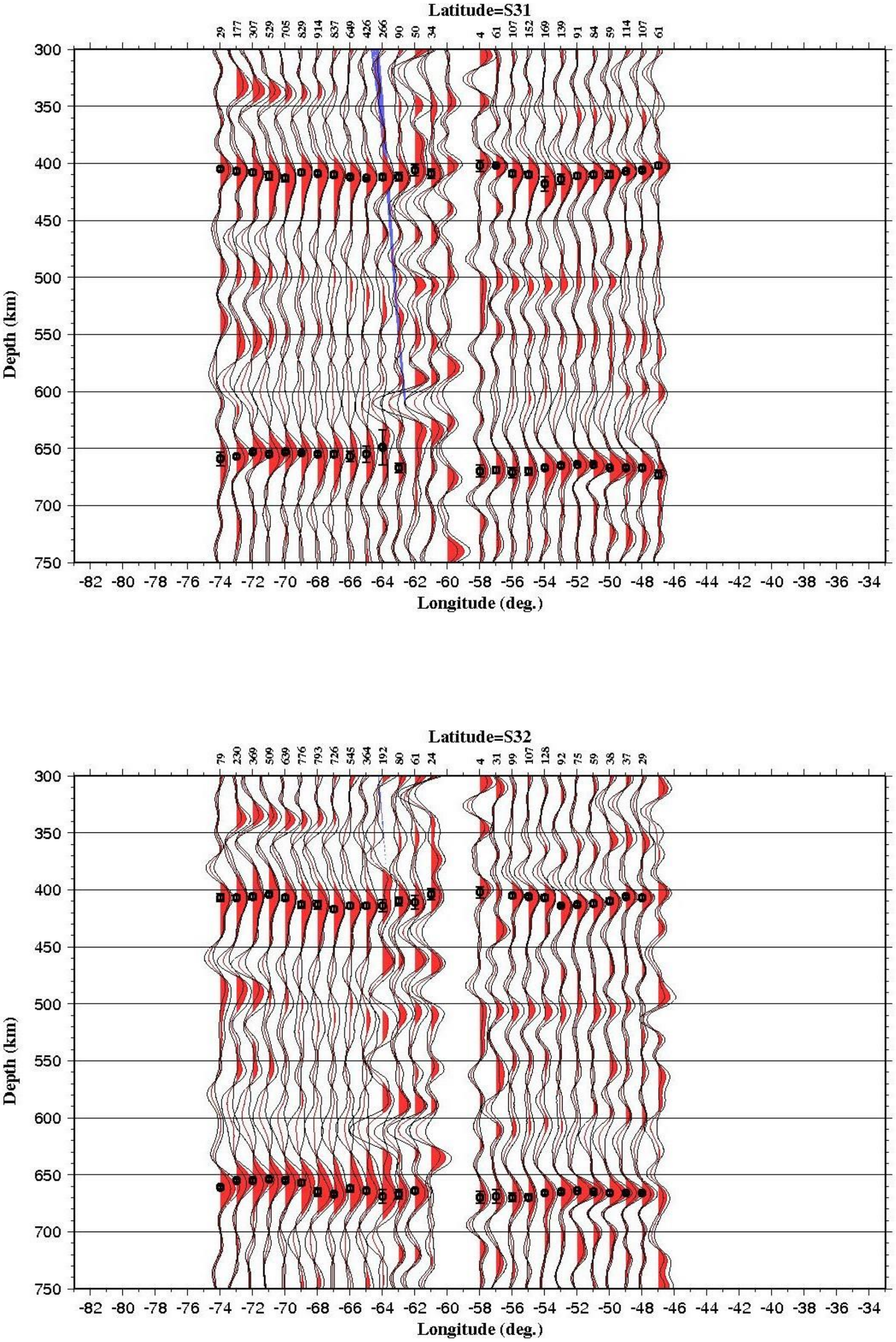

Figure 1. E-W MTZ Cross sections. Cont.

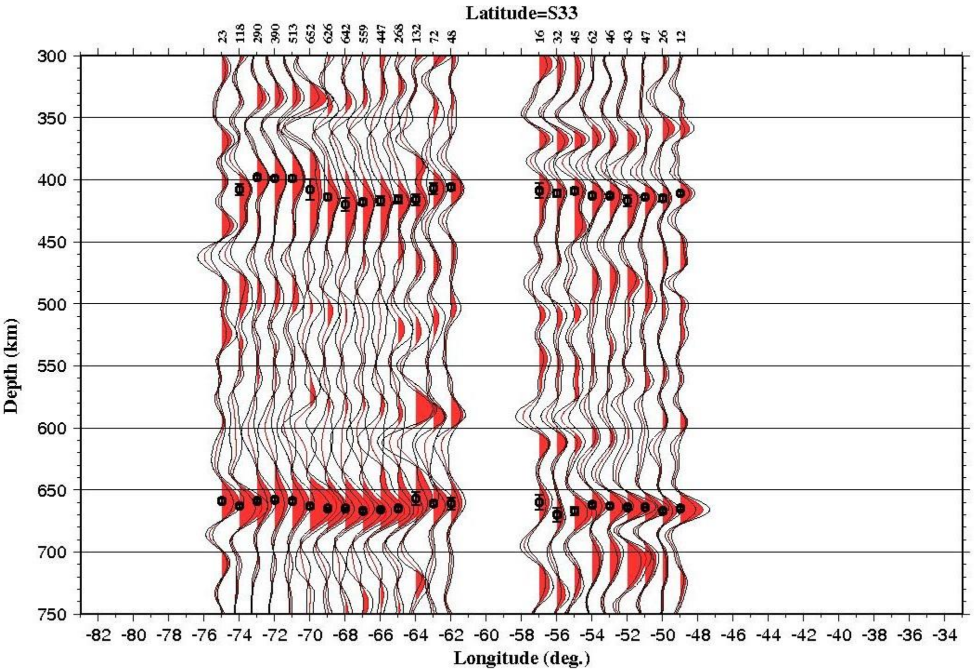

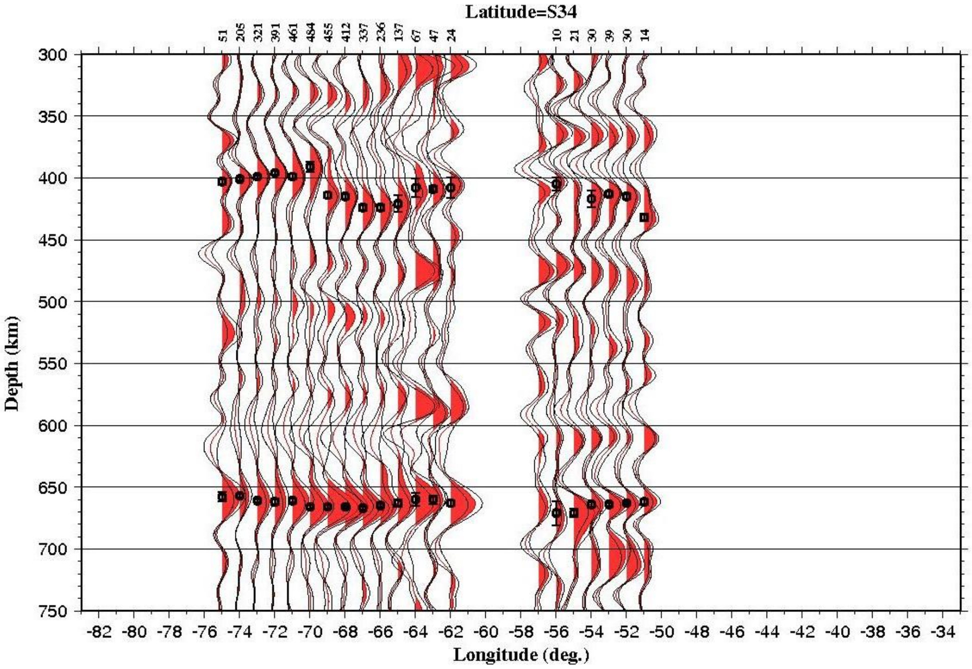

Figure 1. E-W MTZ Cross sections. Cont.

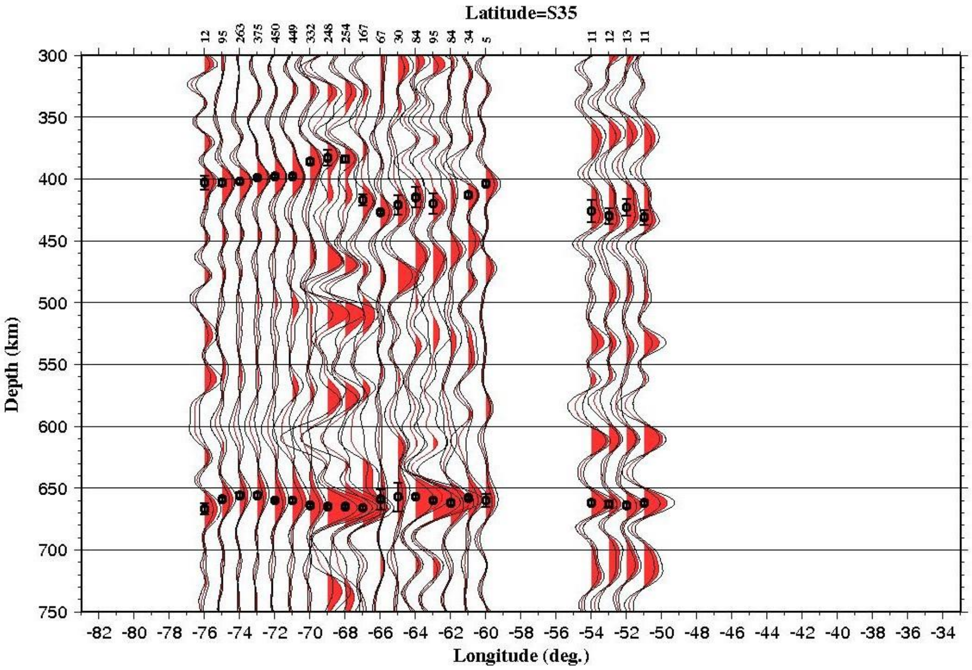

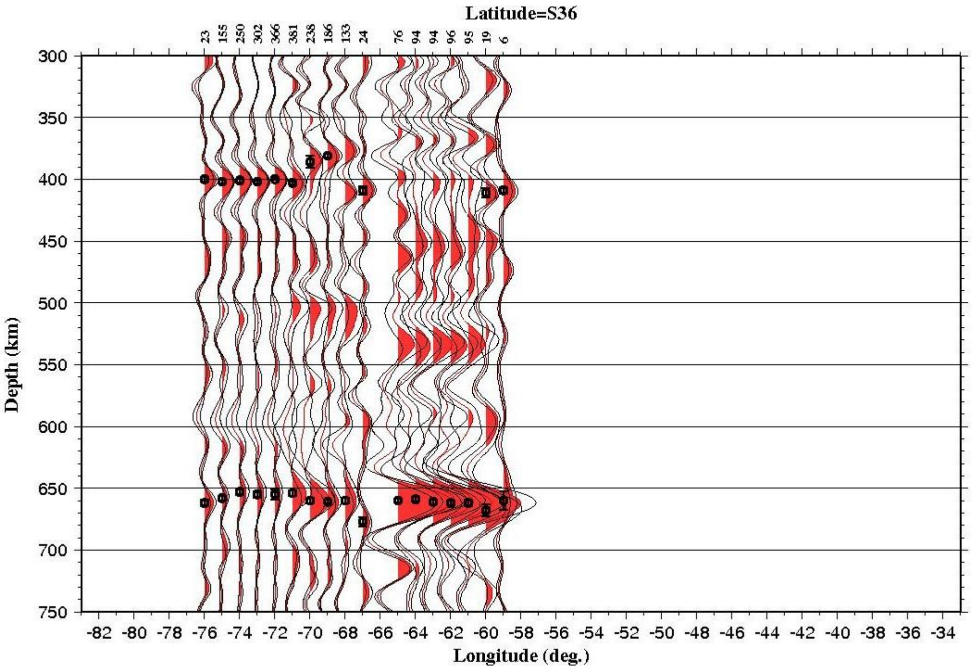

Figure 1. E-W MTZ Cross sections. Cont.

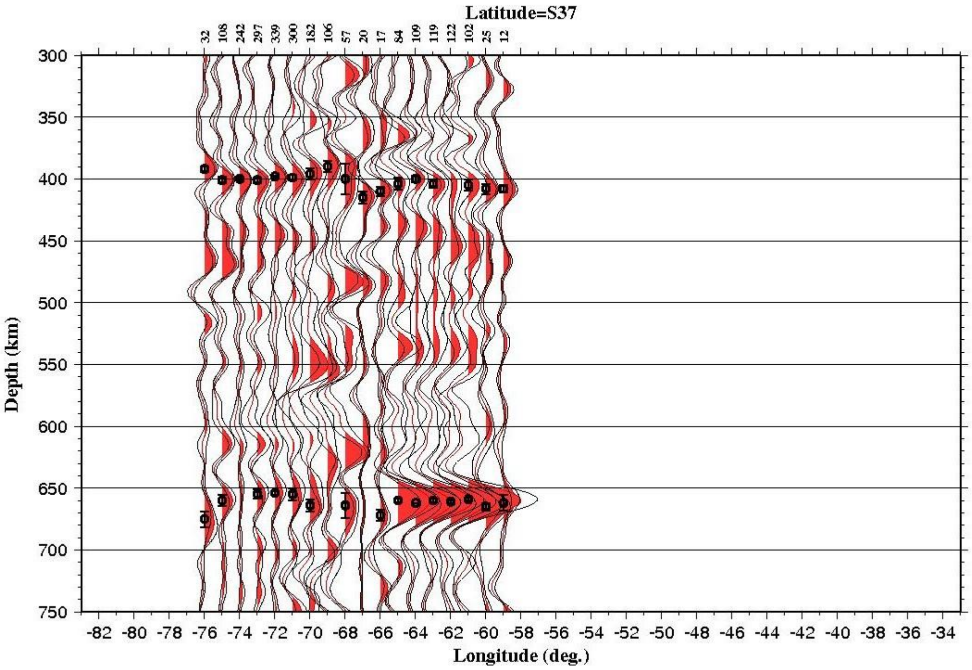

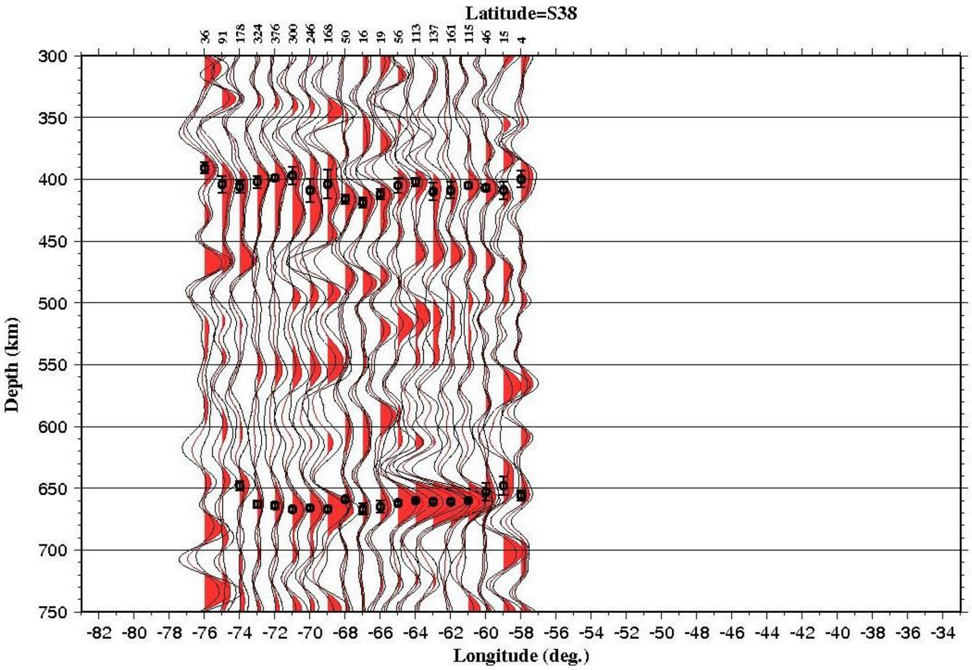

Figure 1. E-W MTZ Cross sections. Cont.

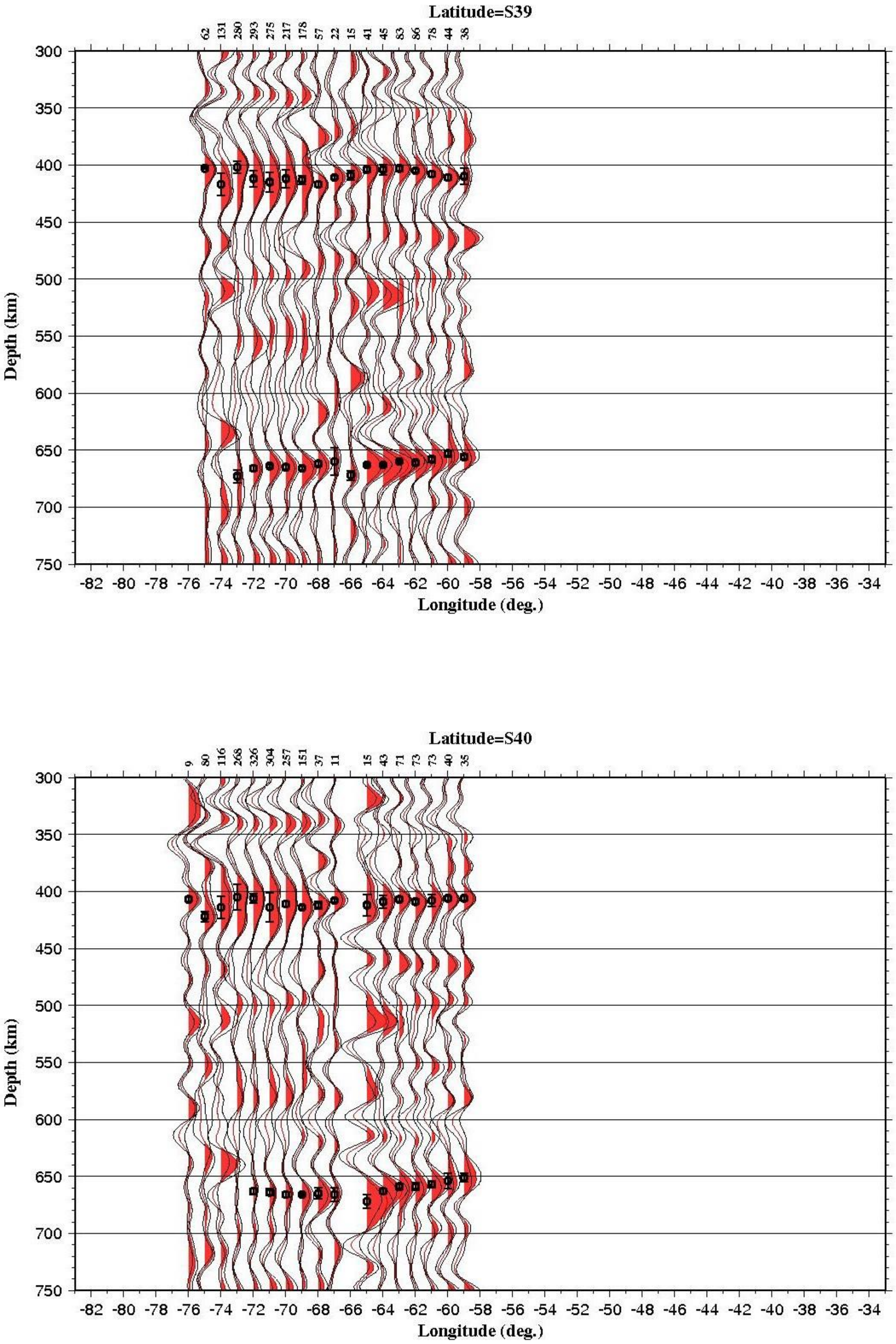

Figure 1. E-W MTZ Cross sections. Cont.

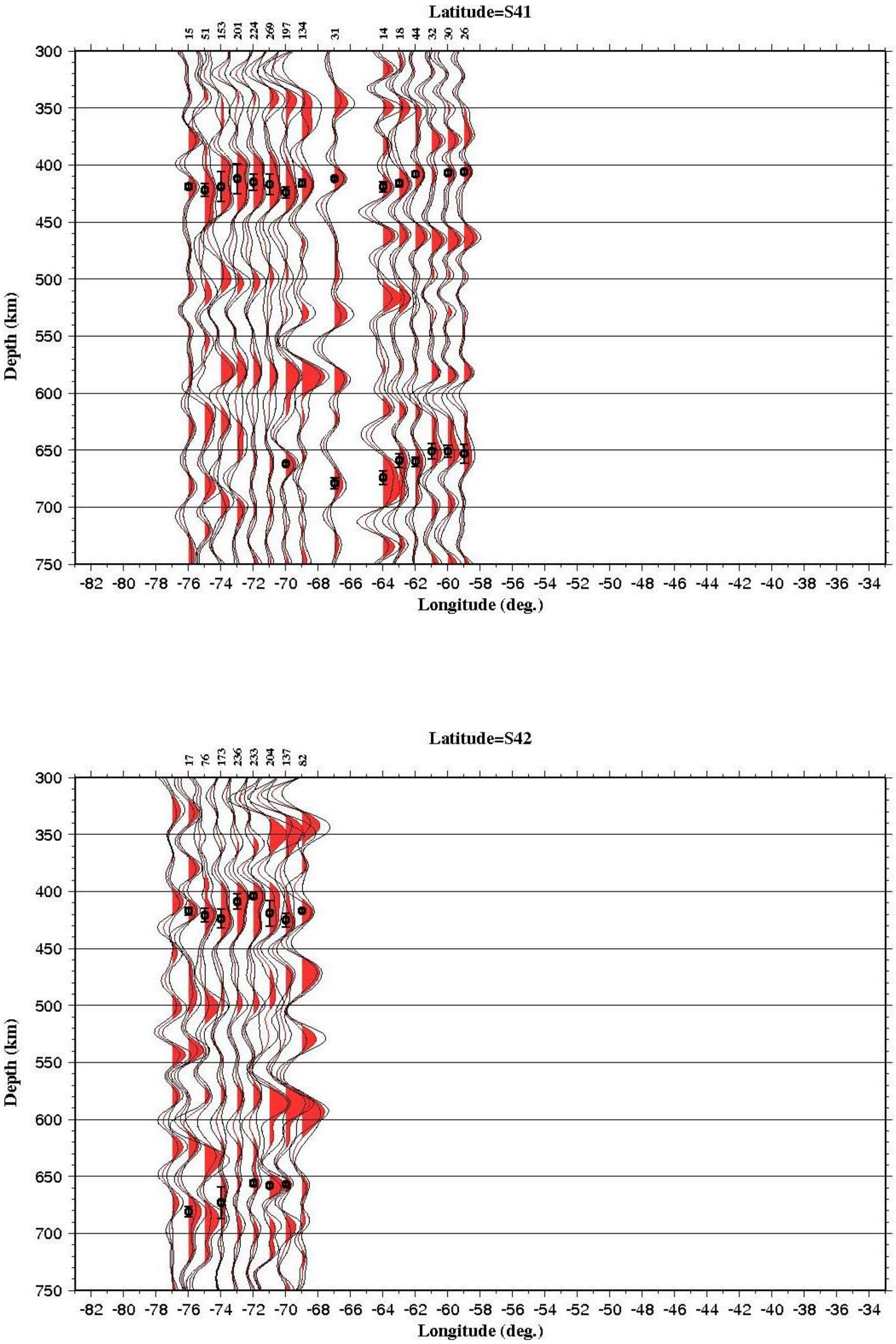

Figure 1. E-W MTZ Cross sections. Cont.

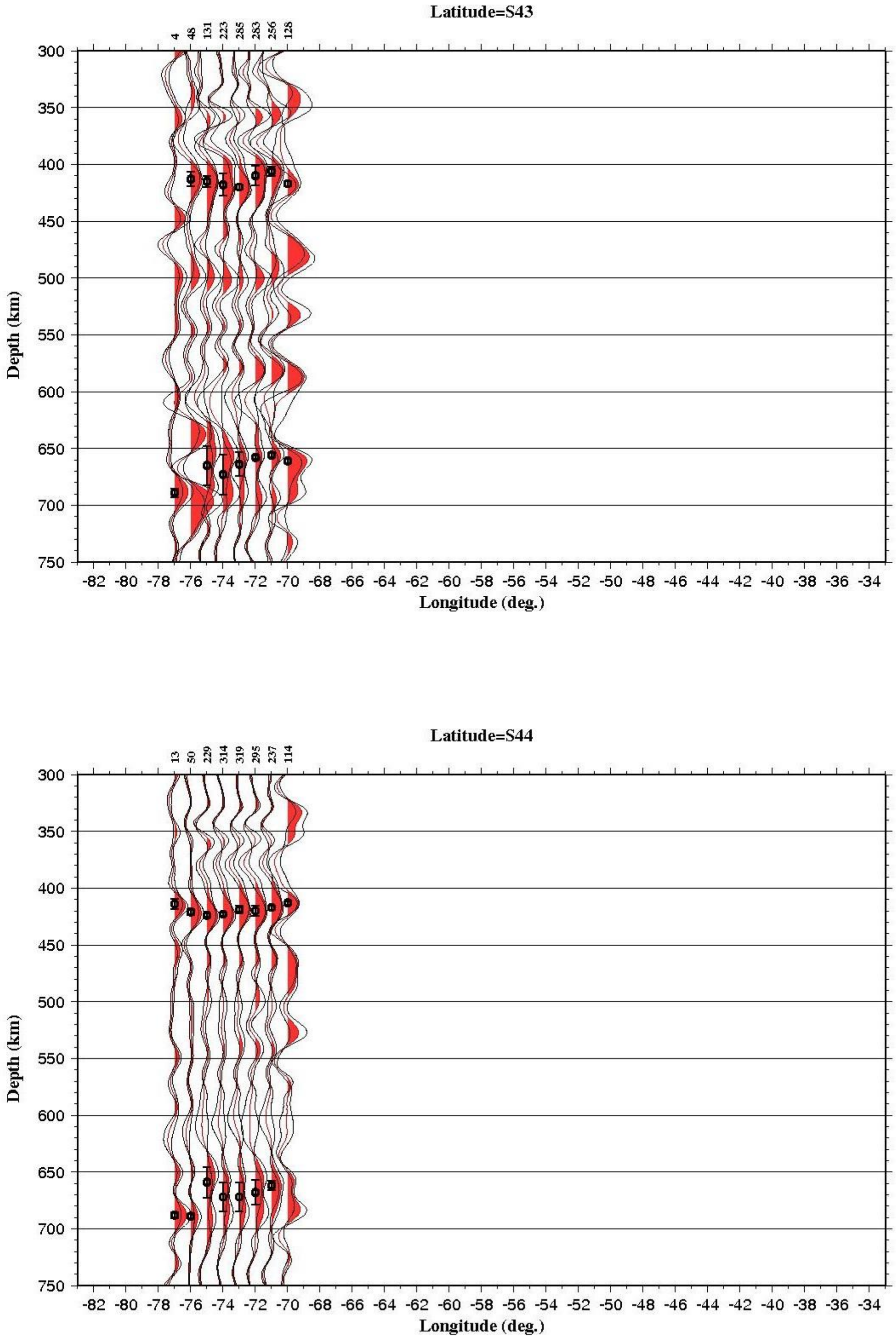

Figure 1. E-W MTZ Cross sections. Cont.

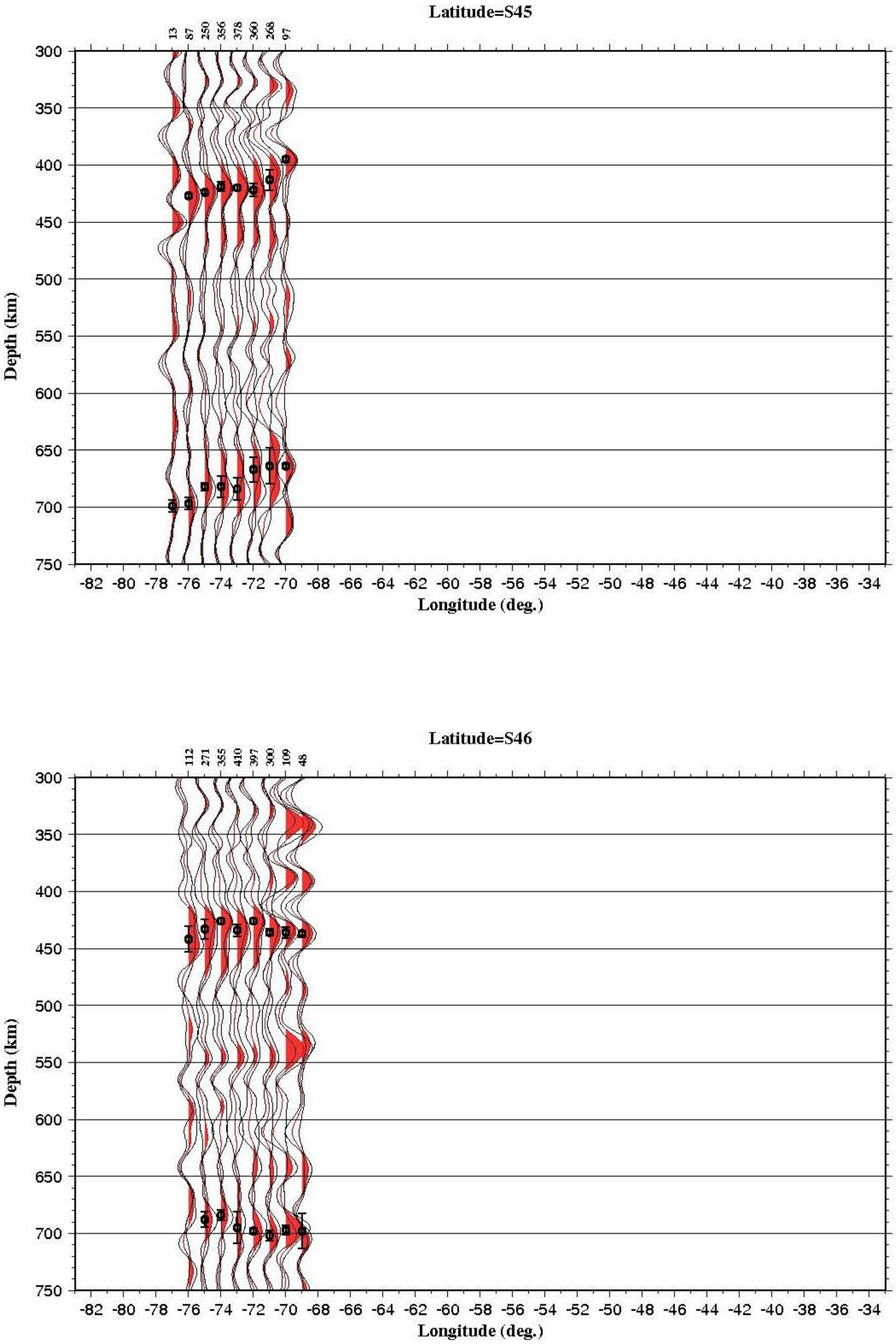

Figure 1. E-W MTZ Cross sections. Cont.

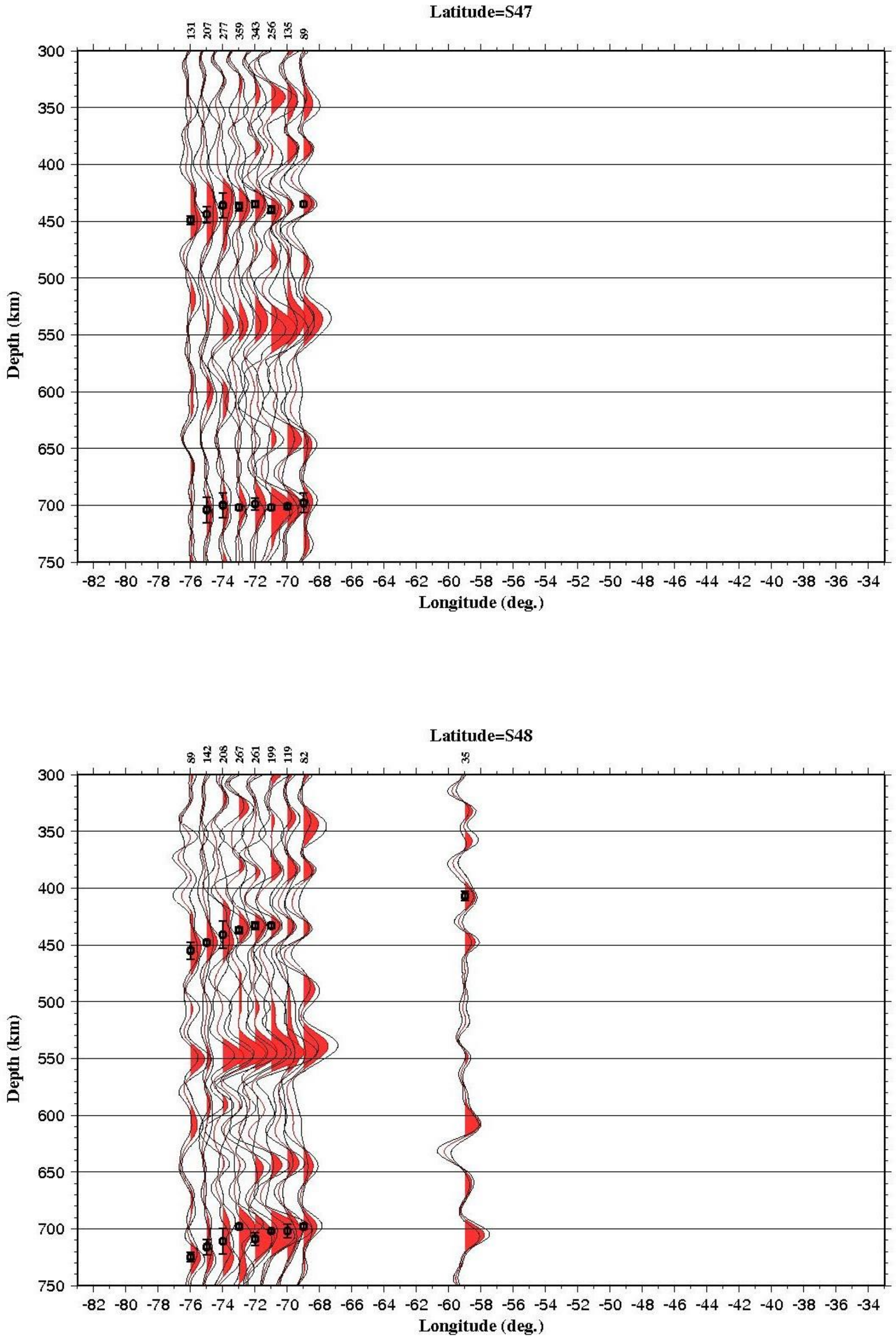

Figure 1. E-W MTZ Cross sections. Cont.

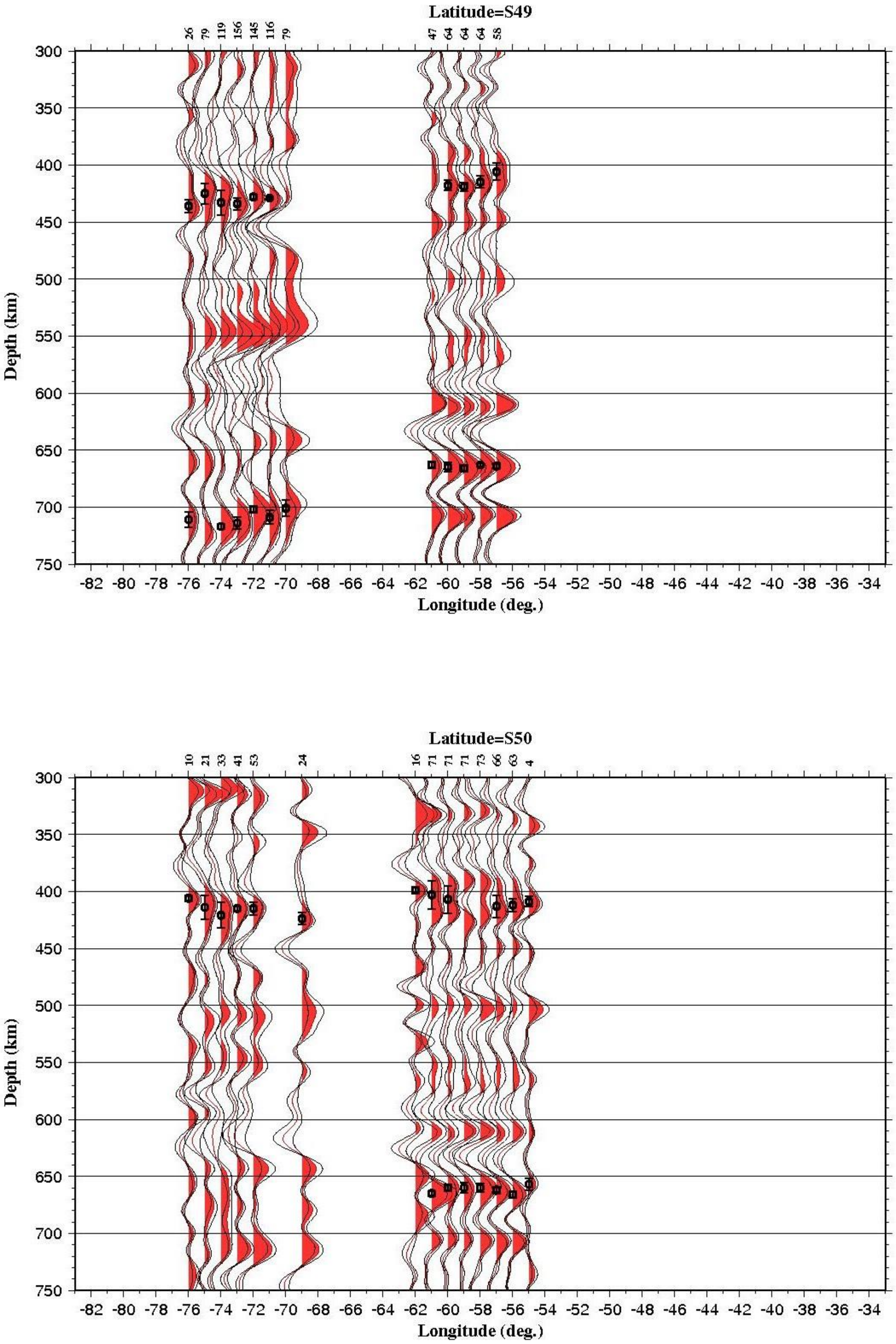

Figure 1. E-W MTZ Cross sections. Cont.

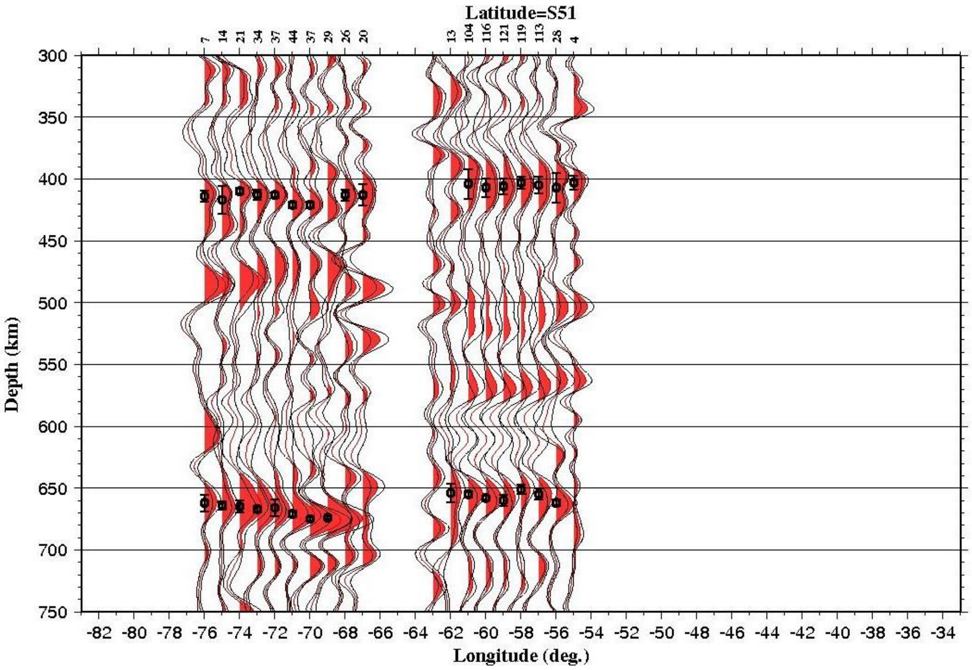

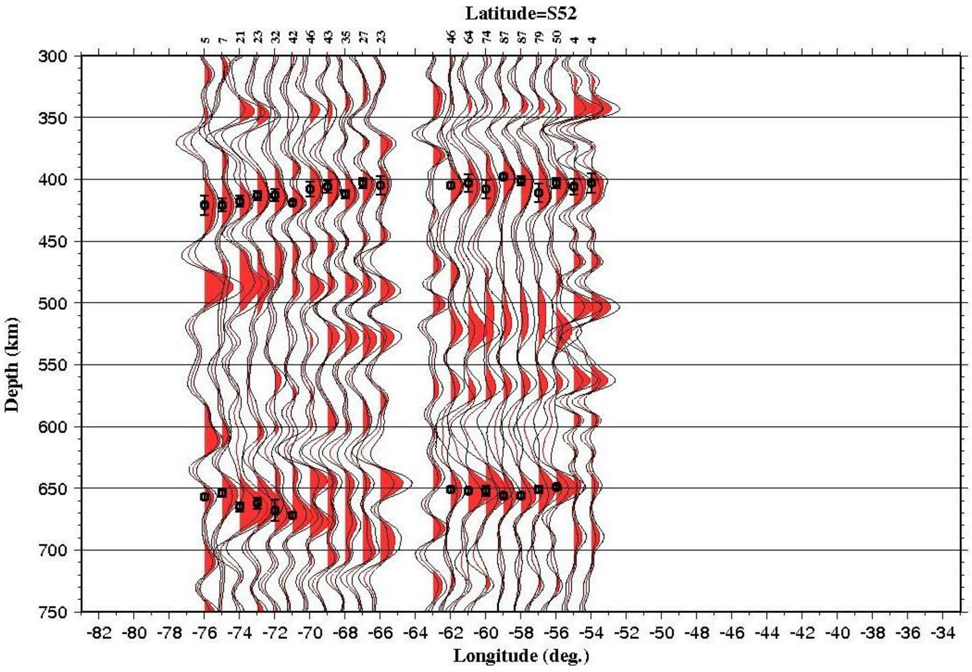

Figure 1. E-W MTZ Cross sections. Cont.

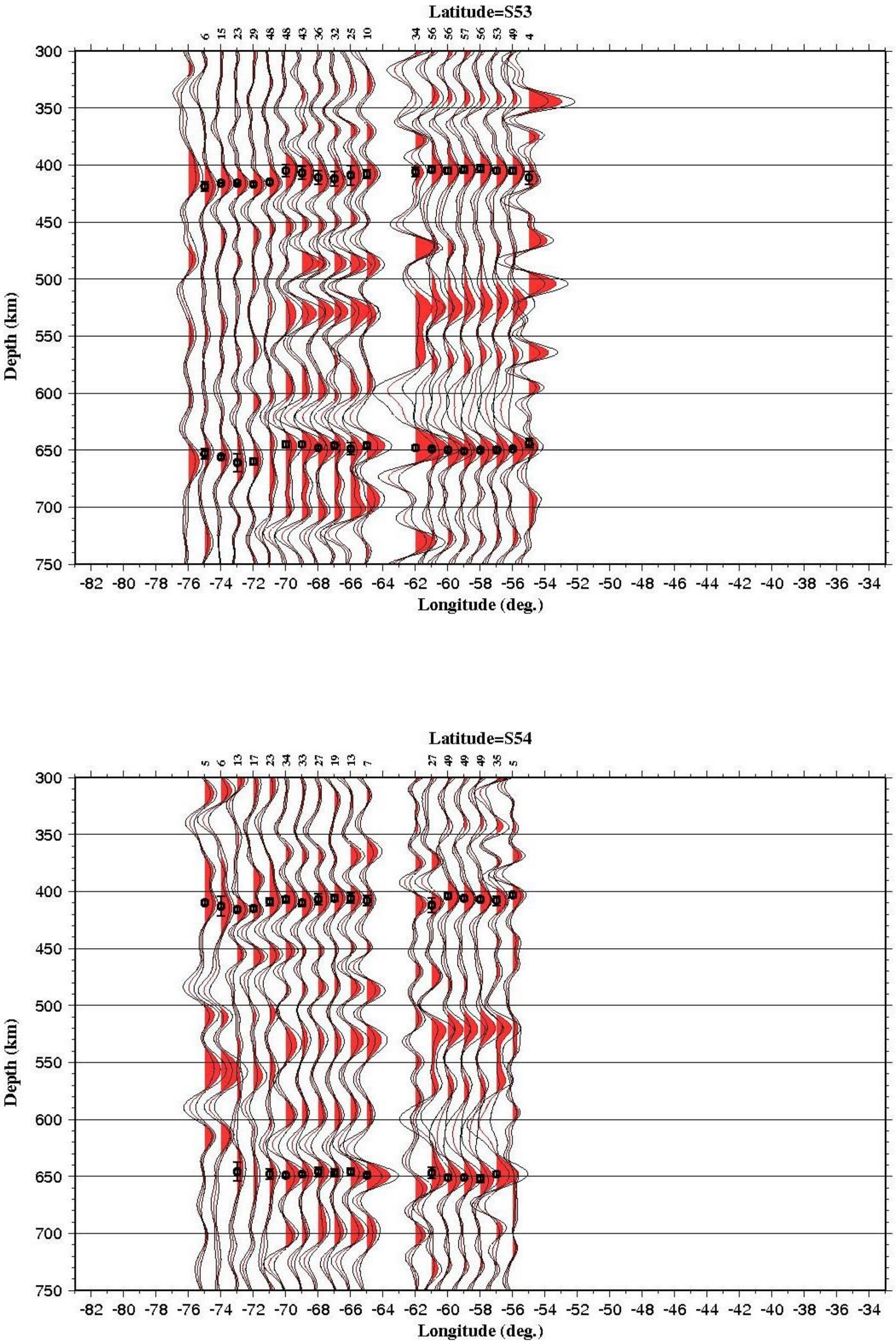

Figure 1. E-W MTZ Cross sections. Cont.

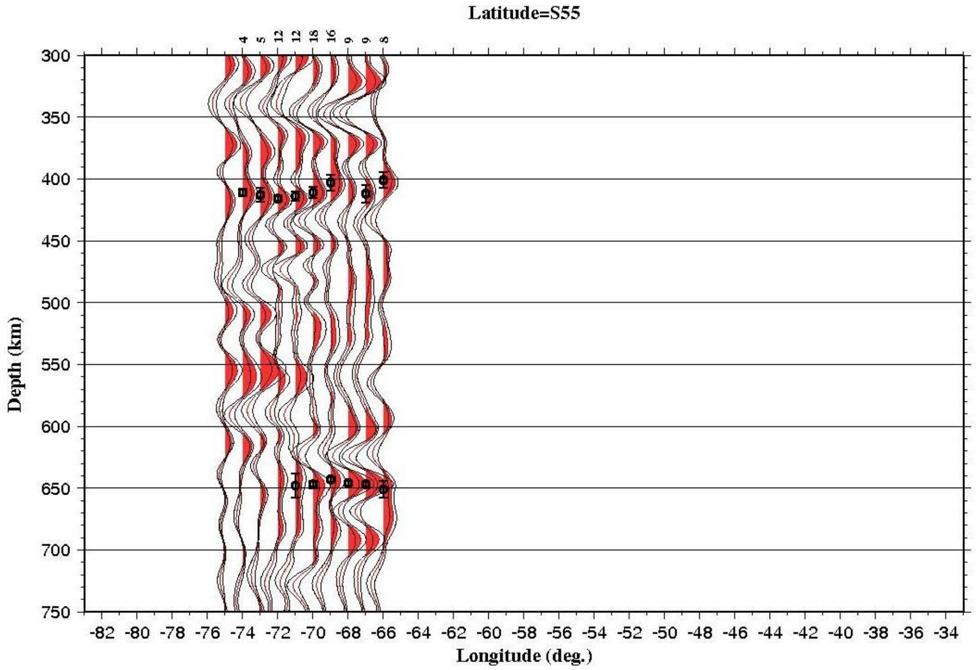
Latitude=S55

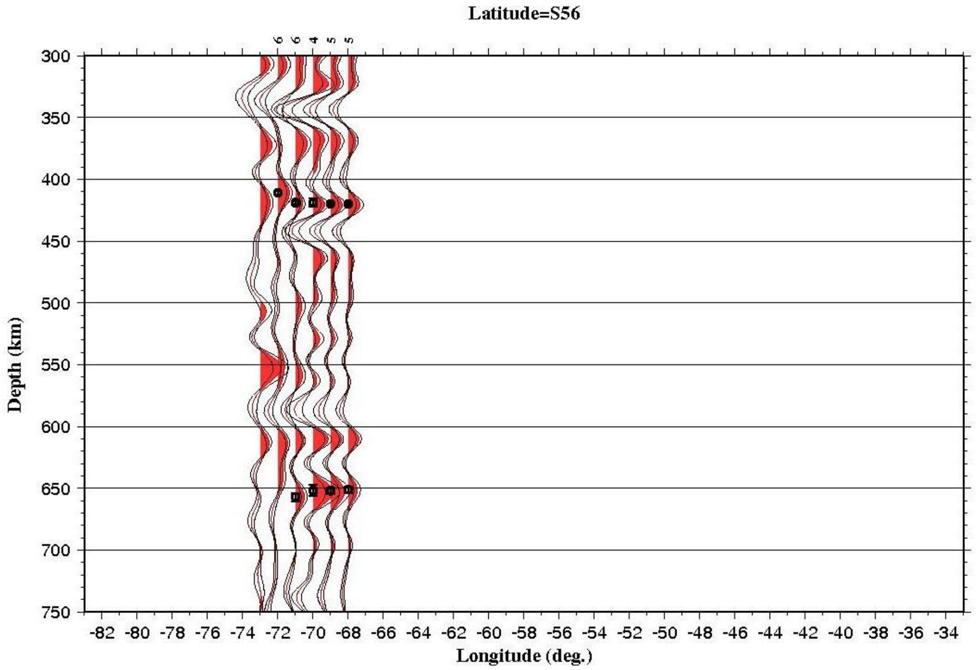
Latitude=S56

Figure 1. E-W MTZ Cross sections. Cont.

APPENDIX C

N-S MTZ CROSS SECTIONS

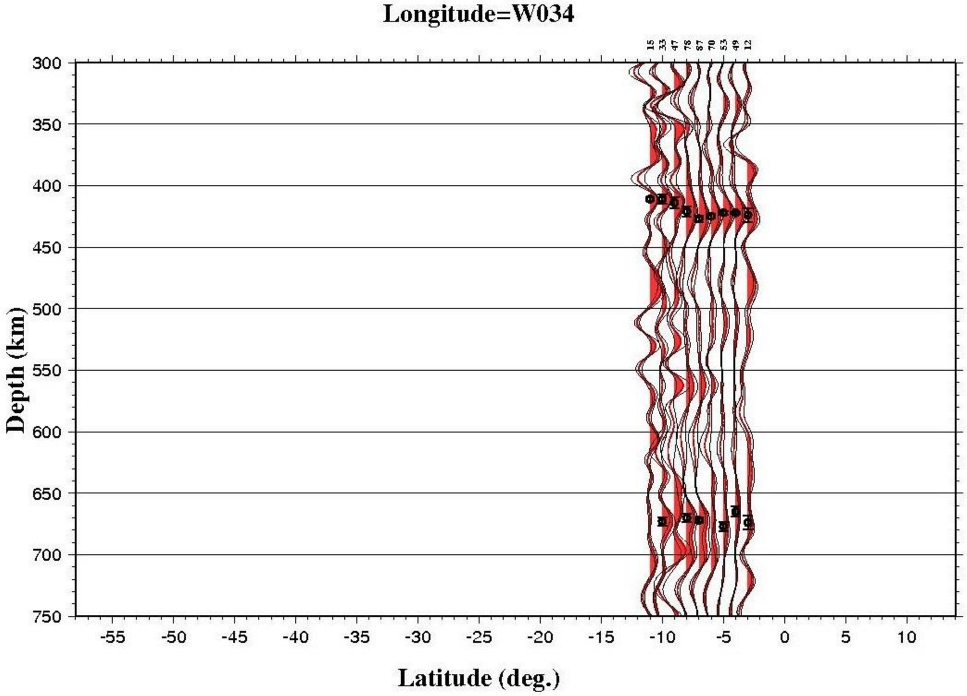

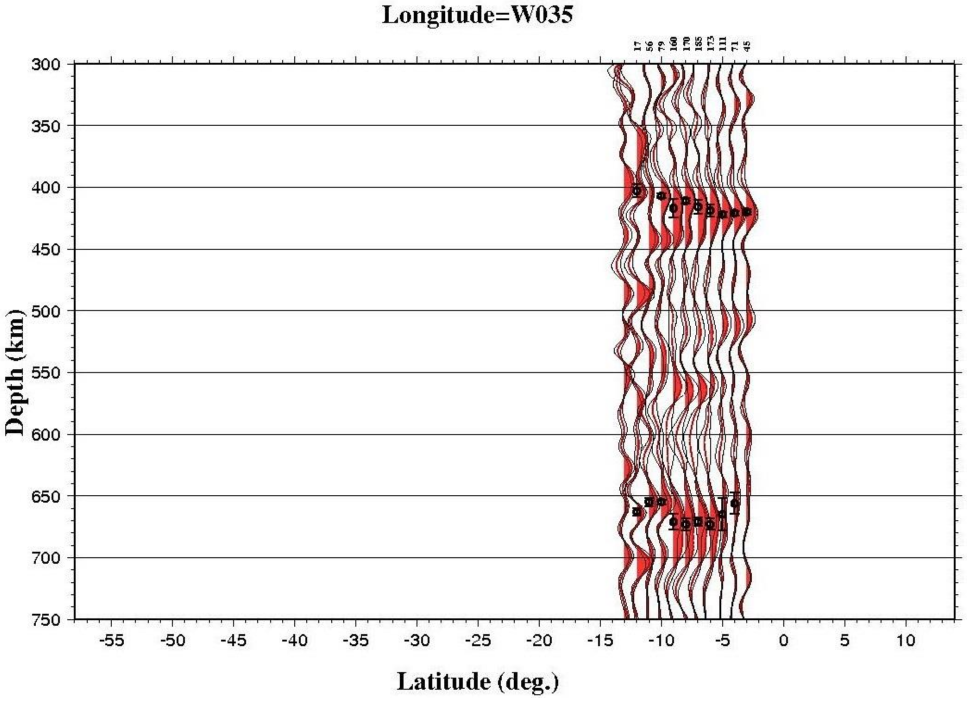

Figure 1. N-S MTZ Cross sections. Black circles are the interpreted discontinuities peaks with uncertainty bars, blue lines are slab contours and green (Magnitude<6) and yellow (Magnitude≥6) dots are earthquakes. Numbers of RFs in each stacked trace are indicated on the top of it.

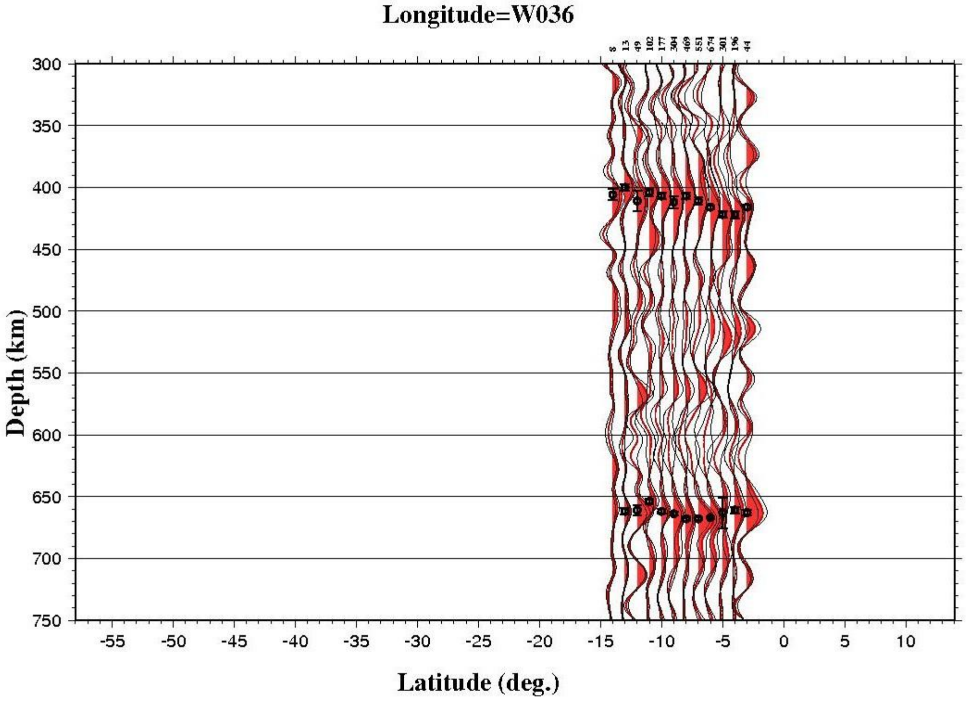

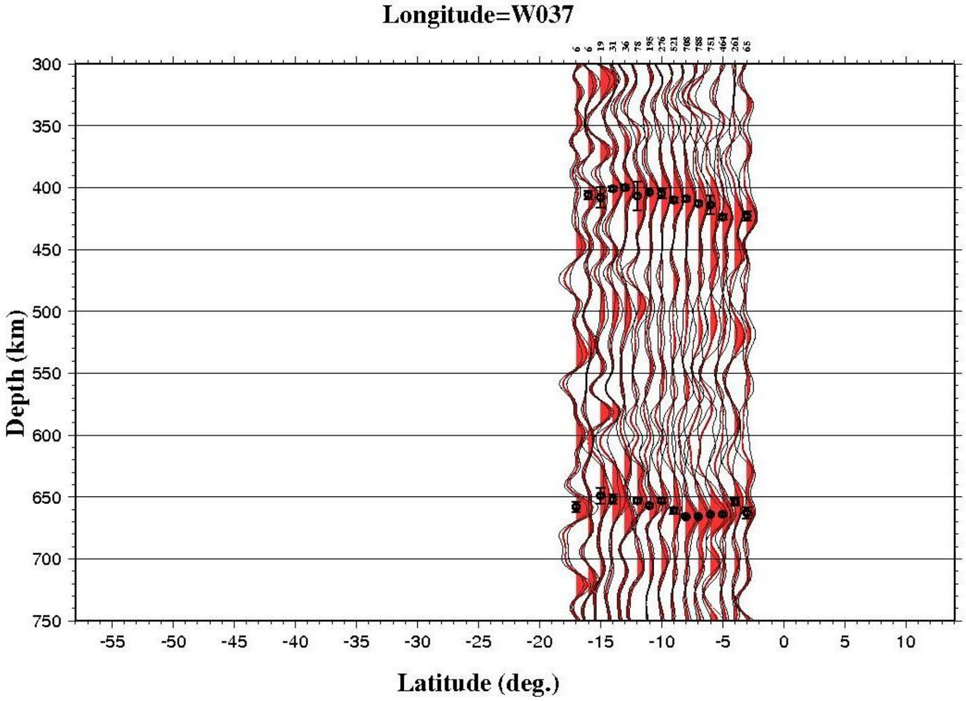

Figure 1. N-S MTZ Cross sections. Cont.

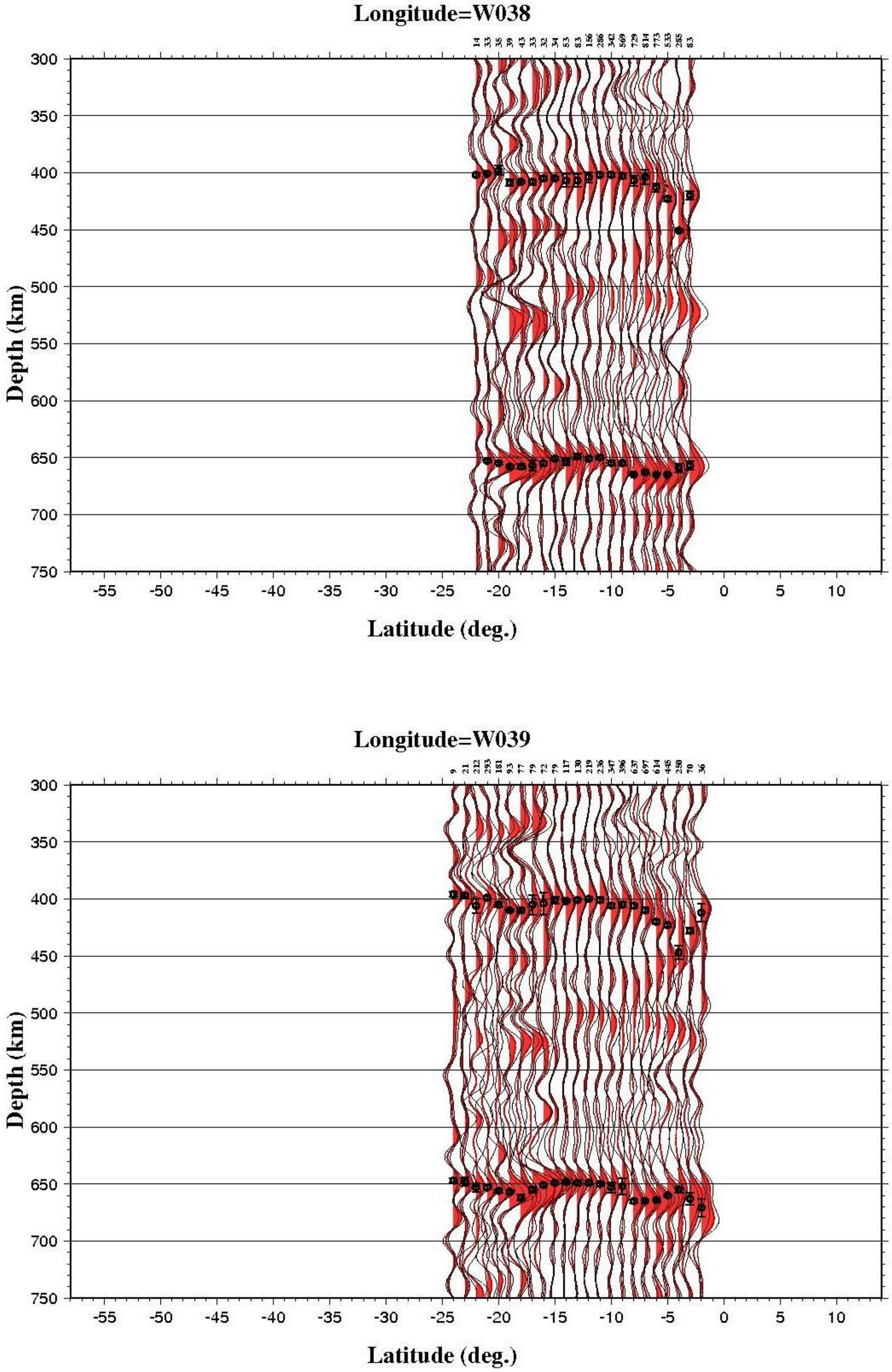

Figure 1. N-S MTZ Cross sections. Cont.

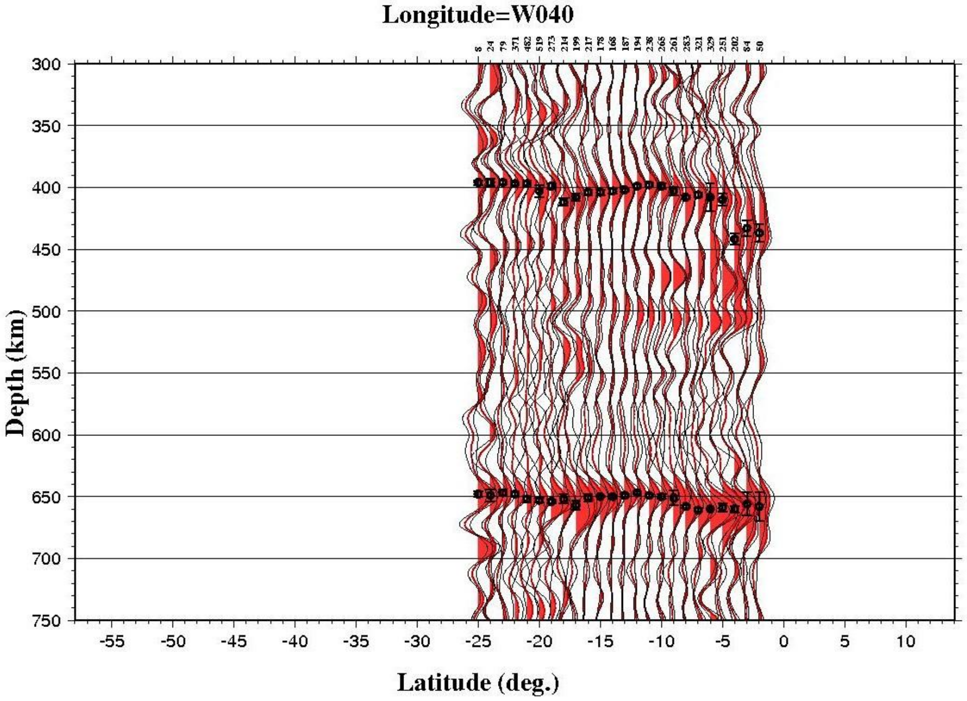

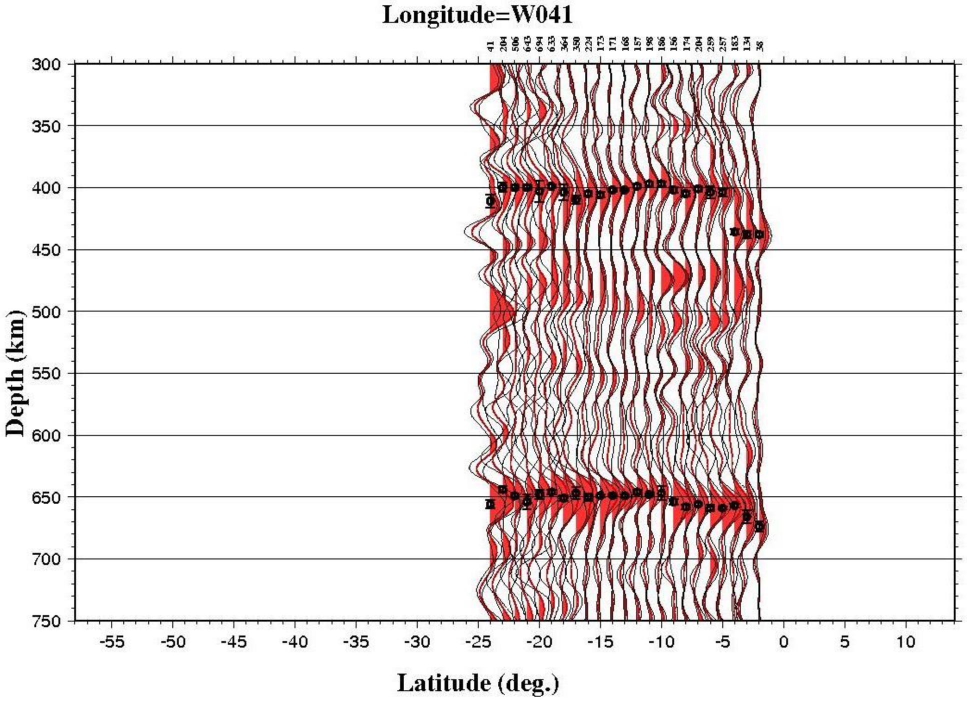

Figure 1. N-S MTZ Cross sections. Cont.

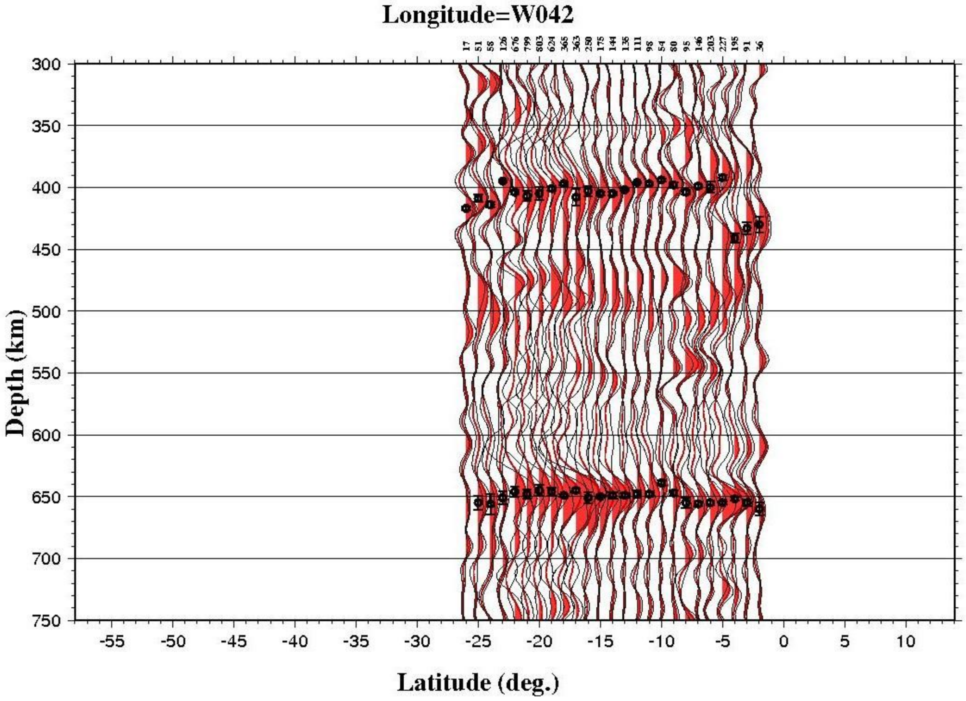

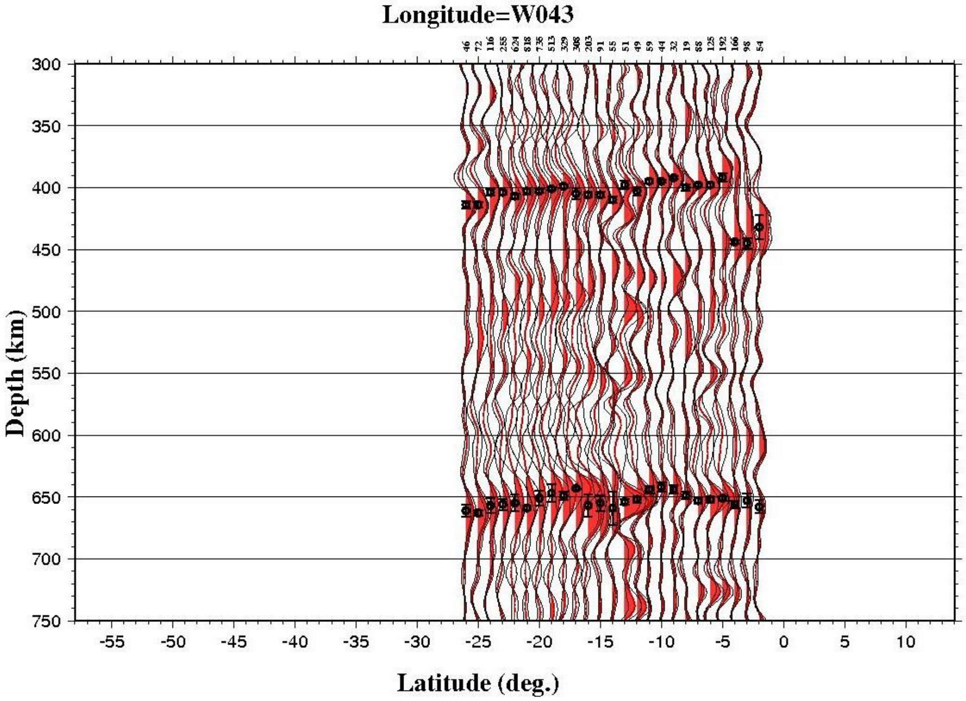

Figure 1. N-S MTZ Cross sections. Cont.

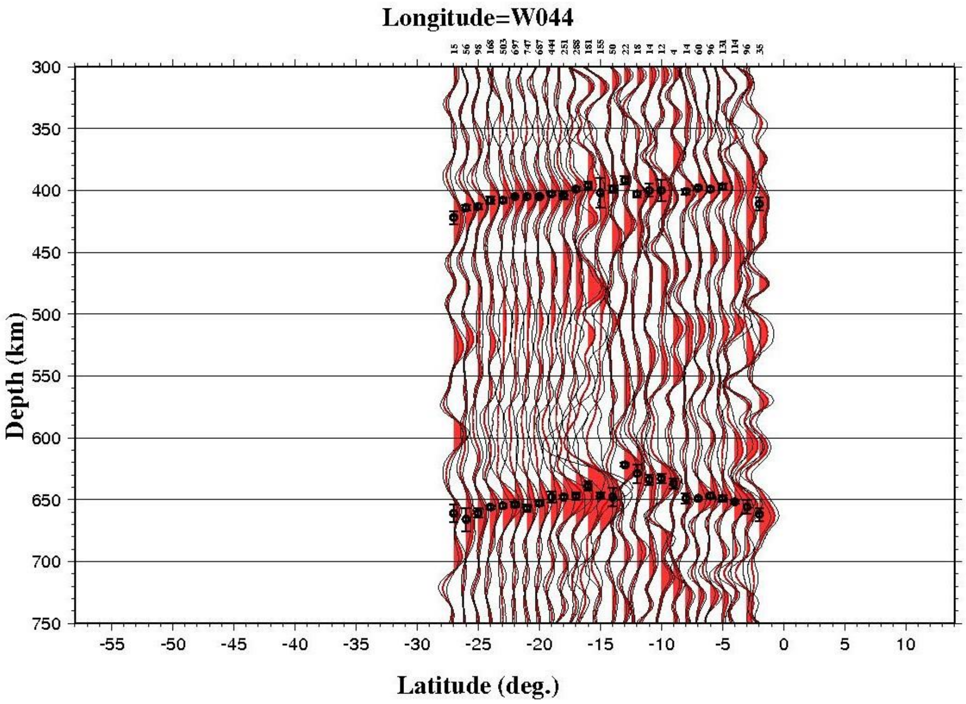
Longitude=W044

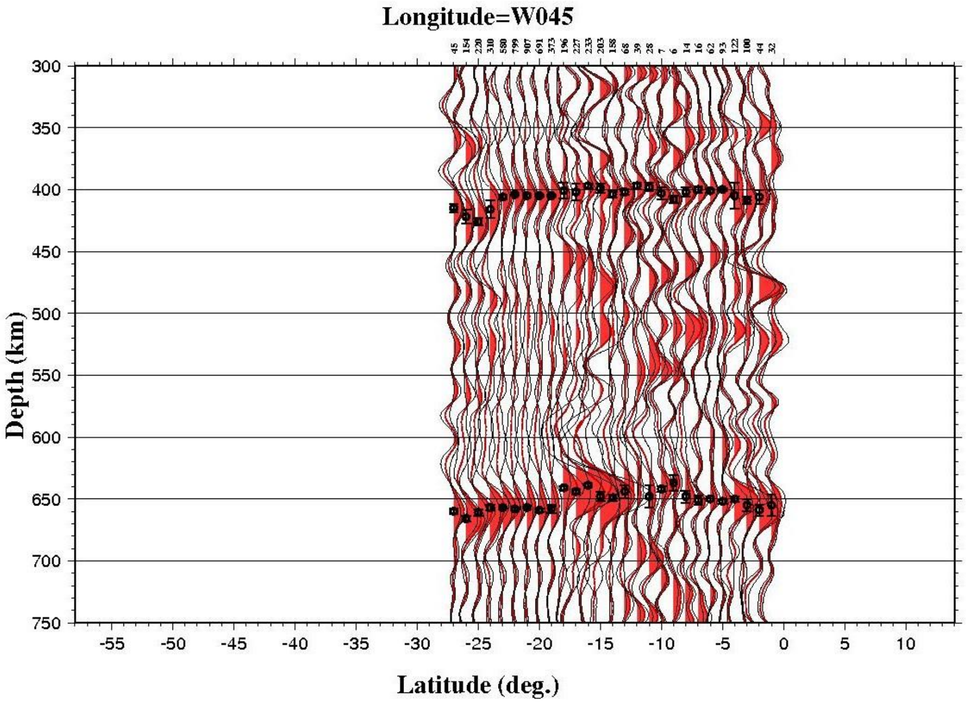
Longitude=W045

Figure 1. N-S MTZ Cross sections. Cont.

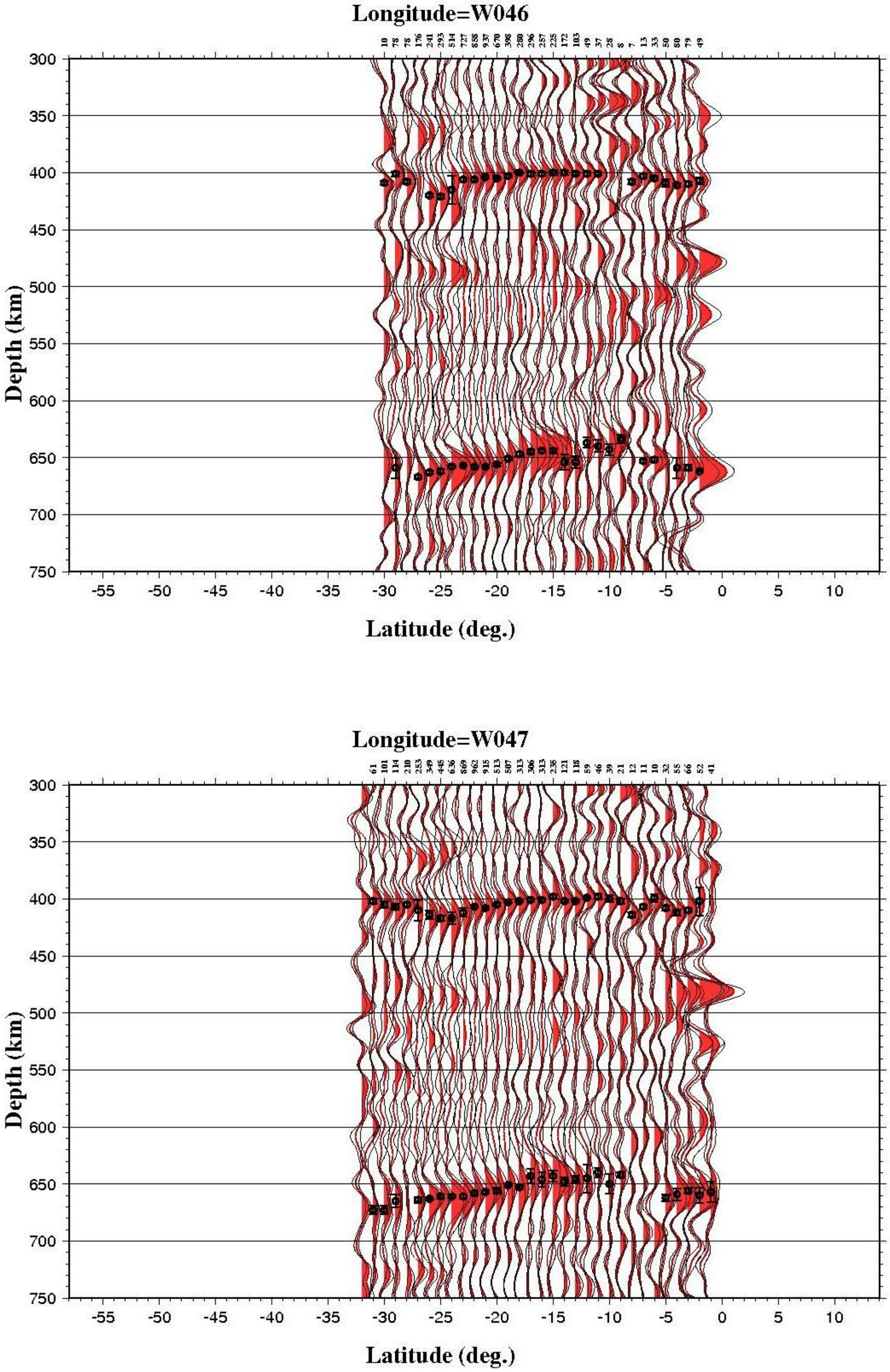

Figure 1. N-S MTZ Cross sections. Cont.

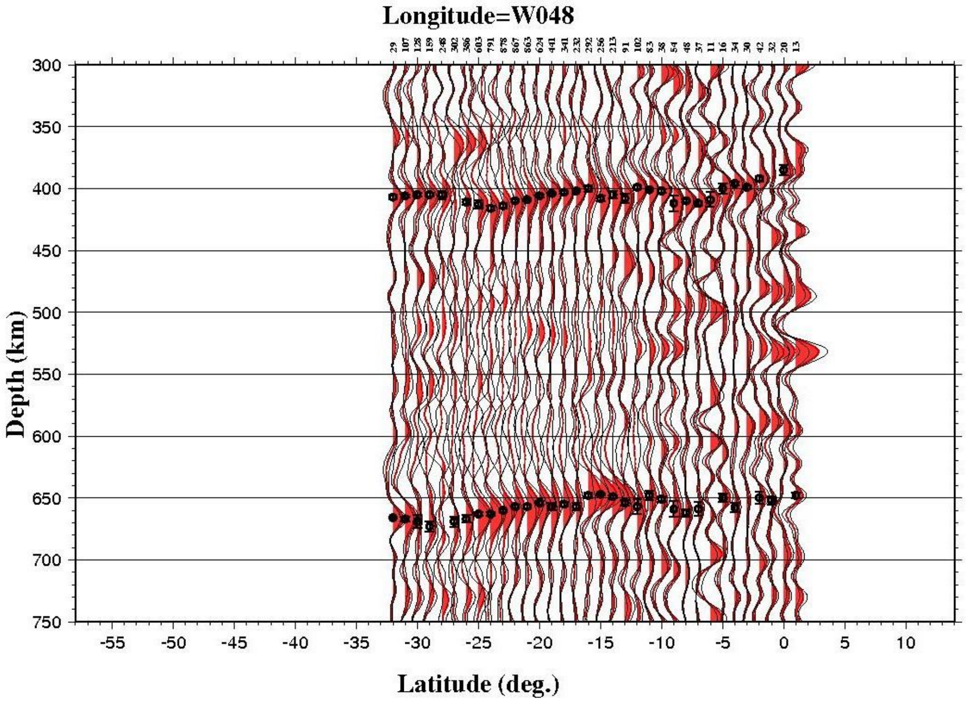

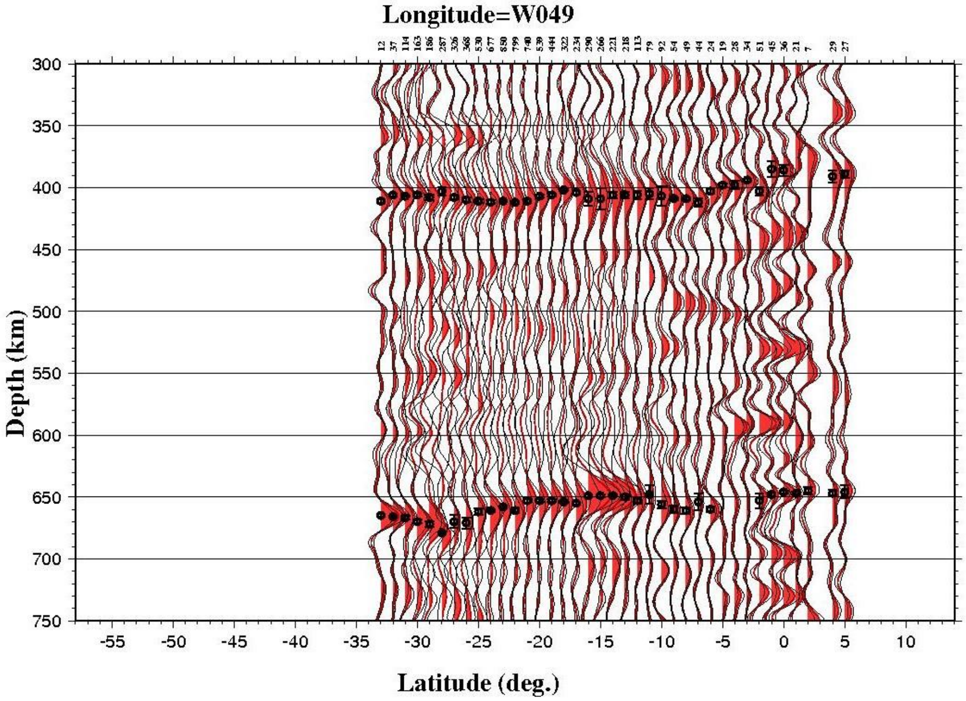

Figure 1. N-S MTZ Cross sections. Cont.

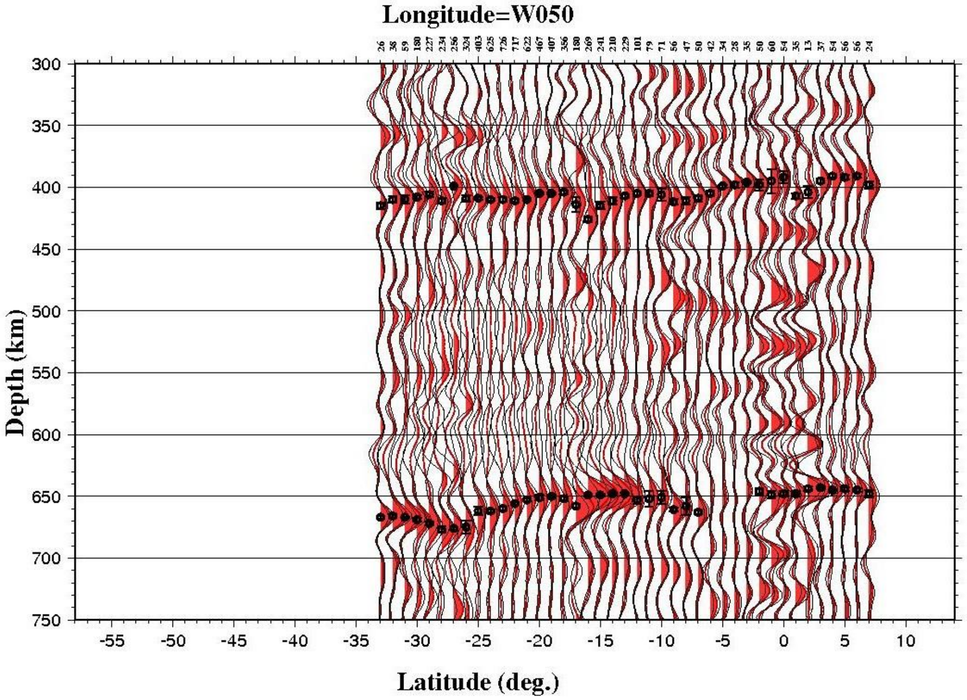

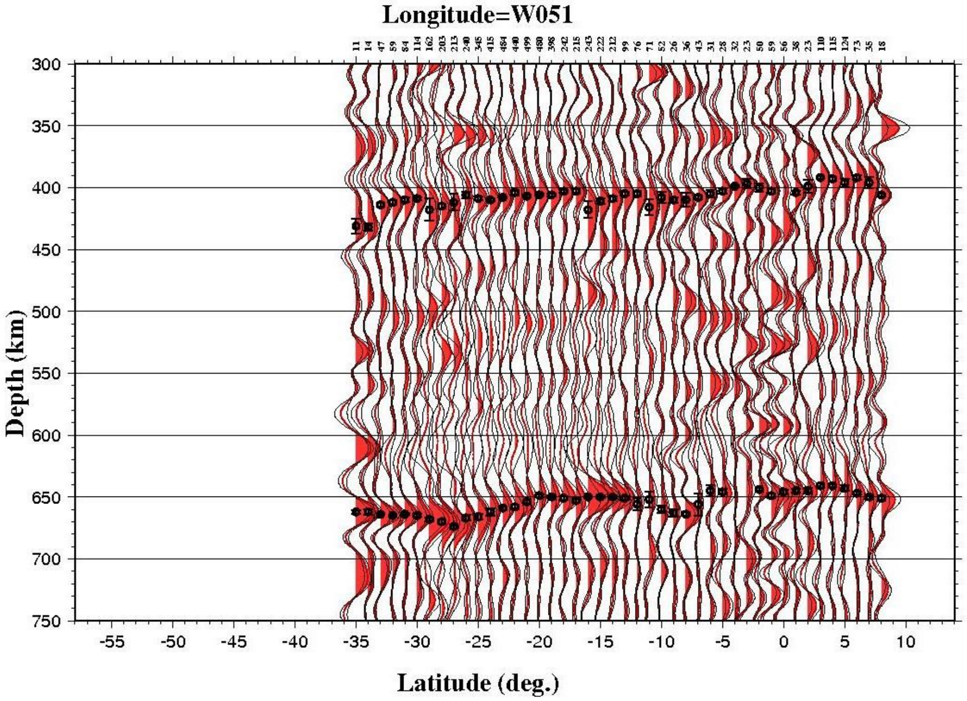

Figure 1. N-S MTZ Cross sections. Cont.

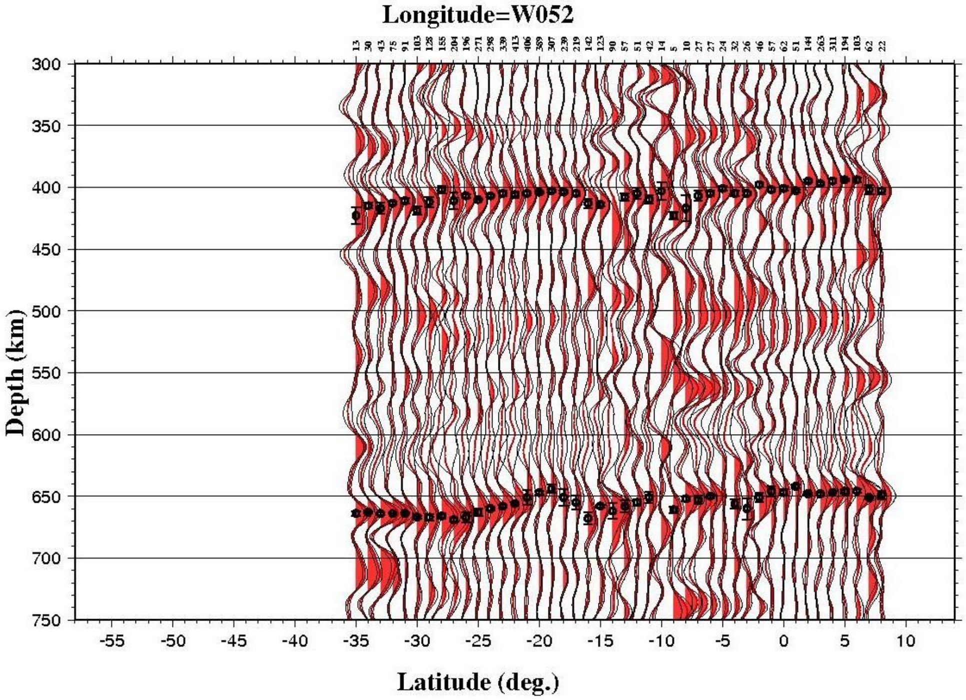

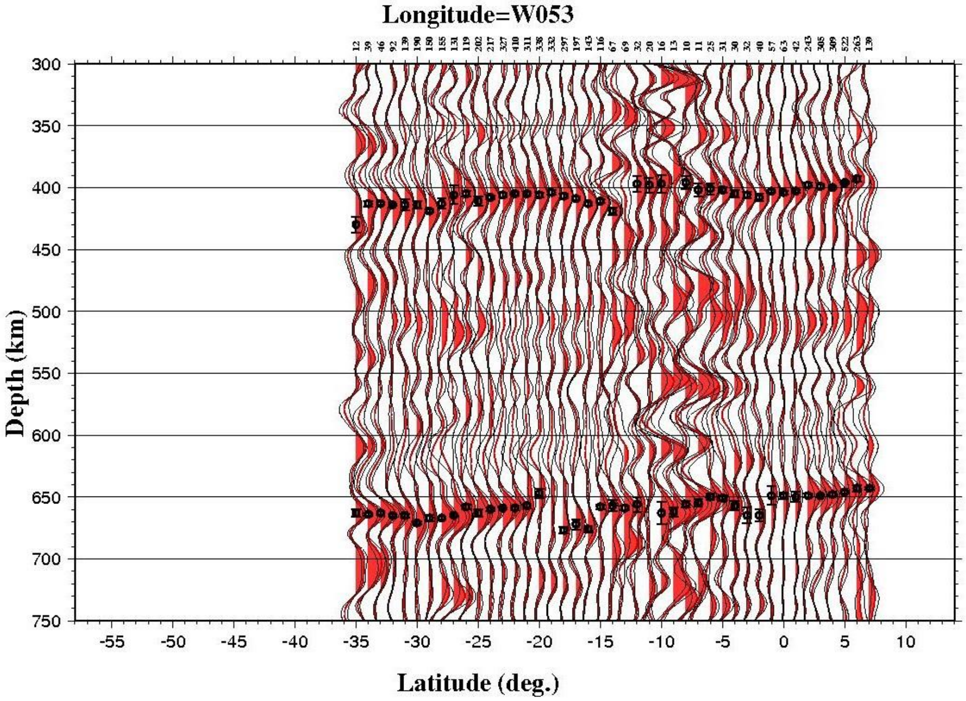

Figure 1. N-S MTZ Cross sections. Cont.

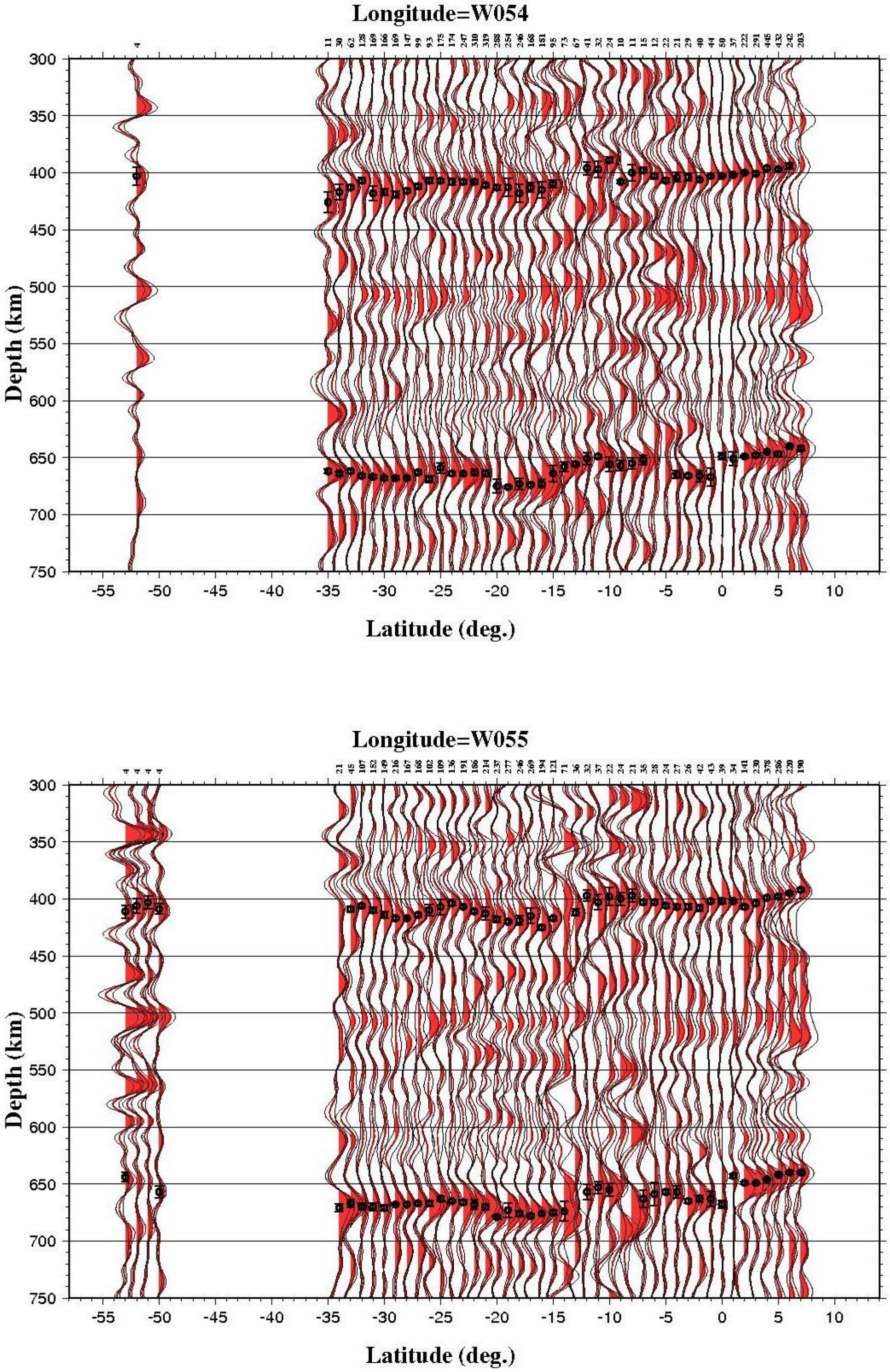

Figure 1. N-S MTZ Cross sections. Cont.

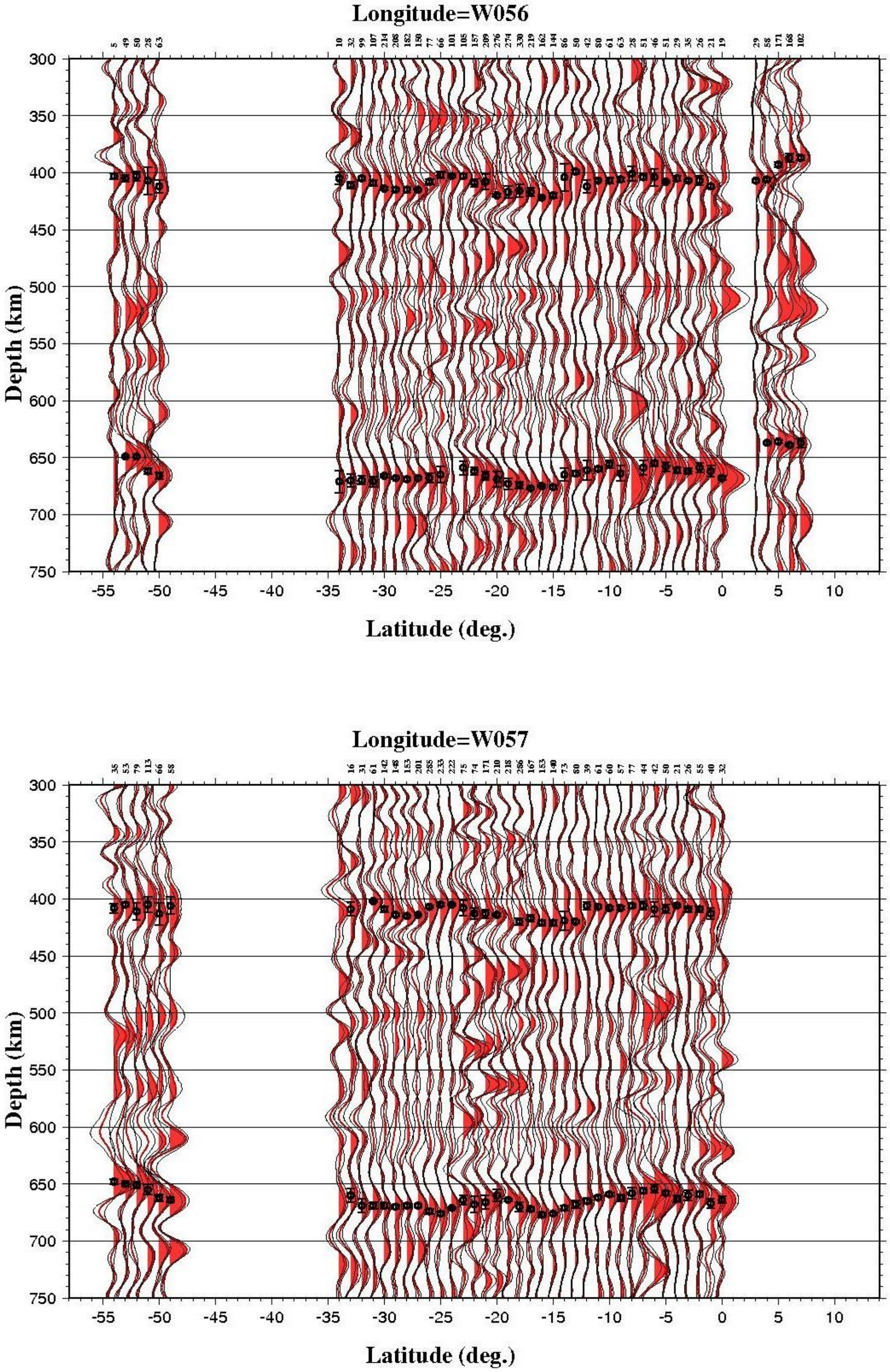

Figure 1. N-S MTZ Cross sections. Cont.

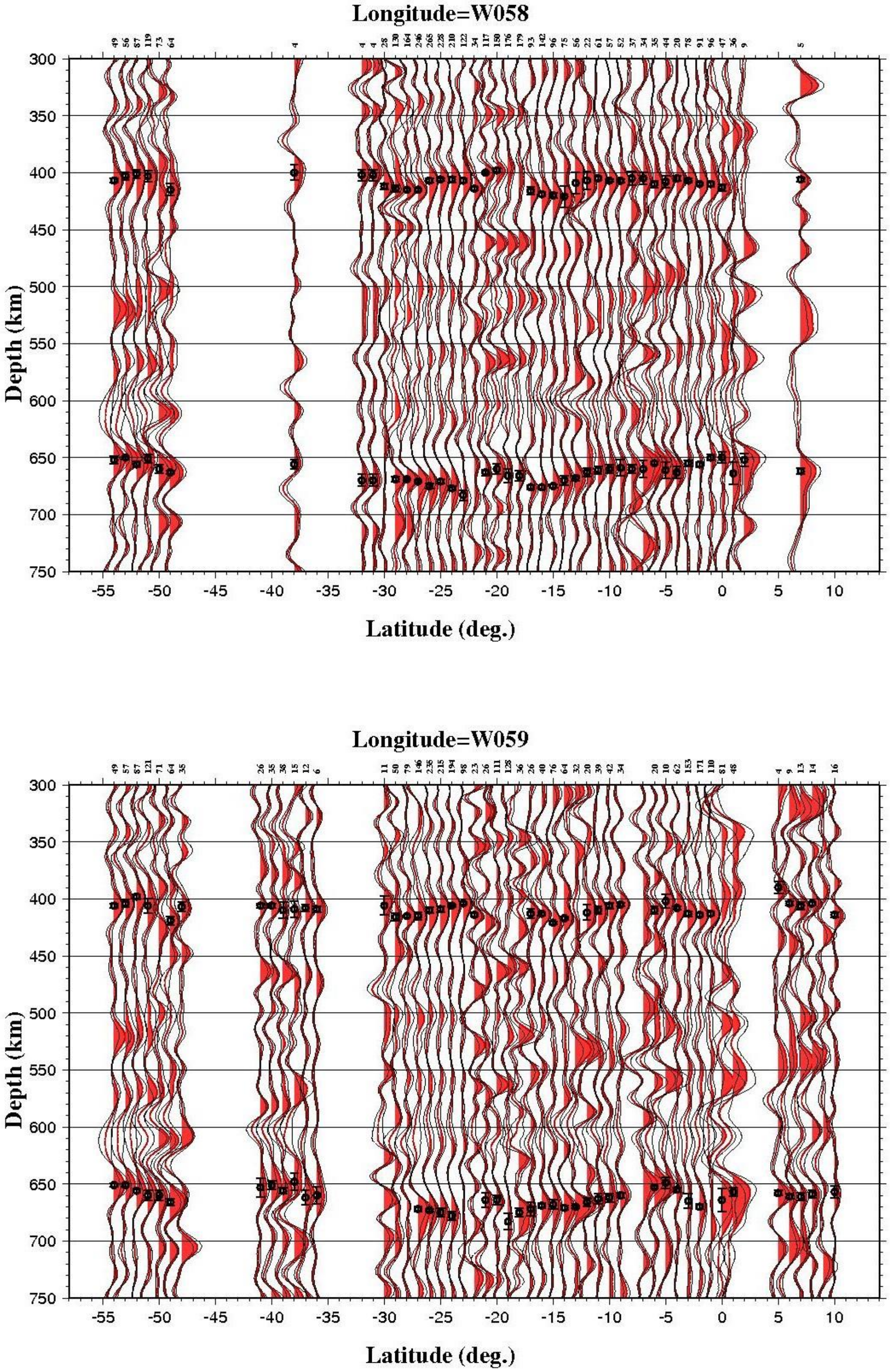

Figure 1. N-S MTZ Cross sections. Cont.

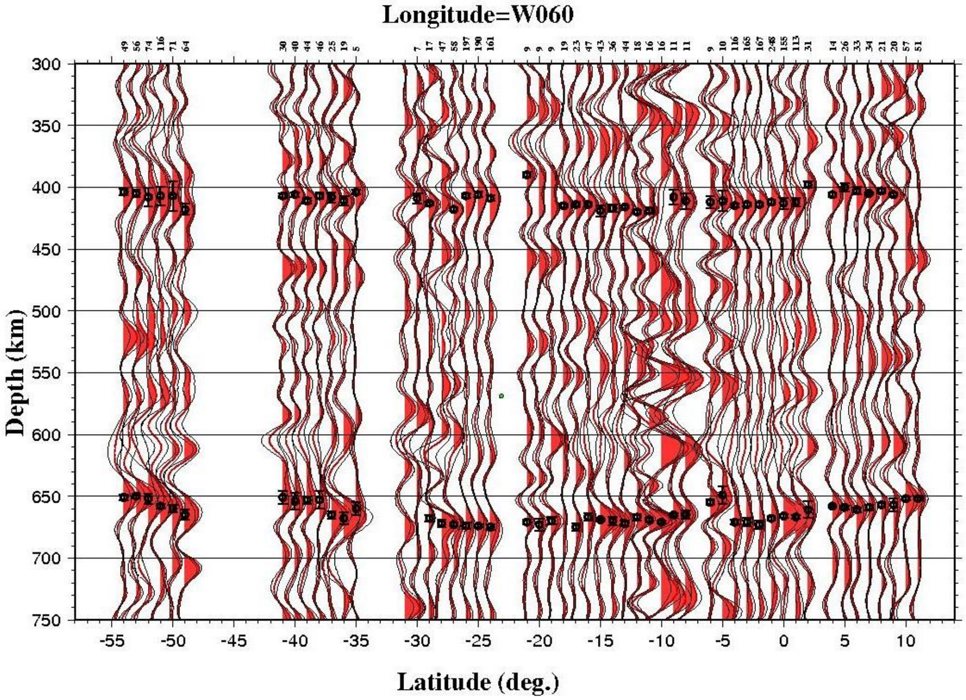

Longitude=W060

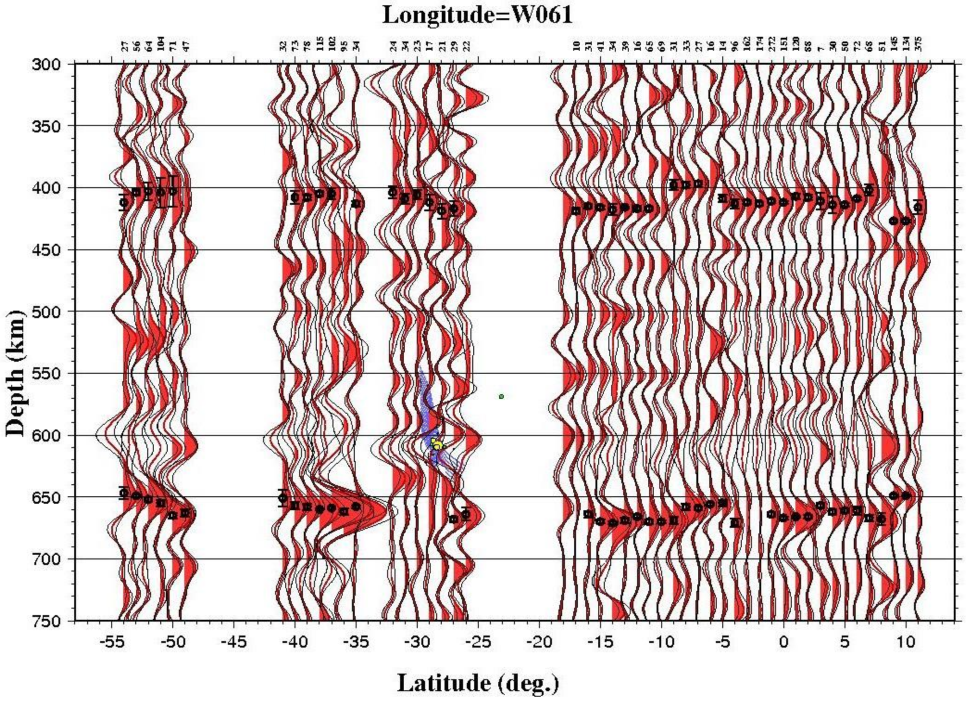

Longitude=W061

Figure 1. N-S MTZ Cross sections. Cont.

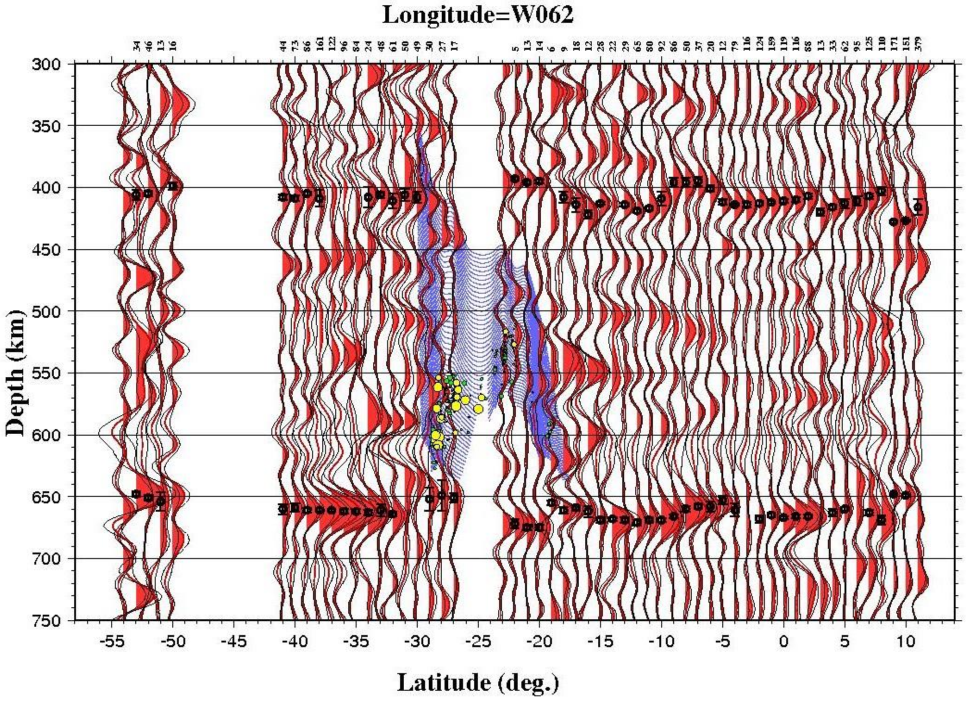

Longitude=W062

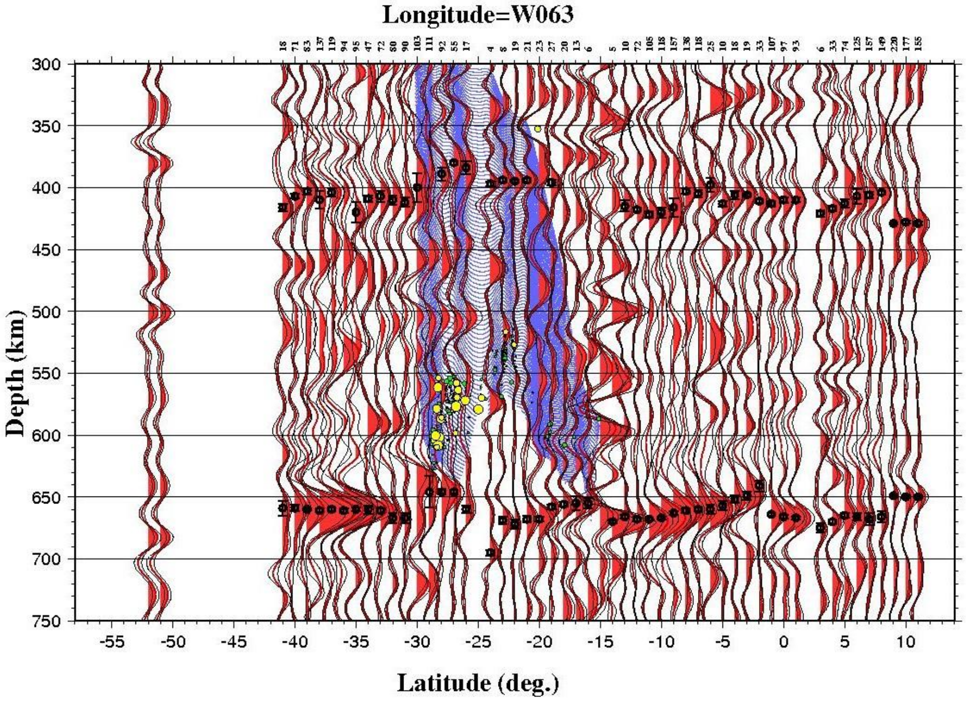

Longitude=W063

Figure 1. N-S MTZ Cross sections. Cont.

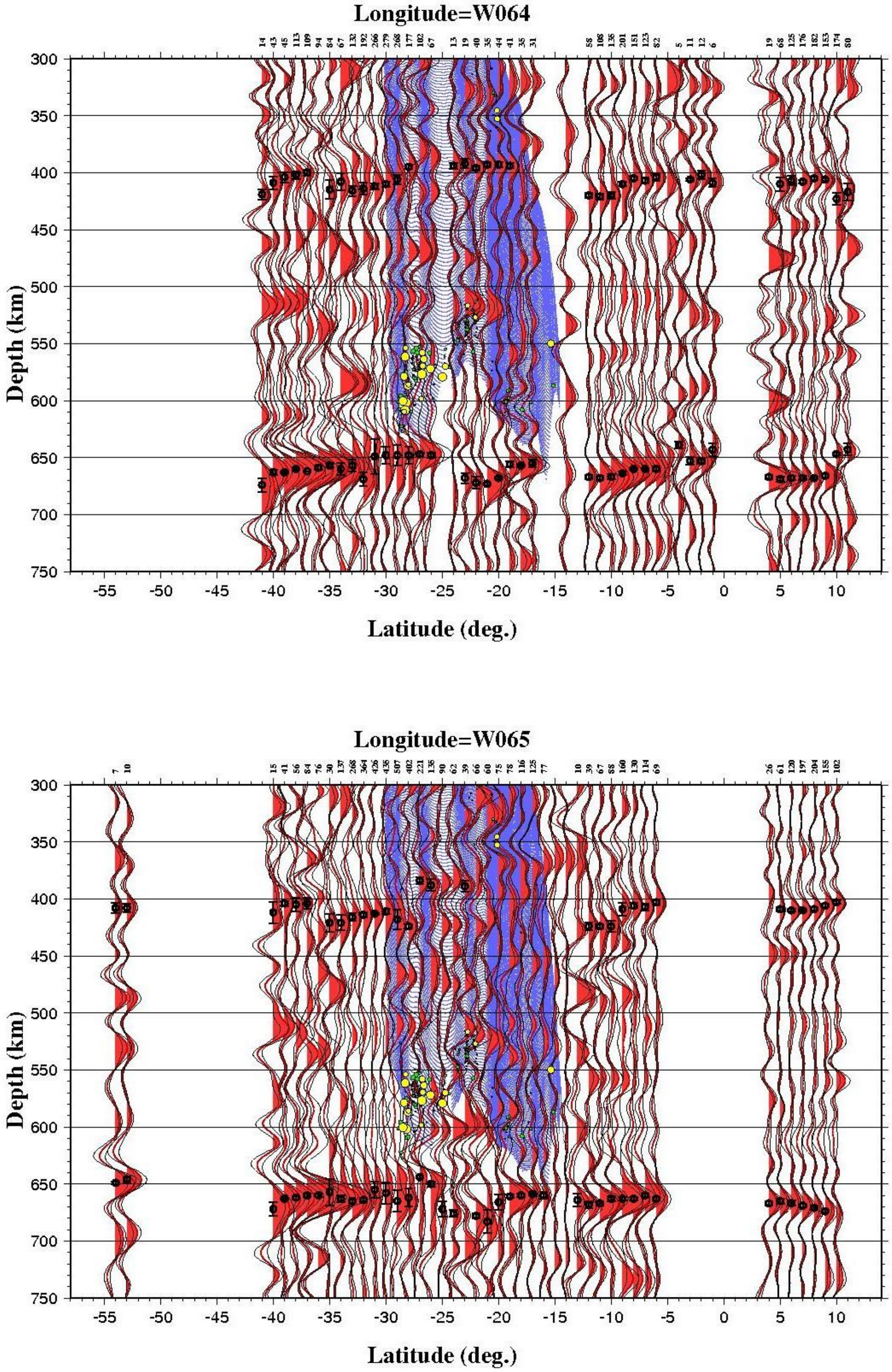

Figure 1. N-S MTZ Cross sections. Cont.

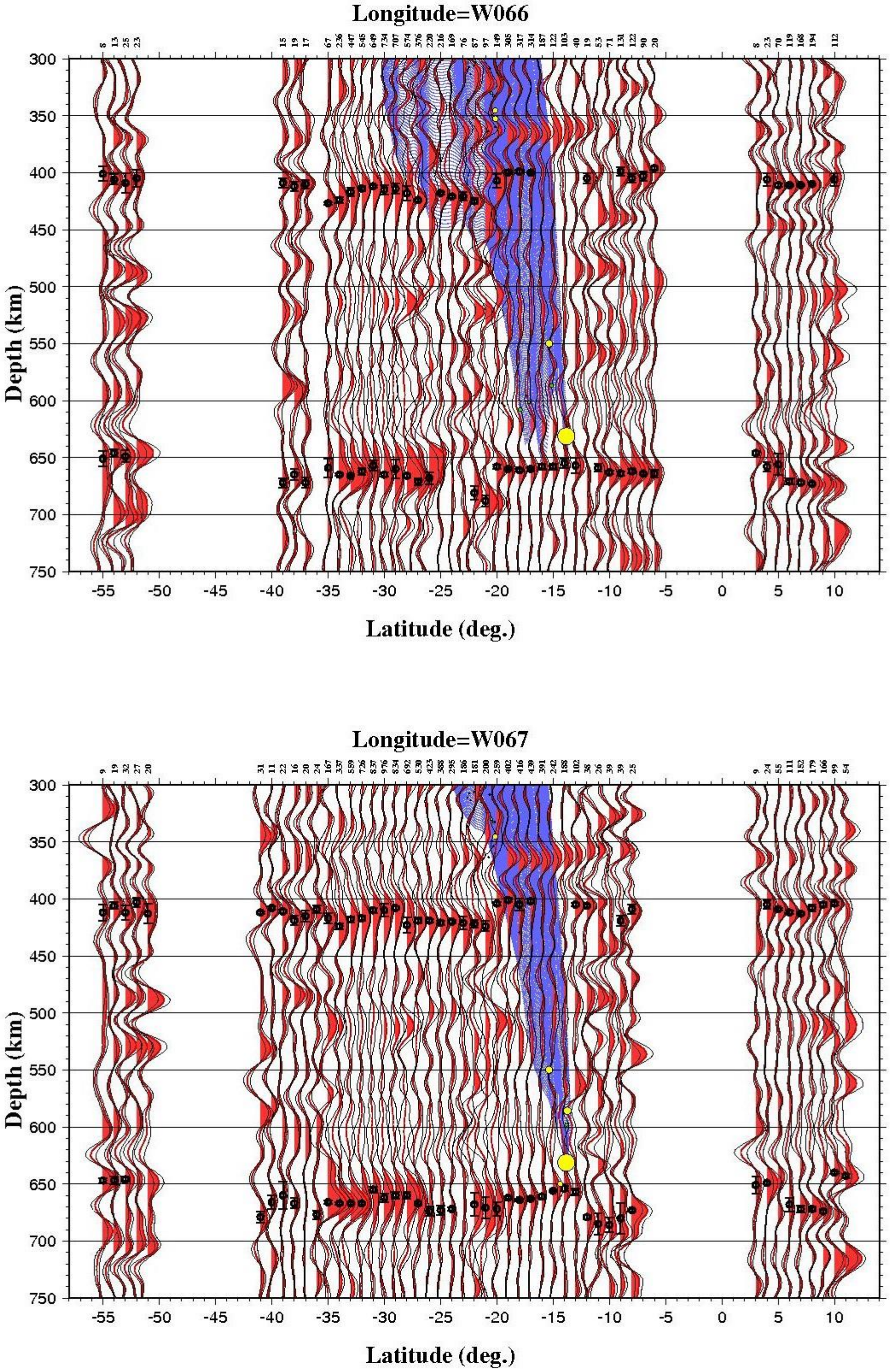

Figure 1. N-S MTZ Cross sections. Cont.

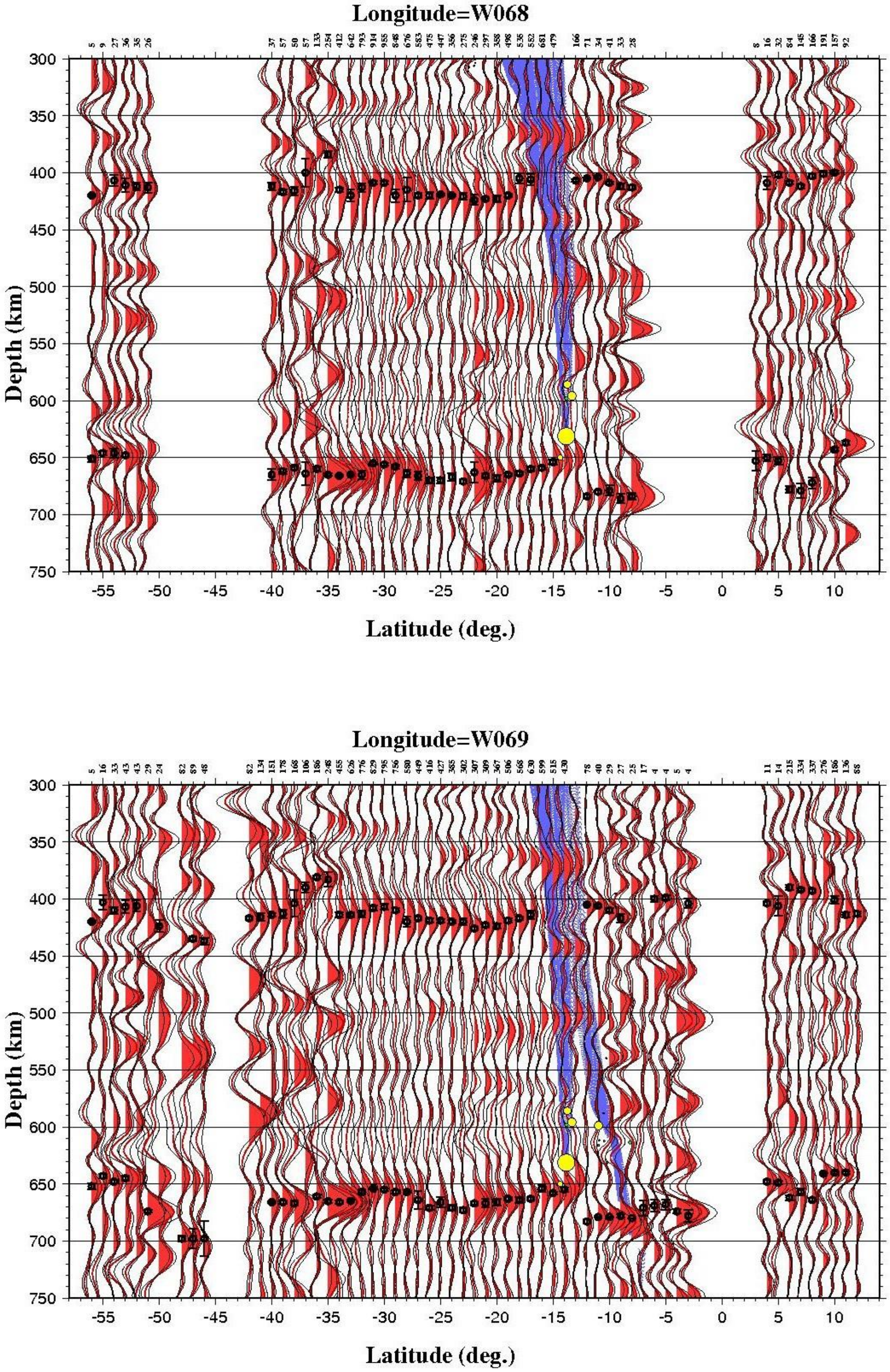

Figure 1. N-S MTZ Cross sections. Cont.

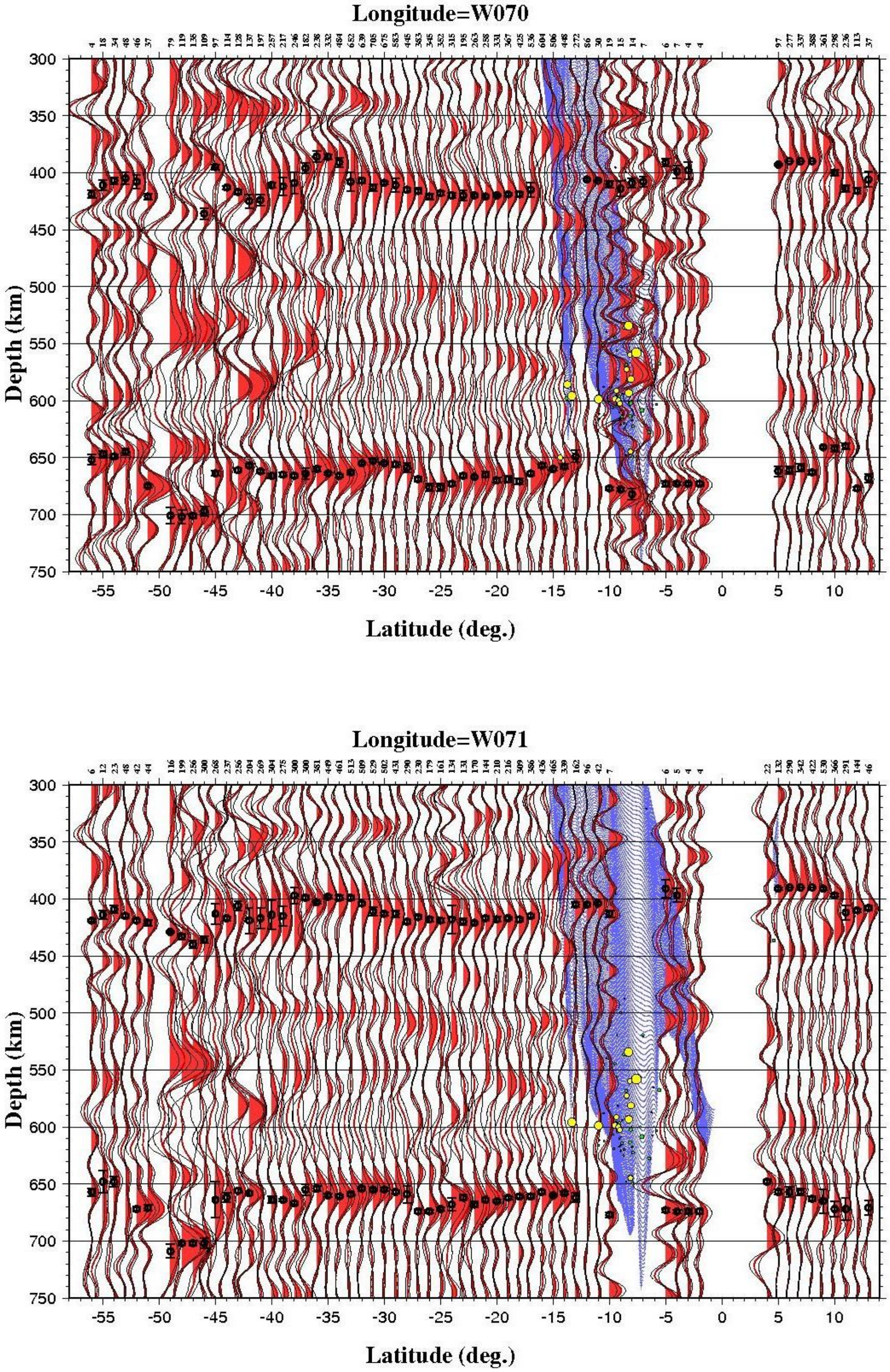

Figure 1. N-S MTZ Cross sections. Cont.

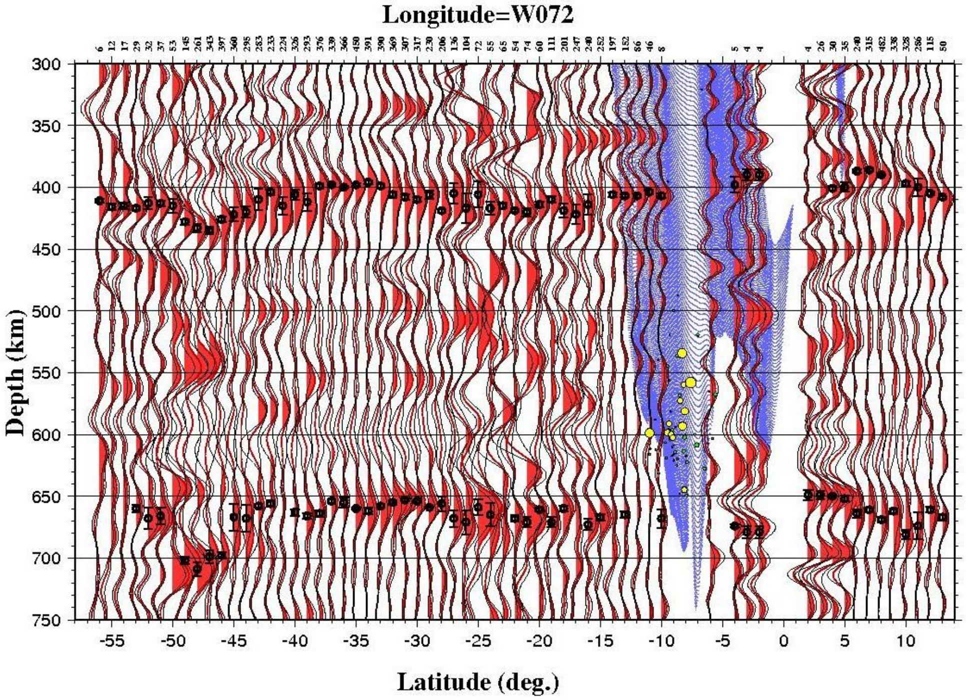

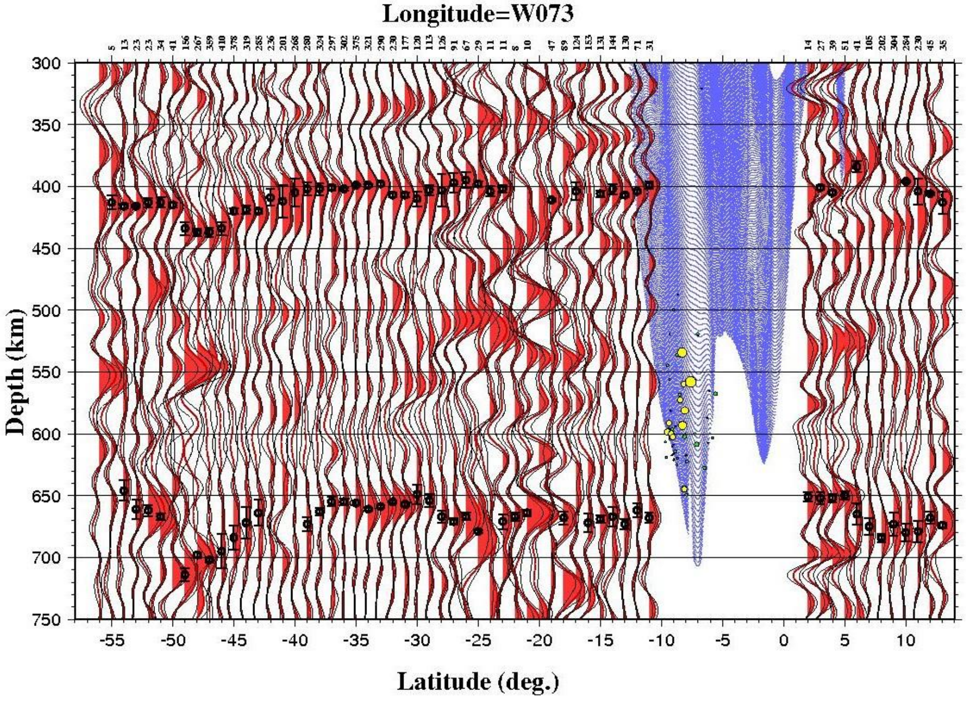

Figure 1. N-S MTZ Cross sections. Cont.

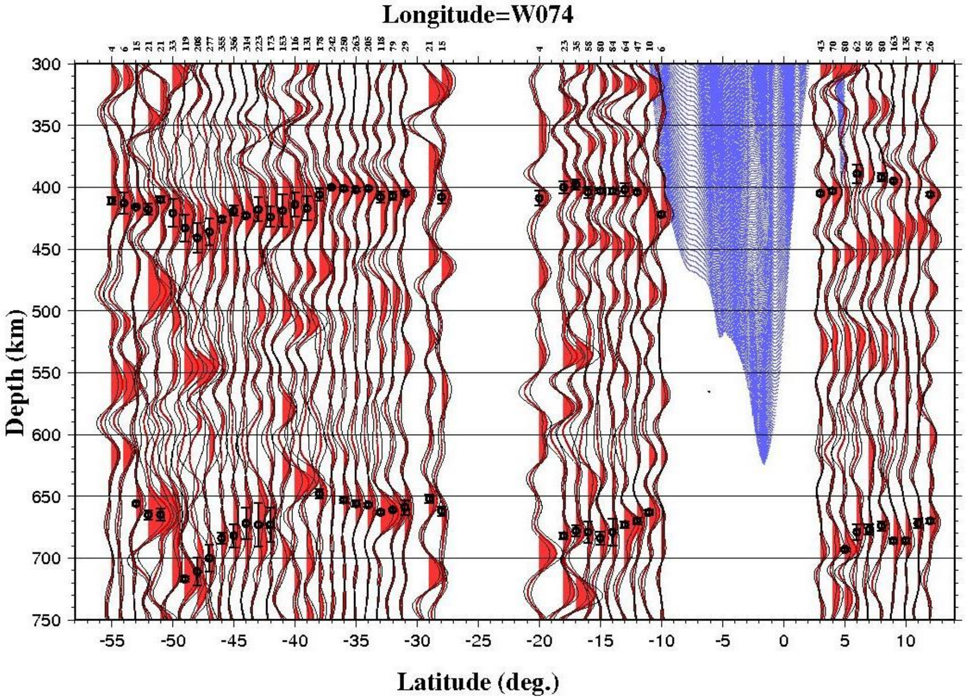

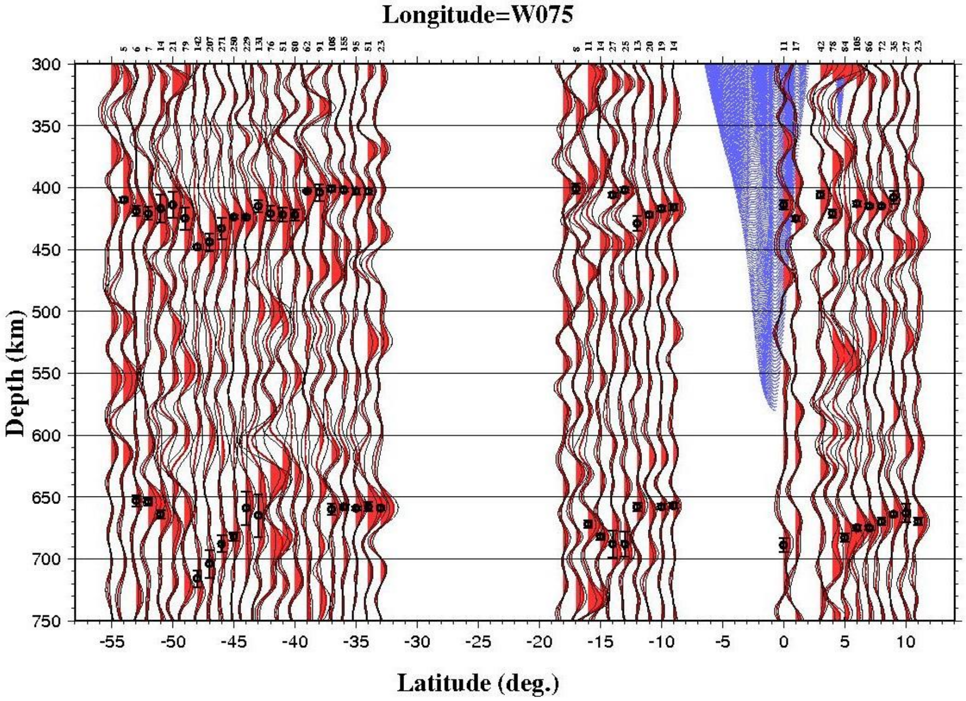

Figure 1. N-S MTZ Cross sections. Cont.

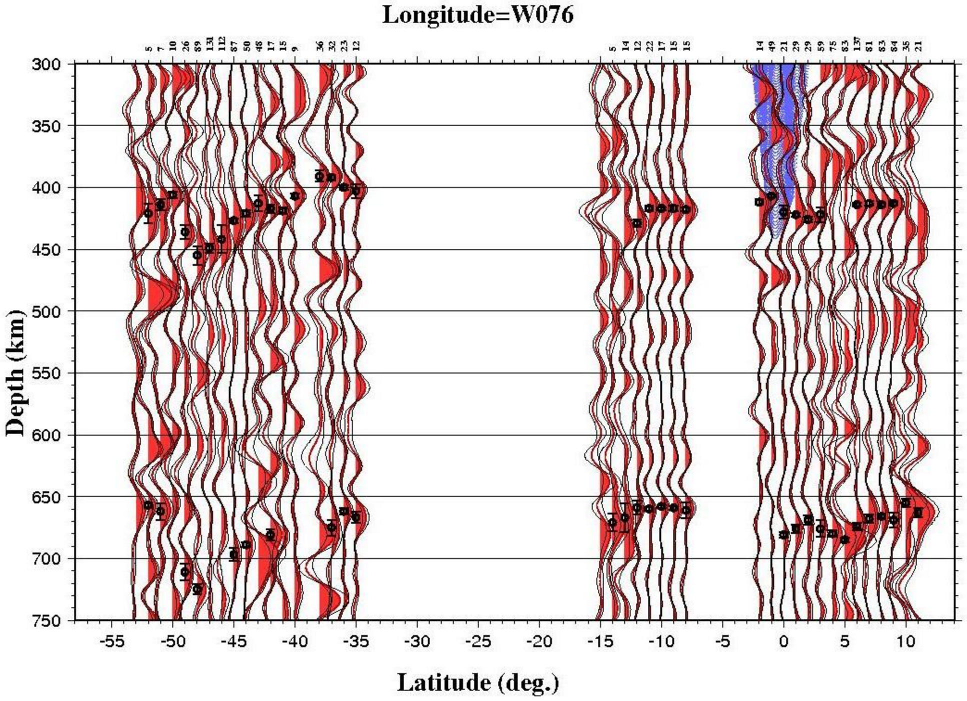

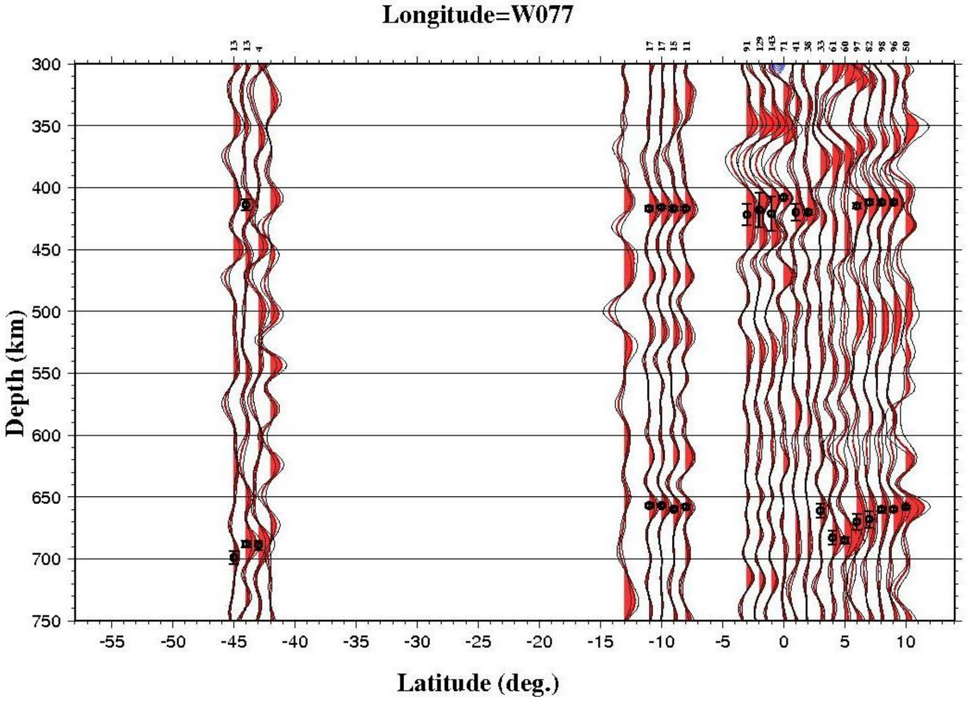

Figure 1. N-S MTZ Cross sections. Cont.

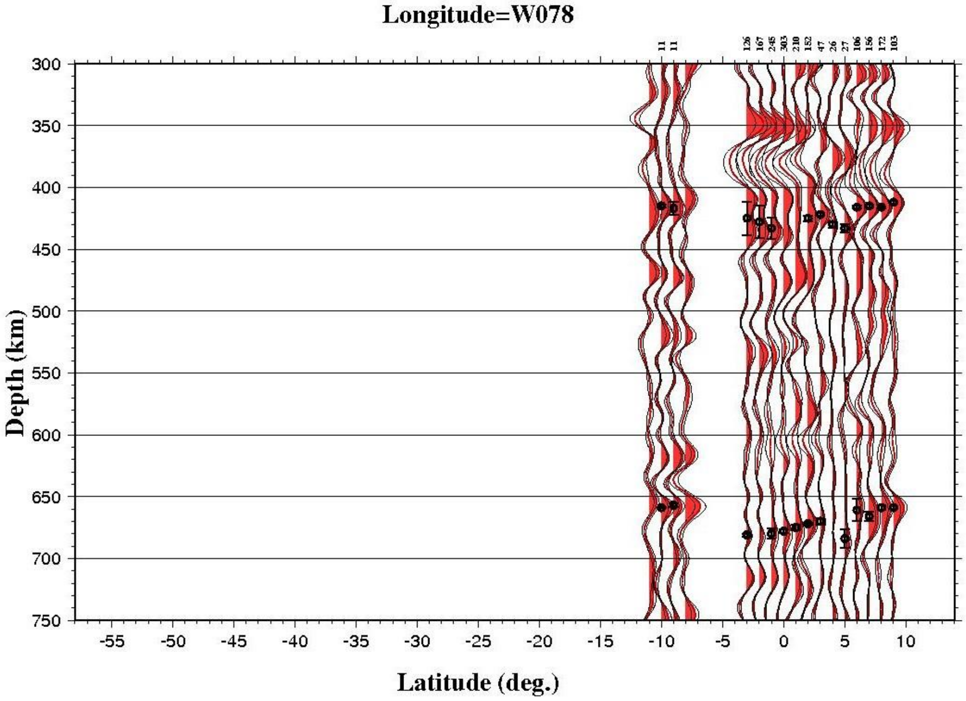

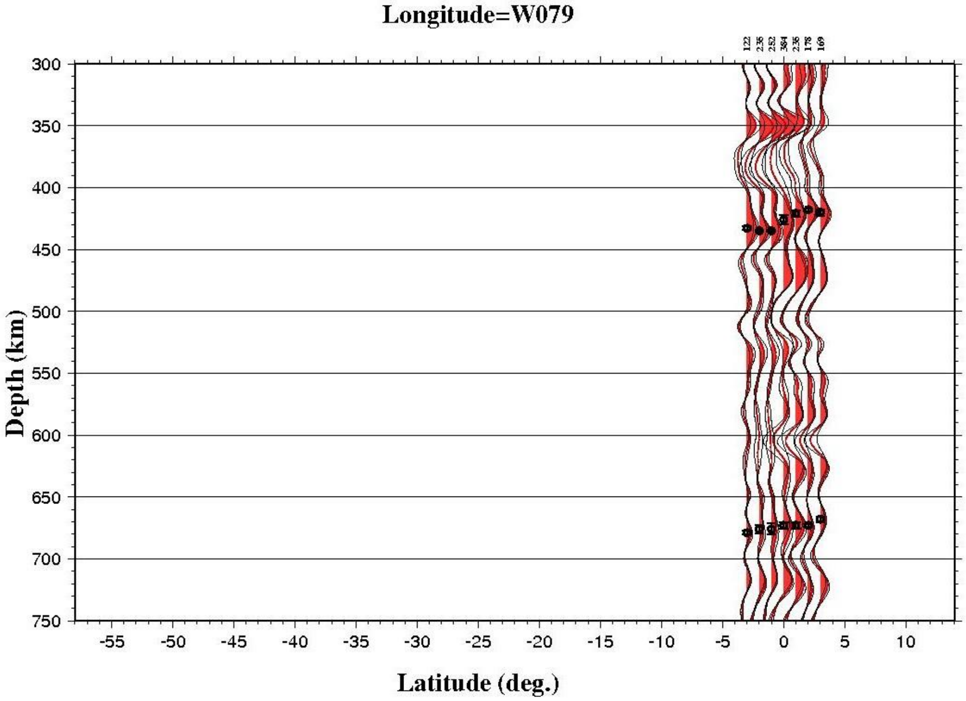

Figure 1. N-S MTZ Cross sections. Cont.

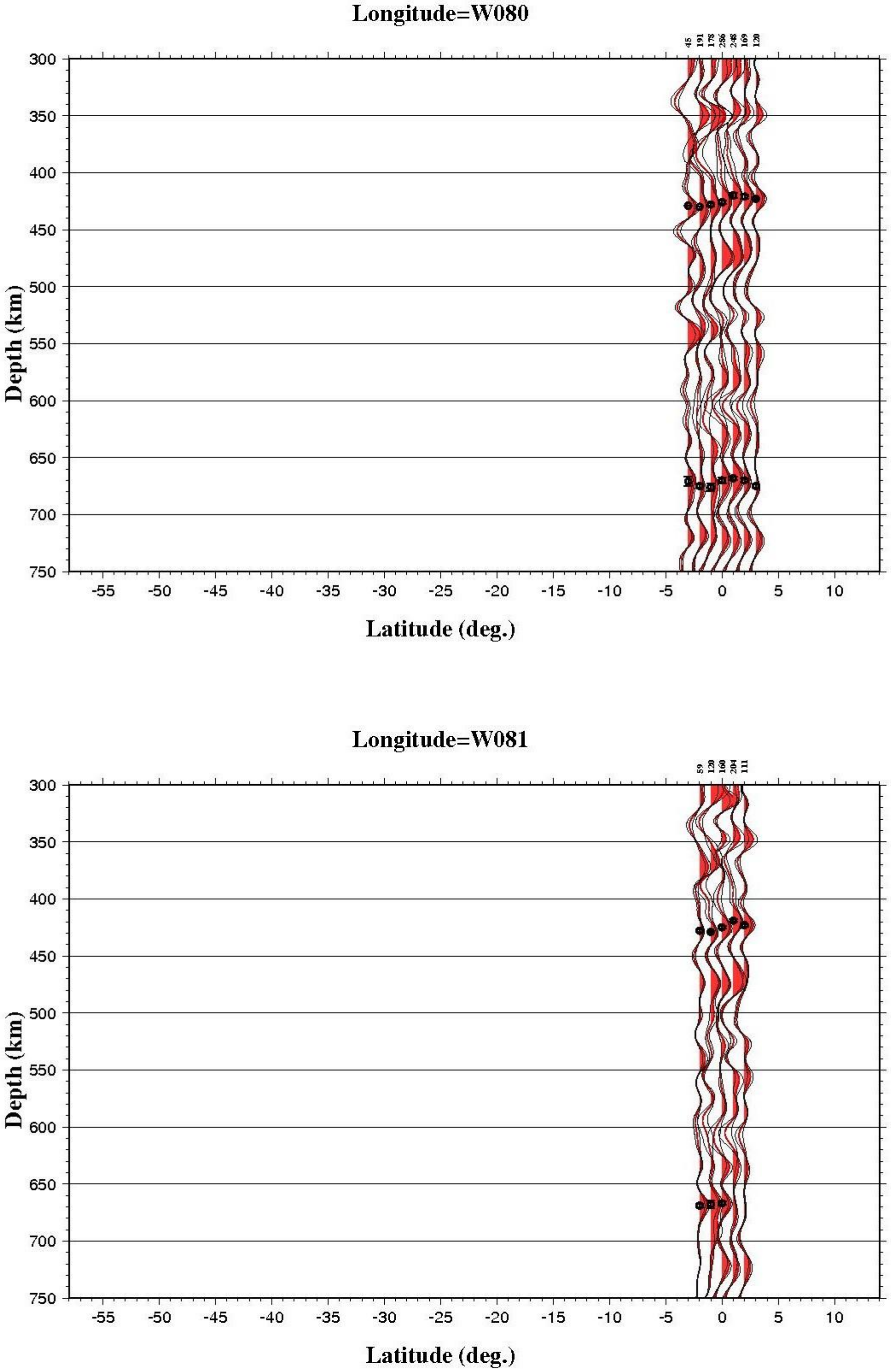

Figure 1. N-S MTZ Cross sections. Cont.

APPENDIX D

TRUE DEPTH MAPS

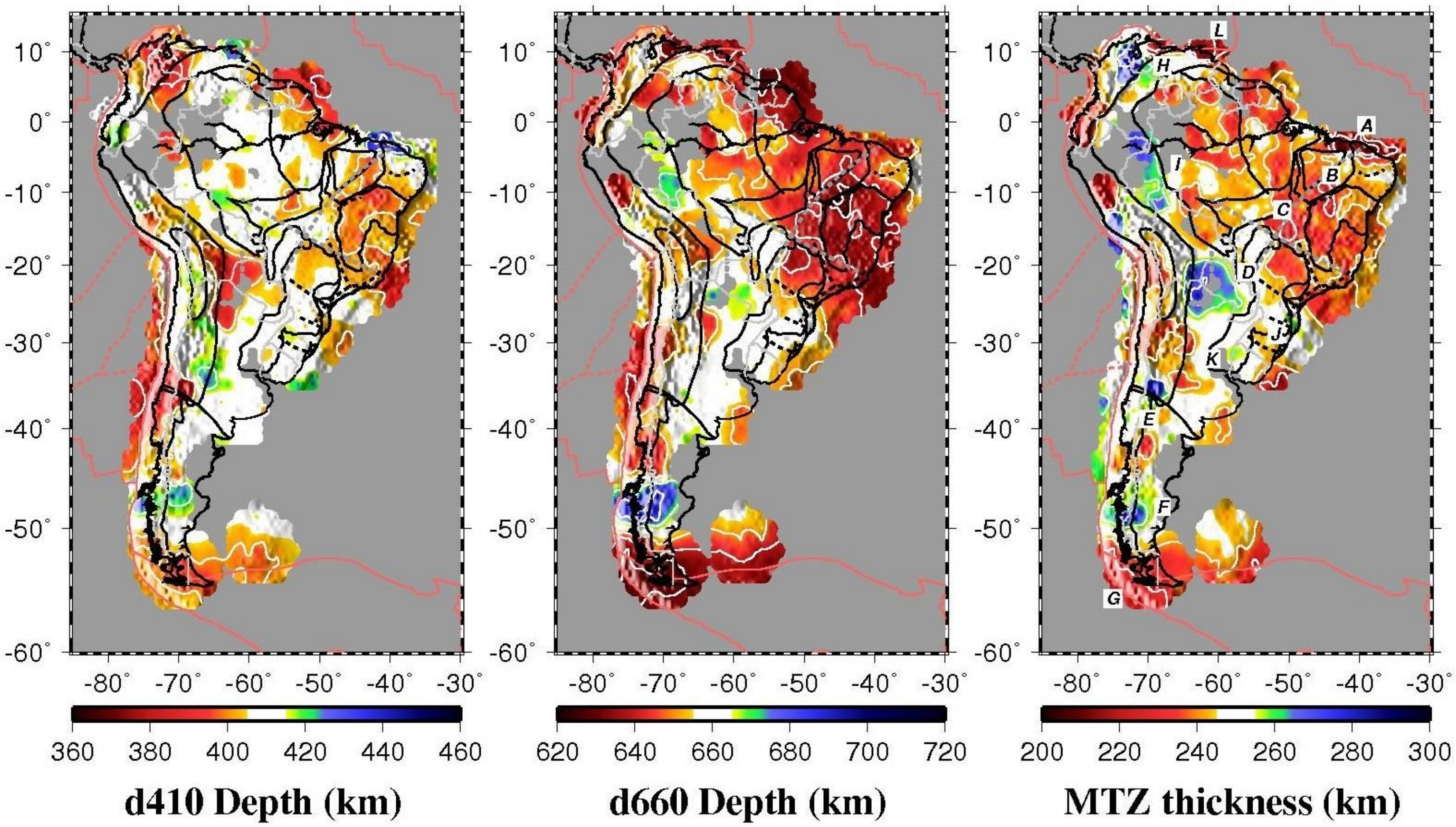

Figure 1. True depth MTZ model using the GyPSuM (Simmons *et al*., 2010) velocity model. Symbols are the as in the Figure 3.1 of the main text.

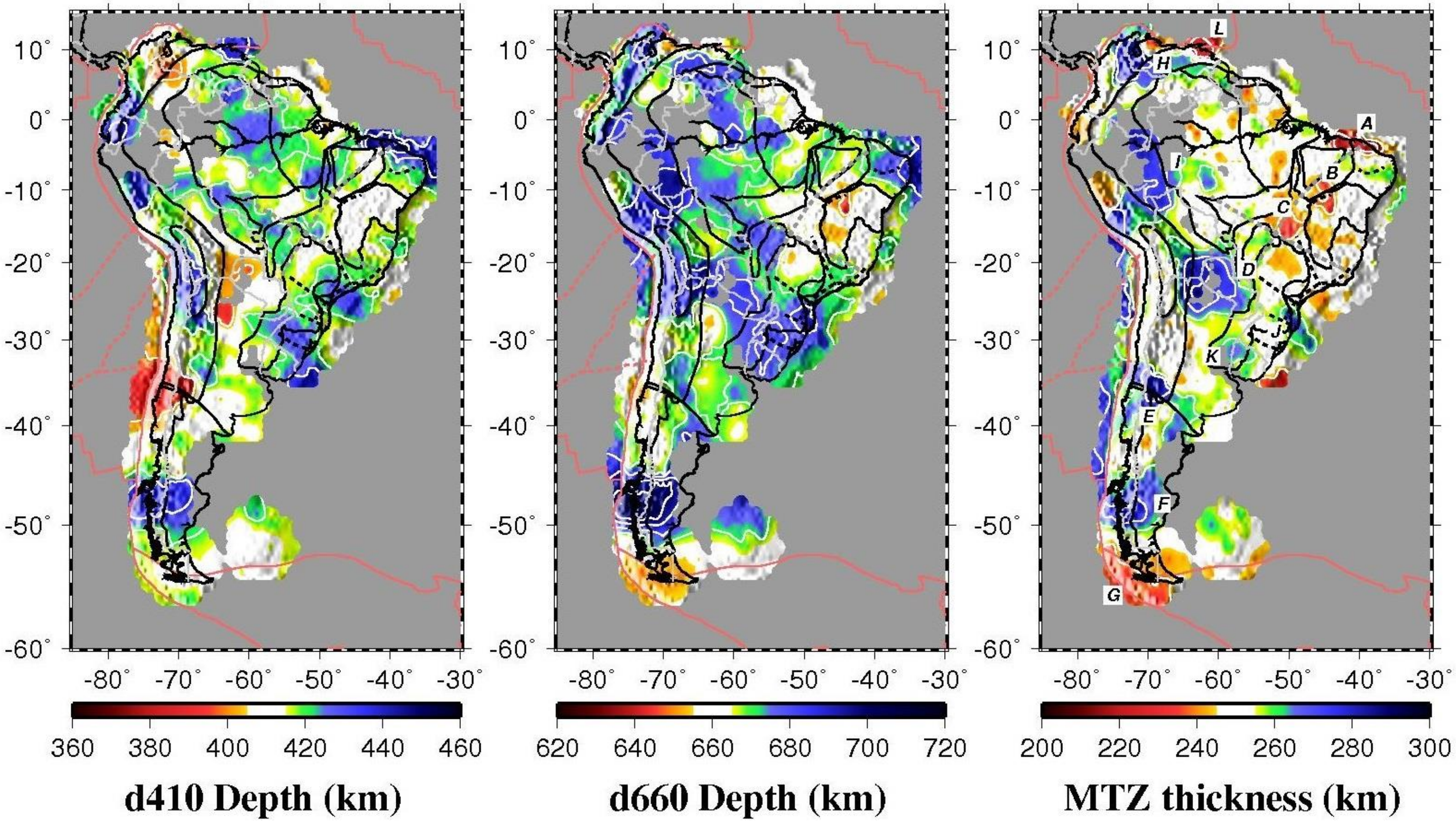

Figure 2. True depth MTZ model using the HMSL (Houser *et al*., 2008) velocity model. Symbols are the as in the Figure 3.1 of the main text.

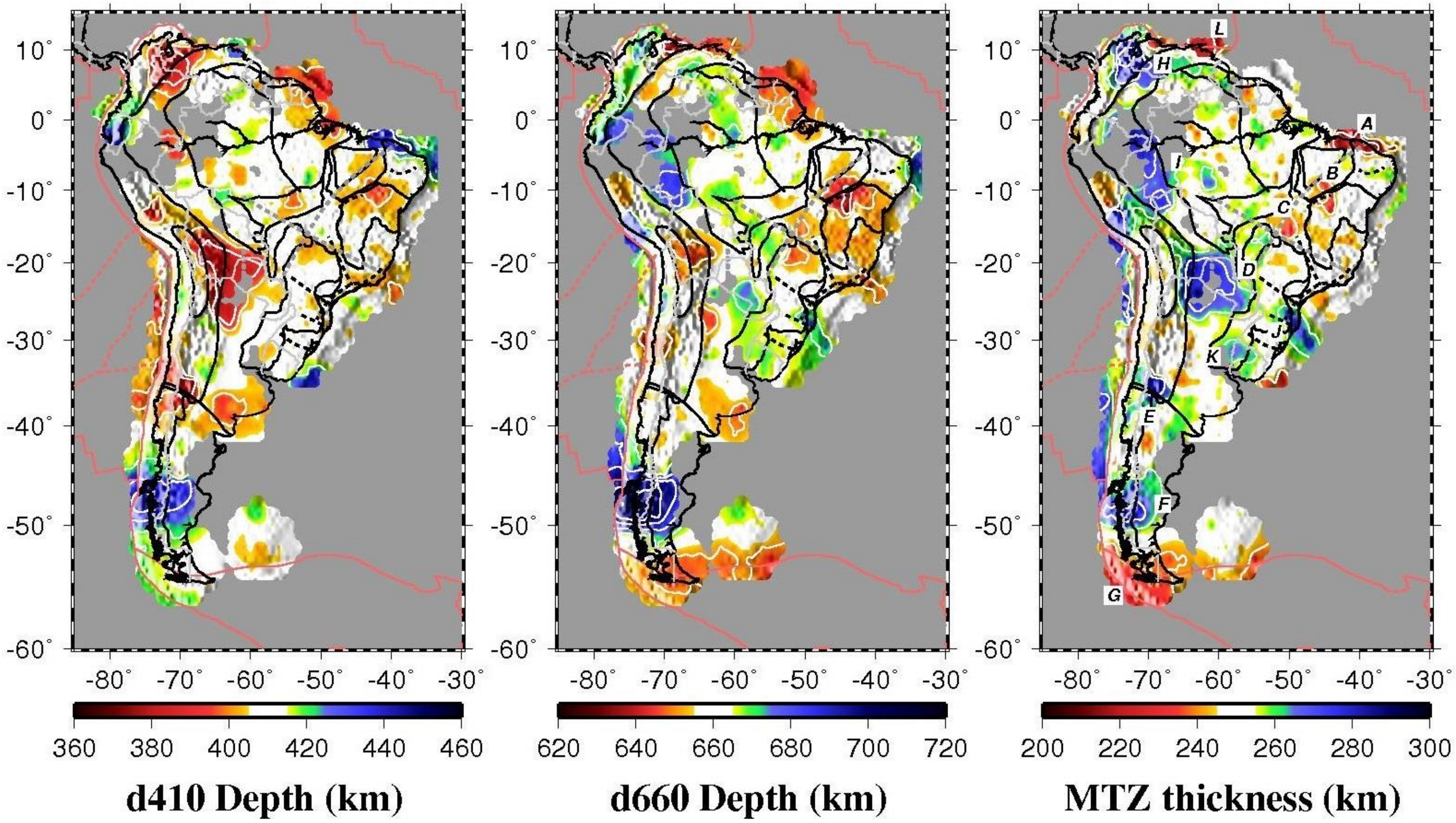

Figure 3. True depth MTZ model using the JOINT (Feng *et al*., 2007) velocity model. Symbols are the as in the Figure 3.1 of the main text.

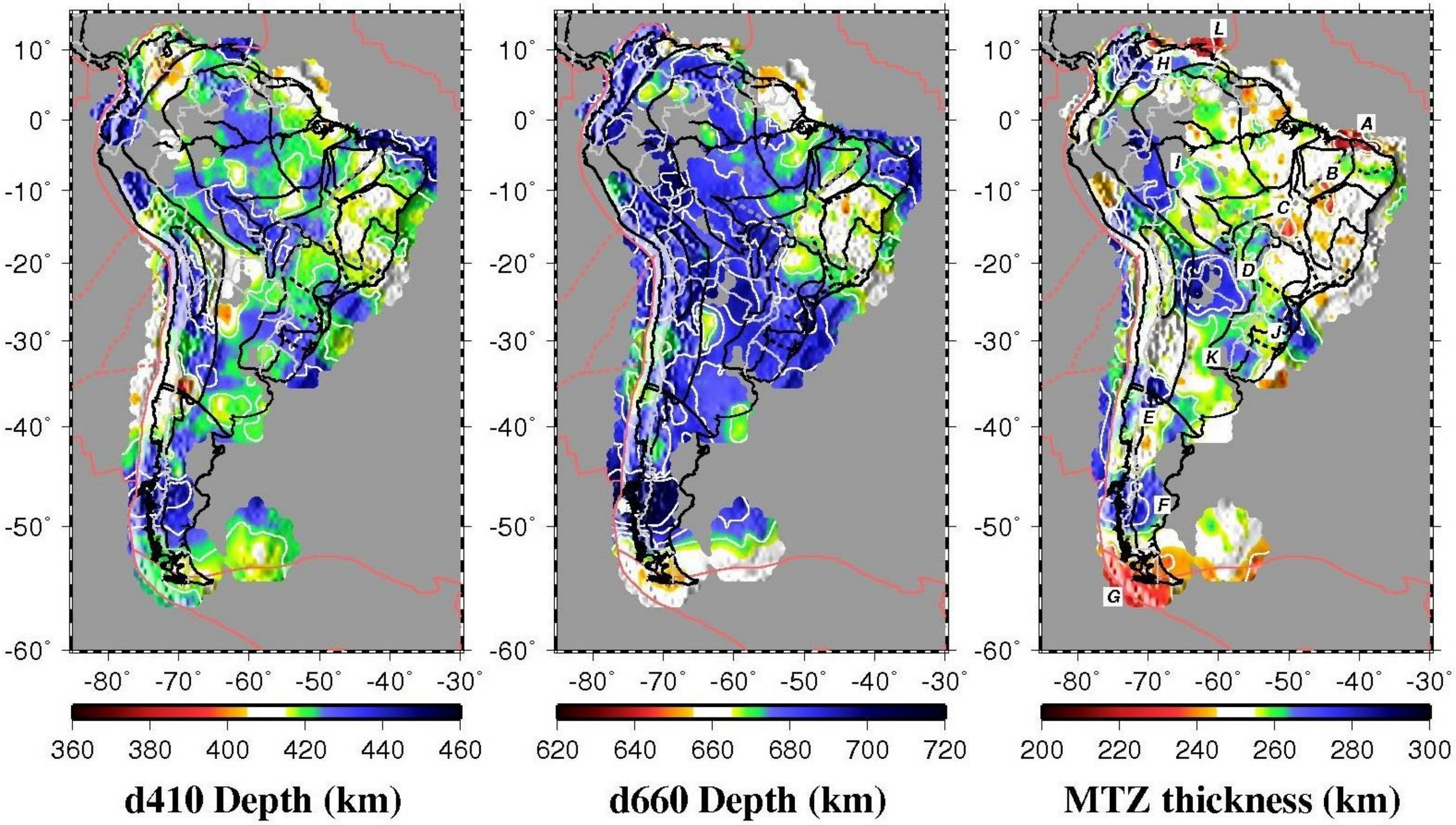

Figure 4. True depth MTZ model using the S362ANI+M (Moulik and Ekstrom 2014) velocity model. Symbols are the as in the Figure 3.1 of the main text.

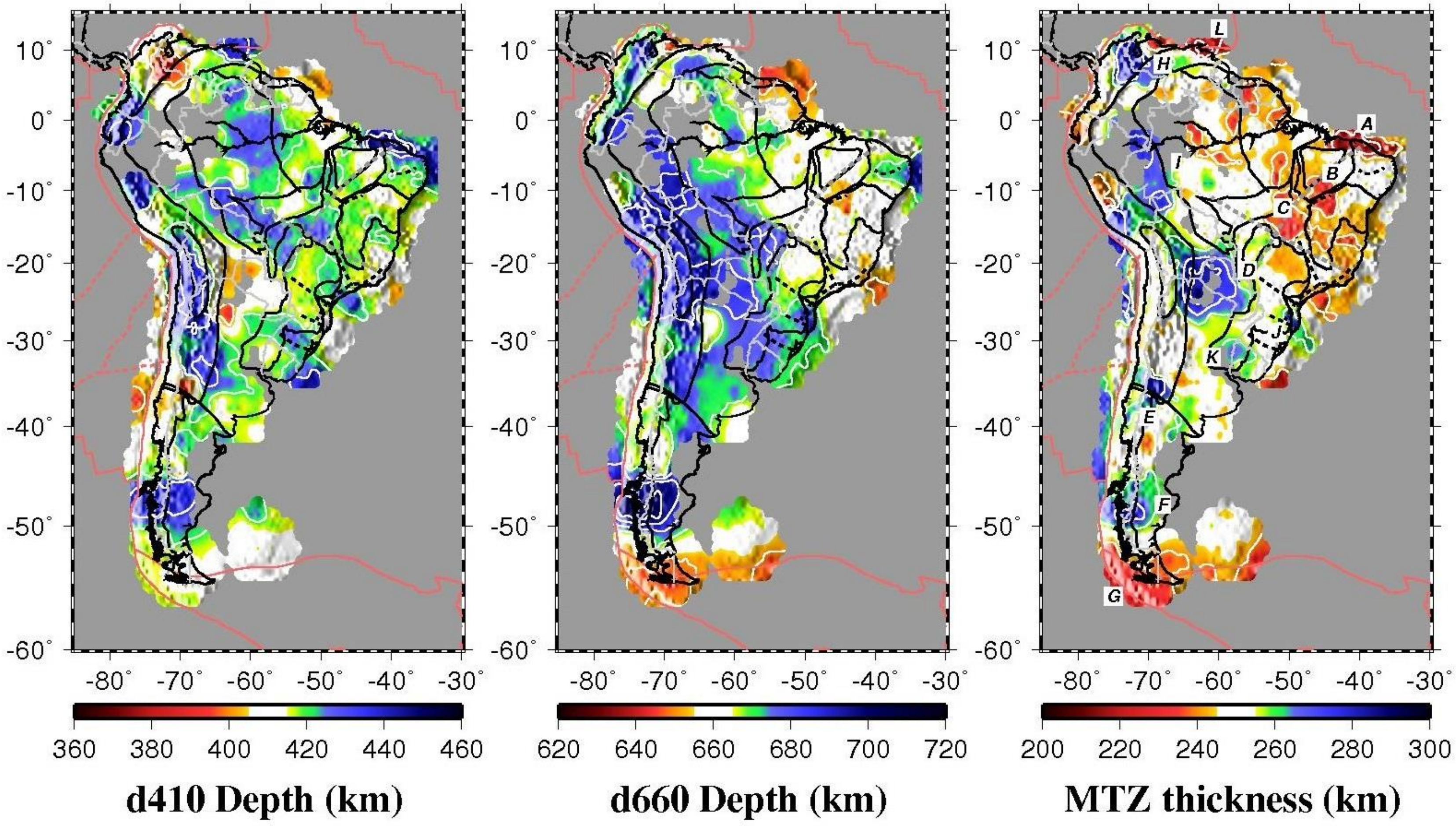

Figure 5. True depth MTZ model using the SAW642ANb (Panning *et al*., 2010) velocity model. Symbols are the as in the Figure 3.1 of the main text.

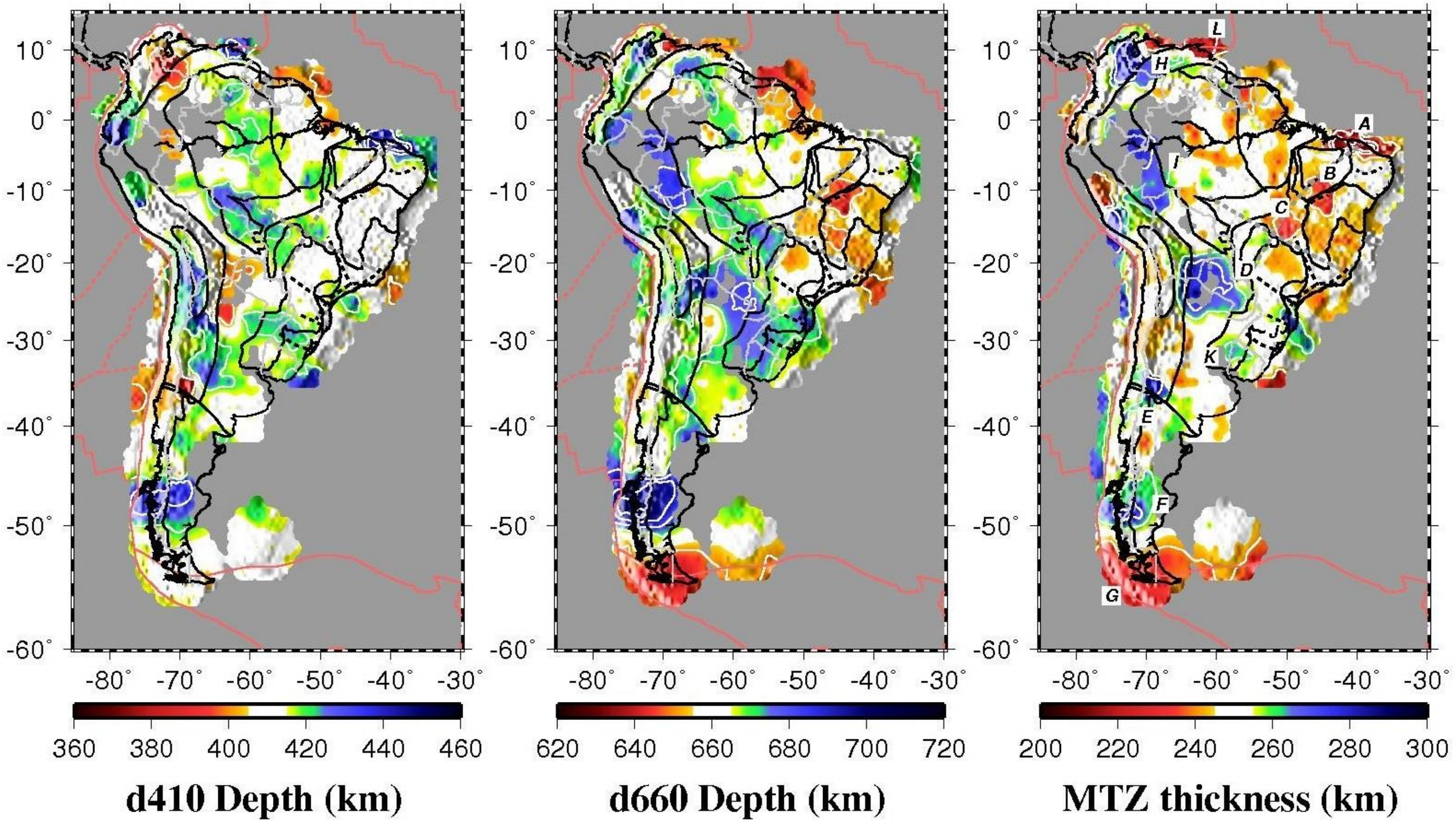

Figure 6. True depth MTZ model using the TX2011 (Grand 2002, and IRIS DMC 2011a) velocity model. Symbols are the as in the Figure 3.1 of the main text.

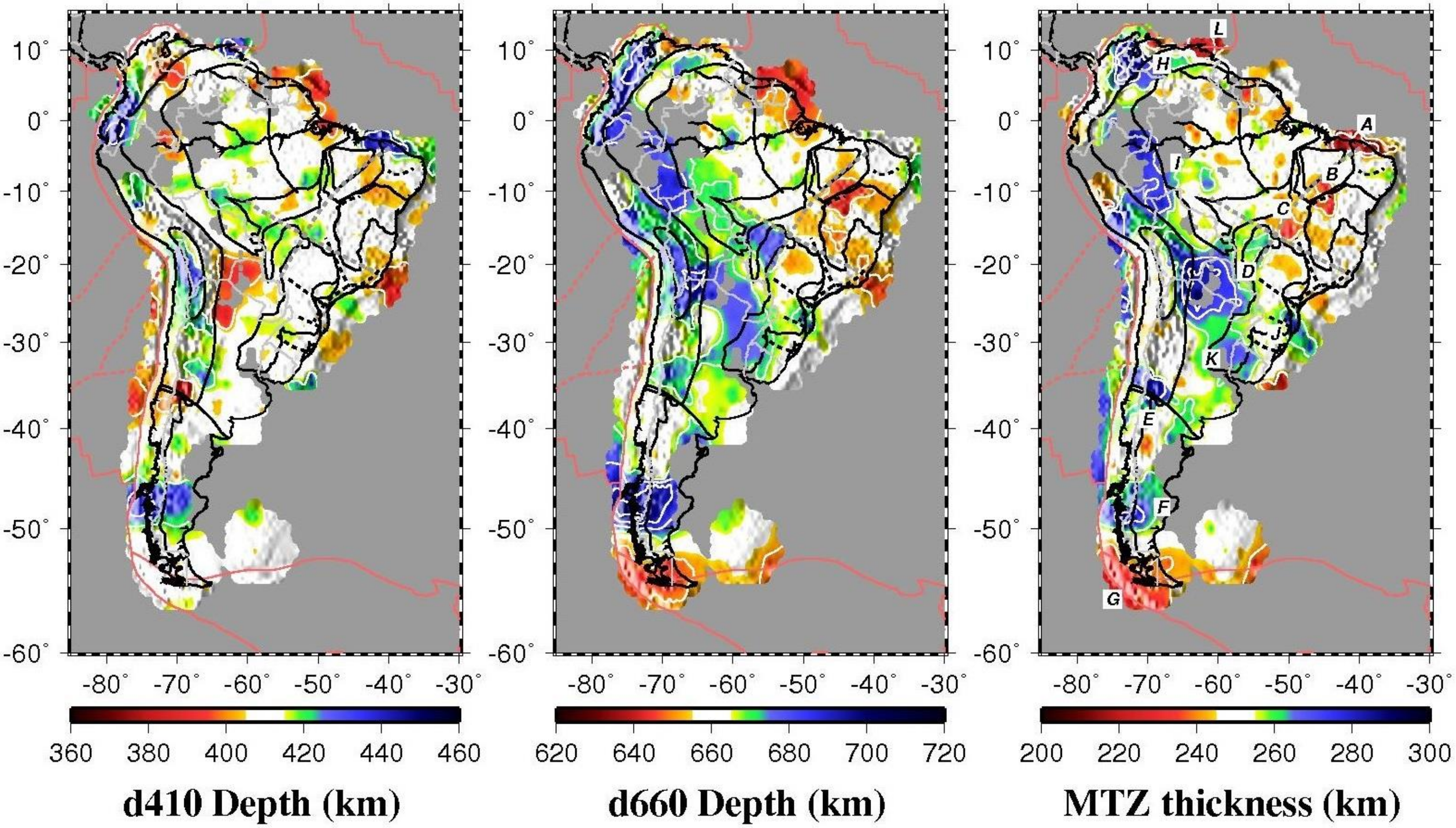

Figure 7. True depth MTZ model using the SEMUCB-WM1 (French and Romanowicz 2014) velocity model. Symbols are the as in the Figure 3.1 of the main text.

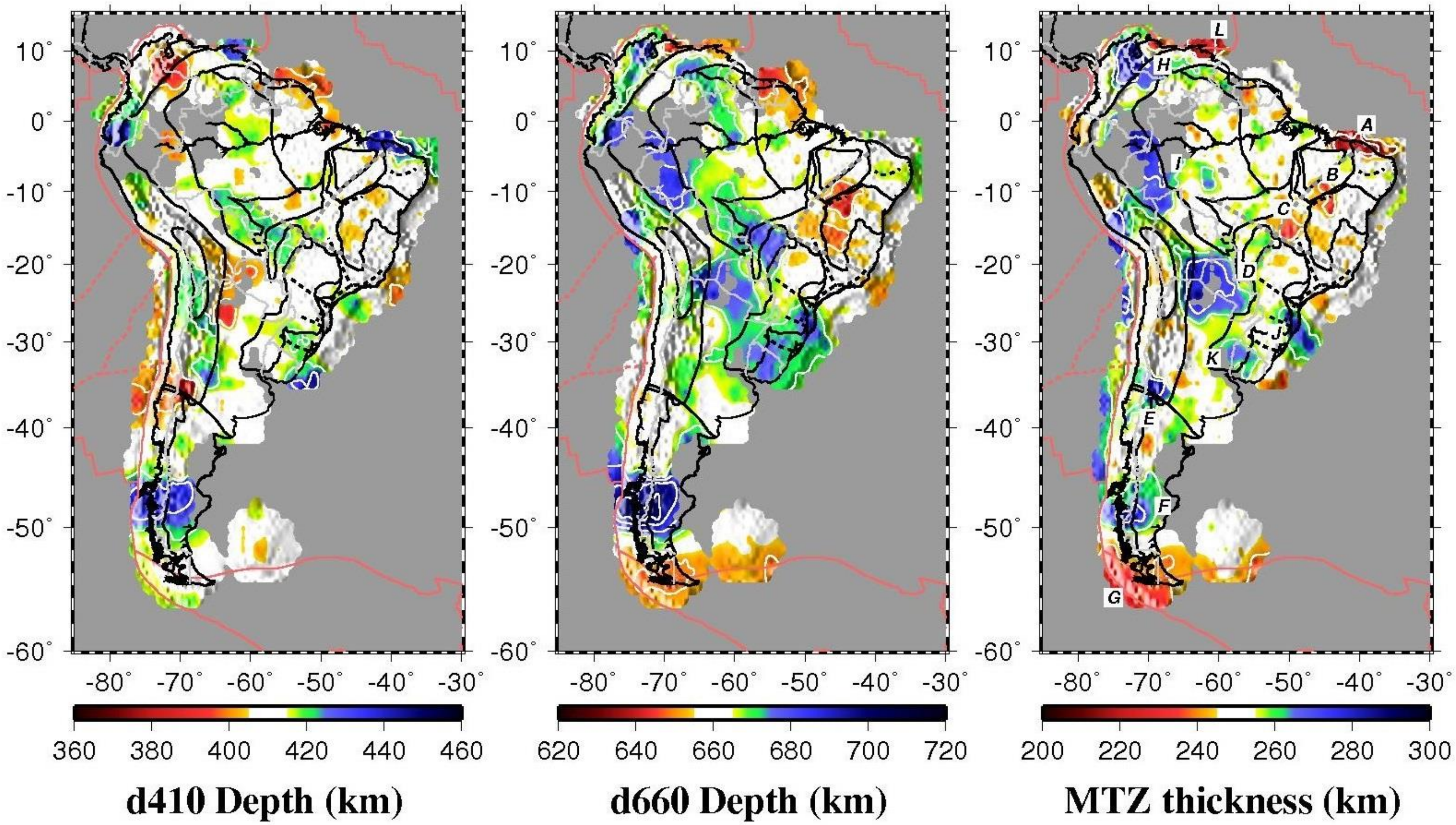

Figure 8. True depth MTZ model using the S40RTS (Ritsema *et al*., 2011) velocity model. Symbols are the as in the Figure 3.1 of the main text.

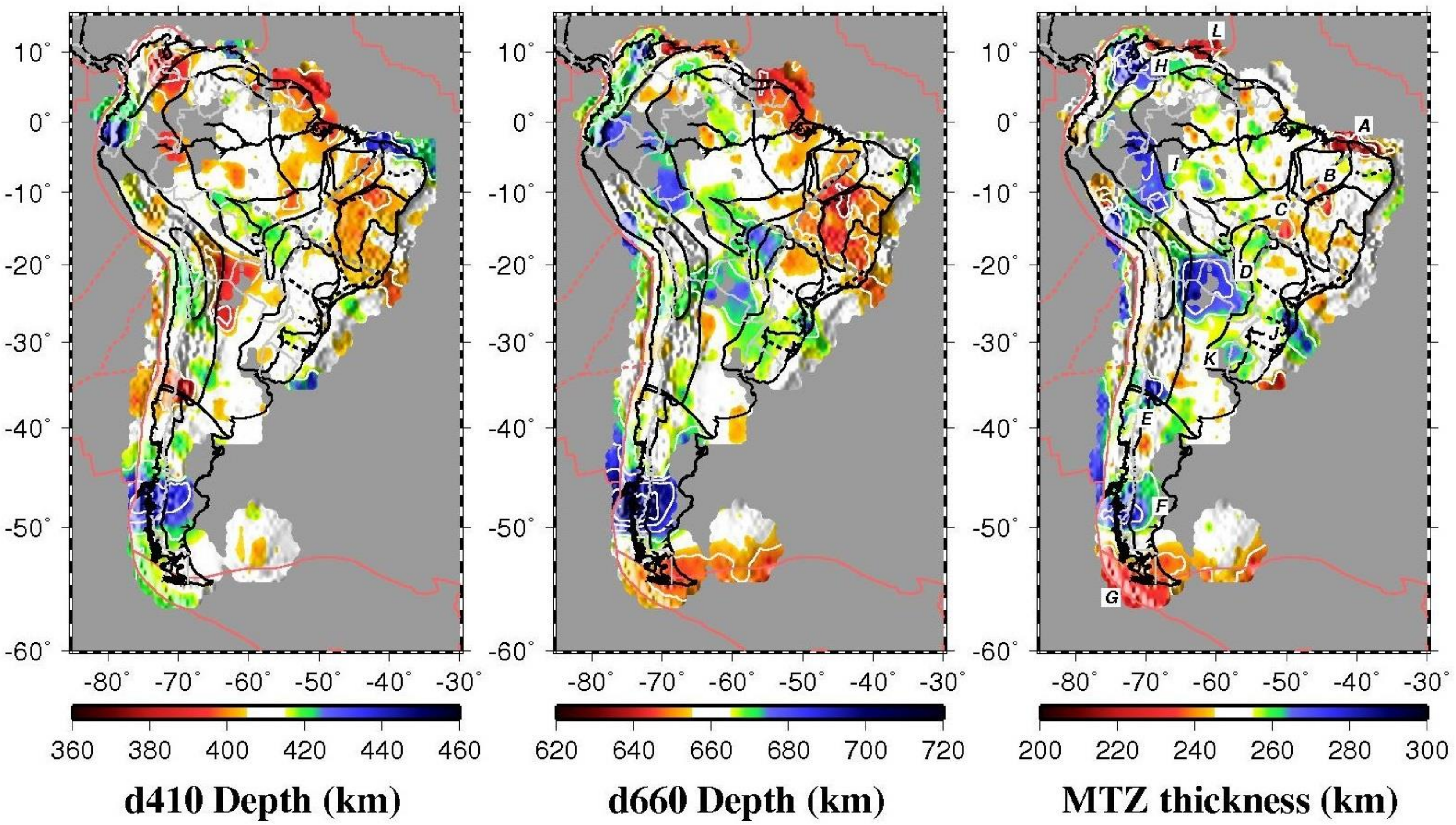
d410 Depth (km)

d660 Depth (km)

MTZ thickness (km)

Figure 9. True depth MTZ model using the LHEB08 (Li *et al*., 2008) velocity model. Symbols are the as in the Figure 3.1 of the main text.

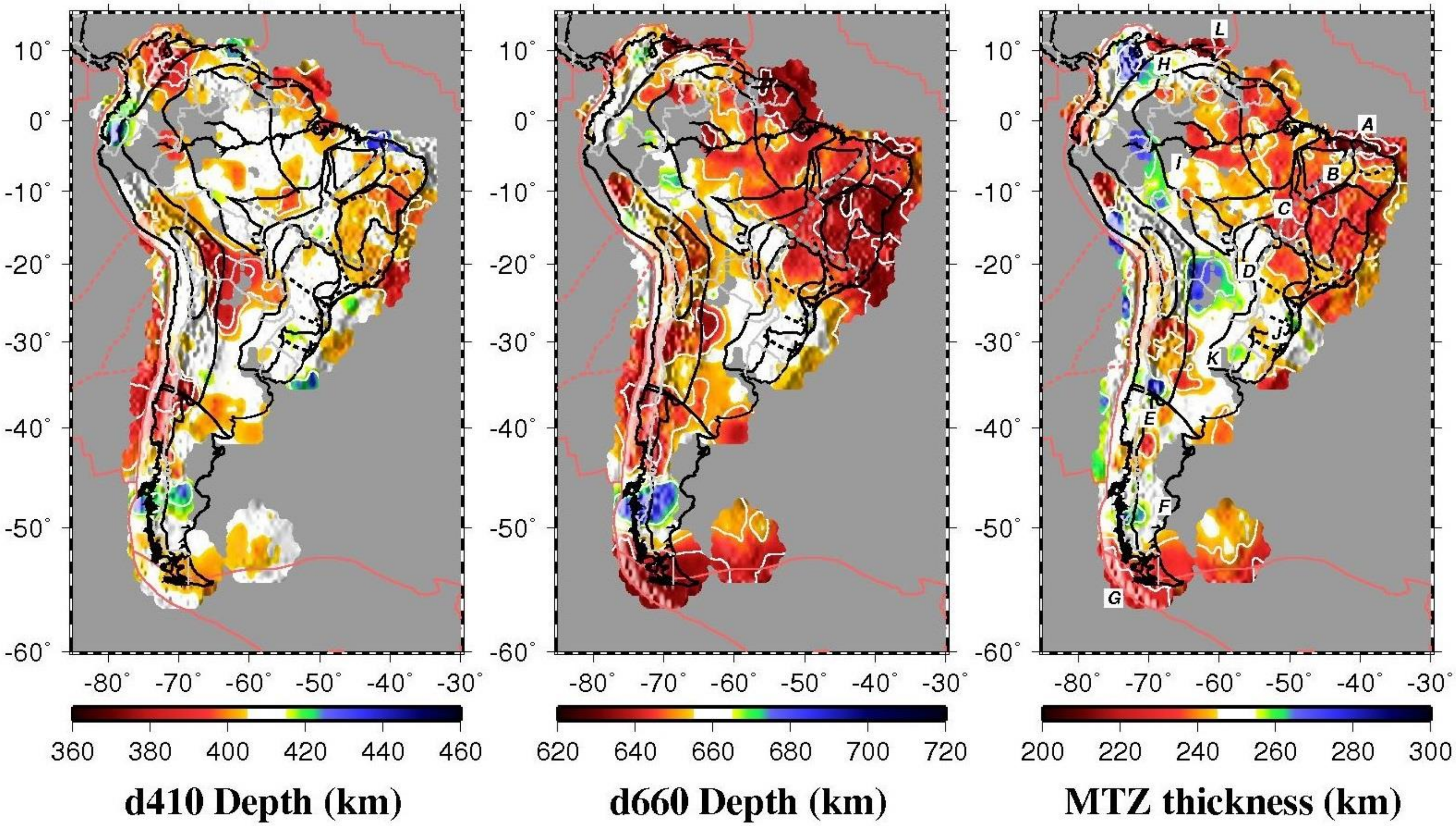

Figure 10. True depth MTZ model using the SPani (Tesoniero *et al*., 2015) velocity model. Symbols are the as in the Figure 3.1 of the main text.

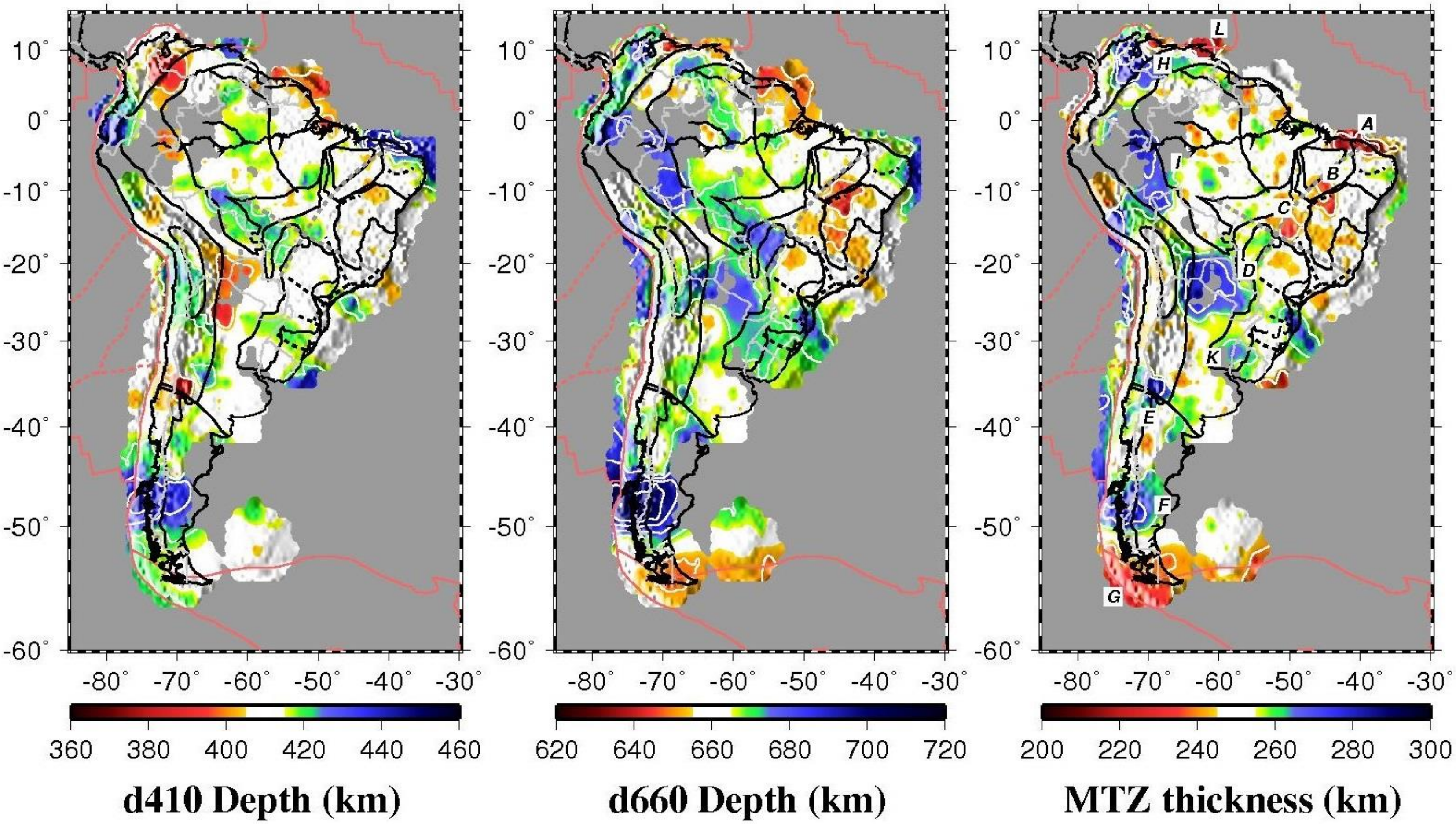

Figure 11. True depth MTZ model using the LLNL-G3Dv3 (Simmons *et al.*, 2012) velocity model. Symbols are the as in the Figure 3.1 of the main text.

BIBLIOGRAPHY

Alkmim, F. F. (2015), Geological background: a tectonic panorama of Brazil, In: *Landscapes and Landforms of Brazil*, edited by B. C. Vieira, A. Salgado, L. Santos, 9-17, Springer, Netherlands, doi: 10.1007/978-94-017-8023-0_2.

Almeida, F. F. M., (2006), Ilhas oceânicas brasileiras e suas relações com a tectônica atlântica, *Terrae Didatica*, *2*(1), 3-18.

Almeida, F. F. M., and C. D. R. Carneiro (1989), Magmatic occurrences of post-Permian age of the South American Platform, *Boletim IG-USP*, *Série Científica*, *20*, 71-85.

Almeida, F. F. M., C. D. R. Carneiro, and A. M. P. Mizusaki (1996), Correlação do magmatismo das bacias da margem continental brasileira com o das áreas emersas adjacentes, *Brazilian Journal of Geology*, *26*(3), 125-138.

Almeida, F. F. M., C. D. R. Carneiro, D. L. Machado JR., and L. K. Dehira (1988), Magmatismo pos-paleozoico do Nordeste Oriental do Brasil, *Revista Brasileira de Geociencias*, *18*(4):451-462.

Ammon, C. J. (1991), The isolation of receiver effects from teleseismic *P*-waveforms, *Bull. Seismol. Soc. Am.*, *81*, 2504–2510.

Ammon, C. J. (1997), Isolating the Receiver Response Langston's Source Equalization Procedure. Available at: http://eqseis.geosc.psu.edu/~cammon/HTML/RftnDocs/seq01.html.

Anderson, D. L. (2007), The eclogite engine: Chemical geodynamics as a Galileo thermometer, *Geological Society of America Special Papers*, *430*, 47-64, doi: 10.1130/2007.2430(03).

Anderson, D. L. (2010), Hawaii, boundary layers and ambient mantle—geophysical constraints, *Journal of Petrology*, egq068, doi:10.1093/petrology/egq068.

Anderson, M., P. Alvarado, G. Zandt, and S. Beck (2007), Geometry and brittle deformation of the subducting Nazca Plate, Central Chile and Argentina, *Geophysi. J. Int*, *171*, 419-434, doi: 10.1111/j.1365-246X.2007.03483.x.

Angelim, L.D.A., J.R. Nesi, H.H.R. Torres, V.C. Medeiros, C.A. Santos, J.P. Veiga Júnior, V.A. Mendes, P. Oliveira, M. Sampaio, and R. Araújo (2007), Geologia e recursos minerais do Estado do Rio Grande do Norte, *Recife: CPRM-Serviço Geológico do Brasil. 119*.

Archanjo, C. J., M. G. Araújo, and P. Launeau (2002), Fabric of the Rio Ceará–Mirim mafic dike swarm (northeastern Brazil) determined by anisotropy of magnetic susceptibility and image analysis, *Journal of Geophysical Research: Solid Earth*, *107*(B3), doi:10.1029/2001JB000268.

Artemieva, I. M., Billien, M., Lévêque, J. J., & Mooney, W. D. (2004). Shear wave velocity, seismic attenuation, and thermal structure of the continental upper mantle. Geophysical Journal International, 157(2), 607-628.doi: 10.1111/j.1365-246X.2004.02195.x

Assumpção, M., M. Guarido, S. van der Lee, and J. C. Dourado (2011), Upper-mantle seismic anisotropy from SKS splitting in the South American stable platform: A test of asthenospheric flow models beneath the lithosphere, *Lithosphere*, *3*(2), 173–180, doi: 10.1130/L99.1.

Assumpção, M., M. Heintz, A. Vauchez, and M. Egydio-Silva (2006), Upper mantle anisotropy in SE and central Brazil from SKS splitting: Evidence of asthenospheric flow around a cratonic keel, *Earth and Planet. Sci. Lett*, *250,* 224–240, doi:10.1016/j.epsl.2006.07.038.

Barbosa, J. S., and P. Sabaté (2002), Geological features and the Paleoproterozoic collision of four Archean crustal segments of the São Francisco Craton, Bahia, Brazil: a synthesis, *Anais da Academia Brasileira de Ciências*, *74*(2), 343-359.

Bercovici, D., and S. I. Karato (2003), Whole-mantle convection and the transition-zone water filter, *Nature*, *425*(6953), 39-44.

Besse, J., and V. Courtillot (2002), Apparent and true polar wander and the geometry of the geomagnetic field over the last 200 Myr, *Journal of Geophysical Research: Solid Earth*, *107*(B11), doi:10.1029/2000JB000050.

Bezada, M. J., A. Levander, and B. Schmandt (2010), Subduction in the southern Caribbean: Images from finite-frequency P wave tomography, *Journal of Geophysical Research: Solid Earth*, *115*(B12), doi: 10.1029/2010JB007682.

Bezerra, F. H., M. K. Takeya, M. O. Sousa, and A. F. do Nascimento (2007), Coseismic reactivation of the Samambaia fault, Brazil, *Tectonophysics*, *430*(1), 27-39, doi:10.1016/j.tecto.2006.10.007.

Bina, C. R., and G. Helffrich (1994), Phase transition Clapeyron slopes and transition zone seismic discontinuity topography, *Journal of Geophysical Research: Solid Earth*, *99*(B8), 15853-15860.

Bina, C. R., and G. Helffrich (2014), Geophysical constraints on mantle composition, In: *Treatise on Geochemistry*, H.D. Holland and K.K. Turekian, 2nd Ed., *3*, 41-65. Elsevier, Oxford, doi:10.1016/B978-0-08-095975-7.00202-3.

Bird, P., (2003), An updated digital model of plate boundaries, *Geochemistry, Geophysics, Geosystems*, *4*(3), doi:10.1029/2001GC000252.

Bizzi, L. A., M. J. De Wit, C. B. Smith, I. McDonald, and R. A. Armstrong (1995), Heterogeneous enriched mantle materials and Dupal-type magmatism along the SW margin of the São Francisco Craton, Brazil, *Journal of Geodynamics*, *20*(4), 469-491.

Bologna, M. S., A. L. Padilha, Í. Vitorello, and M. B. Pádua (2011), Signatures of continental collisions and magmatic activity in central Brazil as indicated by a magnetotelluric profile across distinct tectonic provinces, *Precambrian Research*, *185*(1), 55-64, doi:10.1016/j.precamres.2010.12.003.

Bologna, M. S., A. L. Padilha, Í. Vitorello, and S. L Fontes. (2006), Tectonic insight into a pericratonic subcrustal lithosphere affected by anorogenic Cretaceous magmatism in central Brazil inferred from long-period Magnetotellurics, *Earth and Planetary Science Letters*, *241*(3), 603-616, doi:10.1016/j.epsl.2005.11.022.

Braunmiller, J., S. Van Der Lee, and L. Doermann (2006), Mantle Transition Zone Thickness in the Central South-American Subduction Zone, *Earth's Deep Water Cycle*, 215-224.

Brenker, F. E., C. Vollmer, L. Vincze, B. Vekemans, A. Szymanski, K. Janssens, I. Szaloki, L. Nasdala, W. Joswig, and, F. Kaminsky (2007), Carbonates from the lower part of transition zone or even the lower mantle, *Earth and Planetary Science Letters*, *260*(1), 1-9, doi:10.1016/j.epsl.2007.02.038.

Bridges, D. L., K. Mickus, S. S. Gao, M. G. Abdelsalam, and A. Alemu (2012), Magnetic stripes of a transitional continental rift in Afar, *Geology*, *40*(3), 203-206, doi:10.1130/G32697.1.

Brito Neves, B. B. (2002), Main stages of the development of the sedimentary basins of South America and their relationship with the tectonics of supercontinents, *Gondwana Research*, *5*(1), 175-196.

Brito Neves, B. B., and R. A. Fuck (2014), The basement of the South American platform: Half Laurentian (N-NW)+ half Gondwanan (E-SE) domains, *Precambrian Research*, *244*, 75-86, doi:10.1016/j.precamres.2013.09.020.

Brod, J. A., S. A. Gibson, R. N. Thompson, T. C. Junqueira-Brod, H. J. Seer, L. C. de Moraes, and G. R. Boaventura (2000), The Kamafugite-Carbonatite association in the Alto Paranaíba igneous province (APIP) southeastern Brazil, *Brazilian Journal of Geology*, *30*(3), 408-412.

Bulanova, G. P., M. J. Walter, C. B. Smith, S. C. Kohn, L. S. Armstrong, J. Blundy, and L. Gobbo (2010), Mineral inclusions in sublithospheric diamonds from Collier 4 kimberlite pipe, Juina, Brazil: subducted protoliths, carbonated melts and primary kimberlite magmatism, *Contributions to Mineralogy and Petrology*, *160*(4), 489-510, doi 10.1007/s00410-010-0490-6.

Burd, A. I., J. R. Booker, R. Mackie, C. Pomposiello, and A. Favetto (2013), Electrical conductivity of the Pampean shallow subduction region of Argentina near 33 S: Evidence for a slab window, *Geochem. Geophys. Geosyst.*, *14*(8), 3192-3209, doi: 10.1002/ggge.20213.

Cammarano F., and B. Romanowicz, (2008), Radial profiles of seismic attenuation in the upper mantle based on physical models. *Geophys. J. Int.* (2008) 175**,** 116–134. doi: 10.1111/j.1365-246X.2008.03863.x

Campos, J. E. G., and M. A. Dardenne (1997a), Origem e evolução da Bacia Sanfranciscana, *Brazilian Journal of Geology*, *27*(3), 283-294.

Campos, J. E. G., and M. A. Dardenne. (1997b), Estratigrafia e sedimentação da Bacia Sanfranciscana: uma revisão, *Brazilian Journal of Geology*, *27*(3), 269-282.

Castro, D. L., R. A. Fuck, J. D. Phillips, R. M., Vidotti, F. H. Bezerra, and E. L. Dantas (2014), Crustal structure beneath the Paleozoic Parnaíba Basin revealed by airborne gravity and magnetic data, Brazil, *Tectonophysics*, *614*, 128-145, doi:10.1016/j.tecto.2013.12.009.

Chevrot, S., L. Vinnik, and J. P. Montagner (1999), Global-scale analysis of the mantle Pds phases, *Journal of Geophysical Research: Solid Earth*, *104*(B9), 20203-20219, doi: 10.1029/1999JB900087.

Chmielowski, J., G. Zandt, and C. Haberland (1999), The central Andean Altiplano-Puna magma body, *Geophysical Research Letters*, *26*(6), 783-786.

Collier, J. D., and G. R. Helffrich (2001), The thermal influence of the subducting slab beneath South America from 410 and 660 km discontinuity observations, *Geophysical Journal International*, *147*(2), 319-329, doi: 10.1046/j.1365-246X.2001.00532.x.

Contenti, S., Y. J. Gu, A. Ökeler, and M. D. Sacchi (2012), Shear wave reflectivity imaging of the Nazca-South America subduction zone: Stagnant slab in the mantle transition zone?, *Geophysical Research Letters*, *39*(2), doi: 10.1029/2011GL050064.

Cordani, U. G., K. Sato, W. Teixeira, C. C. G. Tassinari, and M. A. S. Basei (2000), Crustal evolution of the South American platform, In: *Tectonic Evolution of South America*, U.G. Cordani, E.J. Milani, A. Thomaz-Filho, D.A. Campos, *31*, 19-40, 31st International Geological Congress, Rio de Janeiro.

Deuss, A. (2007), Seismic observations of transition-zone discontinuities beneath hotspot locations, *Geological Society of America Special Papers*, *430*, 121-136, doi: 10.1130/2007.2430(07).

Deuss, A. (2009), Global observations of mantle discontinuities using SS and PP precursors, *Surveys in geophysics*, *30*(4-5), 301-326, doi: 10.1007/s10712-009-9078-y.

Deuss, A., S. A. Redfern, K. Chambers, and J. H. Woodhouse (2006), The nature of the 660-kilometer discontinuity in Earth's mantle from global seismic observations of PP precursors, *Science*, *311*(5758), 198-201.

Dorogokupets, P. I., A. M. Dymshits, T. S. Sokolova, B. S. Danilov, and K. D. Litasov (2015), The equations of state of forsterite, wadsleyite, ringwoodite, akimotoite, MgSiO 3-perovskite, and postperovskite and phase diagram for the Mg 2 SiO 4 system at pressures of up to 130GPa, *Russian Geology and Geophysics*, *56*(1), 172-189, doi:10.1016/j.rgg.2015.01.011.

Dueker, K. G., and A. F. Sheehan (1997), Mantle discontinuity structure from midpoint stacks of converted P to S waves across the Yellowstone hotspot track, *Journal of Geophysical Research: Solid Earth*, *102*(B4), 8313-8327.

Engdahl, E. R., R. D. Van der Hilst, and J. Berrocal (1995), Imaging of subducted lithosphere beneath South America, *Geophysical Research Letters*, *22*(16), 2317-2320. 429–465, doi:10.1111/j.1365-246X.1991.tb06724.x.

Ernesto, M., L. S. Marques, E. M. Piccirillo, E. C. Molina, N. Ussami, P. Comin-Chiaramonti, and G. Bellieni. (2002), Paraná Magmatic Province–Tristan da Cunha plume system: fixed versus mobile plume, petrogenetic considerations and alternative heat sources, *Journal of Volcanology and Geothermal Research*, *118*(1), 15-36.

Espinoza, T. E. M., and L. T. Pinero-Feliciangeli, (2013), Crustal seismic anisotropy at the edge of the south-east border of Caribbean and South American Plates, *Revista Brasileira de Geofísica*, *31*(4), 595-608.

Felgate, M. R. (2014), The petrogenesis of Brazilian kimberlites and kamafugites intruded along the 125° lineament: improved geochemical and geochronological constraints on magmatism in Rondonia and the Alto Paranaiba Igneous Province, Ph.D. Thesis, The University of Melbourne. Melbourne, Australia.

Feng, M., S. Van der Lee, and M. Assumpção (2007), Upper mantle structure of South America from joint inversion of waveforms and fundamental mode group velocities of Rayleigh waves, *Journal of Geophysical Research: Solid Earth*, *112*(B4), doi:10.1029/2006JB004449.

Flanagan, M. P., and P. M. Shearer (1998), Global mapping of topography on transition zone velocity discontinuities by stacking SS precursors, *Journal of Geophysical Research: Solid Earth*, *103*(B2), 2673-2692.

Fodor, R. V., S. B. Mukasa, and A. N. Sial (1998), Isotopic and trace-element indications of lithospheric and asthenospheric components in Tertiary alkalic basalts, northeastern Brazil, *Lithos*, *43*(4), 197-217.

Frank, H. T., M. E. B. Gomes, and M. L. L. Formoso (2009), Review of the areal extent and the volume of the Serra Geral Formation, Paraná Basin, South America, *Pesquisas em Geociências*, *36*(1), 49-57.

French, S. W., and B. A. Romanowicz (2014), Whole-mantle radially anisotropic shear velocity structure from spectral-element waveform tomography, *Geophysical Journal International*, *199*(3), 1303-1327, doi: 10.1093/gji/ggu334.

Fukao, Y., and M. Obayashi (2013), Subducted slabs stagnant above, penetrating through, and trapped below the 660 km discontinuity, *J. Geophys. Res. Solid Earth*, 118, 5920–5938, doi:10.1002/2013JB010466.

Fukao, Y., M. Obayashi, and T. Nakakuki (2009), Stagnant slab: a review, *Ann. Rev. Earth Planet. Sci. Lett.*, *37*, 19-46, doi: 10.1146/annurev.earth.36.031207.124224.

Gao, S. S., and K. H. Liu (2014a), Mantle transition zone discontinuities beneath the contiguous United States, *Journal of Geophysical Research: Solid Earth*, *119*(8), 6452-6468, doi: 10.1002/2014JB011253.

Gao, S. S., and K. H. Liu (2014b), Imaging mantle discontinuities using multiply-reflected P-to-S conversions, *Earth Planet. Sci. Lett.*, *402*, 99-106, doi:10.1016/j.epsl.2013.08.025.

Gao, S.S., P.M. Davis, H. Liu, P. D. Slack, A.W. Rigor, Y.A. Zorin, V.V. Mordvinova, V.M. Kozhevnikov, and N.A. Logatchev (1999), "SKS splitting beneath continental rifts zones" by Gao *et al*. Reply, *Journal of Geophysical Research*, *104*(5), 10791-10794, doi: 10.1029/1999JB900055.

Gao, S., Davis, P.M., Liu, H., Slack, P.D., Rigor, A.W., Zorin, Y.A., Mordvinova, V.V., Kozhevnikov, V.M. and Logatchev, N.A., 1997. SKS splitting beneath continental rift zones. *Journal of Geophysical Research*, *102*, 22-781.

Geraldes, M. C., A. Motoki, A. Costa, C. E. Mota, and W. U. Mohriak (2013), Geochronology (Ar/Ar and K–Ar) of the South Atlantic post-break-up magmatism, *Geological Society, London, Special Publications*, *369*(1), 41-74, doi: 10.1144/SP369.21.

Ghosh, S., E. Ohtani, K. D. Litasov, A. Suzuki, D. Dobson, and K. Funakoshi (2013), Effect of water in depleted mantle on post-spinel transition and implication for 660 km seismic discontinuity, *Earth and Planetary Science Letters, 371*, 103-111, doi:10.1016/j.epsl.2013.04.011.

Gibson, S. A., R. N. Thompson, O. H. Leonardos, A. P. Dickin, and J. G. Mitchell (1995), The Late Cretaceous impact of the Trindade mantle plume: evidence from large-volume, mafic, potassic magmatism in SE Brazil, *J. Petrol*, *36*(1), 189-229.

Gibson, S. A., R. N. Thompson, R. K. Weska, A. P. Dickin, and O. H. Leonardos (1997), Late Cretaceous rift-related upwelling and melting of the Trindade starting mantle plume head beneath western Brazil, *Contributions to Mineralogy and Petrology*, *126*(3), 303-314.

Global Volcanism Program, (2013) Volcanoes of the World, v. 4.4.2. Venzke, E (ed.). Smithsonian Institution, doi: 10.5479/si.GVP.VOTW4-2013.

CPRM (2015), Geobank – GIS Brazil Project, Gonçalves, J. H. (Cord.). Brazil Geological Survey – CPRM, Available at: http://geobank.cprm.gov.br.

Grand, S. P. (2002), Mantle shear–wave tomography and the fate of subducted slabs, *Philosophical Transactions of the Royal Society of London A: Mathematical, Physical and Engineering Sciences*, *360*(1800), 2475-2491.

Gripp, A. E., and R. G. Gordon (2002), Young tracks of hotspots and current plate velocities, *Geophysical Journal International*, *150*(2), 321-361.

Growdon, M. A., G. L. Pavlis, F. Niu, F. L. Vernon, and H. Rendon (2009), Constraints on mantle flow at the Caribbean–South American plate boundary inferred from shear wave splitting, *J. Geophys. Res.*, *114*(B2).

Guarino, V., F. Y.Wu, M. Lustrino, L. Melluso, P. Brotzu, C. de Barros Gomes, and D. P. Svisero (2013), U–Pb ages, Sr–Nd-isotope geochemistry, and petrogenesis of kimberlites, kamafugites and phlogopite-picrites of the Alto Paranaíba Igneous Province, Brazil, *Chem. Geol., 353*, 65-82.

Hayman, P. C., M. G. Kopylova, and F. V. Kaminsky (2005), Lower mantle diamonds from Rio Soriso (Juina area, Mato Grosso, Brazil), *Contributions to Mineralogy and Petrology*, *149*(4), 430-445.

Heintz, M., A.Vauchez, M. Assumpção, G. Barruol, and M. Egydio-Silva (2003), Shear wave splitting in SE Brazil: An effect of active or fossil upper mantle flow, or both, *Earth Planet. Sci. Lett, 211*,79–95, doi:10.1016/S0012-821X(03)00163-8.

Helffrich, G. (2000), Topography of the transition zone seismic discontinuities, *Reviews of Geophysics, 38*(1), 141-158.

Helffrich, G., and C. R. Bina (1994), Frequency dependence of the visibility and depths of mantle seismic discontinuities, *Geophysical research letters, 21*(24), 2613-2616.

Houser C, G. Masters, M. Flanagan and P. Shearer (2008), Determination and analysis of long-wavelength transition zone structure using SS precursors, *Geophys. J. Int.,174,*178–194.

Huang, J., E. Vanacore, F. Niu, and A. Levander (2010), Mantle transition zone beneath the Caribbean-South American plate boundary and its tectonic implications, *Earth and Planetary Science Letters*, *289*(1), 105-111.

Hunt, L., T. Stachel, R. Morton, H. Grütter, and R. A. Creaser (2009), The Carolina kimberlite, Brazil—Insights into an unconventional diamond deposit, *Lithos*, *112*, 843-851.

IRIS DMC (2011a), Data Services Products: TX2011, a global shear-wave tomography model, doi:10.17611/DP/9991721.

IRIS DMC (2011b), Data Services Products: EMC, A repository of Earth models, doi:10.17611/DP/EMC.1.

James, D. E., and M. Assumpção (1996), Tectonic implications of S-wave anisotropy beneath SE Brazil, *Geophys. J. Int.*, *126*, 1–10, doi:10.1111/j.1365 -246X.1996.tb05263.x.

Kaminsky, F. V., and E. A. Belousova (2009), Manganoan ilmenite as kimberlite/diamond indicator mineral, *Russian Geology and Geophysics*, *50*(12), 1212-1220.

Kaminsky, F. V., G. K. Khachatryan, P. Andreazza, D. Araujo, and W. L. Griffin (2009a), Super-deep diamonds from kimberlites in the Juina area, Mato Grosso State, Brazil, *Lithos*, *112*, 833-842.

Kaminsky, F. V., I. D. Ryabchikov, C. A. McCammon, M. Longo, A. M. Abakumov, S. Turner, and H. Heidari, (2015), Oxidation potential in the Earth's lower mantle as recorded by ferropericlase inclusions in diamond, *Earth and Planetary Science Letters*, *417*, 49-56.

Kaminsky, F. V., O. D. Zakharchenko, G. K. Khachatryan, W. L. Griffin, and D. M. D. Channer (2006), Diamond from the Los Coquitos Area, Bolivar State, Venezuela, *The Canadian Mineralogist*, *44*(2), 323-340.

Kaminsky, F. V., S. M. Sablukov, E. A. Belousova, P. Andreazza, M. Tremblay, and W. L. Griffin (2010), Kimberlitic sources of super-deep diamonds in the Juina area, Mato Grosso State, Brazil, *Lithos*, *114*(1), 16-29.

Kaminsky, F. V., S. M. Sablukov, L. I. Sablukova, and O. D. Zakharchenko (2009b), The Fazenda Largo off-craton kimberlites of Piauí State, Brazil, *Journal of South American Earth Sciences*, *28*(3), 288-303.

Karato, S. I., H. Jung, I. Katayama, P. Skemer (2008), Geodynamic significance of seismic anisotropy of the upper mantle: new insights from laboratory studies. *Annu. Rev. Earth Planet. Sci.*36, 59–95, doi: 10.1146/annurev.earth.36.031207.124120.

Karfunkel, J., D. Hoover, A. F. Fernandes, G. N. C. Sgarbi, K. Kambrock, and G. D. Oliveira (2014), Diamonds from the Coromandel area, West Minas Gerais state, Brazil: An update and new data on surface sources and origin, *Brazilian Journal of Geology*, *44*(2), 325-338.

Kearey, P., K. A. Klepeis, and F. Vine (2009), Global Tectonics, Wiley-Blackwell, Hoboken, NJ, USA. 3rd Ed., 482 pp.

Kennett, B. L. N., and E. R. Engdahl (1991), Traveltimes for global earthquake location and phase identification, *Geophys. J. Int., 105*, 429–465, doi:10.1111/j.1365-246X.1991.tb06724.x.

Kennett, B. L. N., E. R. Engdahl, and R. Buland (1995), Constraints on seismic velocities in the Earth from traveltimes, *Geophysical Journal International*, *122*(1), 108-124.

King, S. D. (2007), Hotspots and edge-driven convection, *Geology*, *35*(3), 223-226.

King, S. D., and J. Ritsema (2000), African hot spot volcanism: small-scale convection in the upper mantle beneath cratons, *Science*, *290*(5494), 1137-1140.

Knesel, K. M., Z. S. Souza, P. M. Vasconcelos, B. E. Cohen, and F. V. Silveira (2011), Young volcanism in the Borborema Province, NE Brazil, shows no evidence for a trace of the Fernando de Noronha plume on the continent, *Earth Planet. Sci.Lett.302*(1), 38-50.

Larson, R. L. (1991), Latest pulse of Earth: Evidence for a mid-Cretaceous superplume, *Geology*, *19*(6), 547-550.

Lawrence, J., and P. Shearer (2008), Imaging mantle transition zone thickness with SdS-SS finite-frequency sensitivity kernels, *Geophys. J. Int*., *174*:143–158.

Lebedev, S., S. Chevrot, and R. D. van der Hilst. (2002), Seismic evidence for olivine phase changes at the 410-and 660-kilometer discontinuities, *Science*, *296*(5571), 1300-1302.

Li, C., R. D. van der Hilst, E. R. Engdahl, and S. Burdick (2008), A new global model for P wave speed variations in Earth's mantle, *Geochemistry, Geophysics, Geosystems*, *9*(5).

Lima, E. F. D., R. P. Philipp, G. C. Rizzon, B. L. Waichel, and L. D. M. M. Rossetti (2012), Sucessões vulcânicas, modelo de alimentação e geração de domos de lava ácidos da Formação Serra Geral na região de São Marcos-Antônio Prado (RS), *Geologia USP, Série científica, São Paulo, SP. 12, (2)(ago. 2012), 49-64*.

Litasov, K. D., E. Ohtani, A. Sano, A. Suzuki, and K. Funakoshi (2005), Wet subduction versus cold subduction, *Geophysical research letters*, *32*(13).

Liu, K. H. (2003), Effects of inelasticity on the apparent depth and detectability of seismic discontinuities in the mantle, *Geophysical research letters*, *30*(9).

Liu, K. H., S.S. Gao, P. G. Silver, and Y. Zhang (2003), Mantle layering across central South America, *J. Geophys. Res. Solid Earth (1978–2012)*, *108*(B11).

Masy, J., F. Niu, A. Levander, and M. Schmitz (2011), Mantle flow beneath northwestern Venezuela: Seismic evidence for a deep origin of the Mérida Andes, *Earth Planet. Sci. Lett.*, *305*(3), 396-404.

Milani, E. J., H. D. Rangel, G. V. Bueno, J. M. Stica, W. R. Winter, J. M. Caixeta, and O. P. Neto (2007a), Bacias sedimentares brasileiras: cartas estratigráficas, *Boletim de Geociências da Petrobrás*, *15*(1).

Milani, E. J., J. H. G. Melo, P. A. Souza, L. A. Fernandes, and A. B. França (2007b). Bacia do Paraná, *Boletim de Geociencias da Petrobras*, *15*(2), 265-287.

Mizusaki, A. M. P., A. Thomaz-Filho, E.J. Milani, and P. De Césero (2002), Mesozoic and Cenozoic igneous activity and its tectonic control in northeastern Brazil, *Journal of South American Earth Sciences*, *15*(2), 183-198.

Molina, E. C., and N. Ussami (1999), The geoid in southeastern Brazil and adjacent regions: new constraints on density distribution and thermal state of the lithosphere, *Journal of Geodynamics*, *28*(4), 357-374.

Morais Neto, J., K. A. Hegarty, G. D. Karnerand, and F. F. D. Alkmim (2009), Timing and mechanisms for the generation and modification of the anomalous topography of the Borborema Province, northeastern Brazil, *Marine and Petroleum Geology*, *26*(7), 1070-1086.

Moulik, P., and G. Ekström (2014), An anisotropic shear velocity model of the Earth's mantle using normal modes, body waves, surface waves and long-period waveforms, *Geophysical Journal International*, *199*(3), 1713-1738.

Neto I. C., L. M. Cunha, F. V. Silveira, F. Nannini, R. G. Oliveira, W. S. Souza, and A. K. Bezerra, (2015), Registro dos primeiros corpos com afinidade kimberlítica na Província Borborema, NE do Brasil, *CPRM – Serviço Geológico do Brasil, Informe Técnico*, (2), Brasília, Brazil.

Obayashi, M., J. Yoshimitsu, G. Nolet, Y. Fukao, H. Shiobara, H. Sugioka, H. Miyamachiand Y. Gao (2013), Finite frequency whole mantle P wave tomography: Improvement of subducted slab images, *Geophysical Research Letters*, *40*(21), 5652-5657.

Oliveira, R. G., and W. E. de Medeiros (2012), Evidences of buried loads in the base of the crust of Borborema Plateau (NE Brazil) from Bouguer admittance estimates, *Journal of South American Earth Sciences*, *37*, 60-76.

Padilha, A. L., I. Vitorello, M. B. Pádua, and M. S. Bologna (2006), Lithospheric and sublithospheric anisotropy beneath central-southeastern Brazil constrained by long period magnetotelluric data, *Physics of the Earth and Planetary Interiors*, *158*(2), 190-209.

Panning, M. P., V., Lekićand B. A. Romanowicz (2010), Importance of crustal corrections in the development of a new global model of radial anisotropy, *Journal of Geophysical Research: Solid Earth*, *115*(B12).

Panning, M., and B. Romanowicz (2006), A three-dimensional radially anisotropic model of shear velocity in the whole mantle, *Geophysical Journal International*, *167*(1), 361-379.

Pearson, D. G., F. E. Brenker, F. Nestola, J. McNeill, L. Nasdala, M. T. Hutchison, S. Matveev, K. Mather, G. Silversmit, S. Schmitzand and B. Vekemans (2014), Hydrous mantle transition zone indicated by ringwoodite included within diamond, *Nature*, *507*(7491), 221-224.

Pereira, R. S., and R. A. Fuck (2007), Archean nucleii and the distribution of kimberlite and related rocks in the São Francisco craton, Brazil, *Brazilian Journal of Geology*, *35*(4), 93-104.

Perlingeiro, G., P. M. Vasconcelos, K. M. Knesel, D. S. Thiede, and U. G. Cordani (2013), 40 Ar/39 Ar geochronology of the Fernando de Noronha Archipelago and implications for the origin of alkaline volcanism in the NE Brazil, *J. Volcanol. Geotherm., Res.249*, 140-154.

Pesicek, J. D., E. R. Engdahl, C. H. Thurber, H. R. DeShon, and D. Lange (2012), Mantle subducting slab structure in the region of the 2010 M8. 8 Maule earthquake (30–40 S), Chile, *Geophysical Journal International*, *191*(1), 317-324.

Pinheiro, A. G., and J. Julià, (2014), Normal thickness of the upper mantle transition zone in NE Brazil does not favour mantle plumes as origin for intraplate Cenozoic volcanism, *Geophys. J. Int.*, *199*(2), 996-1005.

Ramos, V. A. (2009), Anatomy and global context of the Andes: Main geologic features and the Andean orogenic cycle, *Geological Society of America Memoirs*, *204*, 31-65.

Ramos, V. A., and A. Aleman (2000), Tectonic evolution of the Andes, In: *Tectonic Evolution of South America*, U.G. Cordani, E.J. Milani, A. Thomaz-Filho, D.A. Campos, *31*, 635-685. 31st International Geological Congress, Rio de Janeiro.

Read, G., H. Grutter,S. Winter, N. Luckman, F. Gaunt, and F. Thomsen (2004), Stratigraphic relations, kimberlite emplacement and lithospheric thermal evolution, Quiricó Basin, Minas Gerais State, Brazil, *Lithos*, *77*(1), 803-818.

Renne, P. R., J. M. Glen, S. C., Milner and A. R. Duncan (1996), Age of Etendeka flood volcanism and associated intrusions in southwestern Africa, *Geology*, *24*(7), 659-662.

Ringwood, A. E. (1975), *Composition and Petrology of the Earth's Mantle*, McGraw-Hill, New York.

Ritsema, J., A. Deuss, H. J., Van Heijst, and J. H. Woodhouse (2011), S40RTS: a degree-40 shear-velocity model for the mantle from new Rayleigh wave dispersion, teleseismic traveltime and normal-mode splitting function measurements, *Geophysical Journal International*, *184*(3), 1223-1236.

Rocha, M.P., M. Schimmel, and M. Assumpção (2011), Upper-mantle seismic structure beneath SE and Central Brazil from P- and S-wave regional traveltime tomography, *Geophys. J. Int.*, *184*, 268–286, doi:10.1111/j.1365-246X.2010.04831.x.

RSBR, (2014), Boletim Sismico Brasileiro v2014.06, Rede Sismografica Brasileira, Available at: http://www.rsbr.gov.br/catalogo_sb.html.

Russo, R. M., and P. G. Silver (1994), Trench-parallel mantle flow beneath the Nazca plate: Results from seismic anisotropy, *Science, 263*, 1105–1111.

Russo, R. M., J. C. VanDecar, D. Comte, V. I. Mocanu, A. Gallego and R. E. Murdie (2010), Subduction of the Chile Ridge: Upper mantle structure and flow, *GSA Today*, *20*(9), 4-10.

Sá, N. C., N., Ussami, and E. C. Molina (1993), Gravity map of Brazil: 1. Representation of free-air and Bouguer Anomalies, *Journal of Geophysical Research: Solid Earth*, *98*(B2), 2187-2197.

Santos, J.O.S., G.J. Rizzotto, P.E. Potter, N.J. McNaughton, R.S. Matos, L.A. Hartmann, F. Chemale, and M.E.S. Quadros, (2008), Age and autochthonous evolution of the Sunsás Orogen in West Amazon Craton based on mapping and U–Pb geochronology, *Precambrian Research*, *165*(3), 120-152.

Schimmel, M., M. Assumpção, and J.C. VanDecar (2003), Seismic velocity anomalies beneath SE Brazil from P and S wave travel time inversions, *J. Geophys. Res.*, *108,* No. B4, doi:10.1029/2001JB000187.

Schmerr, N., and E. J. Garnero (2007), Upper mantle discontinuity topography from thermal and chemical heterogeneity, *Science*, *318*(5850), 623-626.

Schobbenhaus, C. and B.B. Brito Neves (2003), Geologia Do Brasil no Contexto da Plataforma Sul-Americana In: Bizzi, L.A.; Schobbenhaus, C; Vidotti, R.M.; Gonçalves J.H. (Eds.) *Geologia, Tectônica e Recursos Minerais Do Brasil*, Texto, Mapas e Sig. CPRM-Serviço Geológico Do Brasil, 5-54.

Scire, A. (2015), Imaging variations in the Central Andean mantle and the subducting Nazca Slab with teleseismic tomography, Ph.D. thesis, The University of Arizona. Arizona, USA.

Segev, A. (2002), Flood basalts, continental breakup and the dispersal of Gondwana: evidence for periodic migration of upwelling mantle flows (plumes), *EGU Stephan Mueller Special Publication Series*, *2*, 171-191.

Sgarbi, P. B., L. M. Heaman, and J. C. Gaspar (2004), U–Pb perovskite ages for brazilian kamafugitic rocks: further support for a temporal link to a mantle plume hotspot track, *J. South Amer. Earth Sci.*, *16*(8), 715-724.

Simmons, N. A., A. M. Forte, L. Boschi, and S. P. Grand (2010), GyPSuM: A joint tomographic model of mantle density and seismic wave speeds, *Journal of Geophysical Research: Solid Earth*, *115*(B12).

Simmons, N. A., S. C. Myers, G. Johannesson, and E. Matzel (2012), LLNL-G3Dv3: Global P wave tomography model for improved regional and teleseismic travel time prediction, *J. Geophys. Res.*, *117,* B10302, doi:10.1029/2012JB009525.

Tauzin, B., E. Debayle, and G. Wittlinger (2008), The mantle transition zone as seen by global Pds phases: no clear evidence for a thin transition zone beneath hotspots, *Journal of Geophysical Research: Solid Earth*, *113*(B8).

Tesoniero, A., L. Auer, L. Boschi, and F. Cammarano (2015, April), SPani, a whole-mantle VP and VS model: Implications on thermo-chemical structure, In *EGU General Assembly Conference Abstracts* (*17*, p. 10514).

Thiede, D. S., and P. M. Vasconcelos (2010),. Paraná flood basalts: rapid extrusion hypothesis confirmed by new 40Ar/39Ar results, *Geology*, *38*(8), 747-750.

Thompson, R. N., S. A Gibson, J. G. Mitchell, A. P. Dickin, O. H. Leonardos, J. A. Brodand and J. C. Greenwood (1998), Migrating Cretaceous Eocene Magmatism in the Serra do Mar Alkaline Province, SE Brazil: Melts from the Deflected Trinidade Mantle Plume?, *J. Petrol.*, *39*(8), 1493-1526.

Thomson, A. R., S. C. Kohn, G. P. Bulanova, C. B. Smith, D.Araujo, and M. J. Walter (2014), Origin of sub-lithospheric diamonds from the Juina-5 kimberlite (Brazil): constraints from carbon isotopes and inclusion compositions, *Contributions to Mineralogy and Petrology*, *168*(6), 1-29.

Torsvik, T. H., K. Burke, B. Steinberger, S. J. Webb, and L. D. Ashwal (2010), Diamonds sampled by plumes from the core-mantle boundary, *Nature*, *466*(7304), 352-355.

USGS, (2015), National Earthquake Information Center Catalog. United States Geological Survey. Available at http://earthquake.usgs.gov/data.

Van Der Lee, S., D. James, and P. Silver (2001), Upper mantle S velocity structure of central and western South America, *Journal of Geophysical Research. B. Solid Earth*, *106*, 30.

VanDecar, J. C., R. M. Russo, D. E. James, W. B. Ambeh, and M. Franke (2003), Aseismic continuation of the Lesser Antilles slab beneath continental South America, *Journal of Geophysical Research: Solid Earth*, *108*(B1).

VanDecar, J.C., James, D. E., and M. Assumpçao (1995), Seismic evidence for a fossil mantle plume beneath South America and implications for plate driving forces, *Nature*, 378, 25–31, doi: 10.1038/378025a0.

Vauchez, A., A. Tommasi, G. Barruol, and J. Maumus (2000), Upper mantle deformation and seismic anisotropy in continental rifts, *Physics and Chemistry of the Earth, Part A: Solid Earth and Geodesy*, *25*(2), 111-117.

Walter, M.J., S.C., Kohn, D., Araujo, G.P., Bulanova, C.B., Smith, E., Gaillou, J., Wang, A. Steele, and S.B. Shirey, (2011), Deep mantle cycling of oceanic crust: evidence from diamonds and their mineral inclusions, *Science*, *334*(6052), 54-57.

Widiyantoro, S. (1997), Studies of seismic tomography on regional and global scale, Ph.D. thesis, Aust. Natl. Univ., Canberra, A. C. T., Australia.

Wirth, R., C. Vollmer, F. Brenker, S. Matsyuk, and F. Kaminsky (2007), Inclusions of nanocrystalline hydrous aluminium silicate “Phase Egg” in superdeep diamonds from Juina (Mato Grosso State, Brazil), *Earth and Planetary Science Letters*, *259*(3), 384-399.

Wirth, R., F. Kaminsky, S. Matsyuk, and A. Schreiber (2009), Unusual micro-and nano-inclusions in diamonds from the Juina Area, Brazil, *Earth and Planetary Science Letters*, *286*(1), 292-303.

Wessel, P. and W. H. F. Smith, (1998), New, improved version of the Generic Mapping Tools released, *EOS Trans. AGU*, 79, 579.

Wölbern, I., B. Heit, X. Yuan, G. Asch, R. Kind, J. Viramonte, S. Tawackoliand H., Wilke (2009), Receiver function images from the Moho and the slab beneath the Altiplano and Puna plateaus in the Central Andes, *Geophysical Journal International*, *177*(1), 296-308.

Zedgenizov, D. A., A. Shatskiy, A. L. Ragozin, H. Kagi, and V. S. Shatsky (2014a), Merwinite in diamond from São Luiz, Brazil: A new mineral of the Ca-rich mantle environment, *American Mineralogist*, *99*(2-3), 547-550.

Zedgenizov, D. A., H. Kagi, V. S. Shatsky, and A. L. Ragozin (2014b), Local variations of carbon isotope composition in diamonds from Sao-Luis (Brazil): evidence for heterogenous carbon reservoir in sublithospheric mantle, *Chemical Geology, 363*, 114-124.

Zedgenizov, D. A., V. S. Shatsky, A. V. Panin, O. V. Evtushenko, A. L. Ragozin, and H. Kagi (2015), Evidence for phase transitions in mineral inclusions in superdeep diamonds of the Sao Luiz deposit (Brazil), *Russian Geology and Geophysics*, *56*(1), 296-305.

VITA

Bruno de Almeida Goetze was born in Sao Leopoldo, Rio Grande do Sul, Brazil on July 14, 1985. During high-school, he obtained the Telecommunications Systems technician certification, function which he exercised professionally for 5 years. He sought his first college degree after this period, graduating as a Geological Engineer at the Federal University of Pelotas (UFPel, Brazil) in July, 2014. In August of the same year, he started his graduate studies at the Missouri University of Science and Technology. In May, 2016, he was awarded the Master of Science in Geology and Geophysics degree.

As an undergraduate, he was granted a research scholarship to work at the UFPel's Paleontology and Stratigraphy Laboratory for three years, having the opportunity to integrate field work expeditions, attend research events and receive certifications. Among these, his contribution to the organization of the Brazilian Paleontology Meeting (23rd CBP) and stratigraphy certification obtained at the event are highlighted. At UFPel, he acted as vice-president and president of the Geological Engineering student council for two consecutive years, organizing two local meetings.

As a graduate student his focus was dedicated almost exclusively to geophysics. In the majority of his time away from classes, he worked with seismic data from South America. Additionally, he was an active member in the American Geophysical Union (AGU) and Society of Exploration Geophysics (SEG), attending meetings and presenting one poster. Similar affirmations can be made about his involvement in the Brazilian Geological Society (SBG) and poster presentations at the Brazilian Paleontology Meetings (CBP).